Høgskolen i Telemark
Telemark University College

NERSC
Nansen Environmental and
Remote Sensing Center

Sea Ice Studies in the Northern Sea Route by use of Synthetic Aperture Radar

by

Maria Lundhaug

Dr. Ing. Thesis

February 2002

NTNU
the Norwegian University of Science and Technology

URN:NBN:no-2344

Abstract

The main objective of this thesis is to contribute to the understanding of sea ice processes in the Northern Sea Route, mainly with use of remote sensing data from Synthetic Aperture Radar (SAR). Multivariate data analysis is the main tool used in this work. SAR signatures of different sea ice types and open water in winter were studied, and separation of water and sea ice types using different multivariate regression algorithms was done. Polynya areas along the coasts were investigated. Structure characteristics of different sea ice types and open water were investigated. The summer sea ice in the Laptev Sea was also studied. The Laptev Sea as well as other parts of the Northern Sea Route are expected to become important areas for future oil and gas exploration and exploitation.

Results from a statistical analysis of 105 SAR images and corresponding meteorological data are presented, covering parts of the Pechora and Kara Sea in the Russian Arctic. Wind, temperature and other variables for the SAR sample areas were collected, and a manual sea ice classification of the SAR samples was performed. All variables were input to different multivariate regression techniques. First, ice was separated from water. Next, young ice was separated from rough first year ice. The study indicated that the mean and standard deviation of the backscattering coefficients together with temperature values were the most important information to separate the classes.

SAR image data has been used to investigate specific polynya events in detail, addressing widths, refreezing and duration. A polynya index derived from ice concentration data from Special Sensor Microwave Imager (SSM/I) was used in the description of polynya variability during a decade (1990-1999) in response to atmospheric forcing. The observed polynya widths were compared to the results from a simple one-dimensional polynya model. The best agreement was found for the Vize and Ushakova Island and the Novaya Zemlya coast due to low variability of polynya widths. Less agreement was found at the Yamal and Taymyr due to high polynya variability not captured by the model.

Sample areas of open water, young ice and first year ice were investigated by the angle measure technique (AMT) and classified by multivariate regression. The separation of ice and water was relatively sucessfull, opposed to the separation of young ice and first year ice. The individual samples were best separated on one pixel scale, corresponding to backscattering differences between neighboring pixels. The AMT produce mean angle information that to some extent can be related to ice type.

URN:NBN:no-2344

Finally, a demonstration and validation study of the capabilities of SAR imagery to provide accurate ice information to support ice navigation was carried out. The experiment was set up in August-September 1997. RADARSAT and ERS-2 SAR images combined with SSM/I data and *in situ* observations from icebreakers were used. These data were used to analyze ice concentration, ice types, ice drift and other ice features present in this period. The capability of RADARSAT ScanSAR and ERS SAR images to determine these ice parameters during late summer conditions in the Laptev Sea area is discussed.

URN:NBN:no-2344

Acknowledgments

This work was funded by a dr. ing. grant from Telemark University College (HiT), Department of Technology, Porsgrunn, Norway with further support from Nansen Environmental and Remote Sensing Center (NERSC), Bergen, Norway.

I would like to thank my supervisors Prof. Kim H. Esbensen (HiT) and Prof. Ola M. Johannessen (NERSC) for their valuable comments and suggestions during the writing of the thesis. Research Director Stein Sandven (NERSC) has reviewed my work and suggested research approaches. I would also like to thank all the people at NERSC and HiT who have helped and encouraged me in different ways.

The work during these three years would have been much harder without the support and encouragement from Tor, my parents, Kamilla and good friends.

Non numeranda, sed ponderanda argumenta.

URN:NBN:no-2344

Contents

URN:NBN:no-2344

Chapter 1

Introduction

1.1 Background

1.1.1 Northern Sea Route

The Northern Sea Route (North East Passage) is an important ship route for trade between Europe and Northern Asia (Frank, 2000; Peresypkin, 2000; Østreng, 1999). It connects the Barents Sea in west to the Bering Strait in east (Figure 1.1). Compared to other routes from west to east, the shorter distance may give the advantage of saving 6-12 days of sailing time (Peresypkin, 2000). The ice conditions restrict sea transportation, which requires ice classified vessels as well as icebreaker assistance throughout the year. In summer, there is traffic in the whole sailing route, whereas in winter it is mainly in the western part serving ports by the Yenisey River. Since large areas of the Northern Sea Route are ice covered during several months of the year, near real-time sea ice monitoring is of great importance for timely and economical navigation as well as security (Johannessen et al., 2000; Bushuev et al., 1998; Grishchenko et al., 1999; Sandven et al., 1999a).

The regions of the Pechora and the Kara Seas are investigated in this study. The largest concentration of foreign investments in the oil and gas industry is in this western part of the Russian Arctic along the coasts and shelves of the Barents and Pechora Seas due to huge deposits of oil and gas resources (Andreeva, 1998; Granberg, 1998; Khvochtchinski and Batskikh, 1998). Exploitation of oil and gas deposits in the Timano-Pechora

province, the Yamal Peninsula and the shelves of the Barents, Pechora and Kara Seas will increase the activity in the western part of the Northern Sea Route. The benefit of this route is shorter sailing time between Europe and Asia and it is more cost effective compared to the railway system. Low reliability, high risk and lack of regularity of voyages due to the complex ice conditions make this route less useful during winter than other routes (Granberg, 1998).

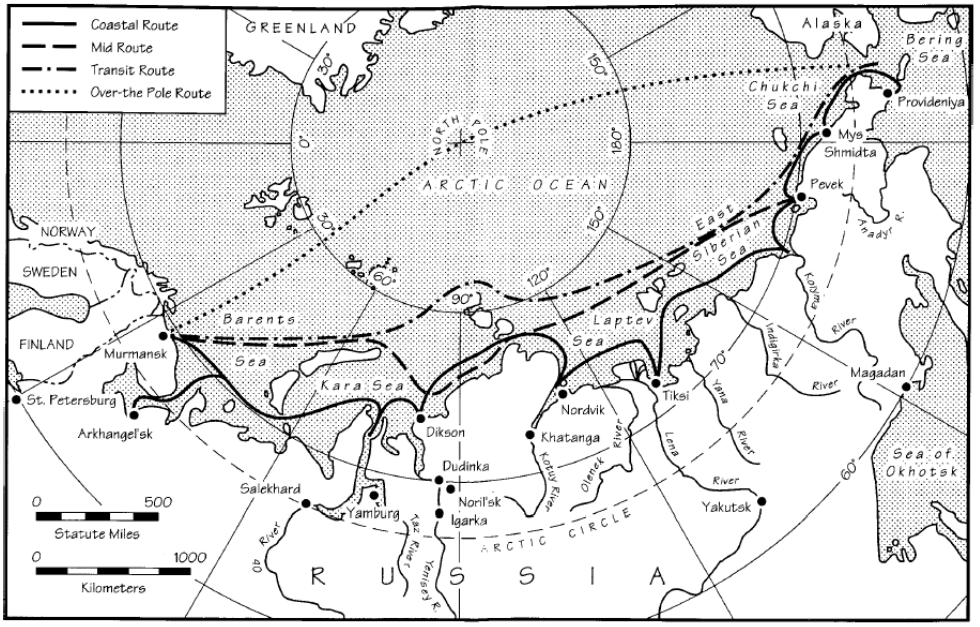

Figure 1.1: *The various options of navigation in the Northern Sea Route (figure from Mulherin et al., 1994).*

Among major threats to the Arctic marine environment of the Pechora region are overfishing, heavy metal and radioactive pollution and contamination from persistent organic pollutants (AMAP, 1998). The most serious concerns are caused by the future large-scale exploitation and transportation of hydrocarbons found in the Yamal and Pechora region (Backlund, 1995). Large oil spills from tanker accidents or pipeline ruptures will have a significant impact on the Arctic environment (Gavrilo et al., 1998; Vefsnmo, 1999). If a possible accident happens during winter, low temperatures and the absence of light will prevent evaporation and photolytical dissociation of the different oil components and thereby increase the period of acute toxicity (Sakshaug, 1992; Wadhams, 2000). Other

sources of oil pollution are the numerous small spills and continual discharges of drill cuttings, drilling muds and produced water during routine operation. They contribute significantly to the oil pollution and are important in their long-term effect on populations.

Industries and agencies operating in ice covered waters include commercial shipping companies, offshore oil exploration companies, fisheries, military, regulatory agencies and research institutions. Other industrial sectors need ice information when designing ship hulls and offshore drilling platforms to perform risk assessment (Brigham, 2000). Remote sensing sensors are cost-effective tools to provide sea ice information to these users (Bertoia et al., 1998). High-resolution image data from remote sensing satellites can be used to identify and map ice types of interest to navigators. Definitions of ice types are based on the age of the sea ice, which is to some extent correlated to its thickness and strength (World Meteorological Organization, 1970). Because of their strength and hardness, multi year sea ice and icebergs are significant hazards to ships and offshore structures (Gill, 2001; Power et al., 2001). Captains of vessels with no ice-strengthening require ice edge and iceberg information in order to plan routes to avoid all ice. Captains of vessels with some degree of ice capability require information about ice thickness and ice concentration distribution. All vessels use information about leads and polynyas to choose paths of least resistance to use less fuel (Bertoia et al., 1998). Generally, the images are interpreted with the use of meteorological data, general ice information and information about ocean currents.

A factor that can impede the progress of ice-strengthened vessels is the movement of the sea ice in response to wind and ocean currents (Johannessen et al., 1997b), and the pressure that is created within the ice floes. Monitoring requires frequent and repeated data coverage. For example, the daily coverage north of 65° N of the satellite sensor RADARSAT ScanSAR makes effective tracking of sea ice motion possible (Bertoia et al., 1998). The ability to track sea ice will degrade at lower latitudes where the revisit period is increased, the floe size smaller and ice velocities faster.

1.1.2 Sea ice in the Arctic

The presence of sea ice influences the temperature and circulation patterns of both the atmosphere and the oceans (Wadhams, 2000). It plays an important role in the surface

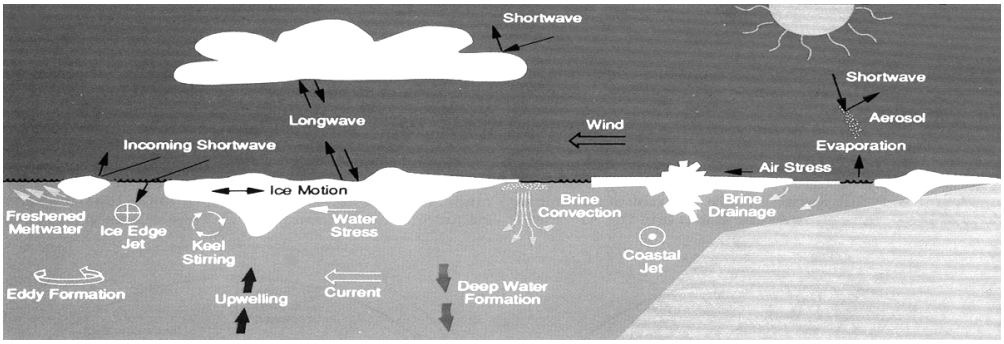

Figure 1.2: *Physical processes of the air, sea and ice interaction (figure from Carsey et al., 1992).*

radiation budget. Sea ice reduces the amount of solar radiation absorbed at the ocean's surface and serves as a strong insulator, restricting exchanges of heat, mass, momentum and chemical constituents between the atmosphere and the ocean. Due to of its high albedo, sea ice can reflect up to 90 % of the solar radiation (Barber et al., 1998). On the other hand, the open ocean absorbs most of the solar energy (85-90 %) due to its low albedo. Ice on the sea increases the global atmospheric circulation by reducing the heat exchange between water and air. The air over polar ice grows colder, increasing the temperature difference between polar and tropical atmosphere, and heat is transported from lower to higher latitudes by the atmospheric circulation. The seasonal freezing and thawing of ice is important in moderating polar temperatures due to the latent heat of fusion. Heat is released to the atmosphere during freezing and absorbed during melting. The density of the water under the ice increases when brine is released during freezing, and this induces convection (Volkov et al., 2002; Wadhams, 2000). When fresh water is created in the melting process, the stability of the upper layer increases, inhibiting convection. Different physical processes of the air, sea and ice interaction are illustrated in Figure 1.2.

Formation of sea ice is dependent of air temperature, wind and ocean currents (Grenfell et al., 1992). Freezing starts at the surface with the formation of small platelets and needles called frazil ice. The different conditions under formation and growth of the ice makes the physical properties very different even for sea ice in the same thickness interval. Figure 1.3 gives an overview of formation of sea ice under different environmental processes.

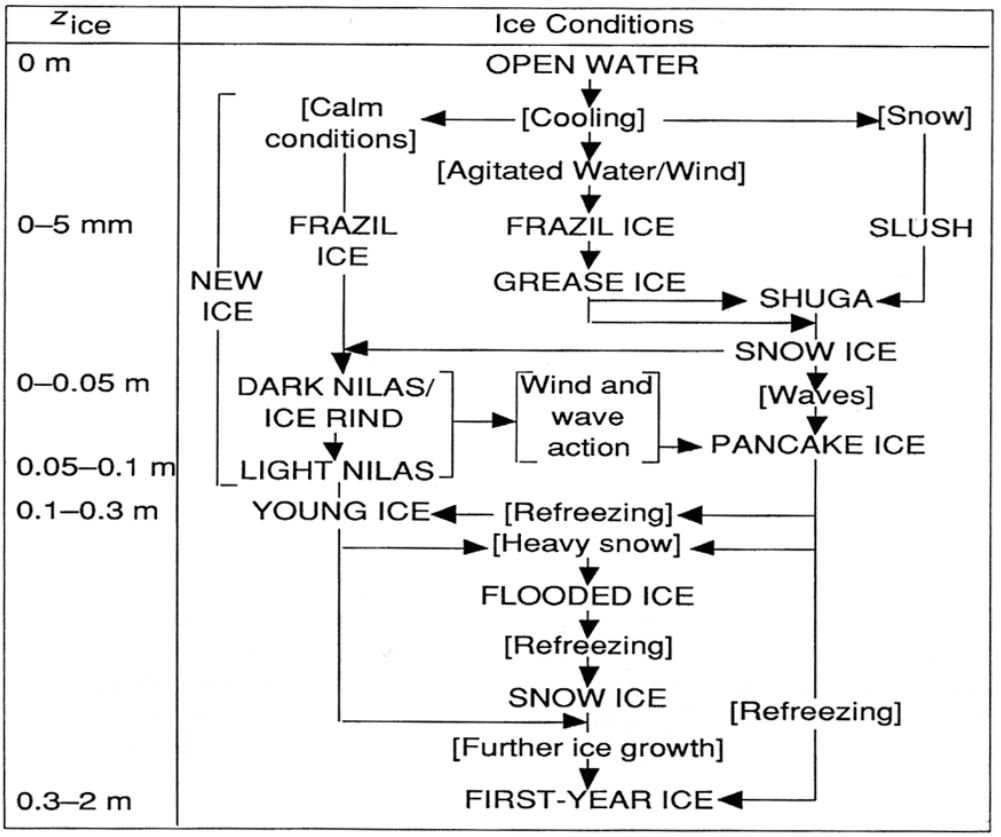

Figure 1.3: *Evolution of sea ice (figure from Grenfell et al., 1992).*

URN:NBN:no-2344

Sea water contains 20-35 parts per thousand salt (Pond and Pickard, 1983). Sea ice consists of frozen water, brine and air. It has been shown that the reflectance and emission properties of the ice are dependent on an average of these constituent parts (Barber et al., 1998). As the sea ice surface consolidates, the salt present in the sea water are slowly rejected from the solution and trapped in elliptical brine pockets. Further ice thickening happens through downward growth as a result of heat loss to the atmosphere and a characteristic columnar structure with vertical basal planes is produced in the ice. The growing of ice releases brine in the ocean. If sea ice could be frozen extremely slowly, pure ice would be the result because of rejection of all salts during the freezing process. However, the freezing rate is normally too rapid to allow pure ice to form, thus brine is trapped in the lattice structure of ice. The dominant mechanisms for brine loss from growing sea ice are gravity drainage and brine expulsion (Tucker III et al., 1992). Ice which has only survived for one season is usually termed first year ice (World Meteorological Organization, 1970). The following warm season may create ponds of melted water on the surface (Yackel et al., 2000; Yackel and Barber, 2000; Hanesiak et al., 2001), but more importantly the brine inclusions will expand and drain into the sea. As a result, ice which has survived for more than one year will be lower in brine content and contain a layer of melted and subsequently re-frozen ice on its surface. Typical values of sea ice salinity are 5-12 parts per thousand for sea ice up to 1 m thickness. For multi year ice up to 3 m the salinity varies up to 5 parts per thousand (Tucker III et al., 1992).

The smooth and thin new sea ice is influenced as it develops by temperature fluctuations, compressive and shear forces, surface currents and wind. Ridge formation and surface roughness increases with age. The angular edges and the smooth surfaces of first year ice floes are transformed into more rounded edges with hummocky-ridged surfaces that are characteristic of multi year ice, or ice that has survived a summer's melt and is more than one year old (World Meteorological Organization, 1970). As winter progresses, the ice thickens and snow accumulates on top of it. Hanesiak et al. (1999) found that diurnal changes in the surface energy balance directly affect the snow depth, albedo and surface temperature. These parameters again affect the seasonal ice evolution.

The sea ice cover is a dynamic system, and openings occur throughout the winter, even when ice concentrations are highest. Leads are elongated, curvilinear or piecewise linear openings in the ice cover. Polynyas are more irregular polygonal openings that often form at the same location (Smith et al., 1990; Miles and Barry, 1998). Lead density are highest

URN:NBN:no-2344

in early winter, decreasing 20 % from November through April. The mean distribution of lead density and lead orientation are associated with large scale mean fields of ice divergence and ice shear respectively (Miles and Barry, 1998). For sea ice, a range of physical scales are of interest (Li et al., 1998). Large scale sea ice dynamics problems involve complex forcing and deformation processes that occur on the scale of hundreds of kilometers and affecting sea ice signatures. Optical and electromagnetic properties of the sea ice are influenced by the sizes of individual brine and gas inclusions (Cole, 2001).

The presence of sea ice affects the biological activities in the ocean since it absorbs most of the solar radiation, which is a vital requirement for marine life (Sakshaug, 1992). The sea ice edge enhanced spring biological productivity is caused by the release of nutrients from melting sea ice. The main physical and ecological processes associated with the summer melt in the marginal ice zone (MIZ) were investigated by Falk-Petersen et al. (2000) in the northern Barents Sea. From early spring, solar radiation penetrated both leads and the ice and initiating algae production under the ice. The melt ponds acted as windows, permitting the transmission of incoming solar radiation through to the underlying sea ice, accelerating the melting process and enhancing the primary production.

1.1.3 Sea ice as a sensitive indicator of climate change

To detect climate change and assess the impact of climate change, the key variables for observation of sea ice are spatial extent, ice thickness distribution, ice motion and open area within the ice cover (Wadhams, 2000). The heat balance is strongly influenced by the ice thickness distribution (Maykut, 1978). Even thin ice less than 0.3 m can reduce the heat flux considerably compared to ice free areas (Eisen and Kottmeier, 2000). Sea ice drift, deformation and shear create openings in the ice as well as ridges in areas of convergence. Changes in ice extent, area coverage and thickness are responses to both atmospheric and oceanic processes (Haas and Eicken, 2001; Willmott et al., 1997).

Remote sensing is the most efficient way to obtain data on a global scale. It can be used to study climatic changes, pollution and land use. One such area of interest is the study of sea ice and its role in the climate system. Two decades of microwave satellite observations have established a 3 % per decade decrease in total ice extent in the Arctic (Johannessen et al., 1995; Johannessen and Miles, 2000; Bjørgo et al., 1997). The area of multi year ice in winter has decreased about 7 % per decade (Johannessen et al.,

1999). Hilmer and Lemke (2000) found a 4 % decrease per decade in sea ice volume. Vinnikov et al. (1999) found that it is not likely that the decrease in sea ice extent found by satellite and surface based observations is a result of natural variability. The extent of ice in the Nordic Seas measured in April has decreased by 33 % over the past 135 year (Vinje, 2001). Model predictions indicate substantial changes in Arctic sea ice extent and thickness, with about 80 % reduction expected in the summer ice extent at the end of this century (Johannessen et al., 2002).

Ice thickness has been more difficult to observe. Sea ice thickness in the Arctic is mostly assessed with data from upward sonar profiling by USA and British submarines since 1958 and 1971, respectively. Rothrock et al. (1999) found 1.3 m reduction of mean sea ice draft comparing the two time periods 1958-1976 and 1993-1997. The decrease was greater in the central and eastern Arctic than in the Beaufort and Chukchi seas. Wadhams and Davis (2000) found a decline in mean sea ice draft of 43 % when comparing two sea ice thickness profiles from 1975 and 1996 between the Fram Strait and the North Pole. From nine cruises from 1976 through 1994 on the Alaska to 90° N section, Tucker III et al. (2001) found abrupt thinning between 1988 and 1990. However, almost no average thinning was found in results from six submarine cruises from Alaska to 90° N during 1991 through 1997 (Winsor, 2001). Holloway and Sou (2001) argue that such rapid thinning is unlikely, and that the extreme results stems from undersampling. Varying winds which readily redistribute Arctic ice create a recurring pattern whereby ice shifts between the central Arctic and peripheral regions, especially in the Canadian sector. Timing and tracks of the submarine surveys missed this dominant mode of variability. These different opinions illustrate that it is important to measure sea ice thickness more accurate in future over as large areas as possible to add information to the knowledge from the sparse sampling available from submarines (Johannessen et al., 2002).

Changes in sea ice motion have been linked to the North Atlantic Oscillation (NAO) by Kwok (2000). Periods of high NAO index are characterized by a weakening of the surface high pressure and surface anti-cyclone in the Beaufort Sea and the intensification of the cyclonic circulation in the eastern Arctic Ocean. During the winters of 1988 through 1995, the oscillation has been in a positive phase affecting regional and total sea ice mass balance of the Arctic Ocean. The ice export through the Fram Strait has increased and the ice import from the Barents and Kara Seas has increased. There has been enhanced eastward ice transport from the Laptev Sea and the Transpolar Drift Stream has weak-

URN:NBN:no-2344

ened (Figure 1.4). The reduction in ice extent in the Nordic Seas and weakening of the Beaufort Gyre was also observed. The response of Arctic Ocean ice to these atmospheric changes has been studied with a thickness distribution sea-ice model coupled to an ocean model (Zhang et al., 2000). During a period of high NAO, a reduction of ice advection into the eastern Arctic from the Canada Basin was observed. Together with an increase of ice export through Fram Strait, both tend to deplete thick ice in the eastern Arctic Ocean and enhance it in the western Arctic. Both the model and satellite data show a significant reduction in ice extent in the eastern Arctic and in the Arctic Ocean as a whole. Monitoring of the global sea ice extent is important to get better parameterizations of sea ice in ocean-ice-atmosphere numerical models, and better understanding of the processes of heat and mass exchange between the ocean, ice and the atmosphere (Preller et al., 1992; Thomas et al., 1996; Zhang and Hunke, 2001; Parkinson et al., 2001).

1.1.4 Sea ice transport of sediments and pollution

The shallow continental shelves surrounding the Arctic Ocean are important for the transport of contaminants within the Arctic for three reasons; they are the primary areas of ice formation and ice melt; they have open water during part of the year, which allows for the exchange of contaminants between water and air; and they have high biological productivity, which provides a route for contaminants into the food web. A large number of radioactive sources are present in the Arctic such as storage of spent nuclear fuel, decommissioned nuclear submarines, nuclear reactors on land and on board ships and contained sources in the environment. Past atmospheric tests of nuclear weapons remain by far the largest global source of radioactive contamination. Most of the atmospheric tests were done before 1962, and atmospheric testing ceased entirely in 1980. Novaya Zemlya in Russia was the only site for atmospheric nuclear weapons tests in the Arctic (AMAP, 1998). The level of radioactive contamination of the Kara Sea is low compared to other seas, and it is at the global level (Volkov et al., 2002). However, the significant amount of dumped solid radioactive waste in the Kara Sea and nuclear facilities located at the Ob and Yenisey watersheds are potential release sources. The former Soviet Union dumped radioactive waste in the Arctic Seas during the years 1959-91, including six nuclear submarine reactors and a shielding assembly from an icebreaker reactor containing spent fuel. The solid waste and the nuclear reactors were dumped in the Kara Sea and in the fjords of Novaya Zemlya at depths of 12-135 m and in the Novaya Zemlya Trough at a

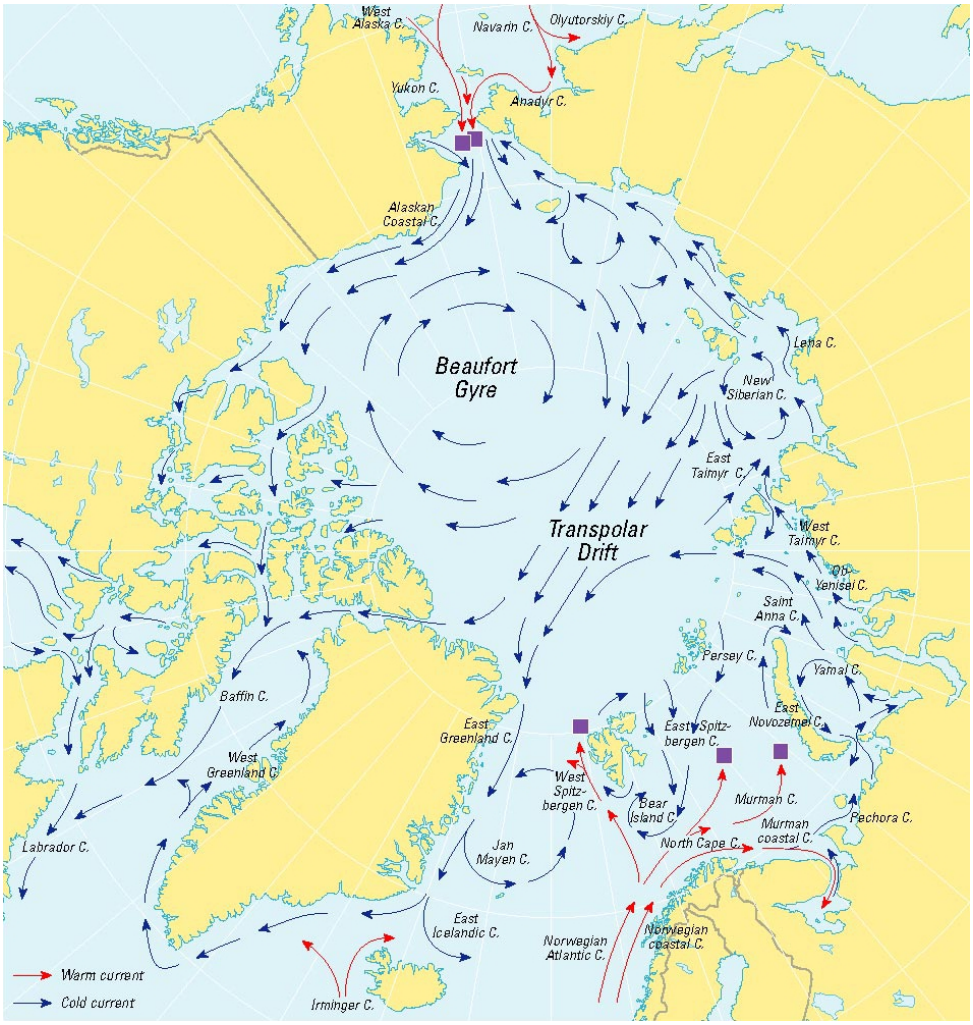

Figure 1.4: *The predominant currents in the Arctic Ocean and their major routes of the Arctic (figure from AMAP, 1998).*

URN:NBN:no-2344

depth of 300 m. The liquid, low-level waste was dumped into the open Barents and Kara Seas. At the time of dumping, experts estimated that the spent nuclear fuels represented a total activity of $8.5 \cdot 10^{16}$ becquerels (AMAP, 1998).

Much of the ice formed in shallow regions with depths less than 50 m of the Siberian Seas entrains sediments and organic material and may therefore incorporate associated contaminants (Pfirman et al., 1995; Pfirman et al., 1997). Sea ice may transport pollutants from source areas to distant wildlife. Pavlov and Stanovoy (2001) found indications that export of radionuclides from the Kara Sea with drifting ice has a significant influence on the radioactive water pollution in the western Greenland Sea and off the shores of Greenland. Eicken et al. (2000) identified a key source area for entrainment and basin wide dispersal of sediments by sea ice near the New Siberian Islands. Ice advection from this area may play an important role in sedimentation downstream the varying Transpolar Drift (Mysak, 2001). The season of the potential release of radionuclides in the western Kara Sea is important (Dethleff et al., 2000). In summer, the radionuclides will be dislocated mainly by surface mixed water, and in winter the transport and dispersal will be connected to new ice formation and dense water rejection. Dethleff et al. (2000) found that a total of $0.39 \cdot 10^6$ tons of sediments can annually be entrained in lead ice along the eastern Novaya Zemlya. The amount of lead ice sediments which may be exported from the Kara Sea to the central Arctic basin is about $0.21 \cdot 10^6$ ton/year.

Laptev Sea is also an important sea ice production area. Ice production in the Laptev Sea flaw lead during the 1991 and 1992 winter season was investigated by Dethleff et al. (1998). Laptev Sea flaw lead produced 2.6 % of the ice annually formed in the entire Arctic Mediterranean Sea and contributed to about 9 % of the volume of the Siberian branch of the Transpolar drift ice system. The contribution of lead ice to the entire volume of annually formed pack in high northern latitudes is only roughly 1.3 %. Rigor and Colony (1997) investigated sea-ice production and transport of pollutants in the Laptev Sea in the period of 1979-1993. They estimated that a mean of 256000 km^2 of sea ice was produced annually in the shallow water area of the Laptev Sea during the October freeze-up and in the flaw lead during winter, accounting for about 20 % of the total ice area fluxing through the Fram Strait per year. Alexandrov et al. (2000a) calculated a mean winter sea ice outflow from the Laptev Sea of 483000 km^2 in the period 1979-1995. Based on remote-sensing data and an expedition during August-September 1993, the importance of the Laptev Sea as a source area for sediment-laden sea ice was studied

by Eicken et al. (1997). They observed that freeze-up started on 26 September and was completed after 19 days. Ice motion was derived from satellite imagery and drifting buoys and mean ice velocities of 0.04 m/s and 0.05 m/s were found. With a best-estimate sediment load of 16 ton/km^2 (ranging between 9 and 46 ton/km^2), sediment export from the eastern Laptev Sea amounted to $4 \cdot 10^6$ ton/year, with extremes of $2 \cdot 10^6$ and $11 \cdot 10^6$ ton/year.

A model study investigated the dispersion of river water from Ob, Yenisey and Lena for the transport of possible river contaminants in the Arctic Ocean (Harms et al., 2000). These Siberian rivers are supposed to be important sources for various contaminants. Kara Sea river water clearly dominates in the Siberian branch of the Transpolar Drift, while the Lena water dominates in the Canadian branch. The Kara Sea retrieves about 55 % (1290 km^3/year) of the total river run-off discharged to the Siberian Arctic (Pavlov and Pfirman, 1995). Yenisey tracers leave the Kara Sea towards the Arctic Ocean or the Laptev Sea, but Ob tracers spread also in the southern Kara Sea. During autumn, the incorporation of particles into freezing sea ice near the estuaries of Ob and Yenisey is very likely. Ice trajectories from Ob and Yenisey estuaries mostly drift towards the Barents Sea where the ice melts close to Svalbard. The model study confirmed that contaminant transport through sediment-laden sea ice offers a short and effective pathway for pollutant transport from Siberian rivers to the Barents and Nordic Seas.

Surface *in situ* observations are rare in areas of the Arctic and remote sensing data offer a possibility to study large sea ice areas for longer time periods. Accurate sea ice information from Synthetic Aperture Radar (SAR) data can support safe and efficient ice navigation and offshore operation in the Northern Sea Route. SAR data can be used to assess areas with open water and thin ice that are important for navigation and incorporation of sediments and pollution in sea ice during freezing. To monitor signs of climate change it is important to observe spatial extent of sea ice, ice motion and open areas within the ice cover.

1.2 Objectives

The main objective is to *improve the understanding of sea ice in the Northern Sea Route using SAR data and multivariate statistical methods.*

The specific objectives are defined to achieve the aim:

- Study SAR signatures of different sea ice types and open water in winter, and separate water and sea ice types using different multivariate regression algorithms (Chapter 3)
- Study polynyas where open water and thin ice areas exist in winter (Chapter 4)
- Study structure characteristics of different sea ice types and open water from SAR (Chapter 5)
- Study summer ice from SAR data (Chapter 6)

Figure 1.5 illustrates the connection between the different type of sea ice information corresponding to the specific objectives.

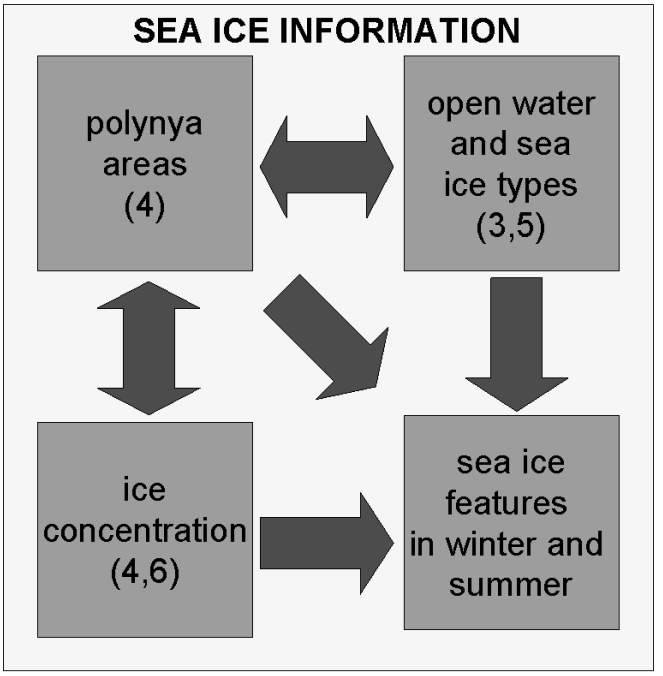

Figure 1.5: *Sea ice information obtained from the work presented in the different chapters.*

1.3 Approach

The time period in focus in this study is the 1990s when data from spaceborne SAR has been available for the research community. Information from ERS and RADARSAT SAR data has mainly been used in the work. Sea ice concentration data from Special Sensor Microwave Imager (SSM/I) data has also been used. Multivariate regression techniques were the most important tool for the work performed (Johnson and Wichern, 1992; Martens and Næs, 1989). These were used because the backscattering values of sea ice observed by SAR are dependent on several instrumental and environmental factors, and it was useful to asses which were valuable to use in the classification work. Also, the angle measure technique (AMT) was tested out for selected ice areas as a characterization tool (Andrle, 1994).

1.4 General outline of the thesis

General background of remote sensing of sea ice with the use of SAR and SSM/I is presented in Chapter 2. The following four chapters meets the objectives of the thesis. Chapter 3 (in press Canadian Journal of Remote Sensing) describes selected sea ice types and water by the backscattering signatures in the Kara and Pechora Seas. Results from a statistical analysis of 105 SAR images and corresponding meteorological data are presented, covering parts of the Pechora and Kara Sea in the Russian Arctic. Wind, temperature and other variables for the SAR sample areas were collected, and a manual sea ice classification of the SAR samples was performed. All variables were input to different multivariate regression techniques, which first were used to separate ice and water samples. In the following regression analyses the classes young ice and rough first year ice were separated from water, and the two ice types were separated from each other. In the separation of all ice types from water, correlation coefficients up to 0.90 between predicted and actual data values were achieved. Correlation coefficients were as high as 0.93 between predicted and actual values for open water and young ice and for open water and rough first year ice. When trying to separate young ice from rough first year, correlation coefficients of about 0.60 were obtained. The study indicated that the mean and standard deviation of the backscattering coefficients together with temperature values were the most important information to separate classes using regression techniques.

Chapter 4 (submitted to Canadian Journal of Remote Sensing) continues the work by focusing on the coastal polynyas that characterizes this area in winter. The main objective is to investigate polynyas in the Kara and Pechora Seas with use of satellite data and a one-dimensional polynya model. This study is limited to winter months in the 1990s, with the main focus on March when the maximum ice distribution in the Northern Hemisphere occurs. Synthetic Aperture Radar (SAR) image data has been used to investigate specific polynya events in detail, addressing widths, refreezing and duration. A polynya index derived from ice concentration data from Special Sensor Microwave Imager (SSM/I) was used in the description of polynya variability during a decade (1990-1999) in response to atmospheric forcing.

From SAR, the largest polynyas were found along the Taymyr Peninsula with mean with of about 40 km. Along the western coast of Yamal Peninsula and the area around the outlets of the Yenisey and Ob Rivers typical polynya widths were in the range of 20 to 30 km, with variability of tens of kilometers. Large polynyas were also measured in the Vaygach area and around Franz Josef Land.

The prevailing wind regime determine the number of polynya days in the south-eastern Kara Sea. With south-westerly winds, polynyas occur frequently such as in 1995 and 1996. Then a polynya occurred 55 and 56 out of 90 days. When the winds are in the opposite direction, polynyas occur less frequently (i.e. 1991, 1994, 1998, 1999). Polynyas occurred only 7 and 8 days in 1999 and 1991, respectively. The largest and longest lasting areas covered by polynyas occur in 1995, and the smallest area with short duration was in 1991.

The observed polynya widths from SAR were are compared to polynya widths calculated by a one-dimensional polynya model for nine different areas. Observed and predicted polynya width and opening time were compared for four days during March 1994 north-east of the Vaygach Island in the Kara Sea. To be from a simple one-dimensional model, the description of the polynya opening time and the steady-state polynya width is reasonable.

The best correspondence between observations and model results were found for the Vize and Ushakova Island and the Novaya Zemlya coast. The lowest variability of SAR observations was found in these areas, and the model predicted these widths better. The Yamal and Taymyr observed polynyas widths were highly variable, and these were not well pre-

dicted by the model. The use of different parameterizations of the collection thickness in the polynya model gave comparable results. The one-dimensional model may be too simple with to many assumptions for use in this area due to relatively complex coastline geometry and influence by currents and tides on sea ice drift. Data about the polynya ice edge relative to coastlines of different orientations and shapes may give valuable information for validation of a two-dimensional model where the affect of the coastline on polynya size and development are accounted for.

Chapter 5 (to be submitted) describes structure characteristics for selected sea ice types defined in the work presented in Chapter 3. The angle measure technique (AMT) is for the first time used to characterize the structure of open water and sea ice from Synthetic Aperture Radar (SAR) data. AMT has been suggested as an alternative to fractal analysis, and was originally developed to produce a data transform that could be used to characterize data variability. Sample areas of open water, young ice and first year ice SAR backscattering coefficients were input to the AMT algorithm. The AMT produces a transform by calculating geometric angles at several points of a vector defined by varying a scale parameter, and then the mean angles are calculated dependent of scale. Multivariate regression were used to separate ice types. Scaling of the input SAR data was found to be less useful through the regression tests. To get better results than could be obtained by AMT mean angles only, mean and standard deviation of the backscattering coefficient together with temperature were included in the regression. In the separation of ice and water the highest correlation coefficients was 0.85. For water and young ice the correlation coefficient was 0.93, and for water and first year the highest was 0.86. For the separation of the ice types young ice and first year ice the correlation was very low, the value 0.40 was achieved. The individual samples were best separated on one pixel scale, corresponding to backscattering differences between neighboring pixels. The mean angles from AMT can be related to ice type to some extent. The speckle property of SAR images may be the reason why this approach was not as useful for SAR data as for other data types. Information from mean and standard deviation of the backscattering coefficient is more useful than results from the more computer-demanding AMT algorithm.

In Chapter 6 (published in Canadian Journal of Remote Sensing) the summer sea ice that has been omitted in the other studies is investigated in the Laptev Sea in the eastern part of the Russian Arctic. The Laptev Sea area, including the Vilkitsky Strait, is an important part of the Northern Sea Route where the presence of sea ice makes navigation difficult

even in the summer season. The objective of this study was therefore to demonstrate and validate the capability of SAR imagery to provide accurate ice information to support ice navigation which is most important in late summer in this region. An experiment was set up in August-September 1997 with joint use of RADARSAT and ERS-2 SAR images combined with SSM/I data and *in situ* observations from icebreakers. These data were used to analyze ice concentration, ice types, ice drift and other ice features present in this period. The capability of RADARSAT ScanSAR and ERS SAR images to determine these ice parameters during late summer conditions in the Laptev Sea area is discussed. The Laptev Sea as well as other parts of the Northern Sea Route are expected to become important areas for future oil and gas exploration and exploitation, which will increase the demand for SAR ice monitoring to support ice navigation, drilling and other offshore operations.

In Chapter 7, summary and conclusions with a discussion of future work are given. A brief background for the multivariate statistical methods is presented in Appendix A. Definitions of sea ice terms are given in Appendix B.

URN:NBN:no-2344

Chapter 2

Remote sensing of sea ice

2.1 Background

Extensive research work has been done in the field of remote sensing of sea ice due to the importance of ice in global change monitoring and operational activities as shipping and offshore oil and gas exploration (Alexandrov et al., 2000b; Barber et al., 2001; Bertoia et al., 1998; Gill, 2001; Johannessen et al., 1999; Sephton and Partington, 1998). Satellite remote sensing of sea ice developed from airborne remote sensing. Reflected, emitted and backscattered electromagnetic energy is measured by different sensors (i.e. Comiso and Kwok, 1996). Cloud cover limits the use of sensors using the visible and infrared part of the electromagnetic spectrum during summer. The polar night is the restricting factor during winter. Visual and infrared observations from the Advanced Very High Resolution Radiometer (AVHRR) on the National Oceanic and Atmospheric Administration (NOAA) satellites are used extensively by meteorological institutes and ice centers (Johannessen et al., 1997a). Frequent cloud cover inhibits regular and reliable ice maps based on these data, especially in near real-time. Wavelengths in the microwave region are not significant attenuated by the atmosphere (Figure 2.1). Scanning Multichannel Microwave Radiometer (SMMR) and Special Sensor Microwave Imager (SSM/I) data have been used as the main data source for long term sea ice information on a global scale (Bjørgo et al., 1997; Cavalieri et al., 1999). The possibility to obtain data for large areas on a regular basis at low costs are the main advantages of this technology. The different Synthetic Aperture Radar (SAR) systems provide high resolution data, but the spatial

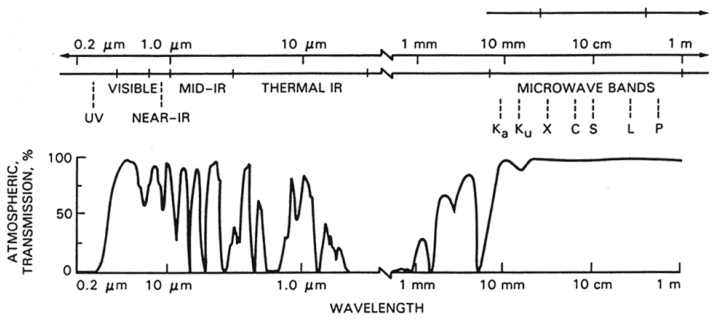

Figure 2.1: *The transmission capabilities of the atmosphere in the microwave area (figure from Henderson and Lewis, 1998).*

and temporal coverage is not as good as from the passive sensors. Scatterometer data has also proven useful for sea ice monitoring despite the coarse resolution (Drinkwater, 1998; Winebrenner et al., 1998).

Barber et al. (2001) reviewed current understanding of the physical and electrical properties of snow-covered sea ice throughout the annual cycle using SAR. Beaven et al. (1996) used active and passive microwave data for sea ice concentration estimates from a hybrid fusion technique by using information of multi year ice from SAR in a passive microwave algorithm. ERS and RADARSAT SAR together with SSM/I data were used for comparison of sea ice concentrations and polynya characterization in the Arctic (Dokken, 2000; 2002). This combination of high resolution SAR data with global coverage of SSM/I can provide increased understanding of both data sources and the physical processes studied.

2.2 Active microwave remote sensing of sea ice

The brief form of the general theory is adapted from basic textbooks and reports where more details can be found (Henderson and Lewis, 1998; Johannessen et al., 1994a; Johannessen et al., 1997a; Olmsted, 1993; Robinson, 1994).

Historical background

The first imaging radars were used during World War II, when the Plan Position Indicator (PPI) airborne radar was developed as an aid to night-time bombing. It produced a

circular image of the ground. After the war, the side-looking airborne radar (SLAR) was developed for terrain surveillance. It illuminates a strip parallel to the flight path. This real aperture radar has the disadvantage that a very large antenna is needed to achieve a high azimuth resolution. The US military developed in the 1950s the side-looking SAR and solved this problem. It uses signal processing to provide high azimuth resolution, independent of the distance between the antenna and the target. In the late 1960s SLAR and SAR technologies were declassified.

The first satellite carrying SAR was the short-lived Seasat (the United States) in 1978. It operated in three months at L band. The S band Kosmos 1870 (the Soviet Union) operated for two years in 1987-1989. There have been three L band shuttle imaging radar missions sponsored by NASA (SIR-A, 1981, SIR-B, 1984 and SIR-C, 1994). Their orbits and 1-week duration precluded significant observation of ice phenomena. An increasing number of SAR systems in the 1990s have provided high resolution data over relatively large areas. Almaz (S band, Russia) was launched in March 1991 and the mission terminated in October 1992. J-ERS-1 SAR (L band, Japan) began operation in April 1992. The three satellite sensors ERS-1 SAR (launched July 1991 and the mission ended in March 2000), ERS-2 SAR (launched May 1995) and RADARSAT-1 (launched November 1995) have provided data for the work presented in Chapter 3 to 6. SAR is especially valuable for sea ice monitoring on a regional scale, to give information for navigation (Vainio et al., 2000), fishing (Kourti et al., 2001), iceberg monitoring (Gill, 2001; Sephton and Partington, 1998) and transportation and exploration of oil and gas. In the remote and extensive areas affected by sea ice, radar remote sensing has been able to provide comprehensive, timely, and accurate information because of their all-weather, day/night and high-resolution imaging capability. Both ERS and RADARSAT SAR are used in operational sea ice monitoring in several countries (Johannessen et al., 1996a; Shokr et al., 1996; Ramsay et al., 1998; Vainio et al., 2000; Gill et al., 2000).

Advantages of microwave technology

The wavelengths of electromagnetic radiation most commonly used for remote sensing of the Earth are the spectrum of visible light, a wide spectrum of radio wavelengths and several infrared wavelengths. The radar (RAdio Detection And Ranging) data is generally independent of solar radiation and atmospheric conditions. The power, frequency

and polarization of the emitted electromagnetic radiation can be controlled for specific objectives.

The ability of the SAR to pass relatively unaffected through clouds and precisely measure distances makes it especially useful for sea ice monitoring (Johannessen et al., 2000), surface deformation detection (Carnec and Delacourt, 2000), glacier monitoring (Gray et al., 2001), crop monitoring (Hill et al., 2000), forest cover mapping (Murtha, 2000), snow cover mapping (Guneriussen et al., 2001), wetland monitoring (Milne et al., 2000), wind extraction from the ocean (Furevik et al., 2001; Vachon and Dobson, 2000) and coastal monitoring (Liu et al., 2000). Monitoring of disasters such as forest fires (Siegert and Hoffmann, 2000), floods (Adam et al., 1998) and oil spills (Gade and Alpers, 1999) are also important.

Basic principles of imaging radar

The high resolution of the SAR in the range direction (Figure 2.2) is achieved by phase coding the transmit pulse with a linear chirp and compressing the echo by matched filtering. Range resolution is determined by the pulse travel time, and the azimuth resolution is achieved by recording the phase and the amplitude of the echoes along the flight path.

Azimuth resolution

The SAR uses the forward motion of the satellite to synthesize a long antenna that enhances the azimuth resolution. As the spacecraft passes over a target, a ground target appears to be first in front of, then next to, then behind the spacecraft (Figure 2.3). In the meantime the SAR has transmitted several pulses and recorded the radar backscatter response of the target several times. The response to each of the pulses is somewhat different, depending on changes in target-sensor geometry and the Doppler effects. The motion of the spacecraft relative to the target increases or decreases the frequency of the signal. By analyzing the return signals from the pulses, the Doppler history of the target can be determined. This information allows the backscatter of the target to be analyzed as though it had been seen by different antennas, or correspondingly of a synthesized antenna with length equal to the distance the spacecraft has traveled while it was able to get backscatter returns from that target. The processed image (3-look) from ERS-2 SAR has a resolution of about 25 meters. The spacecraft travels around 4 kilometers while an

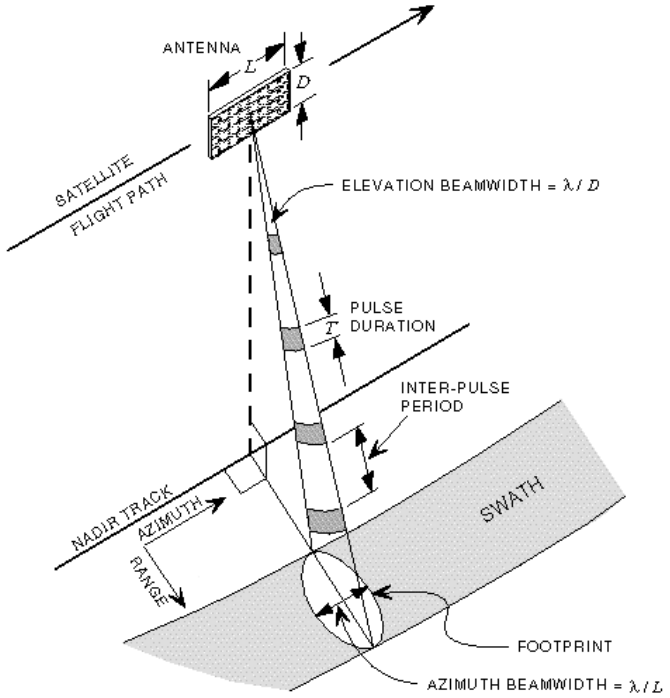

Figure 2.2: *Definitions of terms (figure from Olmsted, 1993).*

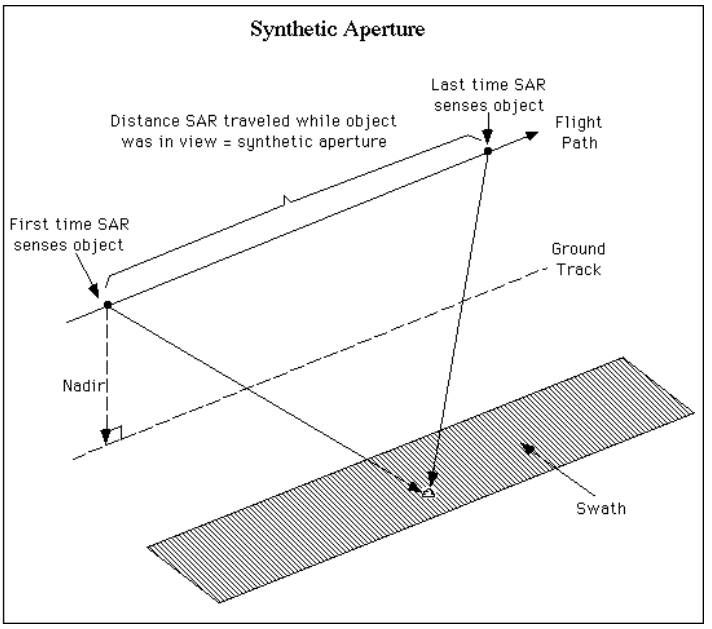

Figure 2.3: *Synthesizing of a large antenna (figure from Olmsted, 1993).*

object is 'within sight' of the radar, implying that ERS-2 10 m radar antenna synthesized a 4 kilometer-long stationary antenna.

Range resolution

The time for a radar wave to travel from the spacecraft to the target and back is used to determine the distance between the spacecraft and the target. The ground range resolution, G_R, is dependent upon the look angle and signal pulse length (Equation 2.1). The initial theoretical resolution along the slant range is half the pulse length (Figure 2.4). The slant range resolution (the resolution along the direction in which the radar waves propagate) is found by multiplying the pulse length, τ, in time by the speed of electromagnetic radiation, c, (in air, $3.0 \cdot 10^8$ m/s) and divide it by 2. To obtain the ground range resolution, the number is further divided by the sine of the look angle, φ (or the cosine of the depression angle, β). Decreasing the pulse length makes the resolution higher, but then the overall energy in each pulse decreases. Though the signal intensity can be increased, the available power of the spacecraft (and heat dissipation capabilities) limits this.

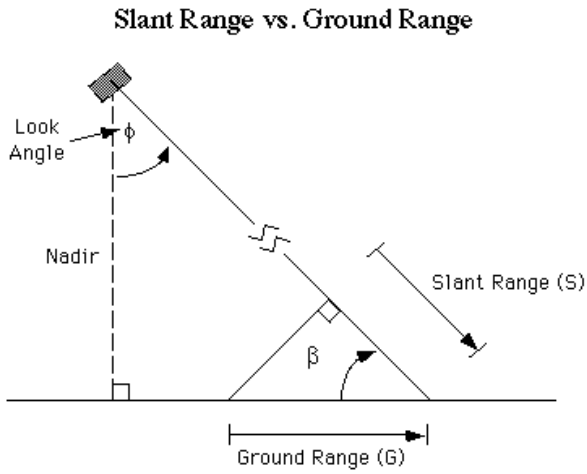

Figure 2.4: *Definitions of terms (figure from Olmsted, 1993).*

$$G_R = \frac{\tau c}{2 \sin \varphi} = \frac{\tau c}{2 \cos \beta} \tag{2.1}$$

This resolution is often too low, and signal processing techniques have been developed to improve it. For example, using the resolution theory outlined above, ERS-2's pulse length of $37.1 \cdot 10^{-6}$ seconds and its range of look angles would result in a ground range resolution on the order of several kilometers. A pulse that changes characteristics over its length is used to overcome this. The ERS-2 pulse is called a chirp (linear frequency modulated pulse). Because the pulse contains different frequencies, sections of it can be separated and be used to simulate even smaller pulses. The ability to resolve a set of frequencies within the pulse defines a new simulated pulse length, which for ERS-2 results in a resolution of 25 m rather than several kilometers.

Backscattering coefficient and scattering mechanisms

The radar equation

The total power received at the sensor, P_R, is determined by the power transmitted, P_T, the antenna gain, G, the wavelength of the system, λ, antenna area, A, the travel distance, R, and the radar backscattering coefficient σ^o (Equation 2.2).

$$P_R = P_T(\sigma^o A)(\frac{G^2\lambda^2}{(4\pi)^3 R^4}) \tag{2.2}$$

The radar backscattering coefficient σ^o is dimensionless, and gives the strength of radar signal reflected by a distributed scatterer. The coefficient is function of radar parameters (frequency, polarization, angle of incidence) and surface parameters (roughness, geometric shape and dielectric properties of the target), and it is usually expressed in decibels (Equation 2.3).

$$\sigma^o_{dB} = 10\log\sigma^o \tag{2.3}$$

The frequency of the incidence radiation determines the penetration depth of the waves. Longer wavelengths give longer penetration depths. The penetration depths are also related to the moisture of the target. Microwaves do not penetrate water more than a few millimeters.

Polarization describes the orientation of the electric field component of an electromagnetic wave. The radar waves can be set up to vibrate in either a horizontal (H) or vertical (V) plane or in a circular fashion. Antennas can transmit in one plane and receive in another. The linear configurations HH, VV, HV and VH are common. As the penetration depth varies with the polarization, it might give information about the form and orientation of small scattering elements that compose the surface.

Scattering

As the radar waves interact with ground surfaces, they can be reflected, scattered, absorbed or transmitted (and refracted) (Figure 2.5). Reflection is often due to the high dielectric constant of the material, usually meaning a high water content. The complex dielectric constant is a measure of the electric properties of the surface material. It consists of two parts (permittivity and conductivity) that are both highly dependent on the moisture content of the material considered. In the microwave regime, most natural materials have a dielectric constant around 3-8 for dry conditions. Water has a high dielectric constant ($\approx$ 81). Change of moisture content generally leads to a significant change in the dielectric properties of natural materials. Smooth surfaces may also lead to reflection. For example, if the imaged surface is smooth sea ice or water, a large part of the incom-

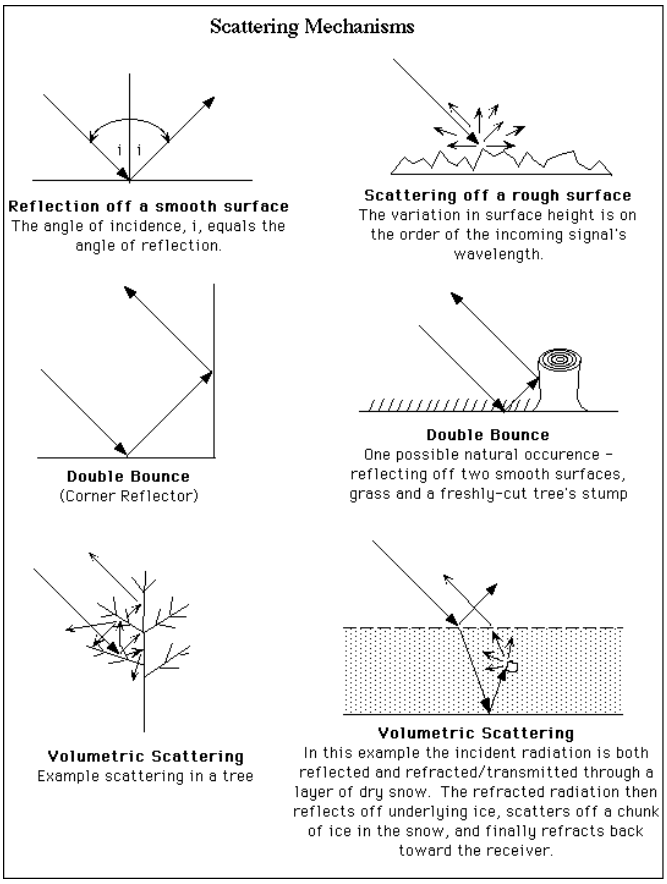

Figure 2.5: *Scattering mechanism for SAR (figure from Olmsted, 1993).*

ing radar waves will be reflected away from the sensor at the same angle as the incidence angle, according to Snell's law.

The radar return is often strongly influenced by surface scattering (Figure 2.5). Surface variations of the same order of magnitude as the radar wavelength will scatter radar waves as specified by the Rayleigh criterion. The height, h, of the surface variation in the direction of the incoming radar waves, $h \cdot \cos$(look angle), is considered. If this height is less than 1/8 of the value of the radar wavelength (5.7 cm for ERS-1 SAR), it is considered as 'smooth'. With the height larger than 1/8, the surface is considered as 'rough'.

If the scatterers are aligned parallel with the flight direction and regularly spaced (periodic), then the radar backscatter is coherently reinforced at particular angles of incidence, dependent of wavelength and spacing of the scatterers. This Bragg scattering leads to

radar power return proportional to the square of the numbers of components. For random scatterers the radar power return is proportional to the number of individual scatterers, and the Bragg scattering produce signal enhancement. The Bragg model is useful for describing the backscatter from the ocean surface (Equation 2.4). L is the vertical spacing between scatterers, θ is the angle of incidence, N is any integer and λ is the radar wavelength. The periodic structure of ocean waves resonates well with radar waves, visible as periodic bands on the image. The enhanced backscatter is due to coherent combinations of signals reflected from a surface of which a subset of scattering elements has features with periodic occurrence in the direction of wave propagation and whose spacing is equal to the half of the wavelength as projected onto the surface.

$$2(Lsin\theta) = N\lambda \tag{2.4}$$

Reflections can, however, bounce again off other objects and thereby be reflected towards the spacecraft, resulting in a stronger return signal. This process is called volume scattering. The return signal is from multiple scatterers, and is the result from a three-dimensional environment rather than from a two-dimensional surface. Other radar waves that are transmitted through the surface, will be refracted depending on the index of refraction. The index of refraction equals the velocity of an electromagnetic wave in a vacuum divided by the velocity of an electromagnetic wave in the particular substance. The radar waves will travel more slowly in the surface material than they did in air, and therefore they will be refracted towards the surface normal. The refracted signal can then either be absorbed by the material, or reflected or transmitted when it hits a region with different properties. For example, a radar wave is often transmitted through cold and dry snow. If the transmitted signal then hits smooth ice underneath the snow, it will be reflected back up through the snow.

Speckle

Important grey level variations may occur between adjacent resolution cells even for a single surface type. This is a characteristic property of the radar images. This variation creates a grainy texture called speckle (Figure 2.6), which is the statistical uncertainty associated with the backscatter of each pixel (picture element). Speckle is generally considered to be noise, and is due to the coherent sum of all the various responses within a

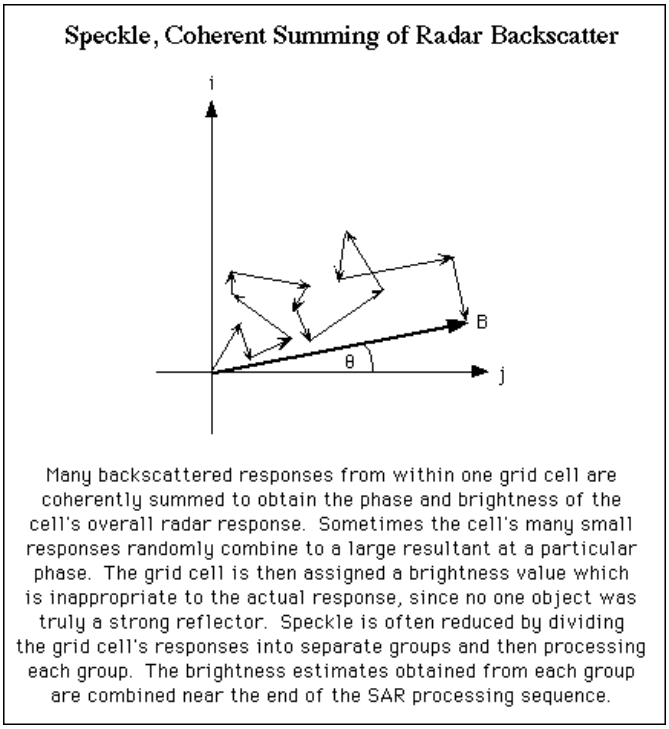

Figure 2.6: *Definition of speckle (figure from Olmsted, 1993).*

resolution cell. Within that area, there exist many different targets, which provide the surface texture necessary for backscatter. These multiple interactions produce returns, which interfere with each other in either a constructive or destructive manner. Constructive interference results in a strong return signal and a bright pixel in the image. Destructive interference results in a weak return signal and dark pixel in the image.

As the spacecraft moves along in its orbit, the radar antenna transmits pulses very rapidly. As a results, it obtains many backscattered radar responses from each object. If all these responses are processed to obtain the radar cross-section of the object, the result often contains a lot of speckle. The data are processed in sections, which are combined to reduce the speckle. Three estimates of the radar cross-section of the objects are done during data processing for the ESA Precision Image (PRI) products. Combining these three estimates (looks), reduces the amount of speckle and the data resolution. Different filter techniques may also be applied for speckle reduction, and some of them are designed to preserve the resolution.

URN:NBN:no-2344

Sea ice imaging

For given radar parameters (frequency, polarization and incidence angle), the intensity of back scattered signals from sea ice and waters to the antenna depends on surface and upper layer characteristics such as snow cover, ice type, surface roughness and dielectric properties. The dominant backscatter mechanism for new, young and first year ice is surface scattering or scattering from a region near the surface. The backscattering coefficient may be expressed as a function of the Fresnel reflection coefficient, Γ, a shape function, SF and a scaling constant, K (Equation 2.5).

$$\sigma^o(\theta_i) = K\Gamma^2(p, f, \theta_i, e_r^*)SF(p, f, \sigma, l) \tag{2.5}$$

The reflection coefficient is a function of incidence angle, θ_i, the transmit-receive antenna polarization, p, frequency, f and the complex dielectric constant, e_r^*. The shape function is determined of the polarization, frequency, the root mean square (rms) surface height, σ, and the surface correlation height, l. The most important parameters are the complex dielectric constant and the surface roughness statistics due to their influence on the shape function.

If the dielectric constant is large, as is the case with sea water, the radar signals do not penetrate into the media, and surface roughness determines the backscatter. For targets with low dielectric constants, as dry snow and ice, the signal will penetrate into the medium. Because of inhomogeneities in the medium, (air bubbles or crystal structures in sea ice) volume scattering will occur at these discontinuities.

Differences in ice type, ice age, surface roughness and snow cover will modify the backscatter intensity of the microwaves differently. Multi year ice with low salinity in the upper layer reflects more of the microwaves due to a combination of volume scattering from the upper layer of the ice and surface scattering from the top of the ice. First year ice, on the other hand, has higher salinity in the upper layer which impedes penetration of microwave into the ice. Therefore the σ^o from first year ice is dominated by surface scattering, and the surface roughness will to a large extent determine the strength of the return signal. For level surfaces, multi year ice will produce higher backscatter than first year ice. The difference in backscatter between the two ice types will depend on incidence angle, frequency and polarization.

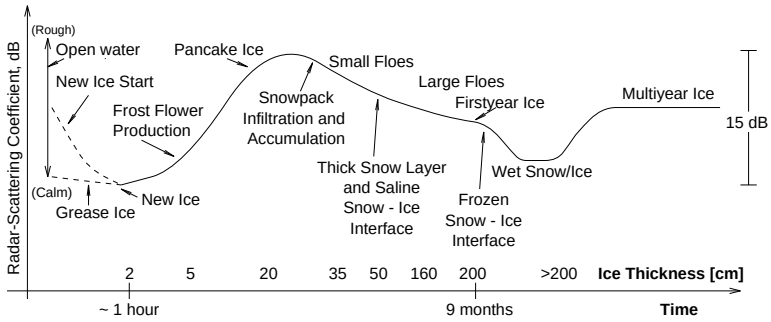

Figure 2.7: Schematic time evolution of σ^o from sea ice (modified figure from Onstott, 1992).

In the marginal ice zone, where the ice is often broken into many small floes with highly scattering edges, the backscatter from the first year ice can be similar and higher than from the multi year ice. New ice types, such as grease ice and frazil ice dampen the short surface waves and produce low backscatter values. As the ice grows thicker (nilas and grey ice) the backscatter signal stays low as long as the ice is level. But as soon as frost flowers start to form on the surface or pancake ice is formed, the σ^o increases rapidly (Figure 2.7). The main features of the time evolution of the σ^o for different stages in the ice growth is outlined in this figure, but the relationship between the σ^o and the ice types is still not fully understood.

Temperature of the ice and snow cover is an important modifying parameter, which especially in the melt season changes the backscatter characteristics of the ice and snow significantly. Dry snow on multi year ice has little effect on σ^o, while dry snow on first year ice can have significant effect in some cases, depending on the SAR parameters and the snow characteristics. Moist snow has considerable effect on the σ^o because dry and wet snow have very different dielectric properties. The most pronounced effect of temperature is to moisten the snow cover so that the σ^o is determined by the snow cover, which makes discrimination of the two ice types difficult in the melt season. Also melt ponds on top of the ice have strong effect on the σ^o because they are seem as water comparable to open calm water between floes.

URN:NBN:no-2344

2.3 Passive microwave remote sensing of sea ice

Multi-channel passive microwave radiance measurements made from a number of satellites are used to map, monitor and study the Arctic and Antarctic polar sea ice covers. The data sets are generated from observations made by different spaceborne microwave sensors. It started with the four years (1973 through 1976) of data from the Nimbus 5 Electrically Scanning Microwave Radiometer (ESMR). Then the Scanning Multichannel Microwave Radiometer (SMMR) on NASA Nimbus 7 produced data in the period 1978-1987. It continued with the Defense Meteorological Satellite Program (DMSP) Special Sensor Microwave/Imager (SSM/I) series in 1987. The DMSP designs, builds, launches and maintains these near-polar orbiting, sun-synchronous satellites to monitor the meteorological, oceanographic and solar-terrestrial physical environments. DMSP satellites orbit at an altitude of approximately 830 km above the Earth. The following description is mainly focused on the data from the SSM/I sensor and is based on the work of Cavalieri et al. (1990-2000), Comiso (1990-2000) and Robinson (1994).

Basic principles and the SSM/I sensor

Passive microwave radiometers observe the thermal radiation emitted in the microwave part of the spectrum and are nearly all-weather devices. The microwave radiation is emitted from the surface and the atmosphere. Reflections from the surface from atmospheric and solar emission and the deep-space background radiation is also observed. At these comparatively long wavelengths (1 to 200 GHz) there is little or no scattering by the atmosphere or aerosols, haze, dust or small water particles in the clouds (Figure 2.1). Precipitation does scatter the radiation and can make the atmosphere opaque at some frequencies.

At microwave frequencies, the observed radiance varies linearly with the temperature of the emitting material, according to the Rayleigh-Jeans law. It is usually expressed as the brightness temperature. The emissivity provides information about the electrical and physical properties of the material. Depending on frequency and polarization, the brightness temperature is affected by changing surface, subsurface and atmospheric conditions. The multichannel capability allows for the discrimination of different surfaces and atmospheric effects and allows for the development of algorithms that provide geophysical

information about the surface and the atmosphere.

The SSM/I is a four-frequency, horizontal and vertical polarized, passive microwave radiometric system which measures atmospheric, ocean and terrain microwave brightness temperatures at 19.4, 22.2, 37.0 and 85.5 GHz. Except for the 22.2 GHz, dual polarization measurements are taken, with each linearly polarized frequency occupying a channel of a total of seven channels. The SSM/I continuously rotates about an axis parallel to the local spacecraft vertical at 31.6 rpm. When looking in the forward direction of the spacecraft, the scan is directed from left to right with active scene measurements lying 51.2° about the forward direction. The resulting swath width is 1400 km, which results in daily global coverage except for areas within 2° off the pole. The channel footprint size varies with wavelength. The 85.5 GHz footprint is the smallest with spatial resolution of 14 by 16 km, and the 19.4 GHz footprint is the largest at 45 by 70 km. The 22.2 GHz has a footprint of 40 by 60 km, and the 37.0 GHz footprint is 30 by 38 km. Because the 85.5 GHz footprint is smaller, it is sampled twice as often. It has proven to be a stable, well-calibrated instrument.

For geophysical applications, brightness temperatures are computed from antenna temperatures using the published antenna pattern correction which includes adjustments for antenna side lobe, antenna efficiencies and neighboring pixel contributions. Brightness temperature is used to derive geophysical parameters such as area covered by ice and sea ice edge (Toudal, 1999; Toudal et al., 1999), ice concentration and type (Beaven et al., 1996), sea ice drift (Kwok et al., 1998), precipitation, cloud liquid water and ocean surface wind speed (Liu, 2000), integrated water vapor (Krasnopolsky et al., 2000), soil moisture (Morland et al., 2001), land and sea surface temperature (Xuwu and Smith, 1997; Luis and Kawamura, 2001) and area covered by snow and snow water equivalent (Pulliainen and Hallikainen, 2001).

The naturally emitted microwave radiation intensities are lower in magnitude than those in the visible and infrared. This results in a poorer brightness temperature resolution and consequently poor spatial resolution, of the order 15-30 km (depending on wavelength). While this poor spatial resolution is a disadvantage, the large data volumes generated are useful for global climate studies (Johannessen et al., 1999). The emissivity of a surface such as sea ice is highly dependent upon its physical characteristics, such as roughness and salinity. This has the advantage that first year ice may be distinguished from multi year ice. In addition, multi-frequency measurements allow for correction of

effects from various error sources. This is increasing the classification accuracy of sea ice concentrations.

Observation of brightness temperature

Thermal emission

Thermal radiation is emitted from the surface of the Earth dependent of variations in emissivity and temperature. A black body absorbs all incident radiation and emits according to its temperature. The amount of radiation from material at the surface is less than the corresponding black body radiation would be, and the material emits as a grey body. The amount of radiation from grey bodies are generally referred to as the brightness temperature. The amount observed is dependent on microwave wavelength and incidence angle of the sensor. Thermal emission in the microwave band is given by Planck's radiation law for a non-perfect emitter (Equation 2.6).

$$M_\lambda(\theta,\phi) = \frac{2hc^2\epsilon(\theta,\phi)}{\lambda^5[\exp(hc/\lambda kT)-1]} \tag{2.6}$$

M_λ is the spectral radiance at wavelength λ, in units power per unit solid angle, $d\Omega$, per unit projected area, per unit wavelength interval. $\epsilon(\theta,\phi)$ is the emissivity of the surface in the directions (θ,ϕ). The satellite viewing angles θ and ϕ are defined in Figure 2.8. T is the temperature in Kelvin of the emitter, h is the Planck's constant ($6.626 \cdot 10^{-34}$ Js), c is the speed of light ($3.0 \cdot 10^8$ m/s) and k is the Boltzman's constant ($1.38 \cdot 10^{-23}$ JK^{-1}).

The spectral radiance or brightness, B, is often expressed per unit frequency rather than per unit wavelength (Equation 2.7). The frequency is given by the wavelength by $f = c/\lambda$,

$$\begin{aligned} B_f(\theta,\phi) &= \frac{2hc}{\lambda^3}\frac{\epsilon(\theta,\phi)}{[\exp(hc/\lambda kT)-1]} \\ &= \frac{2hf^3}{c^2}\frac{\epsilon(\theta,\phi)}{[\exp(hf/kT)-1]} \end{aligned} \tag{2.7}$$

and at microwave frequencies, $hf/kT \ll 1$ and $\exp\frac{hf}{kT} \simeq 1 + \frac{hf}{kT}$ gives

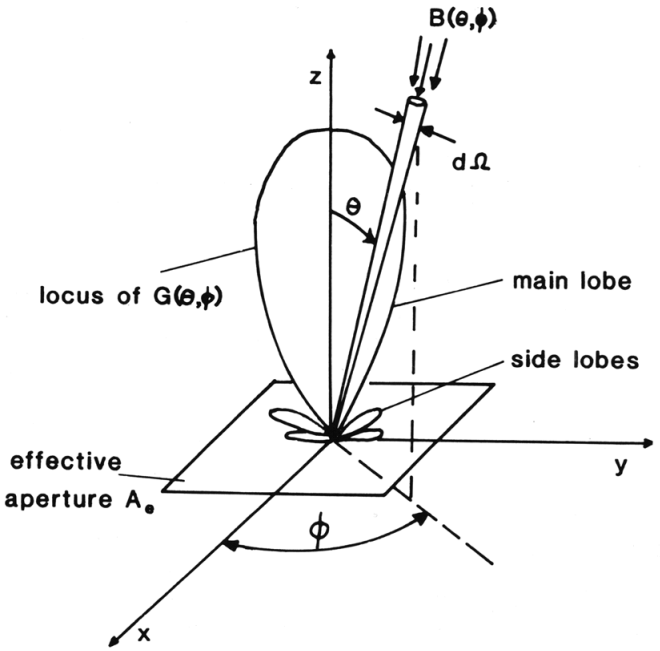

Figure 2.8: *Power pattern shape of a microwave radiometer antenna (figure from Robinson, 1994).*

$$B_f(\theta,\phi) = \frac{2kf^2T\epsilon(\theta,\phi)}{c^2} = \frac{2kT\epsilon(\theta,\phi)}{\lambda^2} \tag{2.8}$$

The Rayleigh-Jeans approximation (Equation 2.8) describes the relationship between brightness and temperature of the emitter. There is a linear correspondence between the temperature and the power emitted, although there will be directional variability depending on $\epsilon(\theta,\phi)$.

Radiation received by the satellite antennae

The antenna has a directional response with a gain of $A_e G(\theta,\phi)$, and $G(\theta,\phi)$ is the normalized power pattern having a typical shape as presented in Figure 2.8. A_e is the effective area of the antenna defined for wavelength λ (Equation 2.9).

$$A_e = \frac{\lambda^2}{\int_{4\pi} G(\theta,\phi)d\Omega} \tag{2.9}$$

The brightness temperature of the emitter $T_B = \epsilon(\theta, \phi)T(\theta, \phi)$ varies with direction, owing to the variability of the temperature in the atmosphere and across the surface. The power received by the antenna is therefore expressed as $P = kT_A\delta f$, where T_A is called the antenna temperature and δf is the bandwidth. T_A is to be seen as the temperature of the medium being viewed by the antenna. If the ambient radiation is uniform from all directions with brightness temperature T_B, then $T_A = T_B$. Otherwise, T_A is related to T_B by Equation 2.10.

$$T_A = \frac{\int_{4\pi} T_B(\theta, \phi)G(\theta, \phi)d\Omega}{\int_{4\pi} G(\theta, \phi)d\Omega} \tag{2.10}$$

The antenna is designed to achieved a power pattern having a strong main beam and low side lobes, so that T_A will be approximate to the average value of T_B in as narrow field of view as possible in a given view direction.

The surface emissivity carries information of the surface characteristics. The emissivity varies with the dielectric properties and the roughness of the surface. Emissivity, ϵ, and absorptivity, a, are related through Kirchhoff's law. Using the power reflection coefficient (reflectivity) defined as $r = 1 - a$, the relation can be written as Equation 2.11.

$$\epsilon_{H,V} = a_{H,V} = 1 - r_{H,V} \tag{2.11}$$

The subscripts H and V denote horizontal and vertical polarization states. For a plane surface, r is dependent on θ and the complex relative dielectric constant, e. The dielectric constant varies with temperature, salinity and frequency. The emissivity is then given through the reflectivity and determined by the dielectric constant (Equation 2.12 and Equation 2.13).

$$r_H = [\frac{\cos\theta - \sqrt{e - \sin^2\theta}}{\cos\theta + \sqrt{e - \sin^2\theta}}]^2 \tag{2.12}$$

$$r_V = [\frac{e\cos\theta - \sqrt{e - \sin^2\theta}}{e\cos\theta + \sqrt{e - \sin^2\theta}}]^2 \tag{2.13}$$

Algorithms to derive sea ice concentration

Several algorithms exist for retrieval of sea ice concentration from SMMR and SSM/I data. Two major types of sea ice have different microwave emissivities, first year ice (ice that is at least 0.3 m thick and not undergone a melt season) and multi year ice (ice that has survived at least one melt season). Also, new and young ice have different microwave emissivities from first year ice (Figure 2.9). However, the presence of new and young ice types within the sensor field of view cannot be determined unambiguously and contributes to errors of the calculated ice concentration.

Data from the open ocean regions can be separated from those in ice covered areas from predictable changes in brightness temperatures in a region when atmospheric forcing and ocean conditions change. This is especially evident in a scatter plot of SMMR 18.0 GHz versus 37.0 GHz brightness temperature data at vertical polarization (Figure 2.10). In the open ocean, the brightness temperatures are linearly related and are clustered distinctly enough for separation from ice covered regions.

The NASA Team algorithm uses three SSM/I channels to calculate sea ice concentration (Cavalieri et al., 1984; Gloersen and Cavalieri, 1986). These are the 19.4 GHz horizontally and vertically polarized and the vertically polarized 37.0 GHz channels. Two microwave channels are needed to derive sea ice concentration using the Bootstrap algorithm (Comiso, 1986; Comiso and Sullivan, 1986). Either the 37.0 GHz horizontally and vertically are used, or the 19.4 GHz vertically and 37.0 GHz vertically. Additional channels may be used to mask the open ocean. The NORSEX algorithm uses two channels, the 19.4 GHz vertical polarization and 37.0 GHz vertical polarization (Svendsen et al., 1983). All algorithms are described in Steffen et al. (1992).

The NASA Team algorithm

The channels used in the calculation of sea ice concentration are the 19.4 GHz horizontally (H) and vertically (V) polarized and the vertically polarized 37.0 GHz. This algorithm is functionally the same as the Nimbus 7 SMMR algorithm (Cavalieri et al., 1984). The radiance from each of the three channels are first mapped to polar stereo-graphic grids. The radiances are then used to calculate the grid values for two independent variables used in the algorithm. These are the polarization (PR) and spectral gradient (GR)

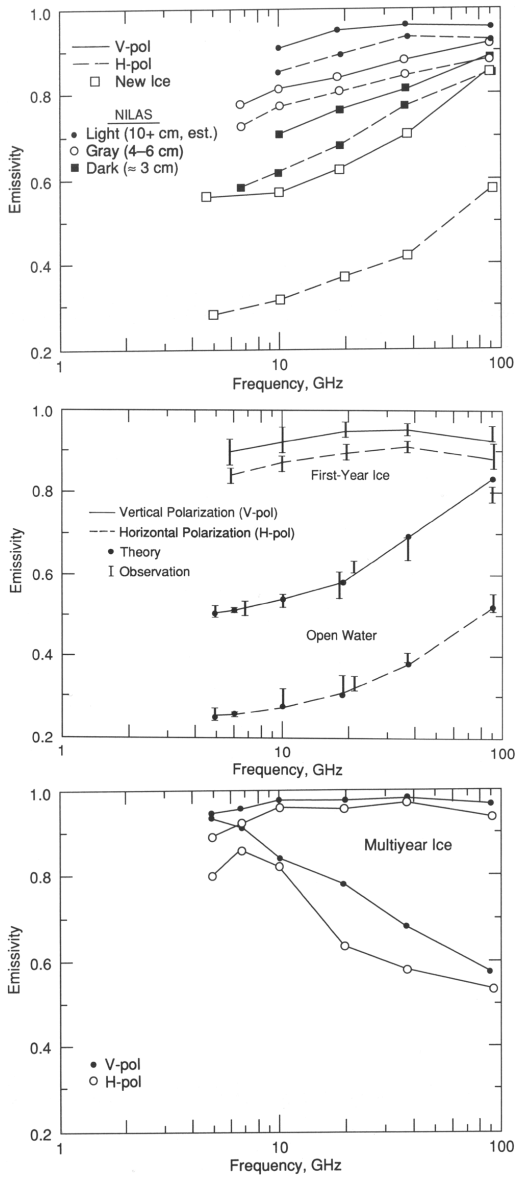

Figure 2.9: *Emissivity for different sea ice types as function of frequency and polarization (figures from Eppler et al., 1992).*

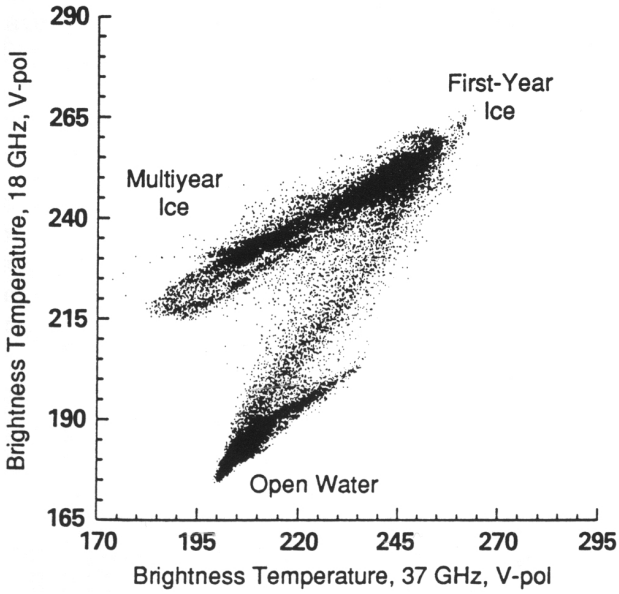

Figure 2.10: *Scatter plot of SMMR 18.0 GHz versus 37.0 GHz brightness temperature data at vertical polarization (figure from Eppler et al., 1992).*

ratios defined by Equation 2.14 and Equation 2.15.

$$PR = [TB(19V) - TB(19H)]/[TB(19V) + TB(19H)] \tag{2.14}$$

$$GR = [TB(37V) - TB(19V)]/[TB(37V) + TB(19V)] \tag{2.15}$$

TB is the observed brightness temperature at the indicated frequency and polarization. From these two parameters the first year ice concentration (C_F) and the multi year ice concentration (C_M) are calculated from Equation 2.16 to 2.18.

$$C_F = (a0 + a1PR + a2GR + a3PR \cdot GR)/D \tag{2.16}$$

$$C_M = (b0 + b1PR + b2GR + b3PR \cdot GR)/D \tag{2.17}$$

$$D = c0 + c1PR + c2GR + c3PR \cdot GR \tag{2.18}$$

The total ice concentration (C_T) is the sum of the first year and multi year ice concentrations (Equation 2.19).

$$C_T = C_F + C_M \tag{2.19}$$

The coefficients ai, bi, and ci ($i = 0, ..., 3$) are functions of a set of nine TBs. These are referred to as algorithm tie points, and are observed SSM/I radiances for each of the three channels over areas of known ice-free ocean, first year sea ice and multi year ice. In addition to constraining the solutions to concentrations between 0 % and 100 %, the algorithm also sets the total ice concentration to 0 % for SSM/I grid cells with GR values greater than a preset thresholds. This reduces errors in ice concentrations caused by weather-related effects over ice-free ocean.

The selection of the SSM/I tie points was based on analysis of TBs from SSM/I, PR and GR distributions, histograms of sea ice concentrations, and on comparisons with near simultaneous measurements from the Nimbus 7 SMMR during July and August 1987. The two sets of SSM/I tie points (one for the Northern Hemisphere and one for the Southern Hemisphere) represent a global set designed for mapping global ice concentrations. While this global set provides a uniform measure of sea ice concentration on the large scale, improved accuracy is obtained with the use of regionally selected tie points (Steffen and Schweiger, 1991). The ice-free (open water) tie points were chosen to be near minimum ice-free ocean TBs (corresponding to near maximum values of PR). By choosing near minimum TBs, the PR range between open water and first year ice is about an order of magnitude. This allows greater algorithm sensitivity of changes in ice concentration.

The ice tie point selection was more difficult, since the passive-microwave ice signatures vary. This is particularly true of Arctic multi year ice. Thus, there is generally a range of TBs that could be used as tie points. The series of SSM/I aircraft underflights helped in this regard (Cavalieri et al., 1991). Mosaic patterns covering several SSM/I image pixels were flown in the central Arctic over a two-week period in March 1988. They provided a constraint on the ice concentrations, which were calculated from passive and active microwave imagery. This allowed adjustment of the ice tie-points to improve the accuracy to within a few percent (relative to the aircraft data).

Correction for land-to-ocean spillover (often referred to as ‘land contamination’) must be

done. Land-to-ocean spillover is mainly caused by strong signal from land affecting the signal from the ocean. It results in false sea ice signals along coastlines. (Land and ice both have much higher brightness temperatures than the ocean.)

The largest source of error is the inability of the algorithm to discriminate among more than two radiometrically different sea ice types (including different surface conditions). Since the algorithm computes only first year and multi year ice, the largest source of error in total ice concentration is caused by the presence of thin sea ice. New and young ice are characterized by polarization differences between open water and first year ice. PR for thin ice will vary in proportion to ice thickness and will increase in proportion to the fraction of thin ice filling the SSM/I field of view.

Seasonal variations in sea ice emissivities can be large. Multi year ice loses its characteristic microwave signature (negative GR) during spring and summer. It becomes indistinguishable from first year ice, and only total ice concentration can be calculated. The formation of melt ponds on the ice surface makes the ponded region indistinguishable from open water, leading to ice concentration errors. The percent coverage of melt ponds varies both spatially and temporally across the Arctic. Non-seasonal variations in sea ice emissivity include local variations, resulting from fluctuations in the physical and chemical properties of sea ice, and regional variations resulting from environmental differences.

Weather effects are due to atmospheric water vapor, cloud liquid water, rain and sea surface roughening by wind. These effects on calculated sea ice concentrations are greatly reduced over open ocean at polar latitudes by the algorithm weather filter. They may contribute to the sea ice concentration error at concentrations greater than about 15 %.

The Bootstrap algorithm

With the Bootstrap algorithm, ice concentration can be derived without *a priori* assumption about the type of ice surface within the satellite footprint. This is possible only because consolidated ice data points appear linear in scatter plot of the 37.0 GHz horizontal (H) versus 37.0 GHz vertical (V) channel. This is used in the algorithm to obtain ice concentration in the Central Arctic region.

In the seasonal sea ice regions, the sole use of the 37.0 GHz H and V channels does not provide consistent identification of consolidated ice data points. Consolidated ice may

be difficult to distinguish from mixtures of ice and water due to presence of snow cover, flood or roughness effects. The 19.4 GHz and 37.0 GHz data, at vertical polarization, were found to be considerably more consistent and accurate in this regard. This set of data is thus used primarily in the seasonal ice region.

The ice concentration, C_i, corresponding to an observed brightness temperature, T_b, is given by Equation 2.20.

$$C_i = (T_b - T_o)/T_i - T_o \tag{2.20}$$

T_o and T_i are reference brightness temperatures for open water and sea ice, respectively. The sea ice concentration may be reflecting any single ice type or a combination of the various ice types. Equation 2.20 uses appropriate values of T_i and T_o, which are determined from the channels 1 or 2 (either 37.0 H and V, or 19.4 V and 37.0 V). For any set of channels, the ice concentration, C, for any data point, B, can be derived from Equation 2.21. T_{1i} and T_{2i} are the reference brightness temperatures for ice, and T_{1o} and T_{2o} are the reference brightness temperatures for open water.

$$C = ([(T_{1B} - T_{1o})^2 + (T_{2B} - T_{2o})^2]/[(T_{2i} - T_{2o})^2 + (T_{1i} - T_{1o})^2])^{1/2} \tag{2.21}$$

The brightness temperatures used as reference point for open water within the ice pack are inferred from scatter plots of ice-free ocean. The point chosen is close to the minimum value due to the usually uniform and smooth surface and low surface temperature within the ice pack. In the open ocean, atmospheric effects, waves, higher temperatures and foam cause the brightness temperatures to increase substantially in some areas. Application of the algorithm in these areas produces unrealistic ice concentration values in the open ocean.

Under ideal winter situations, when only thick ice and open water are present, ice concentration can be derived with the Bootstrap algorithm at an accuracy of about 5 to 10 %. This is based on standard deviations of emissivities used in the formulation. Errors are higher in the seasonal ice region than in the central Arctic region due to higher standard deviations of consolidated ice in the 19.4 versus 37.0 GHz plots. This is partly caused by spatial changes in surface temperature.

The constantly changing emissivities of surfaces cause unresolved problems. For example, when leads open up during winter, the open water is exposed to the cold atmosphere. Grease ice quickly forms at the surface. The surface develops from grease ice, to nilas, to young ice and then to first year ice with snow cover. During these transitions, the emissivity of the surface can change considerably from one stage to another (Comiso et al., 1992; Comiso et al., 1997). Since these changes are not adjusted for in the ice concentration algorithm, the derived fractions of open water are not strictly open water and may include areas of grease ice and new ice. In the spring and summer, the emissivity of thick ice also changes with time, especially over the perennial ice region in the Arctic. Despite adjustments, the error is substantial and can be larger than 20 % due to spatial variations in melt and effects of meltponding.

The NORSEX algorithm

The basic algorithm was developed on basis of the NORSEX marginal ice zone experiment near Svalbard in 1979 conducted by the NORSEX Group (Farrelly et al., 1983). The algorithm computes concentration of total ice and concentration of multi year ice and first year ice (Svendsen et al., 1983). Two channels are used, the 18.0 GHz and the 37.0 GHz vertical polarization for SMMR. The channels used for SSM/I are the 19.4 GHz and 37.0 GHz vertical polarization. Only vertical polarization is used since it was found to be significantly less sensitive to surface structure (snow layering, snow density, roughness) than horizontal polarization.

The ice emissivities and the atmospheric opacities used in the algorithm were basically measured during the NORSEX'79 experiment. Ocean water emissivities are theoretical values. Brightness temperature of the surface is modeled as the linear combination of the area-fraction of water, first year and multi year ice in the field of view. A simple atmospheric model with surface air temperature as parameter is used to convert satellite-observed brightness temperature to surface-observed brightness temperature (Equation 2.22).

$$TB_E = [T_A - 2\delta T_{atm}\tau + \delta T_{atm}\tau^2 - T_{sp}]/[1 - \tau - \beta\delta(\tau - \tau^2) - \beta\frac{T_{sp}}{T_{atm}}] \quad (2.22)$$

TB_E is the effective brightness temperature at the surface, T_A is the antenna tempera-

ture, δT_{atm} is the weighted average atmospheric temperature, τ is the total atmospheric opacity, T_{sp} is the temperature from free space and β is a constant close to unity. τ is a function of frequency, but not of polarization.

A rough estimate of the average surface air temperature over 100 % pack ice from climatological data is used as input for each scene. The NORSEX algorithm output is % water (f_W), % first year ice (f_{FY}) and % multi year ice (f_{MY}) with a spatial resolution of approximately 60 km for SSM/I which is the resolution of the 19.4 GHz channel (Equation 2.23 to Equation 2.25). The assumption that $f_W + f_{FY} + f_{MY} = 1$ is used. T_{ICE} is the physical temperature of ice, T_W is the physical temperature of water and e_x^y is the emissivity of surface type x in channel y.

$$f_W = [T_{ICE}(e_{MY}^{19V} - e_{FY}^{19V})(TB_E^{37V} - T_{ICE}e_{FY}^{37V}) + T_{ICE}(e_{MY}^{37V} - e_{FY}^{37V})(T_{ICE}e_{MY}^{19V} - TB_E^{19V})]/D \quad (2.23)$$

$$f_{MY} = [(T_W e_W^{19V} - T_{ICE}e_{FY}^{19V})(T_{ICE}e_{FY}^{37V} - TB_E^{37V}) + (T_W e_W^{37V} - T_{ICE}e_{FY}^{37V})(T_E^{19V} - T_{ICE}e_{FY}^{19V})]/D \quad (2.24)$$

$$D = T_{ICE}(e_{MY}^{19V} - e_{FY}^{19V})(T_W e_W^{37V} - T_{ICE}e_{FY}^{37V}) - T_{ICE}(e_{MY}^{37V} - e_{FY}^{37V})(T_W e_W^{19V} - T_{ICE}e_{FY}^{19V}) \quad (2.25)$$

The algorithm requires that the input brightness values are adjusted with a few degree K to give 100 % water over calm open polar water. These adjustments are made based on a few suitable scenes where the state for the atmosphere and the surface is known, and thereafter mainly kept unchanged. Adjustments are different for SMMR and SSM/I.

The NORSEX-85H is an extension of the NORSEX algorithm. The extended version takes advantage of the improved spatial resolution of the 85.5 GHz channels provided by the SSM/I system which is currently in operation. The NORSEX-85H algorithm was developed for use under the SIZEX'92 experiments in the Greenland and Barents Sea (Sandven et al., 1994). The ice edge defined by the 30-50 % contour lines is well correlated with the ice-water boundary seen in near-simultaneous SAR images both under

SIZEX'92 and under later experiments. The 85.5 GHz channel with horizontal polarization (85H) is very sensitive to the difference between water and first year ice as well as to the atmosphere. This channel is used to sharpen the ice-water boundary. The 85H is spatially low-pass filtered to a resolution of 60 km. Concentration values are then multiplied with the ratio of the 85H-signal to the low-pass-filtered 85H-signal. This results in data with a spatial resolution of 15-20 km, given by the 85H-signal, and with ice concentration values given primarily by the basic NORSEX algorithm.

2.4 Physical basis for microwave remote sensing of sea ice

This section is based on the work by Hallikainen and Winebrenner (1992), Eppler et al. (1992) and Onstott (1992).

Sea ice and snow are physically and dielectrically inhomogeneous media consisting of pure ice, brine, air and fresh water (melt season). Water and ice represent very different materials from a radiometric perspective. Large dielectric constants and loss factors of fresh water, sea water and brine causes these materials to strongly affect the dielectric properties and signature of sea ice. Sea water has a power reflection coefficient of order 0.5 in the microwave region due to a large dielectric constant. Scattering takes place at the surface and varies with wind speed. Microwave transmission into sea water and the proportion that is absorbed are small, and the emission from sea water is low. Typical brightness temperatures are in the order of half the physical temperature, and horizontal polarized temperatures are lower than the vertical polarized temperatures.

As new and young ice forms it retains a considerable amount of brine and the temperature is not very different from the sea water. The effective dielectric constant is smaller than for sea water and larger than for thicker ice types. New and young ice transmit a larger amount of microwave radiation across their upper surface than sea water, and radiation is also absorbed. Typical brightness temperatures are within a few percent of the physical temperature for vertical polarization, even for a few centimeters thick ice. For horizontally polarization, the brightness temperatures are 10 % to 15 % lower. Backscattering from new and young ice range from very strong from deformed ice (i.e. pancake ice) to very low for bare undeformed ice (no frost flowers present). Strong backscattering is associated with rough surface scattering from the air - ice or the snow - ice interface.

URN:NBN:no-2344

As the ice grows to first year ice, it loses brine and the surface gets colder and usually rougher with a snow layer. The lower brine volume and the consequently lower electromagnetic absorption and increased roughness tend to increase scattering. Brightness temperatures decrease only a few percent as the ice develops into thick first year ice, and the difference between vertically and horizontally polarized brightness temperatures decreases. Backscattering from first year ice is higher than for new and young ice. A thin snow cover can increase backscattering (formation of slush at the ice - snow interface) and lower brightness temperatures.

Old ice has survived the summer melt and has fresh raised areas (i.e. hummocks) with porous (bubbles) low-density upper layers and lower areas with high density (i.e. refrozen melt ponds). The melt ponds are usually fresh, but may be saline. Snow cover is generally thickest on old ice, but this is variable. These different factors lead to highly variable ice signature. The millimeter sized bubbles and low absorption in the upper part of the ice lead to strong volume scattering, making average backscattering much higher than for first year ice. Passive signatures give small polarization difference and decreasing brightness temperature with increasing frequency. Melt ponds give lower backscattering and higher brightness temperatures more like first year ice.

The onset of spring melting leads to the presence of liquid water in the snow and on the ice and alters the microwave signatures. Volumetric snow wetness of just 1-2 % increases absorption so that a snow layer of 10 cm gets opaque in most of the microwave spectrum. A thin layer of wet ice may mask the underlying ice. The backscattering of old ice falls and the brightness temperature rise to values near first year ice. The change in first year ice signatures are less drastic and monotonic, the passive signatures change little during melting.

2.5 Problems in remote sensing of sea ice

Radar is sensitive to the physical properties of sea ice (salinity, micro-structure and surface roughness) that vary with ice concentration, type, age and thickness (Barber et al., 2001; Onstott, 1992). Elements that are employed to visually discriminate ice types in SAR imagery include the structural characteristics of floes, such as the shape and presence of ridges, fractures and melt ponds. The ability to discriminate ice types is highly dependent on the geographic region (Gineris and Fetterer, 1994; Kwok and Cunningham,

1994) and the season of imaging because different ice types exist in different regions and at different times of the year. During the drier months of winter the surface texture is the primary key for discrimination. In the warmer months, when free water is present, the differences between old and first year ice become more difficult to discriminate in particular when the overlying snow pack is saturated with water and the differences in backscatter are significantly reduced (Gogineni et al., 1992). Classification ambiguity can be reduced by consulting the past history of ice features in a particular region, ice climatology and current meteorological conditions.

The main problem for remote sensing of sea ice is that the surface and volume are changing rapidly, limiting the possibilities for validation studies both for data from passive and active microwave sensors. For distant areas, with few sources of data, it is not easy to find cases where image data and ground data are available for the same area at the same time for research purposes. A rather large data set was needed for separation of sea ice types and validation of the results (presented in Chapter 3). Then classification of SAR samples on the basis of available data was decided to be used as test material, because it was easy to get. The next step must be to verify that these methods also can be used when an optimal data set with SAR images and ground data will be obtained. It might also be a problem to relate SAR observations over an area of 100 by 100 m to for instance a point observation like a ice core sample. Field data are difficult to use because of limited coverage compared with the large footprint of the satellite sensors. This problem can be addressed using a combination of geographical boundaries and physical property boundaries. Different bays or seas may be regarded as distinct geographical regions. The use of geographical boundaries provides an opportunity to take advantage of the time history of the ice pack. For example, if a bay is ice-free during the summer, it is unlikely that it would have multi year ice during the subsequent winter. In such a region, the primary ice types would be first-year ice and new ice.

Physical property boundaries can also be associated with the different ice regimes, such as the outer, inner, divergence, convergence and perennial zones. The outer zone, which includes the marginal ice zone, is perhaps the easiest to identify in the passive microwave data because of the marked difference in emissivity between the ocean and the ice covered regions at some frequencies. It is also characterized as the region where loose pancakes are located and where the effect of waves dominates (Liu and Peng, 1998). Alternatively, the inner zone is the region where the ice cover is practically a continuous sheet of ice

except where there are leads and polynyas. The divergence zone is the area of extensive lead formation while the convergence zone is the area of extensive rafting and ridging. The perennial zone is the area where much of the multi year ice floes are located.

Ice types are more accurate determined from SAR when the ice analyst has access to times series of data from the actual area and data from other sensors or sources (Bertoia et al., 1998). The season, location, oceanographical and meteorological conditions may also be incorporated in the analysis. Texture, size and shape are used in an intuitive way. An automatic system that can operate with all these parameters, not all easy to define, is difficult to design. Automatic systems handle large amounts of data for analysis, presentations and distribution of information to different users. Ice centers have made their own systems for this process (Bertoia et al., 1998).

The general conclusion from the review article by Cracknell (1998) is that it is important to realize that it is not easy to find out what exactly gives rise to the signal detected and recorded in a pixel. An overview of a very large area can be obtained, but the pixels may be large compared to the objects to be observed. The mixed pixel problem is important when sub-pixel size objects contribute to the pixel intensity (Fisher, 1997). An ‘ice pixel’ may be a sum of signals originating from open water, ice ridges and thinner to thicker ice types. Also, pixel intensities are not independent, there is auto-correlation among them (Henderson and Lewis, 1998). This makes it difficult to compare sea ice pixels to ground data for validation of the data or sea ice classification products.

Chapter 3

ERS SAR studies of sea ice signatures in the Pechora and Kara Sea region

by

M. Lundhaug

Accepted for publication in Canadian Journal of Remote Sensing, 2001, in press.

Abstract

Results from a statistical analysis of 105 Synthetic Aperture Radar (SAR) images and meteorological data are presented, covering parts of the Pechora and Kara Sea in the Russian Arctic. Wind, temperature and other variables for the SAR sample areas were collected, and a manual sea ice classification of the SAR samples was performed. All variables were input to different multivariate regression analyses, which first were used to separate ice and water samples. In the next regression analyses the classes young ice and rough first year ice were separated from water, and the two ice types were separated from each other. In the separation of all ice types from water, correlation coefficients up to 0.90 between predicted and actual data values were achieved. Correlation coefficients were as high as 0.93 between predicted and actual values for open water and young ice and for open water and rough first year ice. When trying to separate young ice from

rough first year, correlation coefficients of about 0.60 were obtained. The study indicated that the mean and standard deviation of the backscattering coefficients together with temperature values were the most important information to separate classes using regression techniques.

3.1 Introduction

3.1.1 Background

Arctic sea ice plays an important role in the global climate system (Aagaard and Carmack, 1989), as well as for shipping and offshore operations (Johannessen et al., 2000; Proshutinsky et al., 1999; Wohl, 1995). It influences heat exchange between ocean and atmosphere on diurnal and seasonal time scales (Maykut, 1978), including the amount of solar radiation that is reflected from the earth's surface. It is also considered as a sensitive indicator of long term climate change (Johannessen et al., 1999; Rothrock et al., 1999; Vinnikov et al., 1999).

The Kara and Pechora Sea region represents a part of the Northern Sea Route (NSR), the sailing route in the Russian Arctic between the Barents Sea and Bering Strait. There are different sailing alternatives for the NSR depending on the ice conditions. Near coastal routes include straits such as the Kara Gate between Pechora and Kara Sea. The Vilkitsky Strait further east connects the Kara Sea with the Laptev Sea (Mulherin et al., 1994; Mulherin, 1996). Another possible route is north of the Novaya Zemlya, avoiding the difficult ice area near Kara Gate. There is a strong seasonal and regional variability in the sea ice distribution in the Kara and Pechora Seas (Proshutinsky et al., 1999). This is an important sea ice production region in winter because of low air temperatures and repeated opening and closing of polynya areas caused mainly by wind of variable direction. Most of the ice melts during summer, increasing the fresh-water contribution to the ocean surface layer.

Regular airborne sea ice observations in the NSR began in 1941/1942 and use of satellite data started in 1969, mainly IR/visual radiometer, passive microwave radiometer, side-looking radar (SLR) and experimental use of Almaz-1 SAR (Bushuev et al., 1998). Use of ERS SAR data was introduced by the ICEWATCH project, which started in 1995 (Johannessen et al., 1996a; 2000). This was the first joint project in Earth observation

between the Russian Space Agency (RKA) and the European Space Agency (ESA). The objective of the project was to demonstrate pre-operational satellite monitoring to support navigation through ice in the NSR using SAR and SLR data.

The Nansen Environmental and Remote Sensing Center (NERSC) in Bergen demonstrated use of ERS-1 SAR images in near real-time ice mapping in the NSR for the first time in August 1991, a few weeks after the launch of this satellite. The French polar vessel L'Astrolabe sailed from Norway to Japan using sea ice maps derived from ERS-1 SAR images which were transmitted by fax to the captain and sea ice experts onboard the vessel (Johannessen et al., 1992b). During the 1990s, several expeditions in the NSR with nuclear icebreakers from Murmansk Shipping Company used ERS SAR and RADARSAT ScanSAR images to support ship navigation. The SAR technology represented an opportunity in operational ice monitoring, which was positively evaluated by captains and navigators in the Arctic region. Several hundred SAR scenes were collected and analysed, to study various ice parameters, processes and phenomena. Improved knowledge for selection of more optimal routes through areas of new and young ice was gained. It was estimated by Russian Marine Operational Headquarter that use of SAR data for navigational support may increase the overall ship speed by a factor of at least two (Pettersson et al., 2000). Limiting factors for use of SAR data were the coverage of the communication satellite INMARSAT, the data ordering procedure and the amount of data available.

3.1.2 Description of the Pechora and Kara Sea region

Pechora Sea is a semi-enclosed sea, surrounded by Kolguyev Island to the southwest, the Russian mainland to the south, Vaygach Island to the east and the Novaya Zemlya to the north (Figure 3.1). The eastward-flowing Kolguyev Current is dominant in the southern part. Kara Sea is situated between the islands of Novaya Zemlya, Franz Josef Land, Severnaya Zemlya and the coast of Siberia. The islands of Novaya Zemlya prevent the relatively warm extension of the North Atlantic Current that affect the Barents and Pechora Seas from significantly influencing the Kara Sea (Barnett, 1991; Mulherin et al., 1994; Romanov, 1995). The major amount of freshwater transported into the sea is from the Pechora River. A seasonal ice cover characterizes Pechora Sea, where the melting period starts in early June and the freezing period starts in November. Both melting and

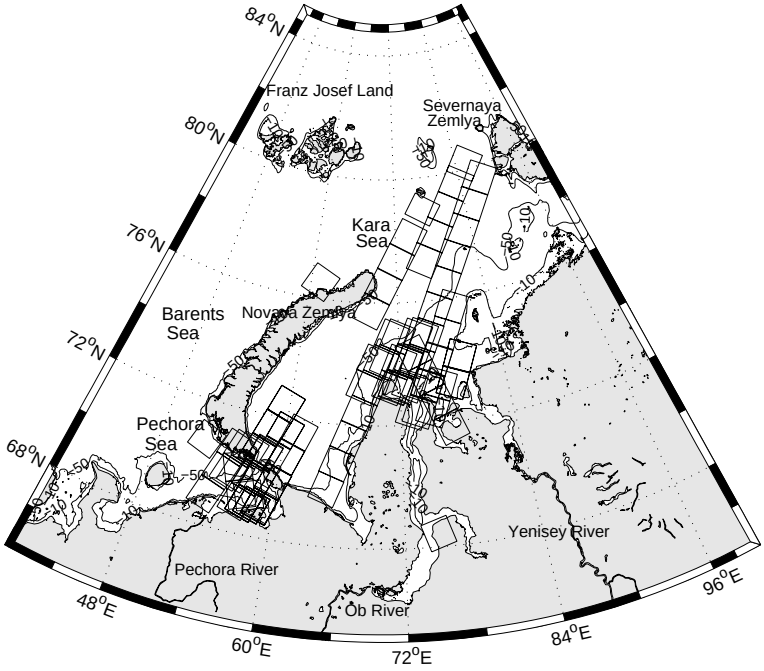

Figure 3.1: *The Pechora and Kara Seas with the 10 and 50 m sea depth contours plotted. The selected ESA ERS-1/2 SAR Precision Image scenes are marked with frames.*

freezing dates show high interannual variability. The ice formation starts in the eastern areas and moves westwards. Due to frequent passages of atmospheric low pressures, both sea ice drift and ocean currents are dominated by wind forcing. The sea ice in the Pechora is more ridged and rafted compared to first year ice in the Kara due to the stronger influence by wind and waves.

The Kara Sea is usually ice covered from November to June, and it is characterized by land fast ice along major parts of the coasts. Freezing begins in September in the northeastern part of the Kara and in early October in the central part where the Ob and Yenisey Rivers discharge. These rivers comprise more than half of all runoff from Siberia. The southwestern sector normally remains open until November. Seaward of the fast ice boundary, the ice cover is in constant motion due to ocean currents and wind. Throughout fall and winter, the only important openings in the ice cover usually occur at the boundary between the fast ice and the pack ice. The ice motion produces leads and polynyas in the divergent areas, and ridges and fields of broken ice in the convergent areas. During the

URN:NBN:no-2344

freezing period (September to May), new ice is continually produced in the leads. In the areas of convergence, broken ice freezes into much thicker and stronger masses. The presence of leads in the winter season is very useful for navigation (Mulherin et al., 1994).

The melting period starts in late May or early June. There is considerable year-to-year variation in the freezing and melting dates. Summer melting in the Kara Sea typically begins at the outer edge of the fast ice. A few weeks later the fast ice breaks free and drifts seaward. Warm spring runoff produces early open water areas at the major estuaries. By midsummer, the western part of the Kara Sea is normally ice free as far north as 75° N. There may be open water as far north as 82° N during a mild summer. Most parts of the Pechora Sea and the eastern part of Kara Sea are shallow, less than 50 m. Islands and peninsulas affect the ice conditions in both seas, especially the formation of coastal polynyas and the extent of fast ice. Exchange of water and ice between the Barents and Kara is through the Pechora Sea area, through the wide Kara Gate, the narrower Yugor Strait and between the Novaya Zemlya and Franz Josef Land.

In general, in winter the Kara Sea is in a transition zone between a large and stable high-pressure cell over central Siberia and low-pressure ridges over the Barents and Norwegian Seas (Harms and Karcher, 1999). From October to March, a cyclonic curl prevails with main wind directions from south to southwest for central Kara Sea, and the wind speeds are high and stable. In summer, the Siberian high-pressure cell decreases and a high pressure cell develops over central Arctic. The wind speeds are lower and wind directions are more variable, but northerly and northeasterly winds are dominant.

Monitoring of sea ice in the Pechora and Kara Sea region is very important both for economic and environmental reasons. Extensive oil and gas resources are found here, and exploitation of these as well as cargo transport along the Northern Sea Route may cause environmental problems. These can be prevented or limited by improved knowledge of the ice conditions. Contaminant transport by ice is also an important issue (AMAP, 1998). This study focuses on Synthetic Aperture Radar characterization of sea ice types in the Pechora and Kara Sea. Regional signatures during the ice season from the early formation of thin ice to the melt period are investigated. ERS 1 and 2 (ERS-1/2) SAR image data is used, as SAR data is especially valuable in the Arctic due to its ability to image the surface through clouds and in darkness. Temperature and wind data is used to better understand the SAR signatures of the ice during the year under different weather conditions. All parameters are used as input to multivariate statistical analyses, by which

URN:NBN:no-2344

separation of ice and water and separation of ice types are investigated. The relative importance of the input variables for water and sea ice separation is also discussed.

3.2 Data analysis

3.2.1 SAR data

ERS-1/2 SAR data was used exclusively. ERS-1 was launched July 17 in 1991 and ERS-2 was launched May 20 in 1995. The satellite orbits are sun-synchronous, near polar and have mean altitude of 785 km. The sensors transmit and receive vertically polarized micro-wavelength energy at an average frequency of 5.3 GHz (C band). The SAR looks to the right of the spacecraft at a 23 degree average angle of incidence.

Although the relatively narrow swath width of 100 km limits the use of ERS-1/2 SAR for global sea ice monitoring, it is very useful for regional and local mapping of straits, river estuaries and other difficult ice navigation areas. Image data from the Kara and Pechora Seas in the Russian Arctic was collected from the archives at NERSC. Three look image data with 12.5 m pixel spacing was delivered by ESA via the UK-PAF. All of the Precision Image (PRI) products of 25 m resolution have been calibrated according to Laur et al. (1998). From early winter of 1994 to the spring of 1998, 105 images were chosen with emphasis on February and March 1996. A database of these images was established to cover as much of the variation of the sea ice signatures through the year as possible. Each scene was resampled to a pixel spacing of 100 m. Locations of the image scenes are marked in Figure 3.1. The images cover the main ice seasons and a broad range of weather situations.

The inter-calibration between ERS 1 and 2 was checked using sub-samples from an ERS-1 scene from 26 January and an ERS-2 scene from 27 January 1996. The scenes covered the same ice area, the meteorological conditions were the same after 24 hours, and only minor changes in the ice distribution in the area had occurred. Absolute differences of less than 1 dB were found for the ten ice areas compared. This is considered to be within the error bounds (Laur et al., 1998).

3.2.2 Temperature and wind data

Wind and temperature data was used to facilitate more accurate interpretations of environmental and surface effects in the SAR data, as done by Winebrenner et al. (1994; 1996). Meteorological data extracted from the European Centre for Medium-Range Weather Forecasts (ECMWF) analysed data sets were used, available every six hours. The grid point distance is 1.1213 degree in latitude direction and 1.1250 degree in longitude direction. Data from the grid points closest to the SAR image centres and with the shortest time difference to the image acquisition time was used. Maximum time difference is up to three hours, and maximum spatial difference is about half a degree in each direction. Temperature, wind speed and direction (u- and v-components of wind at 10 m, temperature at 2 m) were added to the database. These temperature and wind data may not represent the actual conditions at the surface, due to errors in the ECMWF data. They are nevertheless indicators of the weather conditions, as *in situ* meteorological data was not available.

3.2.3 SAR analysis

Studies of ERS SAR backscattering coefficients have been carried out for different seasons. Melt onset (Winebrenner et al., 1994), autumn freeze-up (Winebrenner et al., 1996), winter conditions (Fetterer et al., 1994; Gineris and Fetterer, 1994; Kwok and Cunningham, 1994) and summer conditions (Comiso and Kwok, 1996; Haverkamp and Tsatsoulis, 1999) have been investigated. In addition, seasonal characteristics of the perennial sea ice have been studied (Kwok et al., 1996). All these investigations have used SAR data from different areas in central Arctic, East Siberian, Beaufort and Chukchi Seas. Sandven et al. (1999b) have performed sea ice studies during the Seasonal Ice Zone Experiment 1992 (SIZEX92) in the Barents Sea. Less attention has been paid to the area chosen for this study. Few Russian research papers regarding this area are translated to English, and often ERS SAR data is not used in these studies (Bertoia et al., 1998; Bushuev et al., 1998). As proposed by several authors (Gineris and Fetterer, 1994; Kwok and Cunningham, 1994; Onstott, 1992), the regional location of the sea ice observed by SAR may affect the backscattering values. These are the motivations to examine this part of the Russian Arctic more in detail.

Both Sandven et al. (1999b) and Fetterer et al. (1994) indicated that there is considerable

overlap between the distributions of backscattering coefficients of the different sea ice types identified from SAR. These and other studies indicate that meteorological data may give improved results when interpretation and classification is the goal.

Popular approaches for classification of sea ice in SAR images are use of first-order statistics (mean, variance) and second-order statistics (texture). The grey level co-occurrence matrix (GLCM) derived statistics were used in the studies of Barber and LeDrew (1991), Barber et al. (1993), Nystuen and Garcia (1992) and Shokr (1991). Texture statistics from the GLCM are computational expensive and dependent on the method-parameters chosen (Barber and LeDrew, 1991). Fetterer et al. (1994), Kwok and Cunningham (1994), Shokr et al. (1999), Smith et al. (1995), Steffen and Heinrichs (1994) and Wohl (1995) used backscattering values for their studies. Shokr (1991) and Barber et al. (1993) obtained improved results by using second-order statistics, and Nystuen and Garcia (1992) and Smith et al. (1995) concluded that first-order statistics were sufficient for good results. Among several factors, the number of image scenes, image properties and GLCM parameters have varied in these studies.

In order to build up a representative database for different ice types and open water, samples of ice and water areas were manually extracted. Each of them covered areas of 5 by 5 km from SAR images of 100 by 100 km with 100 m pixel spacing. This placed restrictions on the size and forms of the areas that were possible to investigate. Due to this choice of box size, features of more limited extend like narrow leads, ridges or narrow fast ice areas can not be investigated. Samples from single floes required floe sizes larger than the sample area. The extracted samples from the SAR images were selected to represent the dominant types and forms of ice in the image (at least two samples from each image scene). The samples were collected from homogeneous areas and at different azimuth and range locations in the image scene (Fetterer et al., 1994). Figure 3.2 shows an example of a SAR image with the sample areas marked.

3.2.4 Sea ice classification

Ground truth data was not available for the images used in this study. Manual classification of the SAR images was used as a substitute for classification based on surface *in situ* observations, which are rare in these inaccessible areas. The manual classification was based on extensive experience gathered from previous field expeditions. *In situ* ob-

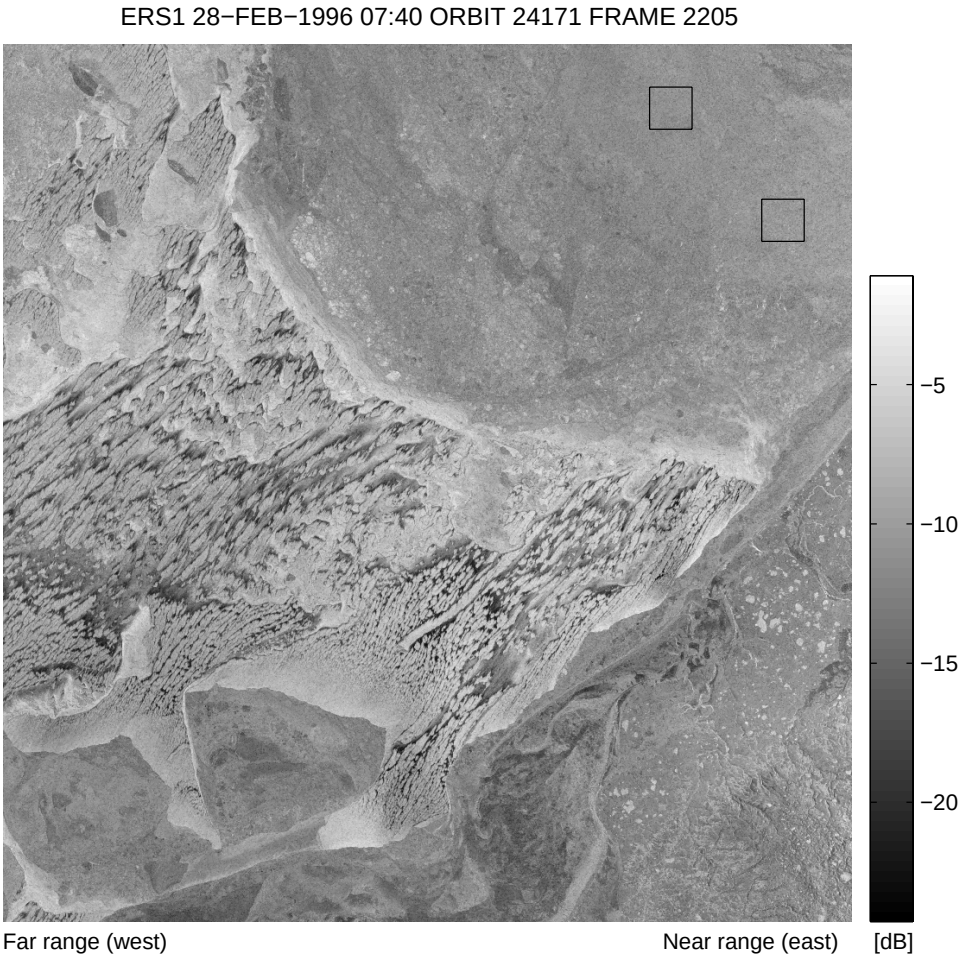

Figure 3.2: *Descending ERS-1 SAR scene along the western coast of Varandey in the Pechora Sea from 28 February 1996. The image size is 100 by 100 km. Two sample areas of 5 by 5 km are marked. Image Data ©European Space Agency/Nansen Environmental and Remote Sensing Center 1996.*

URN:NBN:no-2344

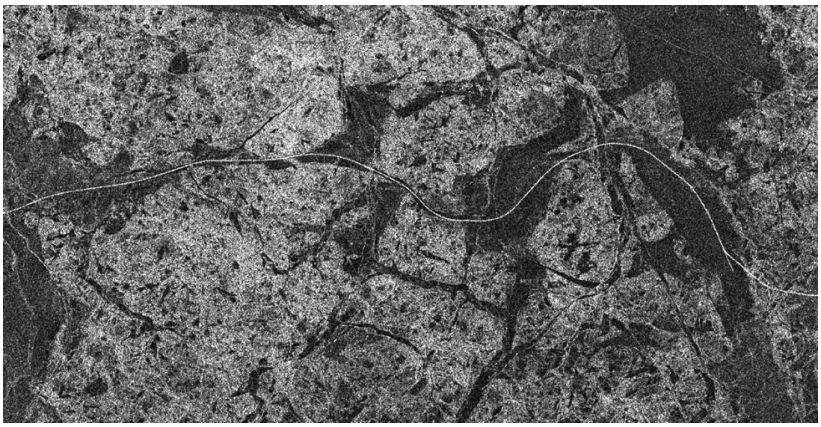

Figure 3.3: *Part of an ERS-2 SAR scene from 6 May 1998, the bright line is the strong return signal of the ship track through the level sea ice areas in the Ob Estuary. The image size is 16 by 31 km. Image Data ©European Space Agency/Nansen Environmental and Remote Sensing Center 1998.*

servations were then collected, as close to the SAR data in time and space as possible. The SAR data was then used both for icebreaker navigation (near real-time) and for subsequent validation of the SAR sea ice classification against observations. These cruises have been conducted in the Barents Sea, Greenland Sea, Pechora Sea and Kara Sea in the period 1991-1999. Icebreakers and research vessels have been using both ERS SAR and RADARSAT ScanSAR data (Alexandrov et al., 1999; Johannessen et al., 1992b; 1996b; 2000; Melentyev et al., 1999; Sandven et al., 1999b).

This data set contains a SAR image also used for navigational support in the Ob Estuary in 1998, where navigation is difficult and dangerous due to broken ice that has been forced upward by pressure (Pettersson et al., 2000). Archived ERS SAR scenes from previous years were used to increase knowledge of the typical ice conditions in the area. Two SAR scenes from 17 April 1998 were used for information about the fast ice to select the optimal route through level ice areas in between the more heavily deformed areas. Figure 3.3 shows the icebreaker track as a bright line through the best sailing areas, when it several weeks later sailed through the estuary.

Different sea ice types modify the backscattering coefficient according to the ice structure, salinity, temperature, voids and surface roughness (Gogineni et al., 1992; Hallikainen and Winebrenner, 1992; Onstott, 1992). The sea ice categories used in this

study can be considered as two major groups, according to how the ice types and forms affect navigation for ice-strengthened vessels and icebreakers. The greatest danger in transiting an ice field is loss of propulsion or manoeuvrability. This can result in a vessel becoming trapped. Where icebreakers are needed, routes through leads or the thinnest ice may be identified, reducing fuel consumption and increasing the rate of progress to the destination. The new ice category consists of all ice types less than 10 cm in thickness (frazil ice, grease ice, slush, shuga and nilas). Young ice consists of grey and grey-white ice, 10-30 cm in thickness (World Meteorological Organization, 1970). These ice types do not significantly affect ice navigation, however they are important for heat exchange between air and water (Maykut, 1978). First year ice, multi year ice and fast ice areas will reduce icebreaker speed and sailing safety, which depends on ice thickness and ice deformation, among other factors. First year ice was divided into the smooth and rough category, because rough first year ice will be more dangerous and slow down the icebreaker speed more than level first year ice (Pettersson et al., 2000).

The greyscale values and texture are used together to identify the ice types in the manual classification. Knowledge of the day of the year, location and the surrounding ice field are also important information for distinguishing the ice types from each other. Time series of SAR images from the same area provide valuable information for separation of the ice types, when the typical signatures of the areas are known. The signal of open water can cover the whole range of backscattering values depending on wind speed. Nilas and grease ice appear as dark ice types in SAR images (Smith et al., 1995). Grey and grey-white ice varies from dark to rather light. First year ice can cover a large range of backscattering values depending on ridging, and is characterized by well-defined angular floes (Bertoia et al., 1998; Wohl, 1995). The first year ice was visually divided into the smooth and rough category. The multi year ice floes are more rounded and are brighter than first year ice (Nystuen and Garcia, 1992). During melting, wet snow can mask the difference of first year ice and multi year ice. In summer, the signal of first year ice may be stronger than the multi year signal. Fast ice areas along coasts are recognized by using knowledge of the area and repeated SAR coverage when available. Ridges are formed due to wind and current forcing and influenced by geographical effects, and they are important for the climate and for navigation purposes (Davis and Wadhams, 1995; Johannessen et al., 2000). Ridged areas also influence the SAR backscattering coefficient (Melling, 1998), but are not investigated in this study.

3.3 Results and discussion

Several of the SAR images used in this study cover the marginal ice zone and dynamic polynya areas. This affects the backscattering coefficient due to the influence from large ranges in floe size, ocean waves propagating in the ice field and variable air temperature (Liu and Peng, 1998). Polynyas are open areas along coasts (shore polynya) or between fast ice along the coast and drifting ice (flaw polynya). If it occurs in the same position every year, it is called a recurring polynya. These are often created by offshore winds. Open water is exposed and refrozen as the ice is blown away from the coast or fast ice, making polynyas sources of ice production. Polynyas may be covered with new ice, nilas or young ice, and/or they contain brash ice (World Meteorological Organization, 1970). They are important for heat transfer in winter (Andreas and Cash, 1999). During winter, polynyas are found north and south of the Kara Gate and along the Yamal Peninsula (Proshutinsky et al., 1999). The classification categories (given a number code) assigned to each extracted sample area are shown in Table 2.1. The relatively high number of samples of young ice originates from these polynya areas.

The backscattering coefficient of young ice can be affected by the presence of frost flowers. Their extent and form depend on the air temperature and the level of supersaturation of the air near the surface (Tucker et al., 1992). Frost flowers covering nilas and young ice are typical for the Arctic during freeze up and in winter (Steffen and Heinrichs, 1994; Ulander et al., 1995; Wohl, 1995). Laboratory studies of the effect of frost flowers on C band radar backscattering from sea ice show that an area of frost flowers may increase the backscattering with about 5 dB (Nghiem et al., 1997). Both the classes new ice and young ice in this study may be affected by frost flower areas, but to what extent is not possible to determine due to lack of *in situ* data.

For each sample area, mean and standard deviation of the backscattering coefficients were calculated (Figure 3.4). The classification categories are as defined in Table 2.1. The definition of standard deviation (in decibels) was the same as used in Kwok and Cunningham (1994). As shown before (Fetterer et al., 1994; Sandven et al., 1999b), there was considerable overlap between the different categories when only mean and standard deviation values were considered. From mean values only, it may be possible to separate smooth first year ice (3) and multi year ice (5), under the assumption that the location is away from the ice edge or an open water area in the winter season. Open

Classification category	Number of samples	Mean SAR backscattering coefficient [dB]	Standard deviation [dB]	Code
Open water	63	-5.79	0.67	0
New ice	12	-11.10	1.39	1
Young ice	63	-9.41	0.83	2
First year ice smooth	24	-13.54	0.95	3
First year ice rough	90	-10.00	0.86	4
Multi year ice	8	-8.42	1.25	5
Fast ice	19	-12.71	0.81	6

Table 3.1: *Classification categories used for the ERS-1/2 SAR sample areas and the number of samples for each category. Mean and standard deviation of backscattering values from all SAR samples in each category are calculated.*

water (0) and multi year ice (5) may be separated using standard deviation values only, but the number of multi year samples was very limited. The category new ice (1) shows considerable variation in the mean and standard deviation values, some samples show mean backscattering coefficients below the ERS-1/2 noise floor of -24 dB, as reported by Fetterer et al. (1994).

As seen in Sandven et al. (1999b), the classification of sea ice is difficult in the marginal ice zone and seasonal ice zone, due to among other reasons the presence of open water areas. Depending on wind speed, the open water areas give mean backscattering values that fall into the ranges defined by the different ice types. The curve described by the connecting line corresponds to the evolution of the microwave signature of first year ice proposed by Onstott (1992), from open water through new ice and young ice to smooth and rough first year ice.

As shown in Figure 3.4, the mean and standard deviation of the backscattering coefficient are not sufficient to reliably separate the different ice types. This corresponds to results from Haverkamp and Tsatsoulis (1999) and Sandven et al. (1999b). In order to investigate these sea ice signatures further, day number, temperature and wind data, latitude, longitude and angle of incidence were added to the SAR sample database. The distribution of the SAR samples through the year is shown in Figure 3.5. The mean values of the backscattering coefficients of the different sea ice categories are plotted as function of day number. The first three months in the year are the best represented regarding number of samples.

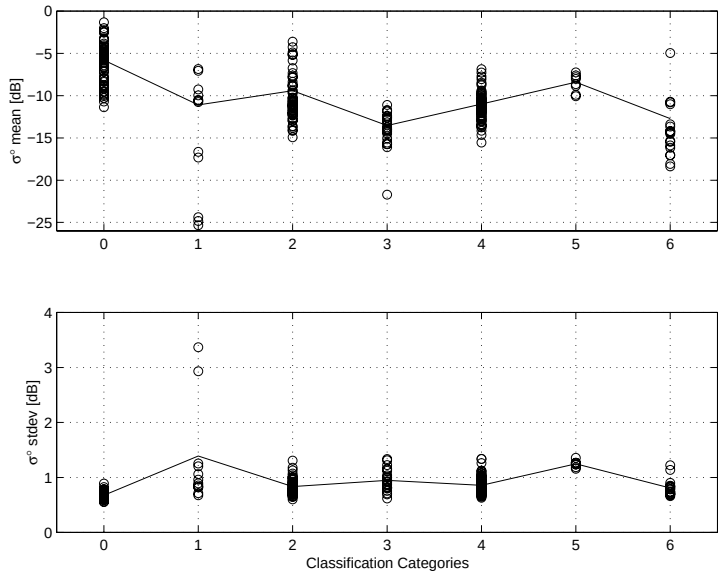

Figure 3.4: *Mean and standard deviation of SAR backscattering coefficients values for all 279 samples. The classification categories are defined in Table 2.1. The connecting line indicates mean SAR values for each category.*

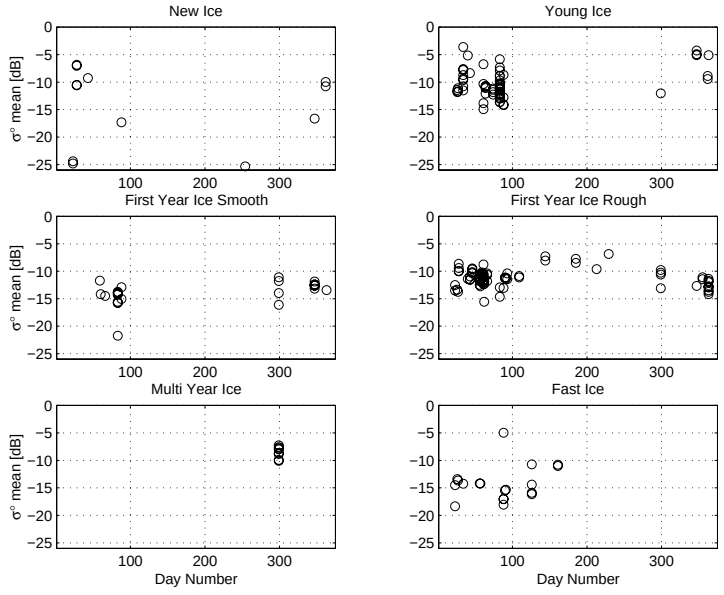

Figure 3.5: *Mean values of the backscattering coefficients for each sea ice sample as function of day number.*

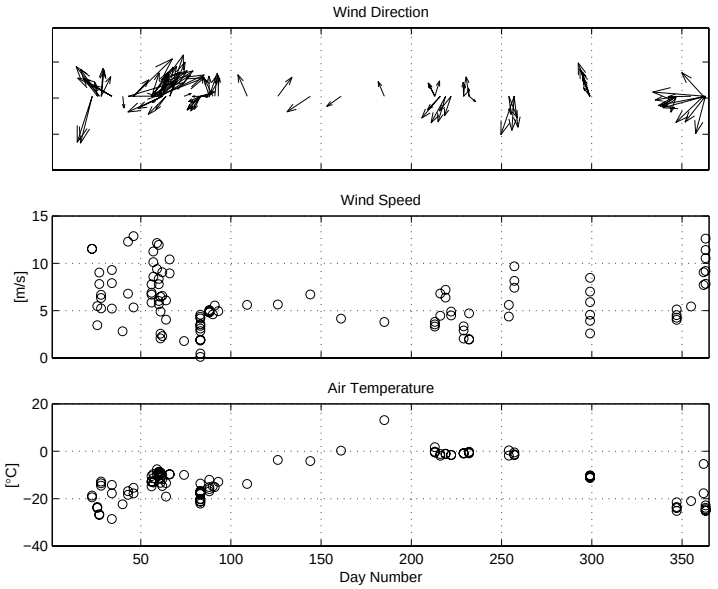

Figure 3.6: *Temperature and wind data from ECMWF for the image scenes marked with frames in Figure 3.1.*

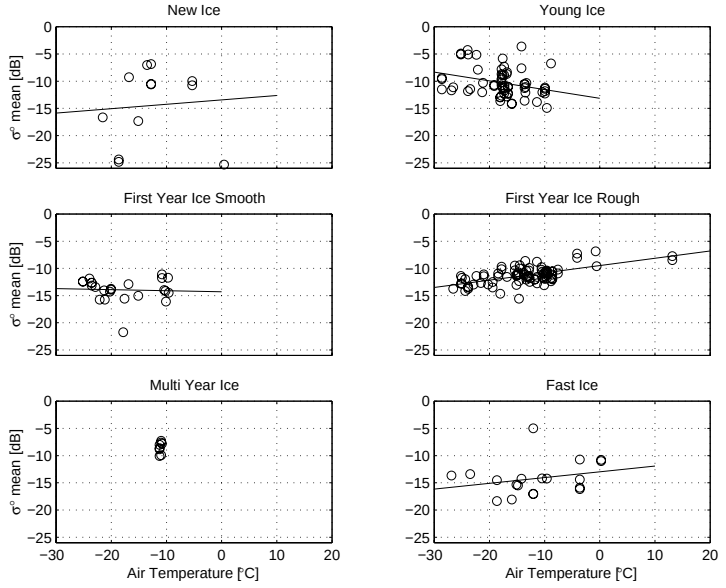

Figure 3.7: *Backscattering coefficient and air temperature for all six sea ice categories. Linear regression lines are marked, except for multi year ice.*

URN:NBN:no-2344

The wind data derived from the ECMWF analyses for each image scene shows that wind directions are variable (Figure 3.6). Most of the images are located near land, and topographic effects may influence the wind direction. For the further multivariate regression study only the wind speed was used as input, due to its influence on the backscattering values of open water (Korsbakken et al., 1998). Wind speeds are generally higher and temperature values are lower in September to March than in the rest of the year.

The relation between the backscattering coefficient and the air temperature is investigated in Figure 3.7. This data set was not extensive enough to draw conclusions about the dependence of the backscattering coefficient on air temperature for the different ice types. However, the data set may indicate some increase in backscattering values with increased air temperature for new ice, rough first year ice and fast ice. The opposite relation was observed for young ice and smooth first year ice. According to a model describing the relationship between temperature and backscatter for first year ice (Onstott, 1992), at 9.6 GHz and an angle of incidence of 40 degrees, the backscattering coefficient is expected to increase with increasing temperature. In the presentation shown in Figure 3.7, no adjustment for the influence by the different angles of incidence was done. The influence of the varying angles of incidence on the backscattering coefficients is presented in Figure 3.8.

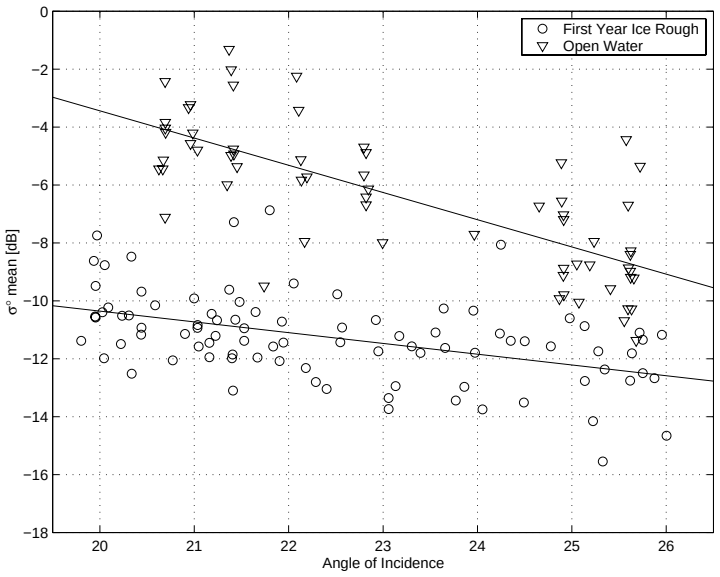

Figure 3.8: *Backscattering coefficient and angle of incidence for the rough first year ice and open water samples.*

URN:NBN:no-2344

The backscattering coefficient values experience a fall-off at increasing angles of incidence, but the sea ice signatures are less dependent on increasing angles than open water signatures. The fall-off was most evident for the rough first year ice category, which has the most samples, but can also be seen for young ice and fast ice (not shown). These results agree with those given in Onstott (1992).

3.3.1 Multivariate regression

Different multivariate regression methods were chosen in order to investigate the separation possibilities of the ice and water classes (Martens and Næs, 1989). The relative importance of the SAR and meteorological variables was also investigated. The data set was divided into two sets, one for training and one for validation. The X variables in the regression were day number, mean and standard deviation values of backscattering coefficient, latitude, longitude, angle of incidence, temperature and wind speed. All variables were scaled to zero mean and unit variance. The values for the classification category Y in the regression were design variables given to separate the two classes in each calculation.

From normal probability plots for each category (not shown), it was seen that the values of the different class samples deviated from the normal distribution. A multivariate normal assumption is not required for the input to the following methods. Multivariate linear regression (MLR) is the most commonly used method for multivariate regression (Johnson and Wichern, 1992). Principal component regression (PCR) is used for forming regression models, rather than MLR when input variables are dependent of each other (Höskuldsson, 1996). Instead of using the original measured variables, the regression is performed on the calculated principal components, which capture the greatest amount of variance in the variables and are orthogonal. Two algorithms for partial least squares (PLS) regression were used (Helland, 1990; Höskuldsson, 1988). PLS can be used to develop regression models that relate a number of X variables to one or more Y variables. Whereas PCR uses factors that are descriptive of variance in the X variables only, PLS finds factors known as latent variables that are descriptive of the variance in the X variables and correlated with the Y variables. An often used algorithm is non-linear iterative partial least squares (PLS NIPALS) (Martens and Næs, 1989). The PLS NIPALS algorithm calculates latent variables (similar to those used in PCR) and an additional set

of weight-vectors. A vector of inner-relationship coefficients must also be calculated. As for PCR, the model converges to the MLR solution if all latent variables are included. Another method developed by Qin and McAvoy (1992) is PLS by neural network inner relationships (PLS NN). The PLS NN models the outer and inner relations with three-layer feed-forward neural networks. This model extends the PLS NIPALS by relaxing the linear assumptions on the outer and inner relations. This is the method that requires most computer resources after the PLS NIPALS.

The focus of this part of the work was to find models for the data set, which can be used to predict the classification categories of new samples. It was not critical if the models did not describe the training data set optimally. The minimum of the root mean square error of prediction (RMSEP) was determined. It was used to find the number of latent variables that optimized the predictive ability of the model. It was found that the optimal number of variables varied slightly with the methods.

Correlation coefficients and the actual and predicted data values for ice and water are shown in Figure 3.9. The results for MLR are not shown, but they correspond to the PCR results. For PLS NIPALS and PLS NN models, comparable results could be obtained with a lower number of latent variables. Similar results were obtained for the different methods regarding the ice and water separation. Reasonable good correlation coefficients were obtained between predicted and actual values from the four methods.

MLR, PCR and PLS NIPALS regression vector coefficients and the X variables are shown in Figure 3.10. The variables with highest absolute values are most important in the regression models. The mean and standard deviation of the backscattering coefficients contribute most, followed by temperature and angle of incidence. With the combined information from these variables it is easier to separate ice and water than on the basis of just one variable. The 95 % confidence intervals were calculated and are marked in Figure 3.10. The intervals for day number, latitude, longitude and wind include zero, and these variables might be dropped from the regression model. Their small contributions to the model lead to minor decrease in the correlation values. The variable latitude was significant for the PLS NIPALS regression model only. Open water areas are found near the peninsulas and islands in the Pechora and southwestern Kara Sea during winter due to the high frequency of polynya areas. To higher latitudes there are few open water areas and this may cause the relatively higher importance of latitude than of longitude in the regression.

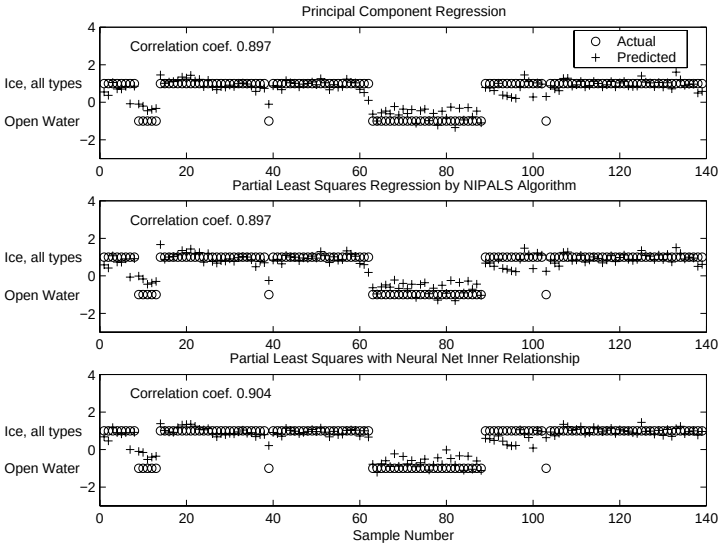

Figure 3.9: *Results from principal component regression, partial least squares regression by the NIPALS algorithm and partial least squares regression with neural network inner relationship. The correlation coefficients are marked.*

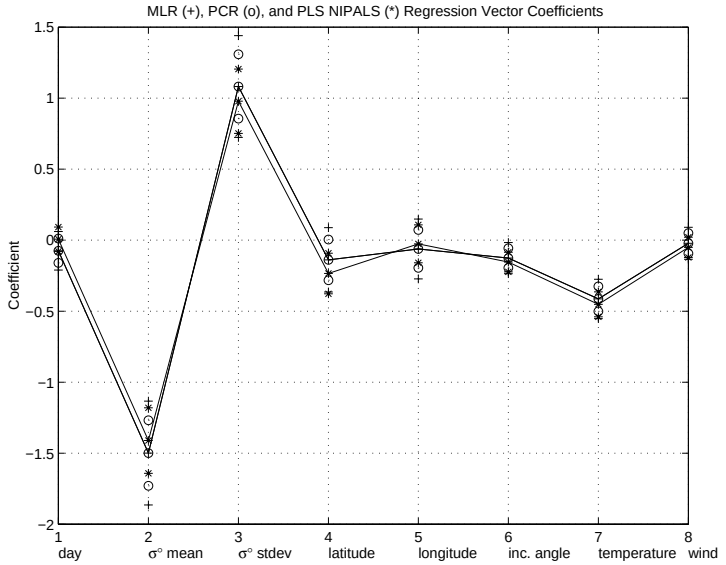

Figure 3.10: *The regression vector coefficient for MLR, PCR and PLS NIPALS as function of the X variables for the separation of all ice types from water. The 95 % confidence intervals are marked.*

URN:NBN:no-2344

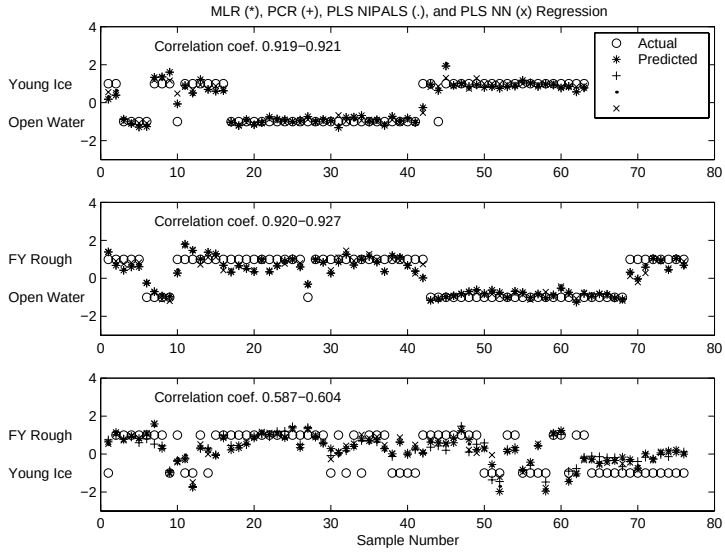

Figure 3.11: *Separation of young ice and rough first year ice from water, and separation of the two ice types by the MLR, PCR, PLS NIPALS and PLS NN methods. Correlation coefficients are marked.*

To make a more specific separation test depending on ice type, young ice and rough first year ice were chosen due to the larger data sets for these compared to the other ice categories (Table 2.1). The data was separated into training and validation sets, and the optimal number of latent variables was determined by evaluating the RMSEP values. MLR, PCR and PLS NIPALS produced rather similar results, and the result from the PLS NN algorithm had the highest correlation value (Figure 3.11). The separation ability for the ice types and the water was good, but the result was poorer when trying to separate the two ice types. Slightly better results for separating ice from water were obtained when considering one ice type at the time instead of using all ice types in the regression as shown in Figure 3.9.

Mean and standard deviation of the backscattering coefficient were the two most important variables for the regression results (Figure 3.12). As for the ice and water separation, the effect of the temperature variable was important. The effect from wind speed on the separation of the two ice types may probably be due to the annual co-variation of the wind speed with the air temperature (Figure 3.6). Wind information from ECMWF was useful for the manual analyses of the SAR images. When it was possible to visually

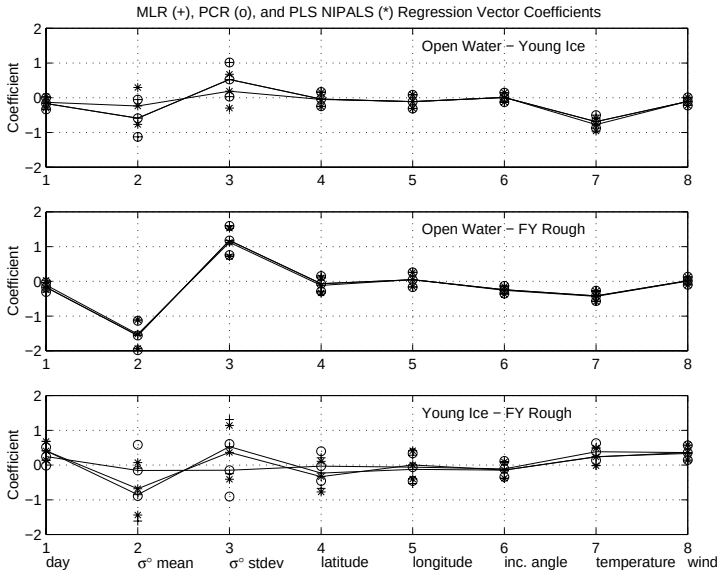

Figure 3.12: *The regression vector coefficients for MLR, PCR and PLS NIPALS as function of the X variables for the three different separations in Figure 3.11. The 95 % confidence intervals are marked.*

derive wind directions from the SAR images, these were often in agreement with the ECMWF directions. However, the regression analyses indicated that wind information was redundant. The ECMWF data may have been inaccurate in this area and, had it been available, wind information from nearby weather stations might have proven more useful in the regression models.

The results obtained in this study are comparable to results from literature for the separations of ice samples from the water samples, and separation of young ice and rough first year ice. Nystuen and Garcia (1992) obtained comparable results to these, when separating first year ice, multi year ice, 'Odden ice' and open water using standard statistics and second order statistics. Also, Steffen and Heinrichs (1994) had problems separating young ice (grey and grey-white ice) from first year ice based on the backscattering values. By using Landsat data together with SAR they achieved good classification accuracy for seven ice classes and open water. Fetterer et al. (1994) reported on problems with classifying new ice and open water due to the wide distribution of the backscattering coefficient for these classes. Smith et al. (1995) had problems with misclassification of open water as first year ice. Shokr et al. (1999) had an overall success rate of 77 % in

their algorithm giving six ice types and concentration from backscattering values.

Improvements in the predictions may be possible by adding other derived SAR variables from the sample areas. Texture measurements (Barber and LeDrew, 1991) may be useful, though authors do not agree about their value for classification. Only slightly better results were obtained by using the more sophisticated and computer demanding algorithms PLS NIPALS and PLS NN than obtained by the MLR and PCR algorithms.

3.4 Summary

Sample areas from calibrated ERS-1/2 SAR PRI scenes from the Pechora and Kara Seas have been extracted. Mean and standard deviation values of the backscattering coefficients have been calculated. The samples were manually classified into seven categories, and day of the year, angle of incidence, latitude and longitude were assigned to the samples. Temperature and wind parameters have also been added to each SAR sample.

There was considerable overlap between the different sea ice categories and open water, when only mean and standard deviation values of the backscattering coefficient were considered. From mean values only, it may be possible to separate smooth first year ice and multi year ice. Under summer conditions this result would not be valid. Open water and multi year ice may be separated using standard deviation values only. As only a small part of the ice cover in the Pechora and Kara Seas is multi year ice, more parameters than mean and standard deviation have to be investigated to get a better separation of the different ice types and open water.

The separation of ice and water by constructing multivariate regression models produced rather promising results. Separation of open water from all ice types, open water from young ice and rough first year ice, and separation of young ice from rough first year ice were done in four calculations. First, in the separation of all ice types from water it was achieved correlation coefficients up to 0.90 between predicted and actual data values. Second, young ice and rough first year ice were separated from the water samples. The correlation coefficients between predicted and actual values for open water and young ice and for open water and rough first year ice were as high as 0.93. When trying to separate the two ice types, correlation coefficients of about 0.60 were obtained. Mean and standard deviation values of the backscattering coefficient, temperature and maybe angle

of incidence are the variables that are useful to keep for further studies using regression models.

Limitations of this study are that the SAR observations are only collected from a small region in the Arctic, and some of our manual sea ice interpretations may be doubtful. In addition, errors in the ECMWF data set were not assessed, and these data is not as optimal as *in situ* measurements of temperature and wind. The data set obtained during this study will be used for further statistical analyses towards a more automated classification procedure designed for this part of the Arctic.

Acknowledgments

The ERS-1/2 SAR image data was obtained within different European Space Agency 'Announcement of Opportunity' projects. This work was funded by a Ph. D. grant from Telemark University College, Department of Technology (IPT/TF), Porsgrunn, Norway and with support from Nansen Environmental and Remote Sensing Center (NERSC), Bergen, Norway. Thanks to K. H. Esbensen (IPT/TF), O. M. Johannessen (NERSC) and S. Sandven (NERSC) for valuable comments and suggestions. I also want to thank three anonymous reviewers for helping me to improve this text.

URN:NBN:no-2344

Chapter 4

SAR and SSM/I study of coastal polynyas in the Pechora and Kara Seas

by

M. Lundhaug and S. Sandven

Submitted to Canadian Journal of Remote Sensing, 2002.

Abstract

The main objective is to investigate polynyas in the Kara and Pechora Seas with use of satellite data and a one-dimensional polynya model. This study is limited to winter months in the 1990s, with the main focus on March when the maximum ice distribution in the Northern Hemisphere occurs. Synthetic Aperture Radar (SAR) image data has been used to investigate specific polynya events in detail, addressing widths, refreezing and duration. A polynya index derived from ice concentration data from Special Sensor Microwave Imager (SSM/I) was used in the description of polynya variability during a decade (1990-1999) in response to atmospheric forcing.

From SAR, the largest polynyas were found along the Taymyr Peninsula with mean with of about 40 km. Along the western coast of Yamal Peninsula and the area around the

outlets of the Yenisey and Ob Rivers typical polynya widths were in the range of 20 to 30 km, with variability of tens of kilometers. Large polynyas were also measured in the Vaygach area and around Franz Josef Land.

The prevailing wind regime determine the number of polynya days in the south-eastern Kara Sea. With south-westerly winds, polynyas occur frequently such as in 1995 and 1996. Then a polynya occurred 55 and 56 out of 90 days. When the winds are in the opposite direction, polynyas occur less frequently (i.e. 1991, 1994, 1998, 1999). Polynyas occurred only 7 and 8 days in 1999 and 1991, respectively. The largest and longest lasting areas covered by polynyas occur in 1995, and the smallest area with short duration was in 1991.

The observed polynya widths from SAR were are compared to polynya widths calculated by a one-dimensional polynya model for nine different areas. Observed and predicted polynya width and opening time were compared for four days during March 1994 north-east of the Vaygach Island in the Kara Sea. To be from a simple one-dimensional model, the description of the polynya opening time and the steady-state polynya width is reasonable.

The best correspondence between observations and model results were found for the Vize and Ushakova Island and the Novaya Zemlya coast. The lowest variability of SAR observations was found in these areas, and the model predicted these widths better. The Yamal and Taymyr observed polynyas widths were highly variable, and these were not well predicted by the model. The use of different parameterisations of the collection thickness in the polynya model gave comparable results. The one-dimensional model may be too simple with to many assumptions for use in this area due to relatively complex coastline geometry and influence by currents and tides on sea ice drift. Data about the polynya ice edge relative to coastlines of different orientations and shapes may give valuable information for validation of a two-dimensional model where the affect of the coastline on polynya size and development are accounted for.

URN:NBN:no-2344

4.1 Introduction

4.1.1 General review of polynyas in the Arctic

Open water areas including leads and polynyas are very important for the heat and moisture exchange driven by the large temperature difference between air and sea water in the Arctic during winter (Smith et al., 1990; Andreas and Cash, 1999; Eisen and Kottmeier, 2000). Heat transfer to the atmosphere through thin ice areas like refrozen leads and polynyas is between one and two orders of magnitude larger than through perennial ice (Maykut, 1978). Ruffieux et al. (1995) investigated from surface observations the average net surface heat flux during the Arctic Leads Experiment (LEADEX) north of Alaska in April 1992. They found fluxes of -75 W/m^2 over pack ice, -130 W/m^2 over leads and -250 W/m^2 over open water. Information about the local distribution and frequencies of open water and thin ice areas are important for the understanding of climatic processes (Wettlaufer et al., 2000) as well as for practical ice navigation and offshore operation in Arctic waters. Several studies suggest that ice growth in polynyas over the Alaskan, Siberian and Canadian continental shelves produce saline water that contributes to the maintenance of the cold halocline layer in the Arctic Ocean (Martin and Cavalieri, 1989; Cavalieri and Martin, 1994; Winsor and Björk, 2000). Polynyas are important formation areas for new ice (ice factory). When this ice is transported away from the polynya area it can carry sediments or pollution from river outflow or other sources across the Arctic Ocean. Studies show that sea ice and dense water formed in polynyas along the eastern and southern coasts of Novaya Zemlya and north of Vaygach Island may transport radionuclides and sediments (Dethleff et al., 2000; Sherwood, 1999). Polynyas and leads are important areas also for marine birds and mammals (Stirling, 1997). Migrating or overwintering species are dependent on polynyas for feeding during the critical time when the sea is largely ice covered.

The extent of polynyas can range from a few hundred meters to hundreds of kilometers (Smith et al., 1990), and they can be covered with new ice, nilas or young ice (World Meteorological Organization, 1970). There are two main categories of polynyas, depending on the formation mechanisms: latent and sensible heat polynyas. Latent heat polynyas generally form along coasts (shore polynya) or between fast ice and drifting ice (flaw polynya). They are usually associated with land features like islands, straits and peninsulas. Large coastal leads and polynyas reflect the high values of ice divergence and shear

rates in the coastal areas (Agnew et al., 1999). These are often created by strong offshore winds, and open water is exposed as the ice is blown away from the coast or from the fast ice. Sensible heat polynyas are caused by up-welling of warm water to the surface, which melts the ice cover and prevents further ice formation (Mysak and Huang, 1992). Examples of large latent heat polynyas are the northern Bering Sea, North East Water (Budéus and Schneider, 1995; Schneider and Budéus, 1995), North Water (Darby et al., 1994), Terra Nova polynya (Van Woert, 1999) and the numerous Siberian shelf polynyas (Smith et al., 1990; Dokken et al., 2002). The polynyas in the Pechora and Kara Seas are part of the Siberian shelf polynya band, which extend from the Barents Sea in west to the Chukchi Sea in east (Proshutinsky et al., 1999). Sensible heat polynyas are polynyas in the Canadian Archipelago, the Okhotsk polynya (Martin et al., 1998), and the Weddel, Cosmonaut and Maud Rise polynyas in the Antarctic (Goosse and Fichefet, 2001). A combination of the two formation mechanisms is also possible, wind induced divergence and transfer to the surface of relatively warm water is suggested as essential for the formation of the spring Ross Sea polynya (Fichefet and Goosse, 1999).

The high-resolution microwave SAR carried by different satellites has good capability to image sea ice processes and parameters independent of cloud and light conditions, with pixel spacing of typical 100 m. A number of studies in the marginal ice zone have been carried out by use of SAR images with focus on eddies, ice tongues, vortex pairs, upwelling, wave-ice interaction and melting/freezing (Johannessen et al., 1992a; Liu et al., 1994). For polynyas studies, ERS-1 SAR data has been used in the North-East Water polynya north-east of Greenland (Gudmandsen et al., 1995), in the Tatarskiy Strait in the Japan Sea (Martin et al., 1995) and in the area of Commonwealth Bay in Eastern Antarctica (Wendler et al., 1997). Dokken et al. (2002) investigated areas in the Arctic with focus on the Franz Josef Land area. Ice production and brine formation in the Storfjorden polynya in Svalbard have recently been investigated by Haarpaintner et al. (2001) using time series of SAR images as an important data source.

4.1.2 Polynyas and other ice characteristics in the Pechora and Kara Seas

Several islands, straits and peninsulas as well as the shallow shelves in the Pechora and Kara Seas, determine the formation and extent of coastal polynyas and fast ice (Figure 4.1a). Along the coasts of large groups of islands (Novaya Zemlya, Severnaya Zemlya

and Franz Josef Land) as well as numerous small islands, polynyas are created when the ice is pushed away during offshore winds. Freezing of the polynya areas occurs during time periods with low temperature. Recurring polynyas are generated when the wind and temperature conditions again are favourable (Proshutinsky et al., 1999; Volkov et al., 2002). Fast ice is formed in the Arctic seas during autumn and early winter. Fast ice may form *in situ* or by freezing of drifting ice to the shore. It extends from a few meters to several hundred kilometers from the coast. Maximum development of fast ice is observed in the shallow waters. The width of fast ice is only about 10-20 km close to coastlines with deeper waters (Proshutinsky et al., 1999). In the eastern Kara Sea shallow waters, highly irregular shorelines and a large number of islands cause the fast ice areas to be large (Figure 4.1a). Radiation fluxes, air temperature and snow cover are factors affecting fast ice thickness (Wadhams, 2000). Model sensitivity studies of areas in the Canadian Arctic showed that inter-annual variability of fast ice thickness is dominated by variability of annual snowfall that modifies the growth rate of the ice (Flato and Brown, 1996). Nearly every summer, warm air masses from land causes the areas of fast ice to melt almost completely (Flato and Brown, 1996). In some areas (i.e. Franz Josef Land and Severnaya Zemlya) fast ice can persist during the summer and become multi year fast ice (Proshutinsky et al., 1999).

The presence of open water and thin ice in the coastal polynyas is very useful for navigation in the winter season (Johannessen et al., 2000; Mulherin et al., 1994). The Kara Gate (Figure 4.1b) is an important and difficult part of the Northern Sea Route. Navigation along this coastal route can save sailing time compared to going north of Novaya Zemlya (Johannessen et al., 1997b).

Summer melting in the Kara Sea typically starts in May and depends on the development of the polynyas, warm river water and the inflow of warmer Barents Sea water (Volkov et al., 2002). Melting begins at the outer edge of the fast ice when ice production ceases, and the ice breaks up and drifts seaward a few weeks later. Large areas of open water are formed along the shores from Vaygach Island to the Vilkitsky Island, where polynya activity is high during winter (Volkov et al., 2002).

South-westerly and south-easterly wind prevail in the Kara Sea in winter (Løset et al., 1999), while the Pechora Sea is dominated by south-westerly winds. The mean air temperature in the Kara is -21° C. In the Pechora Sea, the mean air temperature is higher in the eastern (-17° C) than in the western (-12° C) area (Løset et al., 1999). Monthly mean

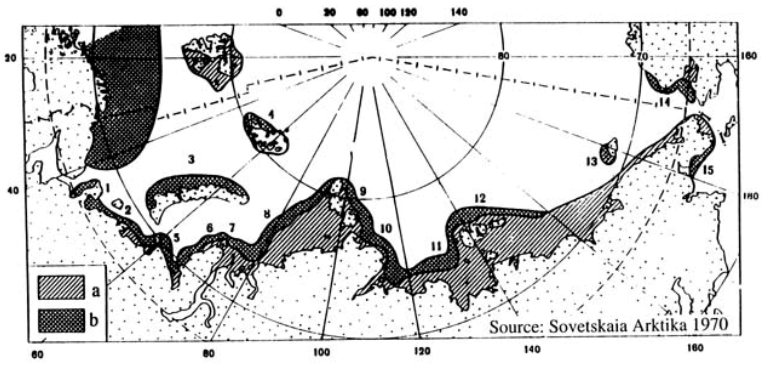

a - fast ice;
b - polynias: 1 - Cheshskaya, 2 - Pechorskaya, 3 - Zapadno-Novozemelskaya, 4 - More Victorii, 5 - Amderminskaya, 6 - Yamalskaya, 7 - Ob'-Eniseyskaya, 8 - Zapadno-Severozemelskaya, 9 - Vostochno-Severozemelskaya, 10 - Taymirskaya, 11 - Lenskaya, 12 - Novosibirskaya, 13 - Zavrangelevskaya, 14 - Alaskinskaya, 15 - Anadirskaya.

(a)

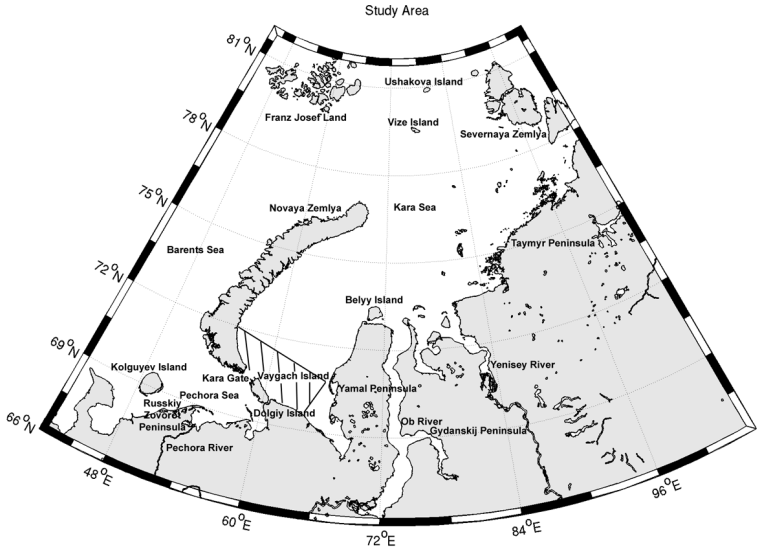

(b)

Figure 4.1: *a. Overview of polynyas in the Russian Arctic (figure from Proshutinsky et al., 1999). b. The study area in the Pechora and Kara Seas, and the marked area shows where the polynya index was calculated from SSM/I sea ice concentration data.*

wind speeds are 6-8 m/s in the Kara Sea in winter.

4.1.3 Outline of the paper

The main objective is to investigate polynyas in the Kara and Pechora Seas with use of satellite data and a one-dimensional polynya model. Ice concentration data from SSM/I, wind and air temperature data are used in the description of polynya variability. Polynya widths are quantified in detail using SAR data covering smaller areas. Then the observed polynya widths are compared to polynya widths calculated by a one-dimensional polynya model for nine different areas. This study is limited to winter months in the 1990s, with the main focus on March when the maximum ice distribution in the Northern Hemisphere occurs. Section 4.2 provides an overview of data and methods used. The polynya model is also described. The results from data analyses and the model are presented in Section 4.3. Section 4.4 gives a summary, and the results and assumptions are discussed.

4.2 Data sets, analysis methods and model description

4.2.1 SAR

Regional mapping of polynyas by SAR

The first data set from ERS-1 was obtained over the same areas with three days interval during the 'Ice Orbit' of ERS-1 in March 1994. The second data set was a combination of ERS-1 and 2 images obtained in February/March 1996 during the ERS-1/2 'Tandem Phase', when data could be obtained with one day interval. ERS SAR data from other periods were available, but not used in the study due to the scattered and unsystematic data coverage. From 1997, archived RADARSAT-1 ScanSAR data has been available, and data from Alaska SAR Facility (ASF) for March 1997 and 1998 has been selected for the study in areas of good spatial and temporal coverage. The data distribution for the four years is presented in Table 4.1. A total of 94 ERS-1/2 SAR scenes and 71 RADARSAT ScanSAR Wide scenes have been acquired and analyzed in the study. The ERS scenes cover 100 by 100 km with 12.5 m (high resolution) and 100 m (low resolution) pixel spacing. The ScanSAR Wide scenes cover 500 by 500 km with 50 m pixel spacing. For several cases, it was not possible to measure the polynya events seen in the ERS-1/2 SAR

Year	Time Period	Number of Scenes	Sensor	Number of Events
1994	3-24 March	61	ERS-1 SAR	28
1996	3 February - 5 March	33	ERS-1/2 SAR	8
1997	5-31 March	34	RADARSAT ScanSAR	42
1998	1-29 March	37	RADARSAT ScanSAR	47

Table 4.1: *Number of scenes used from the sensors for the four years. In 1994 and 1996 the number of events measured are solely from the Pechora Sea and the south-western Kara Sea, north of Vaygach Island.*

data. The scenes covered too small area of the polynya. For the RADARSAT ScanSAR data, more than one polynya event was sometimes possible to measure from each image. The polynya areas covered by RADARSAT ScanSAR and ERS SAR are Vaygach area, Pechora Sea, Yamal coast, the Ob and Yenisey estuaries, Taymyr coast, Novaya Zemlya, Severnaya Zemlya, Franz Josef Land and the Vize and Ushakova Islands (Figure 4.2a and b). Some of the polynyas are described in Section 4.3.1.

Polynya width measurements

Polynyas may be covered with new ice, nilas or young ice and/or contain brash ice (World Meteorological Organization, 1970). For each polynya area, the widths of the polynyas were estimated by calculating the distance from land or fast ice border to the edge of the first year ice. For each image, a characteristic polynya width was found by visually positioning the cursor in the image at two points at the land/fast ice border and at the ice edge border. The measurements were done where a characteristic polynya width could be found. If the polynya was only partly covered by the SAR image, a too small or large width could be measured. In some areas where repeated SAR images were available, the same polynya was measured several times during its development. A total of 125 measurements were obtained. These were compared to predicted polynya widths from a one-dimensional model. The results are presented in Section 4.3.2.

SAR backscattering from polynyas

Four selected ERS-1/2 SAR images from 28 February to 3 March 1996 were calibrated according to Laur et al. (1998) to describe changes in the backscattering coefficient

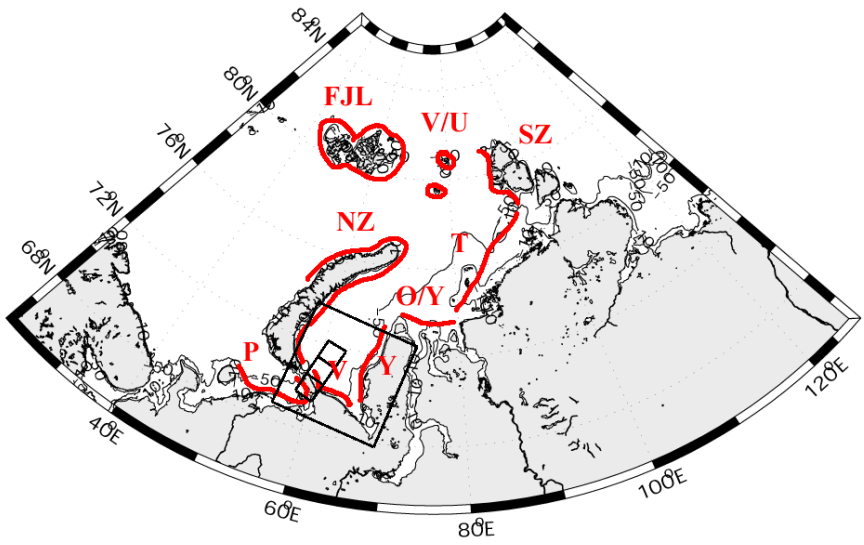

(a)

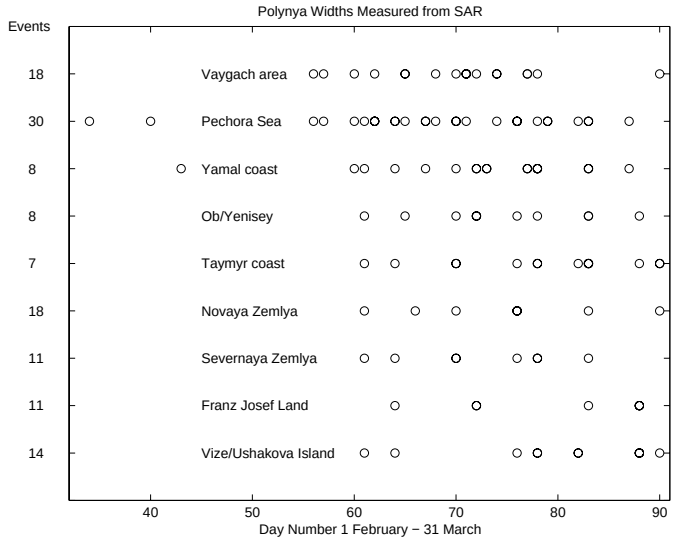

(b)

Figure 4.2: *a. The nine selected study areas are marked wit typical ERS SAR and RADARSAT ScanSAR scene coverage. b. This plot shows the SAR coverage for each area as a function of day number together with number of polynya events for each study area.*

during a polynya event. The accuracy of the backscattering coefficient is ± 0.4 dB. Each scene was re-sampled to a pixel spacing of 100 m. The results are presented in Section 4.3.3.

4.2.2 SSM/I

SSM/I sea ice concentration data have been used as a complementary dataset because these data are available every day and can be used to study inter-annual variability of a polynya area. The SSM/I ice concentration data was obtained from the National Snow and Ice Data Center archive (National Snow and Ice Data Center, 1999). The limitation of the SSM/I data is the coarse resolution from the gridded 25 by 25 km fields, which may especially influence the the possibility to detect small polynyas.

Daily ice concentration field were extracted for January through March from 1990 to 1999. The data were used to estimate the polynya frequency in the south-western Kara Sea, in an area of about 57000 km^2 north and east of the Kara Gate and the Vaygach Island (Figure 4.1b). Large polynyas form here during southerly and westerly winds (Dethleff et al., 2000), and many polynya events were seen in the SAR images covering parts of the area (Figure 4.2b). Since the area is located well away from the marginal ice zone (MIZ), it is possible to automatically extract polynya extent with small risk to make false estimates. Areas of ice concentration less than 80 % were chosen to represent a polynya event according to Comiso and Gordon (1996). Ice concentration less than 80 % indicates that open water and/or new ice can be present in at least 20 % of the area. Polynya extent is defined to be the sum of all pixels in the study region with less than 80 % ice concentration. The polynya index is defined for this study as the polynya extent divided by the total area, providing a normalized estimate of the polynya. This index is used to describe the polynya variability and the results are presented in Section 4.3.4.

4.2.3 NCEP data

Daily averages of air temperature and wind information (10 m) from the global NCEP reanalyzes dataset were used together with the SAR and SSM/I data to investigate the selected polynya areas. It was used for interpretation of the image data and as input to the polynya model. Different grid nodes were selected for the model calculations of polynya widths at locations in the Kara and Pechora Seas. The NCEP/NCAR Reanalysis Project

is a joint project between the National Center for Environmental Prediction (NCEP) and the National Center for Atmospheric Research (NCAR) (Kalnay et al., 1996).

4.2.4 Polynya model

The polynya model concept by Pease (1987) after the original idea by Lebedev (1968) has been applied to all polynya events observed in the SAR imagery along the coasts in order to assess if the model polynya widths are in agreement with observations (Figure 4.3). The fundamental assumption of the model is that change of polynya width (X_P) with time is proportional to the difference between the advection rate of the solidified ice (V_i) from the shore by wind, and the ice production rate (F_i) over the width of the polynya scaled by the collection thickness (H) of frazil ice (Equation 4.1). The frazil collection thickness describes the pile up of frazil ice against the edge of the polynya, and it is probably dependent on wind speed and air temperature (Pease, 1987). The ice production rate is determined by the total heat flux (Equation 4.2). The total heat flux is given by the sum of the short wave radiation (Q_r) and α is the albedo of the sea surface, the long-wave radiation emitted from the surface to the atmosphere (Q_{lu}), the downward long-wave radiation (Q_{ld}), the sensible heat flux (Q_s) and the evaporative heat flux (Q_e). The evaporative heat flux and the short wave radiation are neglected in the total heat flux calculation in the model (Pease, 1987; Biggs et al., 2000). The density of young saline sea ice is set to ρ_i = $0.95 \cdot 10^3$ kg/m^3, and L = $3.34 \cdot 10^5$ J/kg is the latent heat of freezing water containing salt.

$$\frac{dX_p}{dt} = V_i - \frac{X_p F_i}{H} \tag{4.1}$$

$$-\rho_i L F_i = (1-\alpha)Q_r - Q_{lu} + Q_{ld} + Q_s + Q_e \tag{4.2}$$

The long-wave radiation emitted from the surface is set to 301 W/m^2. The downward long-wave radiation is approximated with $\sigma e_a T_a^4$, where σ = $5.67 \cdot 10^{-8}$ W/m^{2}deg^4 is the Stefan-Boltzmann constant and T_a is the air temperature. The cloud cover fraction, Cl, is set to 0.65 (Arctic Climatology Project, 2000; Winsor and Björk, 2000), giving the emissivity of air, e_a, as 0.7829(1+0.2232$Cl^{2.75}$). The sensible heat flux is calculated from $\rho_a C_h C_p V(T_a - T_w)$, where ρ_a = 1.3 kg/m^3 is the air density, C_h = $2.0 \cdot 10^{-3}$ is the

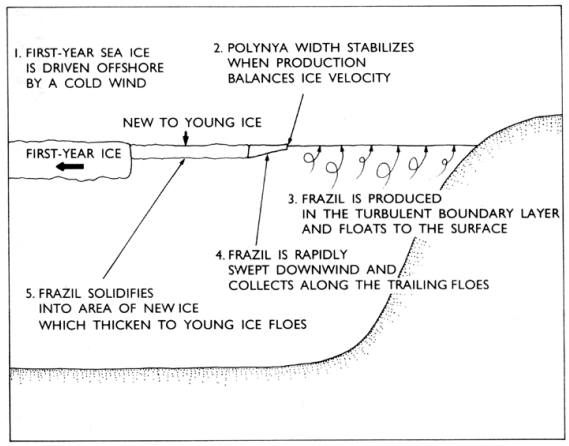

Figure 4.3: *The wind driven coastal polynya model concept (figure from Pease (1987)).*

sensible heat coefficient and C_p = 1004 J/deg kg is the specific heat of air. V is the wind speed, and T_a and T_w = -1.8° C are the air and water temperatures, respectively. The time for the polynya to reach 95 % of its limiting size is calculated from $t_{95} = 3.0 \cdot \frac{H}{F}$ (Pease, 1987).

Frazil ice is produced in the turbulent boundary layer in the water and floats to the surface. It is swept downwind and piles up to form consolidated new ice at the offshore edge. The polynya width stabilizes when ice production balances the ice velocity. If there is no significant ice production, the polynya will open at a constant rate, just dependent of time and ice advection with no equilibrium state. Polynya width is assumed to be dependent of wind speed, fetch and air temperature (Pease, 1987). Increasing wind speed rises both the advection and production rate. Maximum polynya width is strongly dependent on air temperature. The opening rate is dependent of both wind speed and air temperature. The polynya model was driven by wind speed and air temperature derived from the NCEP reanalyzed data.

The Kara and Pechora Seas polynyas are assumed to be purely wind driven (Proshutinsky et al., 1999). In order to apply the simple model, effects of currents, tides and the coastline morphology were neglected. These parameters may affect the size of the polynyas (Willmott et al., 1997). Near the coastlines the residual tidal ice motion will be offshore, since during half of the tidal cycle the ice motion is suppressed by the land boundary (Wadhams, 2000). The tidal currents also influence the polynyas by mixing the shallow

shelf water, bringing heat to the surface.

Pease (1987) and Agnew et al. (1999) assumed that the collection thickness of consolidated new ice at the ice edge is constant (H_P = 0.1 m). Winsor and Björk (2000) suggested a collection thickness that varies linearly with wind speed (H_W = 1/15(1+0.1V)), while Biggs et al. (2000) derived a collection thickness (H_B) that depends on polynya thermodynamics, wind stress and wind generated currents. The steady-state polynya width equals $(cu/F_i)V_i(u - V_i)$ for one dimension. The frazil ice velocity, u, is set to $2V_i$. The constant, c, is set to 0.665 s^2/m. These different versions of collection thickness were tested to compare the polynya widths from the model to the widths estimated from the SAR images. The results are presented in Section 4.3.5.

4.3 Results of data analyses and model calculations

4.3.1 Description of specific polynya events

Novaya Zemlya

A time series of SSM/I data showed that a polynya at the northern tip of Novaya Zemlya persisted from 28 of February to the 8 of March 1998 (Figure 4.4a). SSM/I data (a) and RADARSAT ScanSAR data (b) for 2 March 1998 can be compared from Figure 4.4 to get an overview the difference between the information in the data sets. The four ScanSAR images used were covering large areas giving detailed information about polynyas along the coast of Yamal Peninsula continuing to the Ob estuary, the northern part of Novaya Zemlya and a polynya in the western part of Franz Josef Land. Smaller polynyas exist west of Severnaya Zemlya and in the Pechora Sea. A total of eight polynyas were identified from these four ScanSAR images. Only three polynyas of these were visible in the SSM/I data. These were at the northern part of Novaya Zemlya, at the western part of Franz Josef Land and west of Severnaya Zemlya. The combined information from these data is important. Even if it is not possible to get very detailed information from SSM/I data, it provides the larger overview of the whole area combined with daily coverage, which was not possible with the SAR coverage.

The polynya opened up when the wind shifted from north-westerly to easterly and north-easterly and it stayed open as long as the wind had an easterly component. The polynya

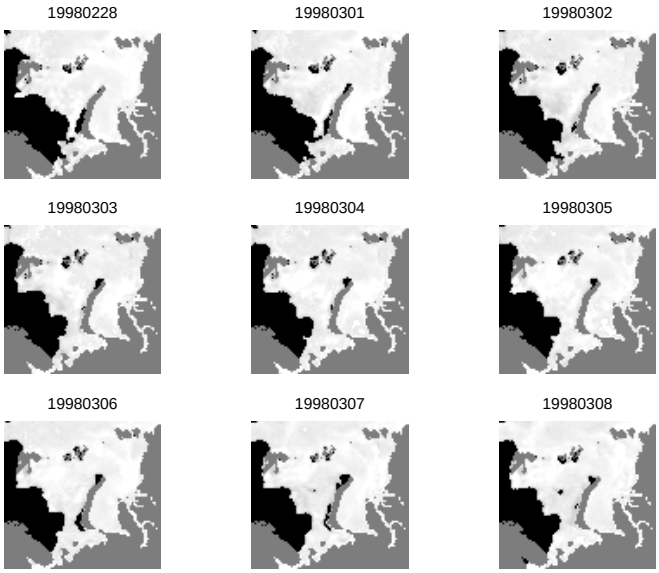

(a)

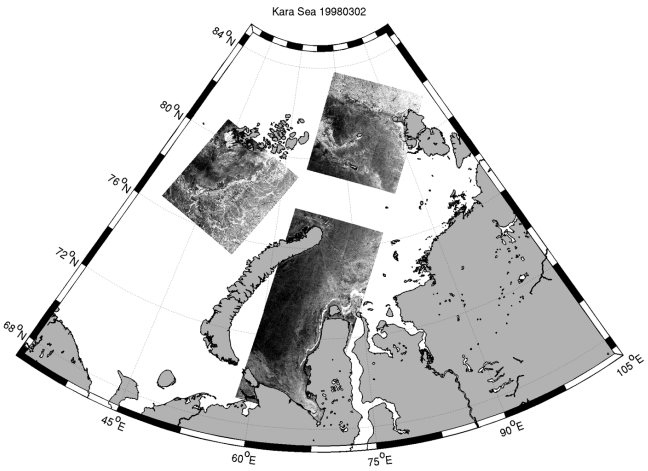

(b)

Figure 4.4: *a. SSM/I sea ice concentration maps from 28 February to 8 March 1998. Open water outside the ice edge and polynyas inside the ice are shown in black. Land areas are grey. b. Four RADARSAT ScanSAR scenes from 2 March 1998 illustrate the increased ability to study details compared to the SSM/I ice concentration data. Image Data ©Canadian Space Agency 1998.*

URN:NBN:no-2344

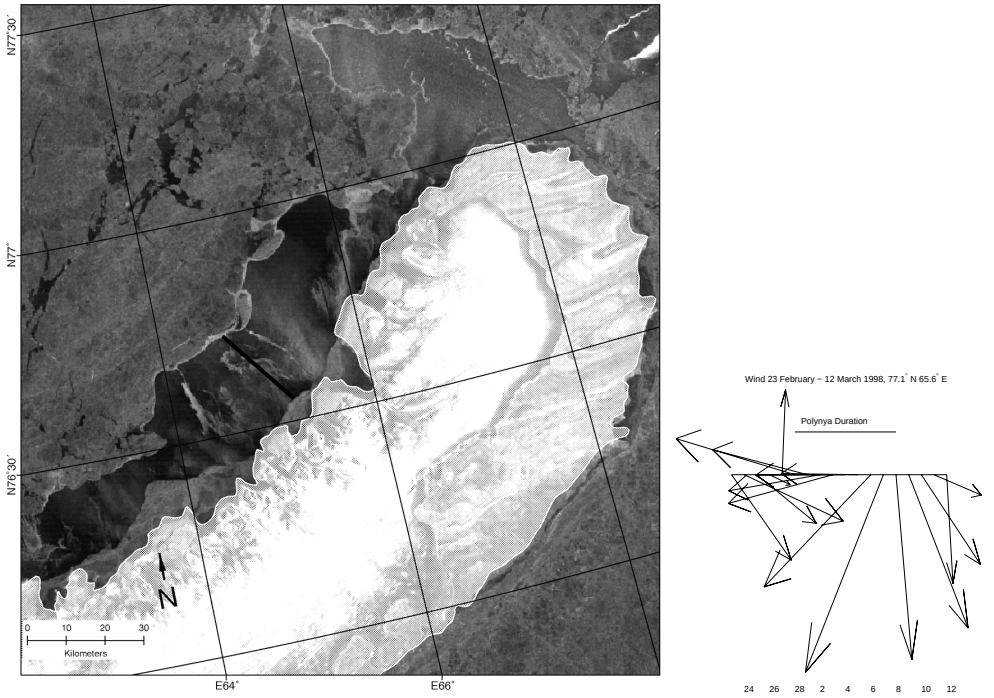

(a) (b)

Figure 4.5: *a. Sub-image from RADARSAT ScanSAR from the north-western tip of Novaya Zemlya from 2 March 1998. Image Data ©Canadian Space Agency 1998. The line defines the measured polynya width. b. Wind directions from the nearest NCEP grid node are plotted from 23 February to 12 March 1998. Maximum wind speed is 11 m/s. The polynya period is marked with a horizontal line.*

URN:NBN:no-2344

closed when the wind turned northerly (Figure 4.5b). The wind speed varied from 6 to 11 m/s, and the air temperature varied from -2° C to -26° C.

A subset of a SAR image from RADARSAT shows the detailed signature of the polynya (Figure 4.5a). The dark signature of the polynya in the SAR image represents grease ice of nilas which forms quickly as the polynya opens up during low air temperatures (-22° C). If the wind speed had been very low (< 3 m/s), the dark signature of the polynya could also have indicated open water. But a wind speed of 7 m/s, found from the NCEP data (Figure 4.5b), would have created higher backscatter. The brighter signature of the thin transition zone between the grease ice/nilas and thicker first year ice is rubble of thin ice that has been piled towards the ice edge. Fast ice areas up to tens of kilometers are also visible between the coast and the polynya (Johannessen et al., 1997a). Regional variations in offshore wind speed due to the topographical effects as well as variations in coastline geometry can lead to the irregularities of the ice edge on the western side of the polynya (Morales Maqueda and Willmott, 2000). Also other mechanisms can generate undulations of the ice edge, such as eddies, jets and meandering of the ocean currents (Johannessen et al., 1992a).

Southern Novaya Zemlya and Kara Gate area

A continuation of the time series of SSM/I ice concentration data in March 1998 shows that the polynya of the northern tip of Novaya Zemlya remained closed for the next two weeks due to the dominance of westerly and south-westerly winds. As a consequence of this wind regime a polynya on the eastern side of the southern Novaya Zemlya, near the Kara Gate, opened up (Figure 4.6).

The RADARSAT ScanSAR image from 18 March 1998 shows the polynya clearly as a band of dark signature along the east coast of Novaya Zemlya (Figure 4.7a). As the previous example, the dark signature is due to grease ice and nilas, while the bright lines along the edge of the first year ice is piled up rubble of thin ice. This is a very typical situation for this area, with southerly winds blowing the first year ice away from the coast. The southerly wind was about 9 m/s and the air temperature was about -8° C this day. During the period from 17 to 24 March, the wind direction shifted between westerly and southerly with wind speed of 5 to 11 m/s (Figure 4.7b). After the 24 March, the polynya closed when the wind turned north north-easterly. The air temperatures varied between

Figure 4.6: *SSM/I sea ice concentration maps from 17 to 24 March 1998. Open water outside the ice edge and polynyas inside the ice are shown in black. Land areas are grey.*

URN:NBN:no-2344

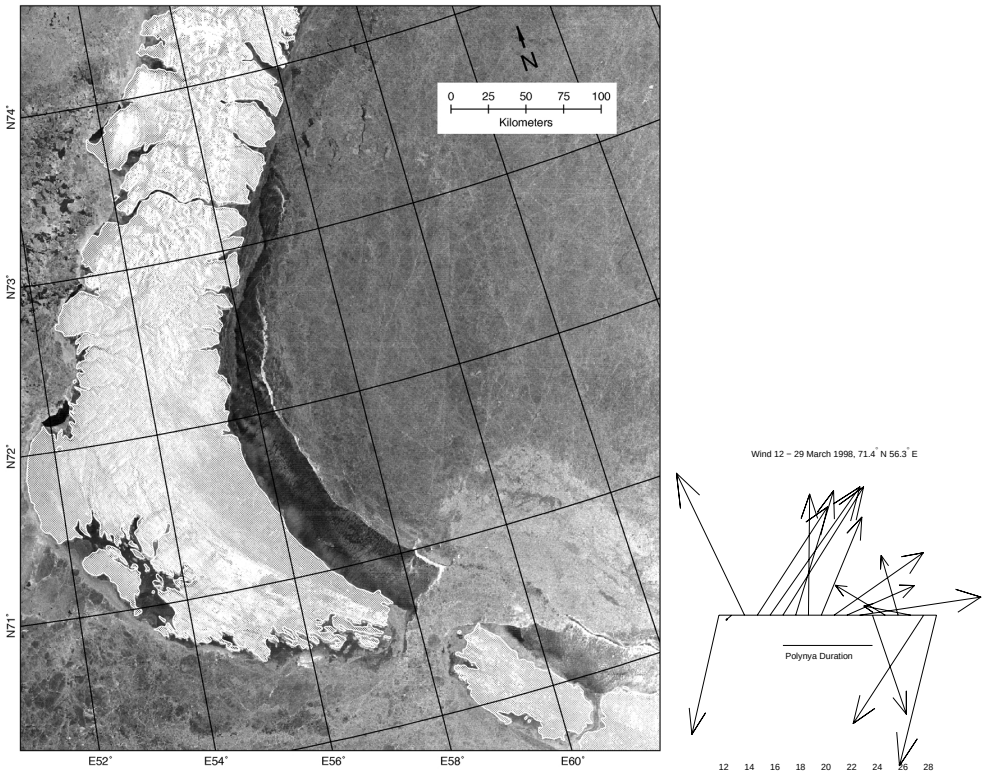

(a) (b)

Figure 4.7: *a. RADARSAT ScanSAR from the south-western Kara Sea from 18 March 1998. The polynya areas are east and west of the Kara Gate. Image Data ©Canadian Space Agency 1998. b. Wind directions from the nearest NCEP grid node are plotted from 12 to 29 March 1998. Maximum wind speed is 11 m/s. The polynya period is marked with a horizontal line.*

URN:NBN:no-2344

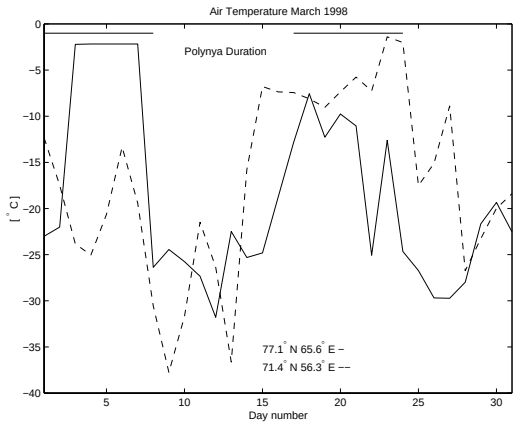

Figure 4.8: *Air temperature from the nearest NCEP grid node from March 1998. The polynya periods are marked with horizontal lines.*

-1° C and -9° C in this period.

These two polynya events were the result of different wind regimes that opened up polynya areas at different locations. From the SSM/I data it could be seen that when the polynya at the northern part of Novaya Zemlya existed, there was no sign of the polynya at the south-eastern part of the Novaya Zemlya and vice versa (Figure 4.4a and Figure 4.6). High air temperatures for both polynya periods were found (Figure 4.8). This is probably the main factor that caused the large open areas. Pease (1987) found that maximum polynya width is a strong function of air temperature, and that higher air temperature gives large polynyas. The polynya width is not very dependent of wind speed. For a given air temperature, the maximum polynya width increases with increasing wind speed up to about 5 m/s (Pease, 1987). For higher wind speeds the maximum polynya width is fairly constant.

East of Vaygach Island

SSM/I sea ice concentration data for March 1994 for the area around Vaygach Island are used to follow the evolution of this dynamic polynya area (Figure 4.9a). A small polynya is visible in the Pechora Sea the first day of the month. This is closed the next day, and the 9 March a new polynya opens in the south-western Kara Sea. The first two days of the month the wind was northerly to north-westerly, then the wind directions shifted to

south-westerly and southerly for several days (3 - 14) and the air temperature increased (Figure 4.9b and Figure 4.9c). This polynya was visible to the 18 March and it did not reappear after that. From the 15 to the 21, the wind direction varied between south-easterly and esterly and the polynya was closed on the 19. On the 22 to the 25 the wind shifted to northerly and then to easterly. This lead to the opening of an extensive polynya in the Pechora Sea starting to open the 23 March. Colder air temperatures accompanied the shrinking of the polynya the last days of the month.

ERS SAR data were available for the area around Vaygach Island every third day from the 3 to the 24 March 1994. They were used to compose eight SAR images (Figure 4.10 a-h). Narrow leads are visible on 3 March (a), only a few kilometers wide and not visible in the SSM/I data (Figure 4.9a). During the period 3 to 12, the polynya was opening and reached the maximum of 51 km on 12 March measured from SAR. The polynya is visible in the SSM/I data from 9 to 18 March. The shift in the wind on 15 March caused the polynya north of Vaygach Island to start to closing. The scene from the 21 March show that the polynya area is ice covered. In the lower part of the SAR image from 24 March, it is possible to see that a polynya has opened up in the Pechora Sea. This extensive polynya south of the Vaygach is verified from SSM/I data, where it can be observed throughout the month (Figure 4.9a). It is caused by the north-easterly winds and relatively high air temperatures in the period (Figure 4.9b and Figure 4.9c).

4.3.2 Polynya widths from SAR

Table 4.2 lists the mean and standard deviation of measured polynya widths for the main polynya areas investigated (Figure 4.2a). Polynya widths from Volkov et al. (2002) are used for comparison for those areas which were available. In 1994 and 1996 the polynya estimates were solely from the Pechora Sea and the south-western Kara Sea using ERS-1/2 SAR data. For 1997 and 1998 the polynya widths are measures for all study areas using RADARSAT data.

The largest polynyas were found along the Taymyr Peninsula with mean with of about 40 km. Along the fast ice boundary located between the coast of Taymyr Peninsula and the Severnaya Zemlya, several leads are opening and closing, making the sea ice signatures in SAR images of this area complex. Along the western coast of Yamal Peninsula and the area around the outlets of the Yenisey and Ob Rivers typical polynya widths were

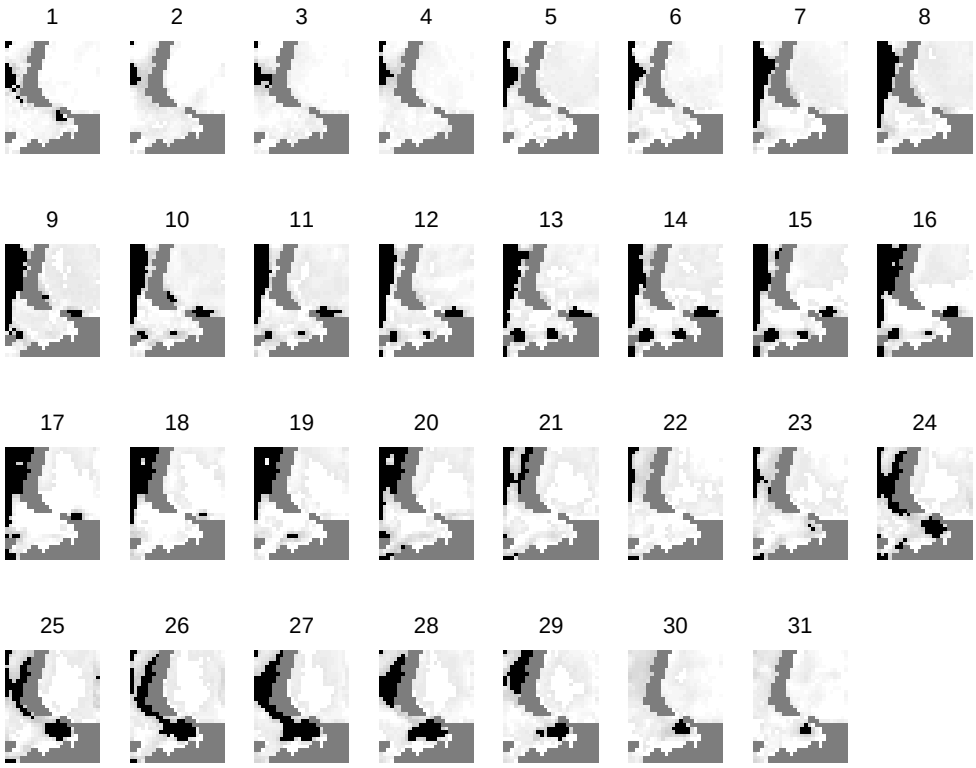

(a)

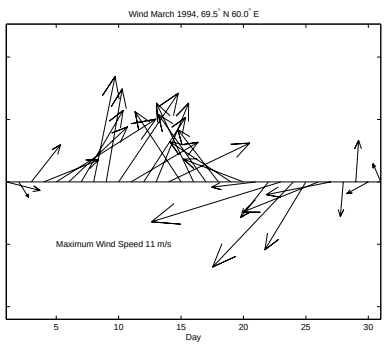

(b)

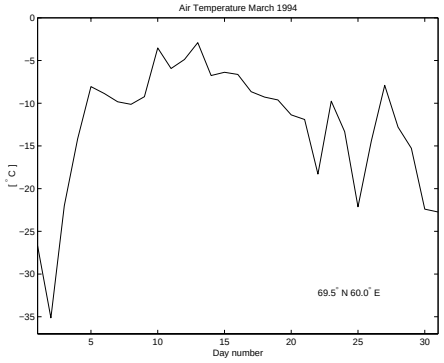

(c)

Figure 4.9: *a. SSM/I sea ice concentration data for March 1994 for the area around Vaygach Island. b. Wind directions from the nearest NCEP grid node for March 1994. Maximum wind speed is 11 m/s. c. Air temperature from the nearest NCEP grid node.*

URN:NBN:no-2344

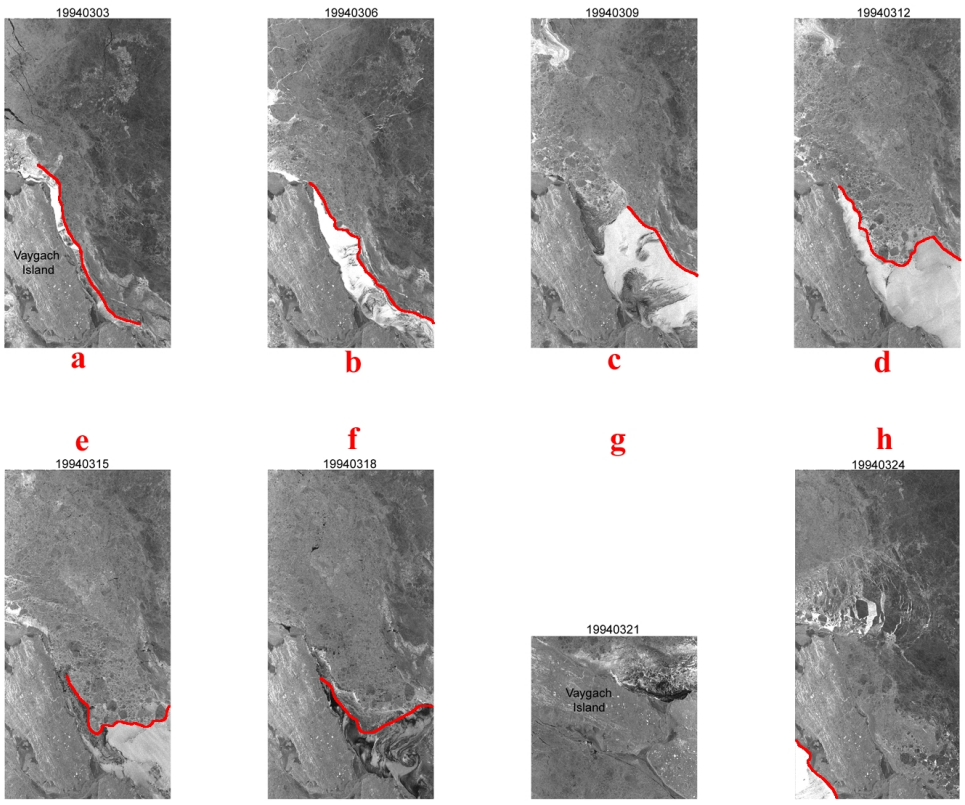

Figure 4.10: *ERS SAR images every third day from 3 to 24 March 1994. A part of an extensive polynya in the Pechora Sea is seen in the lower part of the scene from 24 March (h). Image Data ©European Space Agency 1994.*

Area	Mean [km]	Standard Deviation [km]	Literature [km]
Vaygach area (V)	25	21	30
Pechora Sea (PS)	15	17	
Yamal coast (Y)	30	26	70
Ob/Yenisey estuaries (O/Y)	21	20	120
Taymyr coast (T)	41	27	120
Novaya Zemlya (NZ)	19	16	30-40
Severnaya Zemlya (SZ)	20	18	5
Franz Josef Land (FJL)	23	20	
Vize/Ushakova Island (V/U)	10	7	

Table 4.2: *Polynya statistics based on SAR data for the nine main areas investigated. The areas are presented in Figure 4.1b. Polynya widths from Volkov et al. (2002) are listed in the last column.*

in the range of 20 to 30 km, with variability of tens of kilometers. High values of the mean polynya widths were also accompanies by high standard deviation values. Large polynyas were measured in the Vaygach area (about 25 km) and around Franz Josef Land (about 23 km).

Volkov et al. (2002) refer to Russian work on measurements of the width of polynyas in areas in the Kara Sea in March. It is unclear how many measurement were done and which data was used. In that work the polynyas in the Vaygach area were found to be about 30 km wide. That correspond rather well to these results. Polynyas north and west of Novaya Zemlya were found to be 30-40 km compared to about 19 km for the SAR data. Rather large values were found for other areas. The Yamal polynya was found to be 70 km and meausured to be 30 km from SAR. Polynyas of 120 km were measured along the Taymyr coast north of the Ob and Yenisey Rivers, compared to the SAR measurements of 20 to 40 km. The polynyas near Severanya Zemlya were measured to 5 km, and to about 20 km from the SAR data. For the Vaygach area, Novaya Zemly and the Severnaya Zemlya the values from literature is within the variability of the measurements from the SAR data. The SAR observations were rather few for Yamal coast (8), Taymyr coast (7) and the Ob and Yenisey area (8) (Figure 4.2b). This may explain some of the difference between the polynya widths from SAR and the values from Volkov et al. (2002). For these areas, important variability of polynya widths may not have been captured.

4.3.3 Polynya backscattering characteristics from ERS SAR

The surface characteristics of new and young ice in polynyas can change significantly during the early growth phase. This has strong influence on the microwave signature. SAR backscattering statistics for different ice types in the Kara Sea have been analysed more in detail in Lundhaug (2001), and will only briefly be adressed here. Several studies have focused on this problem in general (Onstott, 1992; Sandven et al., 1999b) and for ice in leads and polynyas in particular (Perovich and Richter-Menge, 1994; 2000).

Four ERS-1/2 SAR images from the 'Tandem Phase' have been selected from the area north-east of the Kara Gate. The images from both satellites have been calibrated to an accuracy of $\pm$ 0.4 dB (Laur et al., 1998). Profiles of SAR backscattering coefficients were extracted from these images for 28 and 29 February and 2 and 3 March 1996. All profiles covers the same geographical position, starting in the first year ice end and extends into the polynya (Figure 4.11). Both the first year ice and the polynya move during the five days period. The first year ice has typical backscatter values ranging from -10 dB to -15 dB, depending on roughness, snow cover, temperature and other factors which have inpact on the SAR microwave return. The profiles through the first year ice area show that the σ^o was gradually decreasing about 5 dB from the 28 of February to the 3 of March. A decrease in σ^o for first year ice with decreasing temperature is in agreement with other SAR studies such as Onstott (1992) for an angle of incidence of 40°, and Drinkwater and Lytle (1997) for the ERS SAR angle of incidence of 23°. The transition zone between first year ice and polynya (with open water/new ice types) are clearly seen in the four images as a significant jump in the σ^o values of 5-15 dB. The character of the transition zone is different in each of the four profiles (Figure 4.12a). The transition zone is characterised by a band of grease ice/nilas with dark signature, observed in all the four images.

Due to relatively warm south-westerly wind the polynya area on 28 and 29 February was mostly wind-roughened open water with similar σ^o values as the first year ice (-5 to -10 dB). Patches and filaments of grease ice (σ^o less than -20 dB) can be seen oriented nearly parallel with the wind direction (Figure 4.12a). On 2-3 March a thin ice cover has formed, as frazil/grease ice has grown to nilas covering most of the polynya with σ^o in the range -15 to -20 dB. Frazil ice typically occurs when the ocean surface is roughened by wind, and it aggregates to form grease ice and shuga during the freeze-up process

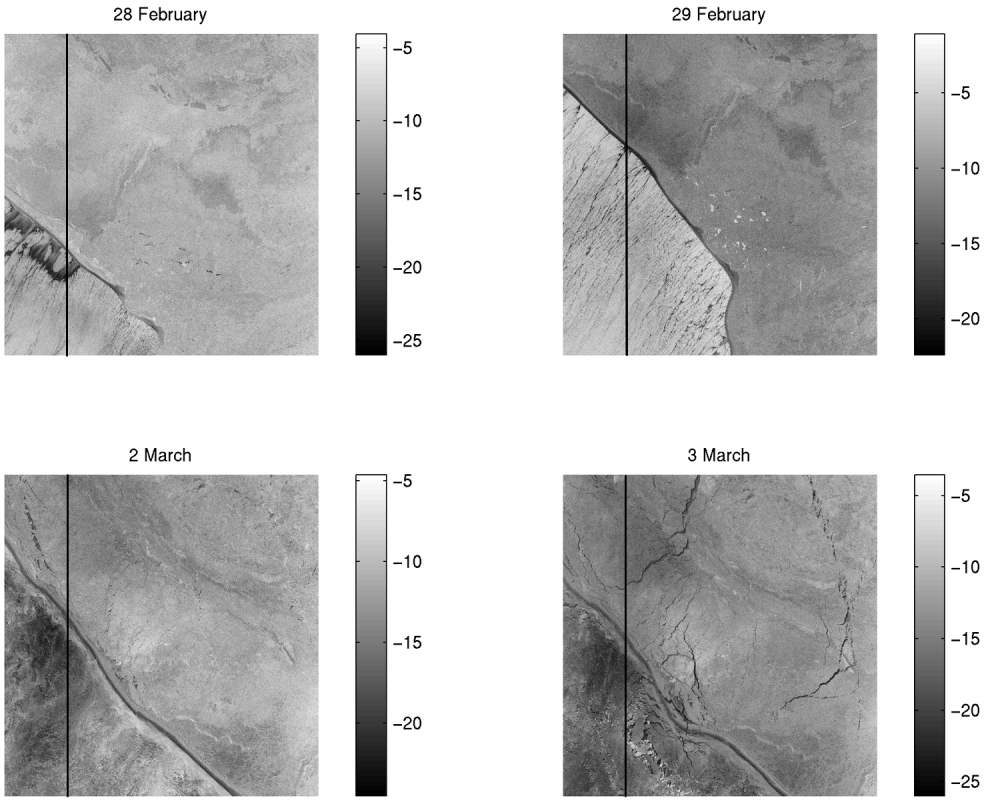

Figure 4.11: *ERS SAR images from 28 February to 3 March 1996 north-east of the Kara Gate. Image Data ©European Space Agency 1996.*

URN:NBN:no-2344

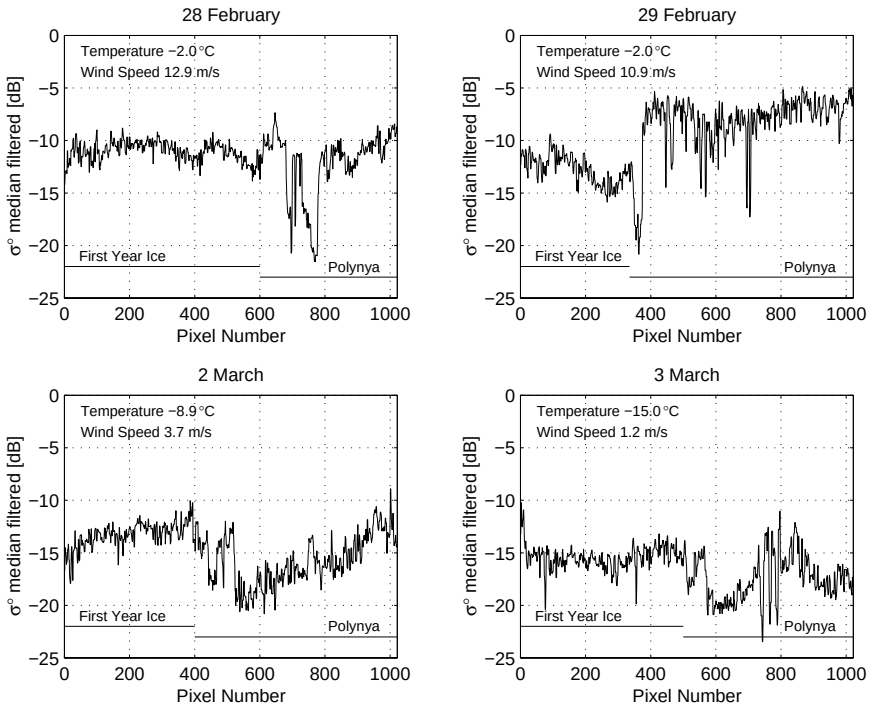

(a)

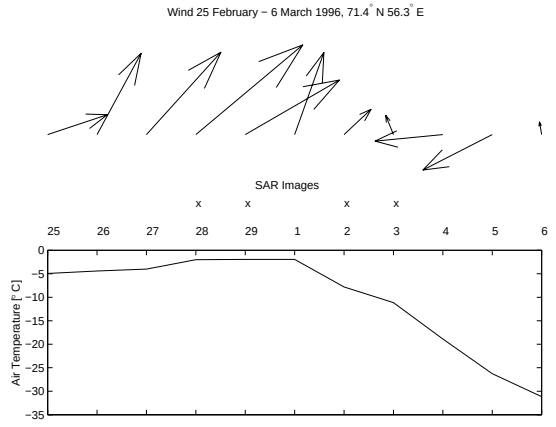

(b)

Figure 4.12: *a. ERS SAR backscattering coefficient for four days in February - March 1996. b. Wind and air temperature for 25 February to 6 March 1996. Maximum wind speed was 13 m/s.*

(Barber et al., 1998). This layer develops to nilas if there is little wind and wave action and further to young ice. Brighter signatures in the polynya is most likely due to young ice which has evolved from nilas. As found in Lundhaug (2001), σ^o for young ice can range from -5 to -15 dB.

The freezing of salt water produces brine which may create frost flowers on the ice surface. Laboratory studies of the effect of frost flowers on C band radar backscattering from sea ice where the temperature was of order -20° C show that an area of frost flowers may increase the backscattering with about 5 dB (Nghiem et al., 1997). Ulander et al. (1995) observed frost flowers in the Arctic from both ERS-1 SAR and from ground observations when the temperature was -5° to -10° C. They found changes in σ^o in the range 5-10 dB caused by frost flowers, and newly formed frost flowers caused a σ^o of -14 dB. It is assumed that some of the pixels from the polynya area the 2 and 3 of March might give higher backscattering coefficients (-15 to -10 dB) due to frost flowers. The results shown here agree with the results presented by Sandven et al. (1999b) for the Barents Sea. They found a comparable increase in the backscattering coefficient from areas of grease ice to areas with assumed frost flowers on young ice.

The backscattering of ice types in polynyas can have very large variability due to the variability in σ^o for young ice as well as open water. Automatic classification of polynyas in SAR images is therefore not a straight forward procedure. Use of simple threshold techniques (i.e. Sandven et al., 1999b) would not be sufficient because several ice types could have similar σ^o values. More advanced methods, where defined image segments can be used as training data for further classification attempts, could possible be used. In this study, however, the polynya indentification has been done manually.

4.3.4 Polynya index from SSM/I analysis

The polynya area north of Vaygach and along the southern part of Novaya Zemlya was selected for polynya index estimation, based on SSM/I data for March 1990 to 1999. The first analysis is presented in Figure 4.13a, showing the number of days in January-March with polynya index above zero, which means that polynyas are detectable in the SSM/I data. The investigated polynyas are oriented towards north-east. The prevailing wind regime will determine the number of polynya days. With prevailing south-westerly winds, polynyas occur frequently such as in 1995 and 1996. Then a polynya occured 55

and 56 out of 90 days. When the prevailing winds are in the oposite direction, polynyas occur less frequently (i.e. 1991, 1994, 1998, 1999). Polynyas occured only 7 and 8 days in 1999 and 1991, respectively.

The polynya area is presented as function of day for each of the ten years (Figure 4.13b). The polynya area is measured by the polynya index, which indicates both size and duration of each polynya event. Favourable ice navigation conditions in the area is directly related to the frequency of polynyas. The largest and longest lasting areas covered by polynyas occur in 1995, and in 1991 only small polynyas with short duration occured (Figure 4.13b).

In order to correlate the polynya index with atmospheric forcing data, daily NCEP air temperature and wind speed and direction have been extracted for the month of March for 1990-1999. The relation between the polynya index and the air temperature and wind for March in the 1990s are presented in Figure 4.14. Polynya index appears to be independent of wind speed, while it is closely correlated with wind direction. As expected polynyas are formed by a wind component in offshore direction, which means a wind direction between 150° and 300°. Figure 4.14 shows that a majority of polynya events occur when the wind direction is in this interval.

Polynya events are also closely correlated with increasing air temperature from about -15° C. This can be explained by the close correlation between south-westerly wind directions and higher temperatures. Temperature is not the driving force for the creation of the polynyas, but refreezing of the polynyas depend on low air temperatures.

4.3.5 Model results

The polynya widths estimated from SAR data were used to validate the results from the one-dimensional polynya model. It was assumed that the widths derived from the images are estimates for the steady-state polynya width. Ou (1988) found through his model studies that the position of the ice edge is in approximate equilibrium with synoptic (order of days) and longer-period atmospheric variability. It does not response to higher-frequency atmospheric fluctuations, and its width is reasonable described by the steady-state polynya width.

Observed and predicted polynya width (X_p) and opening time (t_{95}) were compared for four days during March 1994 north-east of the Vaygach Island in the Kara Sea. The

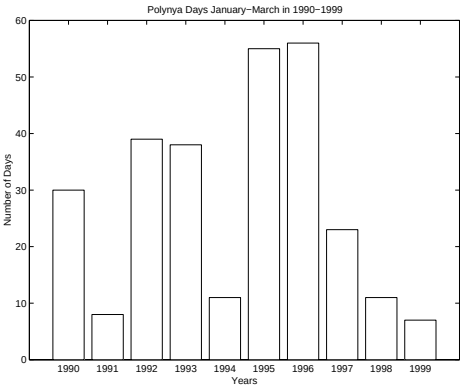

(a)

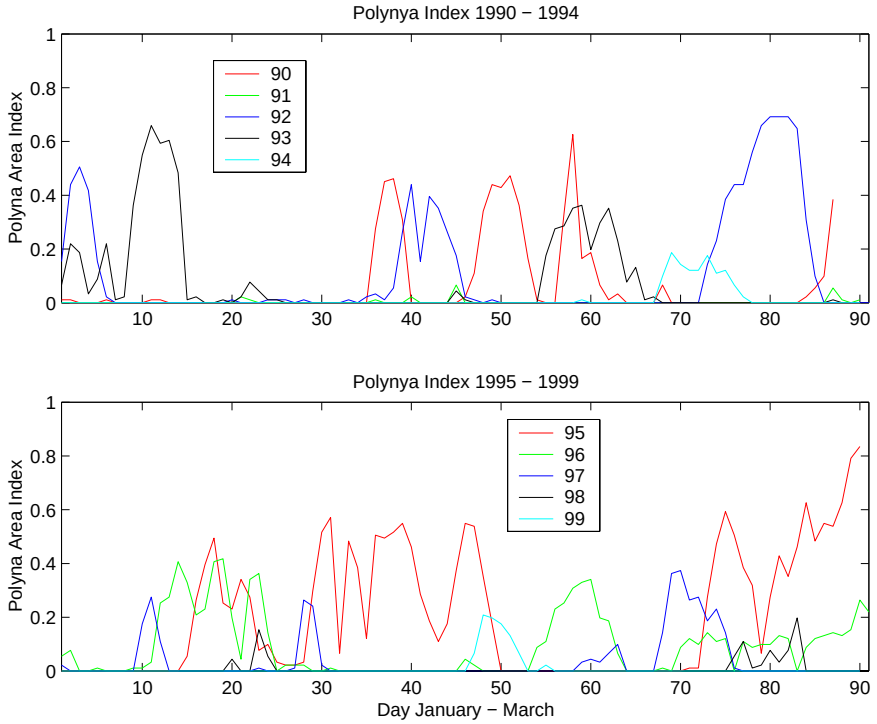

(b)

Figure 4.13: *a. Number of days for each year when the polynya index is larger than zero. The index is based on SSM/I data in the south-western Kara Sea in the 1990s. b. Variation of the polynya index in the 1990s for January to March.*

URN:NBN:no-2344

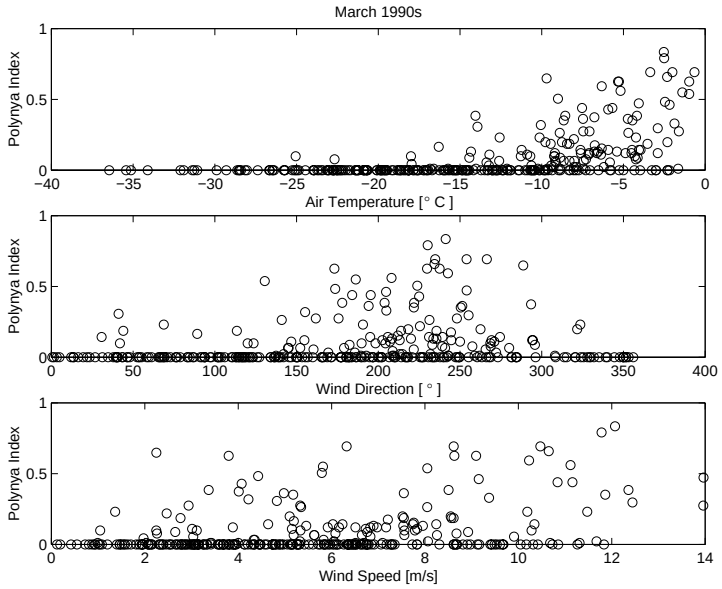

Figure 4.14: *The polynya index compared to the distribution of air temperature, wind direction and wind speed from the NCEP data.*

results are presented in Table 4.3. The polynya opened up in the period 3-12 March as observed in Figure 4.10. In the biginning of the month, there is no sign of a polynya in the area from the SSM/I data (Figure 4.9a). The wind direction was changing to south-westerly on 3 March from westerly (1) and north-westerly (2) and the temperature increased in the period 3-5 March (Figure 4.9b and c). From these data, the opening time was estimated to about one day for the small polynya observed on 3 March. The other observed opening times are deduced from this assumption. The discription of the polynya opening time and the steady-state polynya width is relatively good.

In the simple wind driven polynya model the wind speed and air temperature varied, leading to variable ice drift and collecting thickness (H_W and H_B). The predicted polynya widths were not in agreement with the observed for several areas (Figure 4.15). Root mean square error values are presented in Table 4.4. The best correpondance between observations and model results were found for the Vize and Ushakova Island and the Novaya Zemlya coast when using the root mean square values. The lowest variability of SAR observations was obtained in these areas, and the model predicted these results better (Table 4.2). The Yamal and Taymyr observed polynyas widths were highly variable,

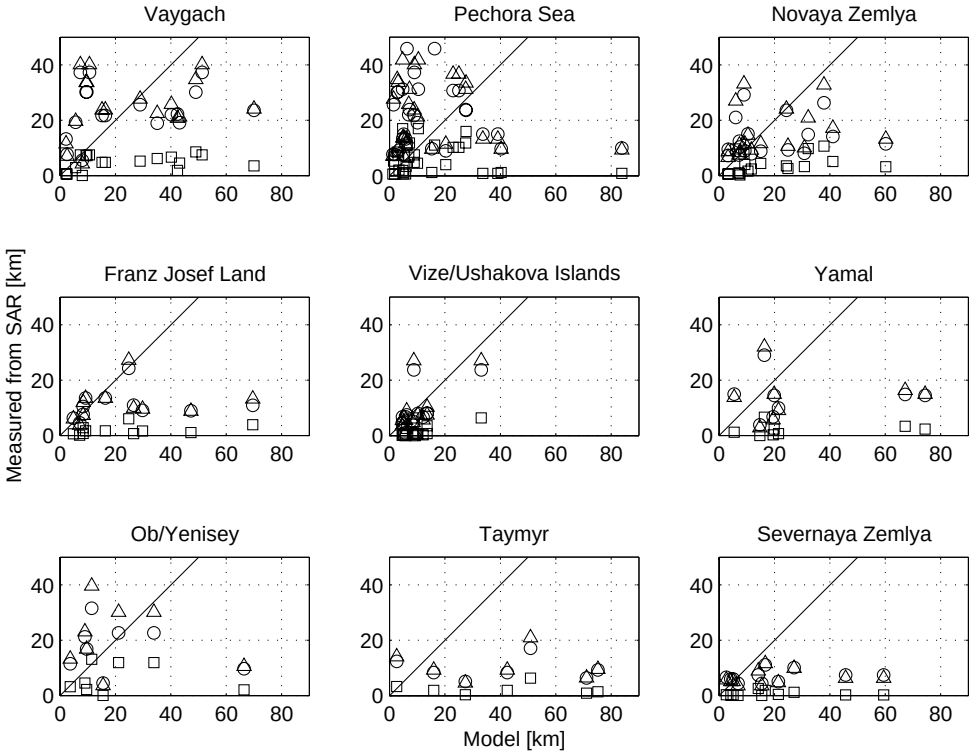

Figure 4.15: *Estimated polynya widths from SAR compared to results from the polynya model. Three different values of the collection thickness were used. The sea ice drift is set to 2 % of the wind speed. The results from using different collection thicknesses are marked as ∘ (H_P), △ (H_W) and □ (H_B) (Biggs et al., 2000; Pease, 1987; Winsor and Björk, 2000).*

Date	Air Temp.	Wind Speed	X_p [km]		t_{95} [days]	
	[° C]	[m/s]	Observed	Predicted	Observed	Predicted
3	-22.0	3.8	3	8	1	3.5
6	-8.9	6.5	16	22	4	5.8
9	-9.2	7.6	40	22	7	5.1
12	-4.9	6.2	51	37	10	10.5

Table 4.3: *Observed and predicted polynya width (X_p) and opening time (t_{95}) for four days during March 1994 north-east of the Vaygach Island in the Kara Sea.*

Area	H_P [km]	H_W [km]	H_B [km]
Vaygach	20	20	28
Pechora Sea	23	25	21
Yamal coast	30	29	37
Ob/Yenisey estuaries	23	24	25
Taymyr coast	41	40	46
Novaya Zemlya	17	16	21
Severnaya Zemlya	21	22	26
Franz Josef Land	23	22	28
Vize/Ushakova Island	6	7	10

Table 4.4: *Root mean square error values for model predicted and actual polynya widths.*

and these were not well predicted by the model. The constant value H_P and the linearly varying H_W gave comparable results for all years. The results from using a collection thickness that depends on polynya thermodynamics, wind stress and wind generated currents (H_B) varied from the two others, and for all areas but the Pechora Sea area, the model deviation from the observations were larger than for the two other parameterisations of the collection thickness. It did not perform very well along the Taymyr and Yamal coast.

4.4 Summary and discussion

Coastal polynyas are found along the Siberian shelf during the ice season from November to May. The presence of open water and thin ice in these polynyas is important for heat transfer and for navigation in the winter season. Polynya areas from selected re-

gions in the Pechora and Kara Seas are investigated with SAR and SSM/I data during the 1990s. A total of 94 ERS-1/2 SAR scenes from 1994 and 1996 and 71 RADARSAT ScanSAR Wide scenes from 1997 and 1998 have been acquired and analyzed. Daily ice concentration field from SSM/I data were extracted for January through March from 1990 to 1999. Daily averages of air temperature and wind information from the global NCEP reanalyzes dataset were also used. This study is limited to winter months in the 1990s, with the main focus on March when the maximum ice distribution in the Northern Hemisphere occurs. Polynya widths were quantified in detail using SAR data covering smaller areas. Ice concentration data from SSM/I, wind and air temperature were used in the description of polynya variability. Then the observed polynya widths from SAR were compared to polynya widths calculated by a one-dimensional polynya model for nine different areas.

The good spatial resolution of the SAR gave valuable information about the selected polynya areas. The largest polynyas were found along the Taymyr Peninsula with mean with of about 40 km. Along the western coast of Yamal Peninsula and the area around the outlets of the Yenisey and Ob Rivers typical polynya widths were in the range of 20 to 30 km, with variability of tens of kilometers. High values of the mean polynya widths were also accompanies by high standard deviation values. Large polynyas were measured in the Vaygach area (about 25 km) and around Franz Josef Land (about 23 km). The SAR backscattering signatures of freezing sea ice was investigated for four days in 1996. The backscattering of ice types in polynyas can have very large variability due to the variability in σ^o for young ice as well as open water, affecting the possibilites for automatic classification of polynyas in SAR images. Among the limitations of this study was that the SAR observations were sparse in time. The day to day development during freezing or fast changes in wind direction are not possible to completely capture with sampling intervals of more than one or two days. The investigated areas are limited regions of the Arctic, and to draw conclusions for the whole Arctic may be doubtful. If the polynya was only partly covered by the SAR image, a too small or large width could be measured due to variable polynya width along the coast.

The polynya area north of Vaygach and along the southern part of Novaya Zemlya was selected for polynya index estimation, based on SSM/I data for March 1990 to 1999. The investigated polynya area was oriented towards north-east. The prevailing wind regime determined the number of polynya days. With prevailing south-westerly winds, polynyas

URN:NBN:no-2344

occured frequently such as in 1995 and 1996. Then a polynya occured 55 and 56 out of 90 days. When the prevailing winds were in the oposite direction, polynyas occured less frequently (i.e. 1991, 1994, 1998, 1999). Polynyas occured only 7 and 8 days in 1999 and 1991, respectively. The polynya area was measured by the polynya index, which indicates both size and duration of each polynya event. Favourable ice navigation conditions in the area is directly related to the frequency of polynyas. The largest and longest lasting areas covered by polynyas occured in 1995, and in 1991 only small polynyas with short duration occured.

Polynya area appeared to be independent of wind speed, while it was closely correlated with wind direction. As expected polynyas were formed by a wind component in offshore direction, which means a wind direction between 150° and 300°. Polynya event were also closely correlated with increasing air temperature from about -15° C. This can be explained by the close correlation between south-westerly wind directions and higher temperatures. Temperature is not the driving force for the creation of the polynyas, but refreezing of the polynyas depend on low air temperatures. Errors in the NCEP dataset were not assessed, and these data may not be as optimal as *in situ* data of air temperature and wind for a single polynya event due to resampling of sparse observations over large areas. However, single point *in situ* measurements may not be representative for a large area, due to local influence on temperature and wind conditions.

The polynya widths estimated from SAR data were used to validate the results from the one-dimensional polynya model. The widths derived from the images were assumed to be estimates for the steady-state polynya width. Observed and predicted polynya width (X_p) and opening time (t_{95}) were compared for four days during March 1994 north-east of the Vaygach Island in the Kara Sea. In this case the discription of the polynya opening time and the steady-state polynya width was relatively good.

The best correpondance between observations and model results were found for the Vize and Ushakova Island and the Novaya Zemlya coast. The lowest variability of SAR observations was found in these areas, and the model predicted these widths better. The Yamal and Taymyr observed polynyas widths were highly variable, and these were not well predicted by the model. The constant value H_P and the linearly varying H_W gave comparable results for all years. The results from using a collection thickness that depends on polynya thermodynamics, wind stress and wind generated currents (H_B) varied from the two others, and for all areas but the Pechora Sea area, the model deviation from

the observations were larger than for the two other parameterisations of the collection thickness. The one-dimensional model may be too simple with to many assumptions for use in this area due to relatively complex coastline geometry and influence by currents and tides on sea ice drift. While the role of ocean currents cannot be assessed within the context of this present study, ocean currents clearly need to be incorporated into any realistic polynya model for the region. It was also assumed that the observed SAR polynya width was a measure for the steady-state polynya width, and this may not be fulfilled for all observations. To what extent this is the case is not easy to assess, due to spare SAR coverage in time for several areas.

This SAR observation dataset will be used for further studies for validation of a two-dimensional polynya model. To extend the observation set with data from the future Advanced Synthetic Aperture Radar (ASAR) sensor could be a possibility to get a more systematic data sampling over several months in a selected small study area like the south-western Kara Sea near Vaygach Island. The Wide Swath Mode will provide nearly daily coverage due to 400 km swath width. This is a key area for sea ice transport of radionuclides and sediments (Dethleff et al., 2000; Sherwood, 1999). Data about the polynya ice edge relative to coastlines of different orientations and shapes may give valuable information for validation of a two-dimensional model where the affect of the coastline on polynya size and development are accounted for (Darby et al., 1995). To use the method of Markus and Burns (1995) to estimate sub-pixel scale polynyas from SSM/I data may also give valuable information for future studies.

Acknowledgments

The ERS-1/2 SAR image data were obtained within different European Space Agency ‘Announcement of Opportunity’ projects. RADARSAT ScanSAR data were obtained from Alaska SAR Facility through NASA Research Announcement NRA-99-OES-10 (ADRO-2 program). Sea ice concentrations from the SSM/I Bootstrap data set were obtained from the NSIDC Distributed Active Archive Center, University of Colorado, Boulder, USA. NCEP reanalysis data was provided by the NOAA-CIRES Climate Diagnostics Center, Boulder, Colorado, USA.

This work was funded by a Ph. D. grant from Telemark University College, Department of Technology, Porsgrunn, Norway and with support from Nansen Environmental

and Remote Sensing Center (NERSC), Bergen, Norway. Thanks to O. M. Johannessen (NERSC) for valuable comments and suggestions and to Ø. Dalen (NERSC) for technical assistance.

Chapter 5

The angle measure technique applied to ERS SAR data

by

M. Lundhaug and K. H. Esbensen

To be submitted, 2002.

Abstract

The angle measure technique (AMT) is for the first time used to characterize the structure of open water and sea ice from Synthetic Aperture Radar (SAR) data. AMT has been suggested as an alternative to fractal analysis, and was originally developed to produce a data transform that could be used to characterize data variability. Sample areas of open water, young ice and first year ice SAR backscattering coefficients ice were input to the AMT algorithm. The AMT produces a transform by calculating geometric angles at several points of a vector defined by varying a scale parameter, and then the mean angles are calculated dependent of scale. Multivariate regression were used to separate ice types. Scaling of the input SAR data was found to be less useful through the regression tests. To get better results than could be obtained by AMT mean angles only, mean and standard deviation of the backscattering coefficient together with temperature were included in the regression. In the separation of ice and water the highest correlation coefficients was 0.85. For water and young ice the correlation coefficient was 0.93, and for water

URN:NBN:no-2344

and first year the highest was 0.86. For the separation of the ice types young ice and first year ice the correlation was very low, the value 0.40 was achieved. The individual samples were best separated on one pixel scale, corresponding to backscattering differences between neighboring pixels. The mean angles from the AMT can be related to ice type to some extent. The speckle property of SAR images may be the reason why this approach was not as useful for SAR data as for other data types. Information from mean and standard deviation of the backscattering coefficient is more useful than results from the more computer-demanding AMT algorithm.

5.1 Introduction

Ice concentration, ice thickness, ice motion and the extent of leads and polynyas are key variables for climate and ecological studies in the Arctic Seas (Falk-Petersen et al., 2000; Johannessen et al., 1995; 1999). Information about the distribution of sea ice thickness is vital for navigation in ice covered regions (Vainio et al., 2000). SAR data has been used by Nansen Environmental and Remote Sensing Center (NERSC) to assist in navigation in areas along the Northern Sea Route for several expeditions (Johannessen et al., 2000). Navigation through thick sea ice areas as rough first year ice or multi year ice lower the navigation al safety and decrease ship speed, compared to areas of young ice. Russian Marine Operational Headquarter has estimated that use of SAR data for navigation al support may increase the overall ship speed by a factor of at least two (Pettersson et al., 2000).

There is disagreement in the research community about the value of estimating sea ice thickness from SAR. Some authors have argued that it should be possible to find information from SAR images that can be linked to the ice thickness. Wadhams and Comiso (1992) reviewed the relationship between the SAR backscattering coefficient and sea ice thickness distribution. Their results are the only quantitative validation of SAR with sonar data from a submarine (Wadhams, 2000). The variance in draft, the distance between the lower surface of the ice and the water level, could only explain 46 % of the variance in backscattering from the SAR. Haverkamp et al. (1995) used a dynamic local threshold approach to separate the sea ice from SAR into thickness classes based on local intensity distributions. Melling (1998) stated that the backscattering coefficient from ERS SAR might give information about the ice age and state of development during the ice growth

under cold conditions. But for older ice, it is a poor indicator of age or thickness because the relative contributions from different surface types as ridges, frost flowers or smooth floes can not be determined. Kwok (1998) described the ice thickness product from the RADARSAT Geophysical Processor System (RGPS) at Alaska SAR Facility (ASF). Information about the sea ice thickness distribution is obtained from the ice age distribution that is calculated from temperature, backscatter values and deformation of grid cells in the SAR images. They also use an empirical relationship between freezing-degree days and ice thickness. The gridded ice thickness histograms are produced weekly during winter at a resolution of 50 km. Kerman et al. (1999) suggested that it might be possible to find estimated statistics of Arctic sea ice thickness from SAR imagery by using backscattering differences between neighboring pixels. Wadhams (2000) refers to inconclusive tests of this method using ERS-2 SAR images. The speckle property of the SAR data was given as a possible reason why the differences between pixel values it is not straight forward to use. Zabel et al. (1996) stated that it is unlikely that surface roughness and ice thickness should be connected, as the surface roughness as seen by SAR may change rapidly due to the action of wind, waves, temperature changes or snowfall.

The objective of this study is to investigate if the angle measure technique (AMT) can give new information to separate sea ice types from SAR data using multivariate regression. The AMT is for the first time used in sea ice studies, and produces mean angles as a function of scale from the input SAR backscattering values. These might give information about the structure of the data. The AMT is first applied to find structure information that can characterize sea ice. Then it is used as a pre-processing tool to give input to multivariate statistical analyses (Esbensen et al., 1996; Kvaal et al., 1998; Huang and Esbensen, 2001), by which separation of ice and water and separation of ice types are investigated. The main surface types in the Pechora and Kara Seas in winter are investigated; open water, young ice and first year ice. ERS 1 and 2 (ERS-1/2) SAR image data is used, as SAR data is especially valuable in the Arctic due to its ability to image the surface through clouds and in darkness. The data sets that have been used are presented in Section 5.2, the AMT method is presented in Section 5.3, and the results, discussion and conclusion are presented in Section 5.4 and Section 5.5.

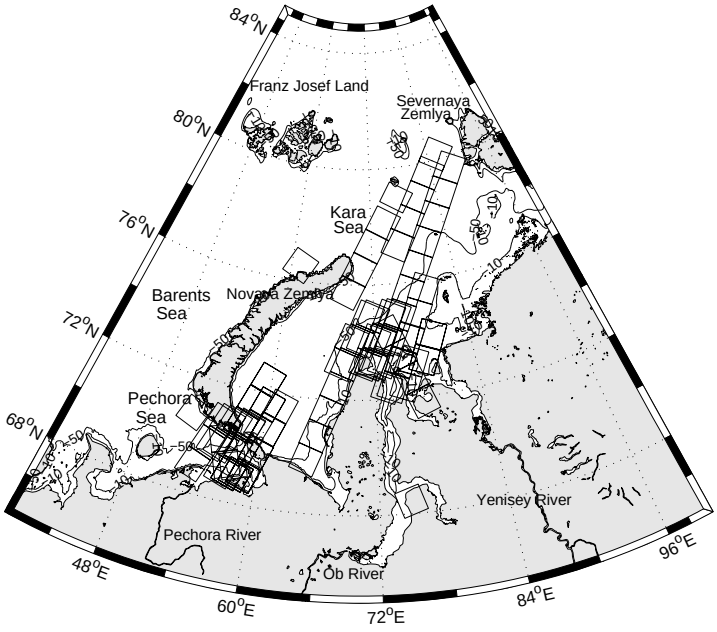

Figure 5.1: *The Pechora and Kara Seas with the ESA ERS-1/2 SAR Precision Image scenes marked with frames.*

5.2 Data sets

5.2.1 ERS-1/2 SAR data

ERS-1 was launched 17 July in 1991 and ERS-2 was launched 20 May in 1995. The satellite orbits are sun-synchronous, near polar and have mean altitude of 785 km. The sensors transmit and receive vertically polarized energy at an average frequency of 5.3 GHz (C band). Archived data at NERSC from the Kara and Pechora Seas was used. Three look image data with 12.5 m pixel spacing was delivered by European Space Agency (ESA) via the UK-PAF. All of the Precision Image (PRI) products of 25 m resolution have been calibrated according to Laur et al. (1998). From early winter of 1994 to the spring of 1998, 105 images were used. The simple and edge preserving median filter was applied to reduce the effect of speckle in the SAR images and to resample them to a pixel spacing of 100 m (Rees and Satchell, 1997). Use of median filter may introduce bias in the data values (Rees and Satchell, 1997). Locations of the image scenes in the Pechora and Kara Seas are marked in Figure 5.1.

URN:NBN:no-2344

Samples of ice and water areas were manually extracted. Each of them covered areas of 5 by 5 km from SAR images of 100 by 100 km. Figure 5.2 presents an example of a SAR image with sample areas of first year ice marked. The samples were collected from homogeneous areas and at different azimuth and range locations in the image scene as recommended by Fetterer et al. (1994). Due to this choice of box size, features of more limited extend like narrow leads, ridges or narrow fast ice areas could not be investigated. Samples from single floes required floe sizes larger than the sample area. The samples were manually classified into open water and different sea ice types (World Meteorological Organization, 1970). Only samples from open water, young ice and first year ice are used for this study. This dataset was used in Lundhaug (2001), which gives further details about the manual classification.

The image samples of backscattering values were transformed from matrices to vectors by unfolding of the matrix rows one after the other. Large differences between the values of the last pixel in one row and the first in the next row could lead to artificial signatures in the AMT analysis. It was found that the homogeneity of the extracted image samples assured that these differences were within the natural variability of the backscattering values. Each SAR sample of 50 by 50 pixels is transformed to a vector of 2500 values of the backscattering coefficient.

5.2.2 Temperature data

Temperature data were extracted from the European Centre for Medium-Range Weather Forecasts (ECMWF) analyzed data sets, available every six hours. The grid point distance is about 1.1 degree in latitude direction and 1.1 degree in longitude direction. Data were extracted from the grid points closest to the SAR image centers and with the shortest time difference to the image acquisition time. Maximum time difference is up to three hours, and maximum spatial difference is about half a degree in each direction.

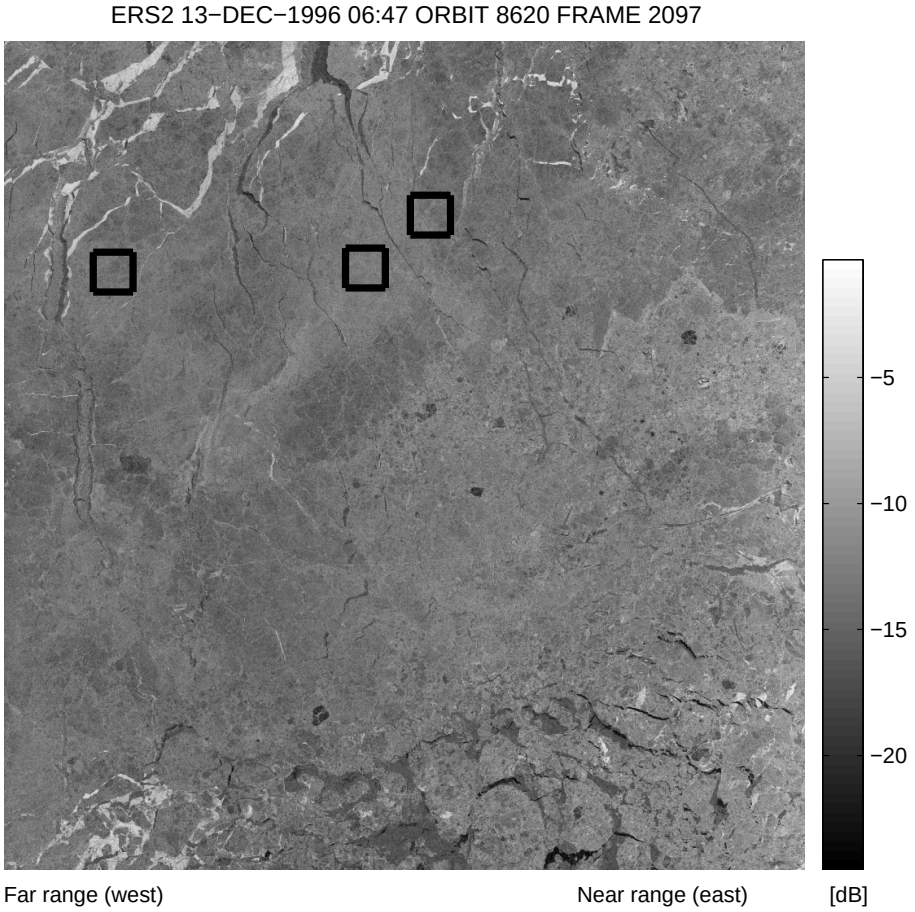

Figure 5.2: *Descending ERS-2 SAR scene with center point at 76.4° N and 74.1° E in the Kara Sea from 13 December 1996. The image is 100 by 100 km. Three sample areas of 5 by 5 km are marked. Image Data ©European Space Agency/Nansen Environmental and Remote Sensing Center 1996.*

URN:NBN:no-2344

5.3 Data analysis

5.3.1 Angle measure technique

Andrle (1994; 1996a; 1996b) proposed in 1994 a method for characterizing the variability of geomorphic lines of natural shapes (i.e. meandering rivers) termed the angle measure technique (AMT). AMT was suggested as an alternative to fractal analysis to characterize the variation in the data. The AMT transforms the data by calculating geometric angle at many points along any data vector for a given set of scales, s. No assumptions are made concerning the relationship between the degree of variability and scale length. AMT is useful in a variety of research fields and was used by Esbensen et al. (1996) for signal processing and image analysis. Kvaal et al. (1998) analyzed the texture of bread samples. Huang and Esbensen (2000; 2001) used AMT for characterization of powder particles with promising results.

The AMT is applied to a vector of SAR backscattering coefficients, V, with values in the range v_{min} to v_{max}. Several randomly chosen entries A_i of of the data vector V is used as a starting points. Points B_i and C_i are defined using a length s in each direction along the vector (Figure 5.3). The radius of the circle illustrates this length. The supplement angles, $(\alpha_i)_s$, to the lines defined by the intersection points A_iB_i and A_iC_i is calculated at scale s and stored in the computer memory. Then the mean angle of the scale length s, $\alpha(s)$, is calculated from the M random points A_i sampled from the vector (Equation 5.1). High values of the mean angle imply a high degree of variability at the corresponding scale.

$$\alpha(s) = \frac{1}{M} \sum_{i=1}^{M} (\alpha_i)_s \tag{5.1}$$

In this study, M = 200 starting points were chosen. The mean angles are calculated at different scales, from s = 1 to the maximum value of s = 250. For large scales, the mean angle decreases towards zero. The results are visualized by plots of mean angles as function of the logarithm of the scale. Characterization of SAR backscattering samples are presented in Section 5.4.1.

The magnitudes of the mean angles are sensitive to the scaling of the values from the image data. Kvaal et al. (1998) stated that scaling of the input data vector was necessary to obtain useful results and Huang and Esbensen (2000; 2001) disagreed to this. A test was

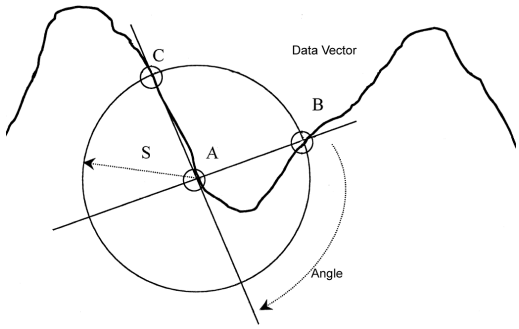

Figure 5.3: *Illustration of the angle measure technique adapted from Esbensen et al. (1996). The curve is given by the magnitude of the data values.*

performed to assess if scaling was useful for characterization of the SAR backscattering values. Scaling of the SAR backscattering values, V^*, were done as proposed by Kvaal et al. (1998). The maximum, v_{max}, and minimum, v_{min}, values of the data vector V were calculated (Equation 5.2). Different constant scaling factors, k, were tested (k = 1, 10, 100).

$$V^* = k\frac{V - v_{min}}{v_{max} - v_{min}} \tag{5.2}$$

5.3.2 Multivariate regression

The objective was to test if the scale dependent mean angles from the AMT can give useful information for separation of sea ice types. Multivariate regression was used to calculate regression models. A non-linear iterative partial least squares algorithm (PLS NIPALS) implemented in the PLS Toolbox was used (Esbensen et al., 2001; Martens and Næs, 1989; Wise and Gallagher, 1998). PLS NIPALS can be used to relate a number of X variables (mean angles) to a Y variable (i.e. ice or water). The values for Y in the regression were design variables (-1,1) to separate the two classes in each calculation. PLS finds factors known as latent variables that are descriptive of the variance in the X variables and correlated with the Y variable.

The data set was divided in a training and a test set with about the same number of samples. The root mean square error of prediction (RMSEP) was calculated in the regression. The minimum of the RMSEP was used to find the number of latent variables that opti-

mized the predictive ability of the model. The optimal number of latent variables to use was found to be two or three during the regression tests. The results are presented in Section 5.4.2.

5.4 Results and discussion

5.4.1 Characterization of SAR samples by AMT

Sample profiles of water, young ice and first year ice were extracted from four SAR scenes presented in Figure 5.4. These were representing typical surface types in the Pechora and Kara Seas. The profile lengths were 300 pixels corresponding to 30 kilometers. Examples of input vectors of the SAR backscattering coefficient to the AMT is presented in Figure 5.5. The two water samples have higher mean backscattering values (-7.9 and -5.1 dB) than the young ice samples (-11.6 and -9.6 dB) and the first year ice samples (-13.4 and -13.3 dB). The water samples have the highest standard deviation of the backscattering coefficients, and the first year ice samples have the lowest. The backscattering values of water is dependent on the wind speed (Furevik et al., 2001), and they may cover a broad range of values.

Results from the input SAR data with and without scaling to the AMT are presented in Figure 5.6. When no scaling of the data is applied, the mean angles are small due to relatively small variation in the original input data values. The mean angles for the water samples are higher than for young ice, and the mean angles for young ice are higher than for first year ice. The relation between them is the same as for the original data vectors of input SAR backscattering coefficients (Figure 5.5). It seems to be correspondence between large mean angle from AMT and high mean backscattering coefficient. The AMT mean angles give information about the degree of variation in the data. The highest variation (characterized by the standard deviation) is for the water samples and the lowest is for the first year ice, probably explaining the variation in mean angle values between the samples. The mean angles are decreasing toward zero when the scale s is increasing, due to the geometric definition. The different samples in each surface category are best separated for scale of one pixel, which corresponds to 100 m pixel spacing.

A large constant k in the scaling of the input data makes the maximum mean angle to increase, due to the increasing of the input values through multiplying them with a larger

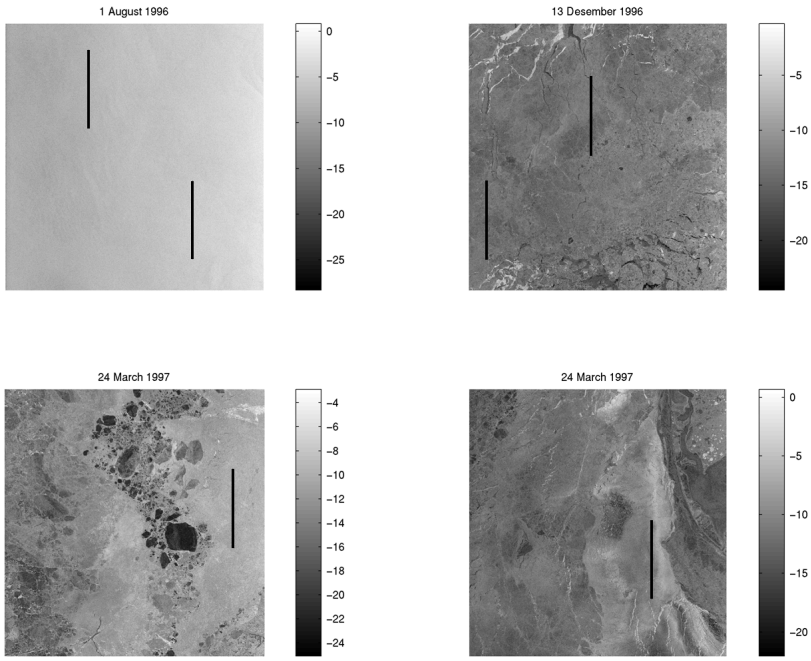

Figure 5.4: *Example images from the Kara Sea 1 August (open water) and 13 December (first year ice) 1996 and from 24 March 1997 (young ice). Image Data©European Space Agency/Nansen Environmental and Remote Sensing Center 1996, 1997.*

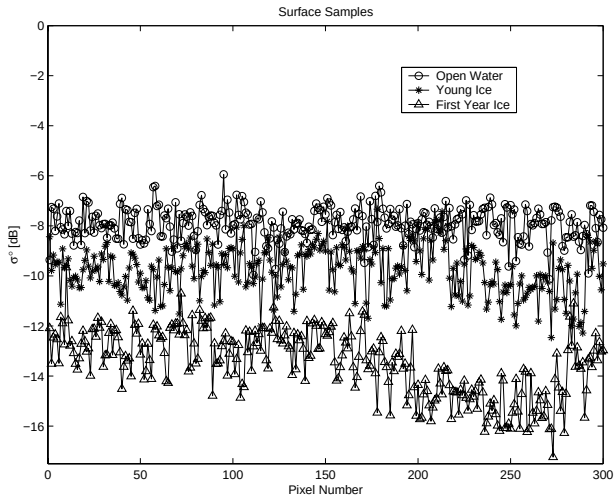

Figure 5.5: *Examples of the input vectors of SAR backscattering values for open water, young ice and first year ice.*

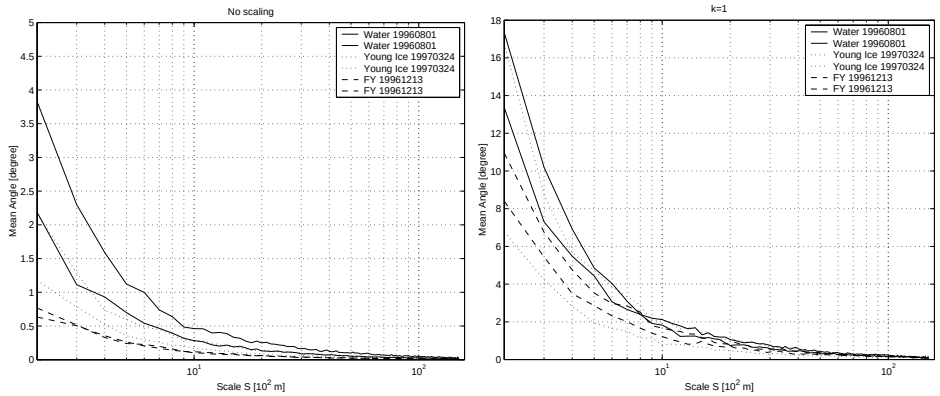

(a) (b)

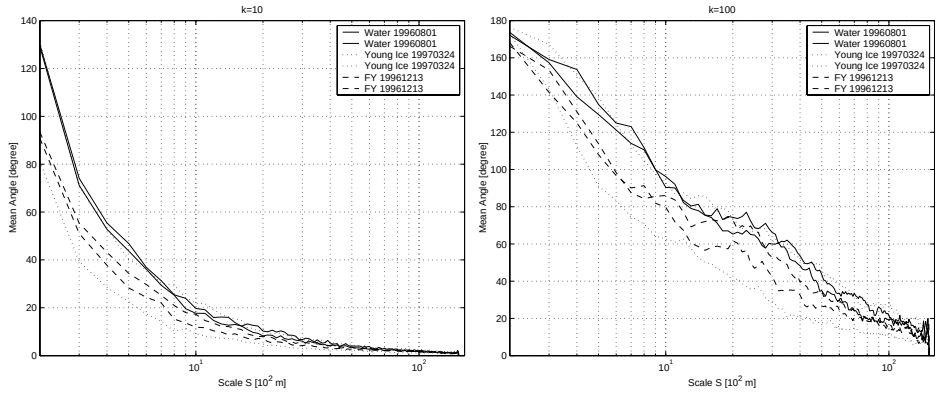

(c) (d)

Figure 5.6: *Mean angle as function of scale for each surface profile marked in the images presented in Figure 5.4. The backscattering values are scaled as described in Equation 5.2.*

URN:NBN:no-2344

number. The correspondence between the mean backscattering value and mean angle is not one to one for the scaled vectors as for the non-scaled data vector. The largest scaling factor (k=100) makes spectrum shift to a rather different shape.

To check if more information could be found from using high resolution SAR data, the same profiles as marked in Figure 5.4 were extracted from the original high resolution data with pixel spacing of 12.5 m. The example images from the Kara Sea on 1 August (open water) and 13 December (first year ice) 1996 and from 24 March 1997 (young ice) were used. Each input vector from the high resolution data has eight times the number of entries as the vectors from the low resolution data. The results are presented in Figure 5.7. The mean angle profiles for high and low resolution data for each ice type are closely related. The mean angle values for the high resolution data are higher than for the low resolution data. The standard deviation for all SAR backscattering vectors from the images with 12.5 m pixel spacing are higher than the standard deviation of the data vectors from images with 100 m pixel spacing. This is due to the larger backscatter variability caused by speckle in the high resolution data, resulting in bias in the mean angle profiles.

Mean angles for all the ERS SAR samples of water, young ice and first year from the Pechora and Kara Seas are calculated with the same scaling of the input vectors as in Figure 5.6. Again, the different samples in each surface category are best separated for scale of one pixel, which corresponds to 100 m pixel spacing. Thus, the AMT produces information on the scale corresponding to differences between neighboring pixel values. This support that the AMT characterization profiles may give information about the different surface types (Kerman et al., 1999). As seen in Figure 5.6, a probably too high scaling factor (k=100) seems to make the mean angle values to be less informative.

5.4.2 Multivariate regression

Mean angles calculated from the large set of samples from water, young ice and first year ice were used for multivariate statistical analysis. To make a quantitative assessment of the effect of the scaling, the original and scaled values of SAR backscattering coefficient (Figure 5.8) were input to multivariate regression using the PLS NIPALS algorithm. Separation of the three sample classes were tested. The data set was divided into two sets, one for training and one for test set validation (Esbensen et al., 2001). All variables of

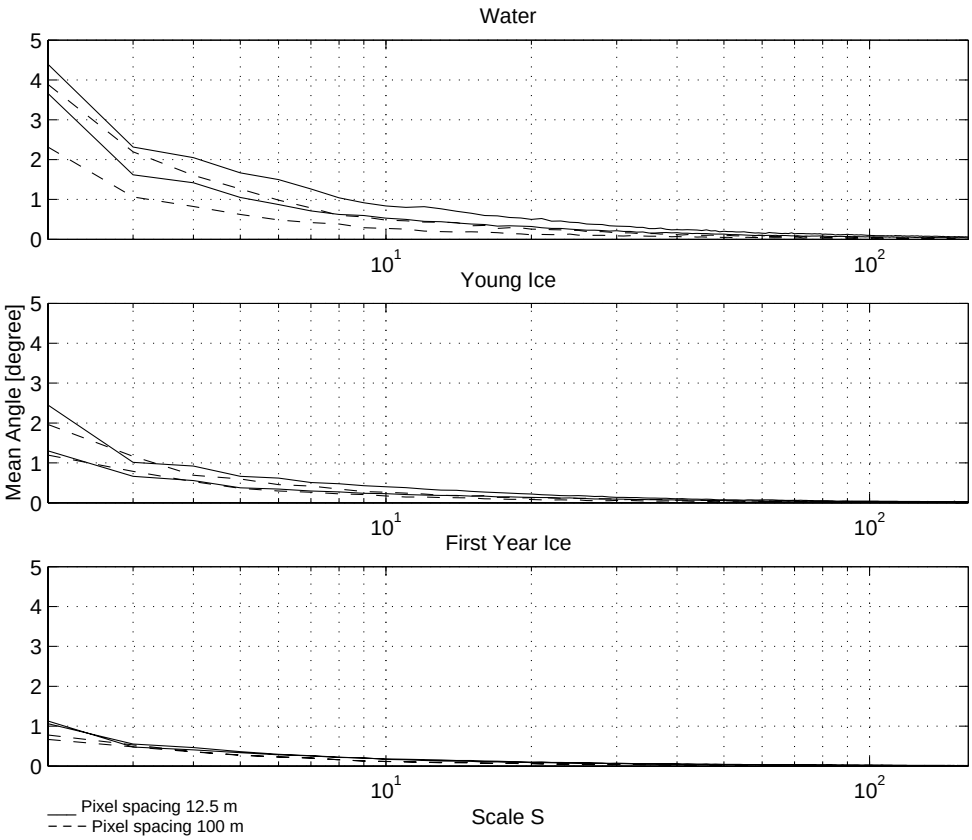

Figure 5.7: *Test of the AMT with input vectors of pixel spacing of 12.5 m and 100 m. Mean angle as function of scale for each surface profile selected from the images presented in Figure 5.4.*

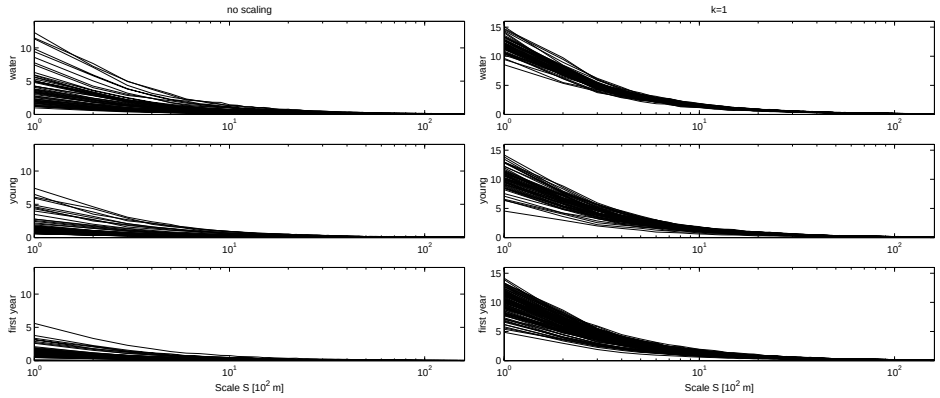

(a) (b)

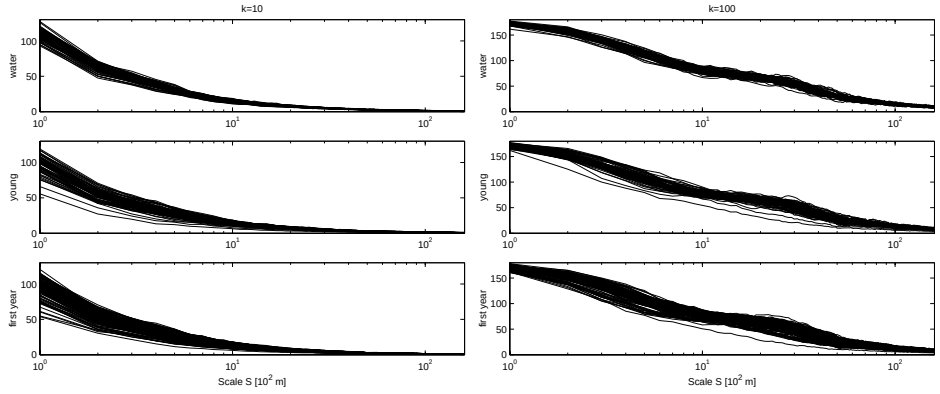

(c) (d)

Figure 5.8: *Mean angles for ERS SAR samples of water (63), young ice (63) and first year (114) ice from the Pechora and Kara Seas. The backscattering values are scaled as described in Equation 5.2.*

Surface types	No scale	k=1	k=10	k=100
Water-ice	0.64	0.50	0.51	0.43
Water-young ice	0.58	0.60	0.57	0.38
Water-first year ice	0.42	0.54	0.57	0.36
First year ice-young ice	0.34	0.18	0.16	0.13

Table 5.1: *Correlation coefficients between predicted and actual data from multivariate regression using the PLS NIPALS algorithm. The mean angles from the AMT calculations are input to the four regression tests. The different scaling applied before calculation of the mean angles from the SAR backscattering values are as presented in Figure 5.8.*

mean angles were mean centered, which is common when the variables are of the same unit (Esbensen et al., 2001). The results from the multivariate regression are presented in Table 5.1.

For separation of water from ice, the mean angles from the original SAR backscattering coefficients with no scaling gave the best results. All of the regression coefficients from these regression tests are low (Table 5.1). For the separation of water from young ice and water from first year ice, better results were obtained when scaling of the SAR backscattering coefficient were applied before calculation of the mean angles. When separating young ice from first year ice, very low correlations were obtained. The best correlation coefficient was obtained using original SAR values. Generally, the separation of water from ice and separation between the two ice types was more successful with no scaling of the SAR data before applying the AMT. The largest scaling factor gives the smallest correlation values, thus the mean angles give less useful information as visually derived from Figures 5.8 and 5.6. It was concluded from the regression tests presented in Table 5.1 to proceed with the original backscattering coefficients as input to the AMT algorithm.

A statistical analysis of 105 SAR images and meteorological data was done by Lundhaug (2001). Wind, temperature and other variables for SAR sample areas were used as input to different multivariate regression analyses, which were used to separate ice and water samples. The classes young ice and rough first year ice were separated from water, and the two ice types were separated from each other. In the separation of all ice types from water, correlation coefficients up to 0.90 between predicted and actual data values were achieved. Correlation coefficients were as high as 0.93 between predicted and actual values for open water and young ice and for open water and rough first year ice. When trying to separate young ice from rough first year, correlation coefficients of

Surface types	Standard Variables	Standard Variables and AMT mean angles
Water-ice	0.85	0.83
Water-young ice	0.93	0.93
Water-first year ice	0.86	0.80
First year ice-young ice	0.40	0.30

Table 5.2: *Correlation coefficients between predicted and actual data from multivariate regression using the PLS NIPALS algorithm. The results in the first column are from the regression with the input variables mean and standard deviation of the backscattering coefficient together with temperature. Then all the mean angle values for the samples are included in the regression with the results presented in the last column.*

about 0.60 were obtained. The results indicated that the mean and standard deviation of the backscattering coefficients together with temperature values were the most important information to separate surface classes using multivariate regression.

Due to these results, mean and standard deviation of the backscattering coefficients together with temperature values for the three classes have been included in the regression tests together with the mean angles for all water and ice samples. Note that the first year samples in this study include both the smooth and rough first year samples described in Lundhaug (2001). Again, the data set was divided into two sets, one for training and one for test set validation. All variables were scaled to zero mean and unit variance, which is common when the input variables are of different units (Esbensen et al., 2001). The results from the multivariate regression are presented in Table 5.2.

When the extended test set was used, the separations of the different samples generally improved compared to the results obtained by using only AMT derived mean angles (Table 5.1). In the separation of ice and water the correlation coefficients were 0.83 and 0.85. For water and young ice the correlation coefficients were 0.93, and for water and first year ice they were 0.80 and 0.86. For the separation of young ice and first year ice, the correlation coefficients were still very low. Only the values of 0.30 and 0.40 were achieved. The best separations were obtained when separating water from young ice and first year ice as presented in Figure 5.9. Comparable results to the separation of open water and young ice obtained in Lundhaug (2001) were found here. Better results for separation of rough first year ice were obtained in Lundhaug (2001). For this study the first year ice class is composed of samples of smooth and rough first year ice, and smooth

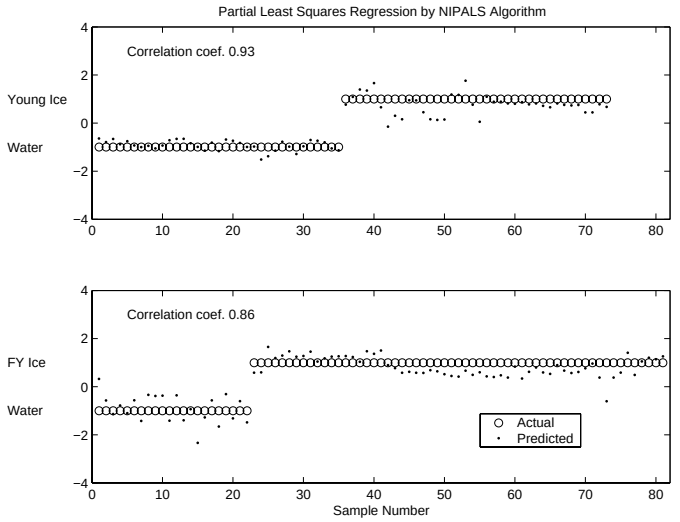

(a)

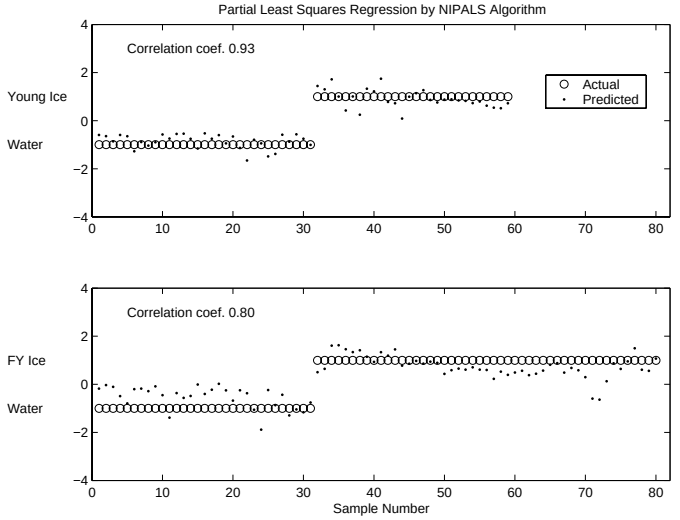

(b)

Figure 5.9: *Results from the multivariate regression for separation of water from young ice and first year ice. The two upper plots were obtained using mean and standard deviation of the backscattering coefficient together with temperature in the multivariate regression. The AMT mean angles are included for the calculations presented in the lower plots.*

first year ice is more difficult to separate from open water than the rough first year ice.

From these regression tests is concluded that the mean angles from the AMT algorithm may give some relevant information for separation of water and ice samples as seen in Table 5.1. The information from the algorithm do not produce results that are more useful than the information that is inherent in the mean and standard deviation of the backscattering coefficient together with temperature values. A possible reason for this may be the characteristics of SAR data. The AMT algorithm has earlier been applied to visual and near-infrared imagery with promising results (Huang and Esbensen, 2000). But a property of the radar image is that even for a single surface type, important grey level variations may occur between adjacent resolution cells. This variation creates a grainy texture called speckle, the statistical uncertainty associated with the brightness of each pixel. Within an area, it exists many different targets, which provide the surface texture necessary for backscatter. These multiple interactions produce signals, which interfere with each other in either a constructive or destructive manner. Constructive interference results in a strong return signal and a bright pixel in the image. Destructive interference results in a weak return signal and dark pixel in the image. This variation may be the reason why the AMT results are not as useful for SAR surface type characterization as the traditional mean and standard deviation measures.

5.5 Conclusion

It was concluded from mean angle plots and multivariate regression that the AMT method gave best results when the original SAR backscattering coefficients were used as input. The tested scaling approach gave less useful results from the separation of water and ice using multivariate regression. Better results were obtained when using the mean and standard deviation of the backscattering coefficient together with temperature data in the multivariate regression. These variables were used together with mean angles from the AMT algorithm. In the separation of ice and water the correlation coefficients were 0.83 and 0.85. For water and young ice the correlation coefficients were 0.93, and for water and first year ice they were 0.80 and 0.86. For the separation of the ice types young ice and first year ice the correlation was still very low, the values 0.30 and 0.40 were achieved. The AMT algorithm may give some relevant information for separation of water and ice samples. Information from mean and standard deviation of the backscatter-

ing coefficient could be an alternative to the results from the more computer-demanding AMT algorithm. The speckle property of SAR images may be the reason why this approach is not as useful for this data type as for other types of data. Kerman et al. (1999) suggested to obtain estimated statistics of Arctic sea ice thickness from SAR imagery by using differences between neighboring pixel values. The speckle property of the SAR data was then given as a possible reason why pixel differences may not be optimal.

A data set with surface data of ice type and thickness with simultaneous SAR coverage would have been optimal to test if the mean angles from AMT algorithm could give useful information for separation of open water and different sea ice types. The future Advanced Synthetic Aperture Radar (ASAR) sensor on ENVISAT will produce multi-polarization data. The Alternating Polarization Mode will provide simultaneous dual-polarized images, either both VV (vertical transmit/vertical receive) and HH (horizontal transmit/horizontal receive), or one of the two combinations of plan polarized and cross polarized images (VV and VH, or HH and HV). The swath width will be 100 km and the resolution will be 30 m. Mean angles from AMT from different polarizations modes could provide input to regression models. *In situ* observations of ice type or possibly ice thickness could be obtained in future ice type validation experiments to test the models.

Acknowledgments

The ERS-1/2 SAR image data was obtained within different European Space Agency 'Announcement of Opportunity' projects. This work was funded by a Ph. D. grant from Telemark University College, Department of Technology (IPT/TF), Porsgrunn, Norway and with support from Nansen Environmental and Remote Sensing Center (NERSC), Bergen, Norway. Thanks to Jun Huang (Camo ASA) who has developed and provided the AMT Toolbox and O. M. Johannessen (NERSC) for valuable comments and suggestions.

URN:NBN:no-2344

Chapter 6

Sea ice investigations in the Laptev Sea area in late summer using SAR data

by

S. Sandven, Ø. Dalen, M. Lundhaug, K. Kloster, V. Y. Alexandrov, and L. V. Zaitsev

Published in Canadian Journal of Remote Sensing, Focus Issue on Ice and Icebergs, Vol. 27, No. 5, 2001, pp. 502-516.

Abstract

The Laptev Sea area, including the Vilkitsky Strait, is an important part of the Northern Sea Route where the presence of sea ice makes navigation difficult even in the summer season. The objective of this study was therefore to demonstrate and validate the capability of Synthetic Aperture Radar (SAR) imagery to provide accurate ice information to support ice navigation which is most important in late summer in this region. An experiment was set up in August-September 1997 with joint use of RADARSAT and ERS-2 SAR images combined with SSM/I data *in situ* observations from icebreakers. These data were used to analyze ice concentration, ice types, ice drift and other ice features present in this period. The capability of RADARSAT ScanSAR and ERS SAR images to determine these ice parameters during late summer conditions in the Laptev Sea area is

URN:NBN:no-2344

discussed. The Laptev Sea as well as other parts of the Northern Sea Route are expected to become important areas for future oil and gas exploration and exploitation, which will increase the demand for SAR ice monitoring to support ice navigation, drilling and other offshore operations.

6.1 Introduction

The Laptev Sea area, which is an important part of the Northern Sea Route (NSR), is bounded by the Severnaya Zemlya Archipelago in the west and by the New Siberian Islands in the east (Figure 6.1a). By the end of October a belt of fast ice starts to form along the Siberian coast. Floes of second-year ice can be embedded into the fast ice during formation in the autumn (Reimnitz et al., 1995). Recurring flaw polynyas are typical for the winter Laptev Sea where new ice is pushed away from the fast ice by wind drift and ocean currents (Zakharov, 1966; Eicken et al., 1997; Dmitrenko et al., 1999). During autumn, winter, and spring sea ice in the Laptev Sea has a net drift northwards to the Arctic Ocean, whereas the ice circulation is more variable in summer (Zakharov, 1966; Gudkovich et al., 1972). During the period 1979-1995 the average winter ice outflow amounted to 483000 km^2, whereas on average 40000 km^2 of sea ice were imported in summer through the northern boundary (Alexandrov et al., 2000a). Ice melting starts in late May or early June centered around the flaw polynyas. The Taymyr ice massif usually persists throughout the summer and can even widen in some years because of southward ice drift and may therefore block coastal routes with thick ice. Icebergs, calving from Severnaya Zemlya outlet glaciers, can frequently be observed in the western part of the Laptev Sea including the Vilkitsky Strait (Govorukha, 1988; Eicken et al., 1994; Abramov, 1996; Zakharov, 1966).

Regular navigation in the Laptev Sea is limited to the summer season, because winter navigation requires icebreakers of the Arktika type, with more than 65000 horsepower, and even these icebreakers can have problems to operate under difficult ice conditions. Therefore high-resolution radar images are particularly important for supporting navigation in this area.

Sea ice charts have been produced for several decades based mainly on aircraft observations and optical satellite images. Satellite radar observations started in 1983 with Okean Side-Looking Radar images (Bushuev et al., 1985). Since 1991 a series of ice monitoring

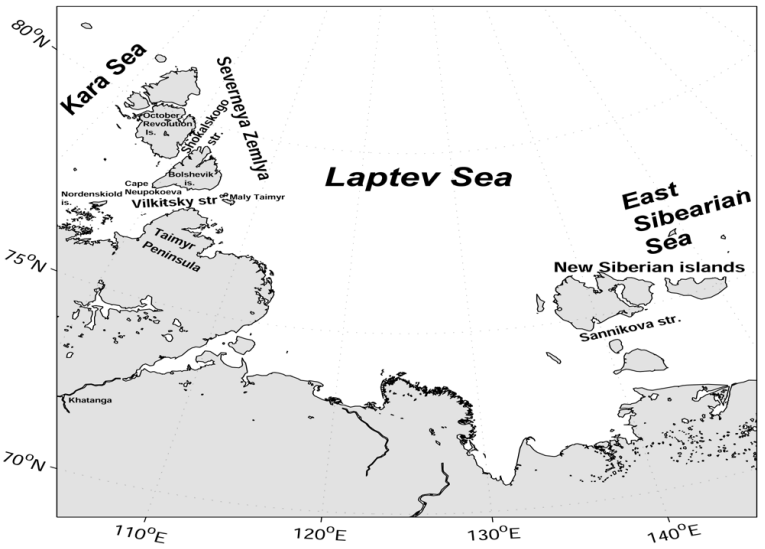

(a)

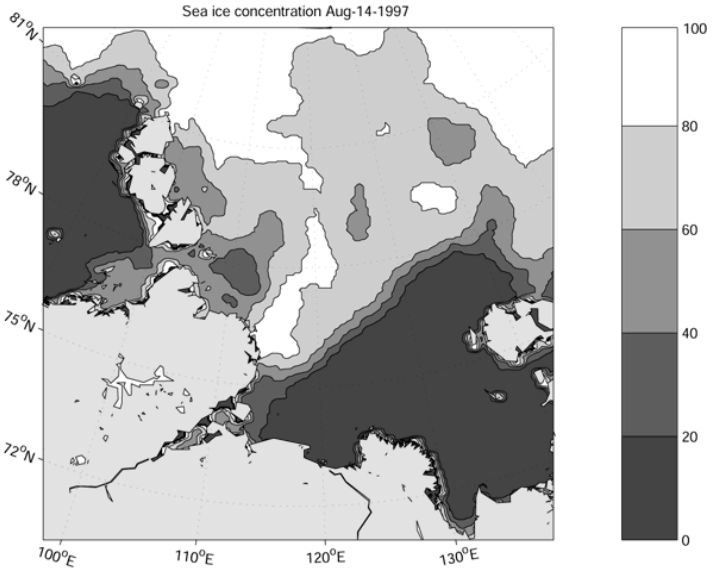

(b)

Figure 6.1: *a. Map of study area with some geographical names. b. SSM/I-derived ice concentration in % for August 14, 1997.*

URN:NBN:no-2344

experiments using ERS SAR images have been carried out by Nansen Centers in Bergen and St. Petersburg together with Murmansk Shipping Company. During these experiments SAR images have been transmitted by INMARSAT to icebreakers to support ice navigation (Johannessen et al, 2000; Pettersson et al., 2000). With ERS SAR images it is possible to identify icebergs, several ice types and phenomena, which can be dangerous for icebreakers (Johannessen et al., 1997b; Kolatschek et al., 1995; Sandven et al., 1999b). RADARSAT ScanSAR data have been used by the Nansen Center to observe sea ice in the Kara Sea region during winter conditions, described by Alexandrov et al. (2000b).

In this paper use of ScanSAR images are demonstrated, supported by some ERS-2 SAR images, for sea ice monitoring in late summer conditions which is the most important period for the ship traffic. SAR signatures of late summer ice types, ice drift and other features have been analyzed and a SAR ice concentration algorithm has been tested and compared with *in situ* ice observations from icebreakers and helicopter. Also ice drift vectors are estimated from consecutive images and used to discuss current- and wind-driven ice motion in the study area.

6.2 Data acquisition and icebreaker expedition

6.2.1 Use of passive microwave satellite (SSM/I) data

To observe the general ice conditions before and during the expedition, Special Sensor Microwave Imager (SSM/I) data were obtained in near-real time and maps of ice concentration were prepared using the NORSEX algorithm (Svendsen et al., 1983) modified for use with the 85 GHz channel. By using this channel it is possible to obtain higher resolution and more accurate localization of the ice edge and reduce the errors near land. A series of SSM/I ice concentration maps, covering the period of 4 weeks from August 10, provided an overview of the ice extent and concentration in the study area. The predominant features were the large open water areas in the northeastern Kara Sea and the southern Laptev Sea (Figure 6.1b). The Taymyr ice massif extended southwards to the Taymyr coast at a concentration of 80 % and more, acting as a barrier for ships sailing from Vilkitsky Strait to the Laptev Sea. The position of this ice massif changed very little in the 4 weeks period when SSM/I data were analyzed. The ice concentration in

the Vilkitsky Strait area was initially about 50 % and decreased to less than 20 % at the end of the period. The large open water areas persisted in the Kara Sea and the southern Laptev Sea throughout the period (Figure 6.1b).

6.2.2 Acquisition and processing of SAR data

The acquired RADARSAT ScanSAR scenes covered the Vilkitsky Strait area and parts of the Laptev and East Siberian Seas over the period from August 14 to September 7 (Figure 6.2a). Several ERS-2 SAR images were acquired in the Vilkitsky Strait area to supplement the RADARSAT images and obtain more frequent temporal sampling (Figure 6.2b). SAR images for the western part of the Laptev Sea were obtained from Tromsø Satellite Station (TSS) in near real-time (3-4 hours delay) and delivered on Internet to the Nansen Center in Bergen. The area west of about 105° E is situated within the station mask of TSS. After the images were geocoded and contrast enhanced with superposition of landmask and latitude/longitude grid, they were transmitted to Murmansk Shipping Company's Headquarters for planning of the expedition and onboard the icebreaker after she left port. Typical turnaround time from SAR acquisition to delivery onboard icebreakers was about 6 hours. For the central part of the Laptev Sea and the area around the New Siberian Islands only archived RADARSAT images could be obtained from Canadian Space Agency (CSA) and Alaska SAR Facility (ASF) after the expedition was completed. The SAR images are summarized in Table 5.1.

6.2.3 Data transmission to I/B Sovetsky Soyuz

I/B Sovetsky Soyuz left Murmansk on September 7 and arrived in the Laptev Sea three days later for supporting ice navigation to Khatanga. The ScanSAR image for September 7 and several SSM/I ice concentration maps were transmitted onboard the icebreaker via INMARSAT and used for planning of sailing routes. The pixel spacing of the RADARSAT image was averaged to 500 by 500 m and JPEG compression was applied to obtain a reasonable file size, less than 1 Mbyte, which could be transmitted in a few minutes. Scientists from the Nansen Center in St. Petersburg received SAR and SSM/I data onboard the icebreaker and collected *in situ* ice observations for support of the SAR ice analysis.

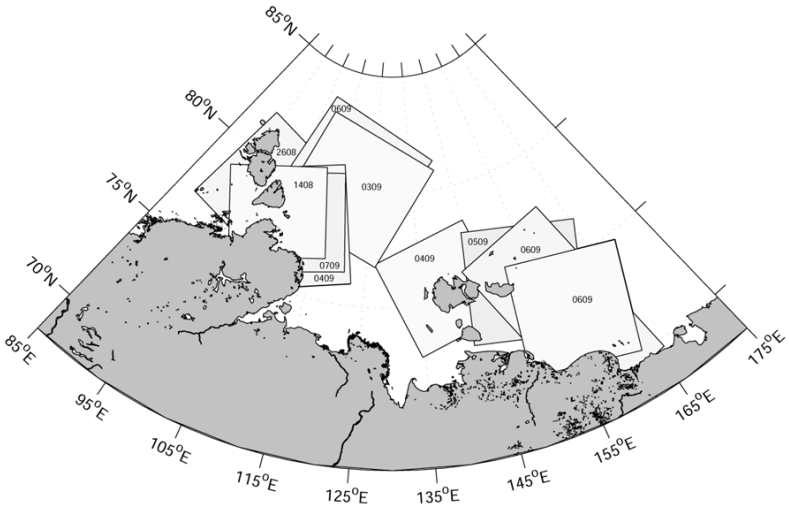

(a)

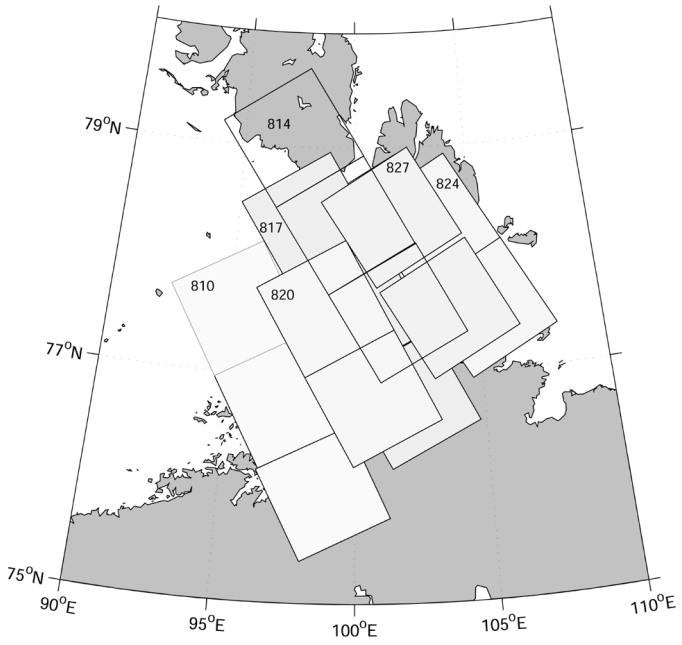

(b)

Figure 6.2: *a. Map of RADARSAT ScanSAR coverage. b. map of ERS-2 SAR coverage. The figures indicate day-month of the SAR scenes.*

URN:NBN:no-2344

Date	Image acquisition time (GMT)		Area	Receiving station
	RADARSAT	ERS-2		
10.08		14:19	Nordenskjold Archipelago	TSS
11.08		13:48	West Vilkitsky Strait	TSS
14.08	09:33	13:54	Vilkitsky Strait area and western Laptev Sea	TSS
15.08	09:04		Vilkitsky Strait area and western Laptev Sea	TSS
17.08		13:59	West Vilkitsky Strait	TSS
20.08		14:05	West Vilkitsky Strait	TSS
24.08		13:40	Central Vilkitsky Strait	TSS
26.08	00:30		Vilkitsky Strait area and western Laptev Sea	ASF
27.08		13:45	Central Vilkitsky Strait	TSS
31.08	09:37		Vilkitsky Strait area and western Laptev Sea	TSS
03.09	23:22		Central - northern Laptev Sea	ASF
04.09	21:12		New Siberian Islands - north/east	ASF
04.09	07:39		New Siberian Islands - north/west	Gatineau
04.09	09:20		Vilkitsky Strait area and western Laptev Sea	Gatineau
05.09	20:44		New Siberian Islands - east	ASF
06:09	20:15		New Siberian Islands - east	ASF
06.09	06:39		New Siberian Islands - east (2 ScanSAR scenes)	Gatineau
06.09	23:34		Central - northern Laptev Sea	ASF
07.09	09:33		Vilkitsky Strait area and western Laptev Sea	TSS

Table 6.1: *SAR images used in the study.*

6.2.4 Meteorological data

In the western Laptev Sea area which was covered by SAR imagery, visual ice observations were obtained from the bridge of the icebreakers and from helicopter ice reconnaissance flights. Sea ice and meteorological data were collected several times per day while the icebreaker operated in ice areas. The meteorological observations included air pressure, wind velocity and direction, sea surface and air temperature. In the 10 day period when I/B Sovetsky Soyuz and I/B Yamal operated in the Laptev Sea, the weather conditions were stable and the sea surface temperature was at the freezing point (-1.8° C) allowing formation of new ice in open water areas. Air temperature varied from typically -3° C at night to +1° C in daytime. The wind speed was moderate, not exceeding 10 m/s, which generally agreed with the European Center for Medium Range Weather Forecasts (ECMWF) data, which were analyzed after the expedition.

6.2.5 Preprocessing of the SAR images

Since the RADARSAT data were obtained from three receiving stations, TSS in Norway, Gatineau in Canada and Alaska SAR Facility, it was necessary to preprocess the images to obtain a set of relatively homogeneous ScanSAR images which could also be compared with the ERS-2 images. For ERS-2 SAR data delivered by TSS as Low-Resolution Images (LRI) there is a standard procedure for correction of the three effects: antenna gain, slant range and incidence angle. A calibration procedure for ERS SAR data is established which also relates corrected pixel values to σ^o, based on a calibration constant from previous sea ice investigations (Sandven et al., 1999b). This procedure gives an accuracy of the σ^o values within approximately 1 dB. For RADARSAT data a common calibration procedure for the three ground stations was not available for the images used in this study. It was not possible to obtain an accurate calibration constant for the RADARSAT images from TSS, but the pixel values were provided as a linear function of log σ^o after correction for incidence angle. The RADARSAT images received from CSA and ASF had pixel values proportional to $(\sigma^o)^{0.5}$ after incidence angle correction, with the calibration constant given in a range varying Look-Up Table (LUT) (RADARSAT, 1997). Since the accuracy of the LUT was unknown, σ^o values could have inaccuracy of several dB. Calibration of ASF data was also unknown, but the coding was assumed to be similar to the CSA data. Therefore RADARSAT images with range-corrected pixels, but

without absolute calibration, were used in the subsequent analysis. Focus of the study has therefore been on ice features and dynamics which only need pattern recognition and relative backscatter difference between water and ice types.

An important point is that wide-swath SAR images have large variations of σ^o across the full swath for most surfaces, and in particular for water. For ScanSAR, σ^o may be up to 15-20 dB lower in far-range compared to near-range. All images used in this study were therefore multiplied by a pre-defined range-normalization function, $(tan\theta)^\beta$, where θ is incidence angle. For most ice types β is about 1.5, while for open water it is near 4.

6.3 Characterization of ice conditions from SAR data

With SAR data available since early August it was possible to provide detailed description of the ice conditions for the following areas and periods:

6.3.1 August 10-11: Nordenskjold Archipelago and western Vilkitsky Strait

SSM/I data from August 10 and onwards showed ice concentration above 50 % in the area of Nordenskjold Archipelago and western Vilkitsky Strait (Figure 6.1b). Also the ERS-2 SAR image of the same day showed the presence of compact ice which drifted eastwards, and open water areas near the coast, within the archipelago and in the northwestern corner of the image (Figure 6.3). West of Nordenskjold Archipelago no ice was observed in this period, suggesting that the eastward drifting ice originated from the area between the archipelago and the Vilkitsky Strait. The ECMWF data showed westerly winds up to 10 m/s in this period, generating high SAR backscatter of open water. The other ERS-2 SAR image in Figure 6.3, obtained on August 11, showed a stream of eastward drifting ice floes in the central and southern part of the Vilkitsky Strait, whereas its northern part was mainly ice free.

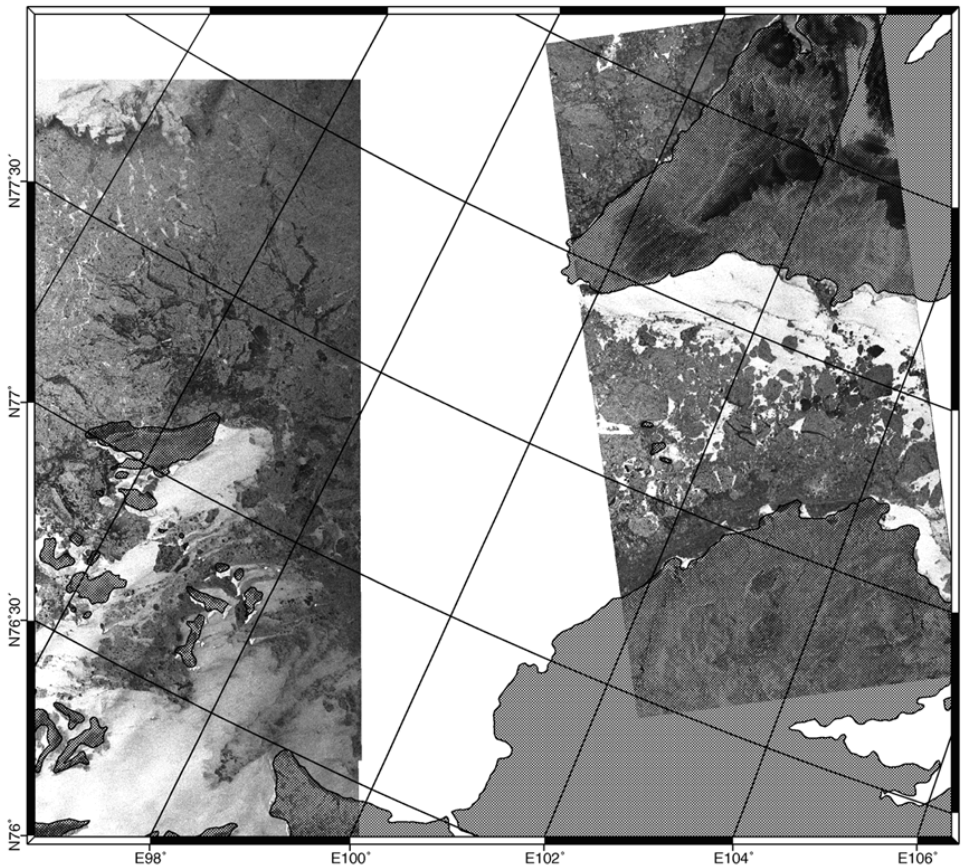

Figure 6.3: *ERS-2 SAR imagery of the Nordenskjold Archipelago (left swath) on August 10 and Vilkitsky Strait (right swath) on August 11, 1997. ©ESA/TSS, 1997.*

6.3.2 August 14-17: First ScanSAR survey of Vilkitsky Strait area and western Laptev Sea

The first ScanSAR survey, obtained on August 14 (Figure 6.4), showed that the ice edge in the eastern part of the Kara Sea is clearly visible due to the brighter SAR signatures of open water as compared to the ice covered areas. The wind speed of 5-10 m/s in this region was sufficient to generate this high backscatter. The eastward ice drift in the Vilkitsky Strait was composed of ice from southwest along the Taymyr coast, and from the northwestern side of Bolshevik Island, where the fast ice of Shokalsky Strait started to break up and drifted southwards. The eastbound surface current through the Vilkitsky Strait formed a wedge of low concentration ice which penetrated into the Taymyr ice massif. Most of the western Laptev Sea area shown in the image was covered by compact thick ice characterized by relatively high backscatter whereas the dark SAR signature east of Severnaya Zemlya could be explained by open water during calm wind or the presence of nilas or grease ice.

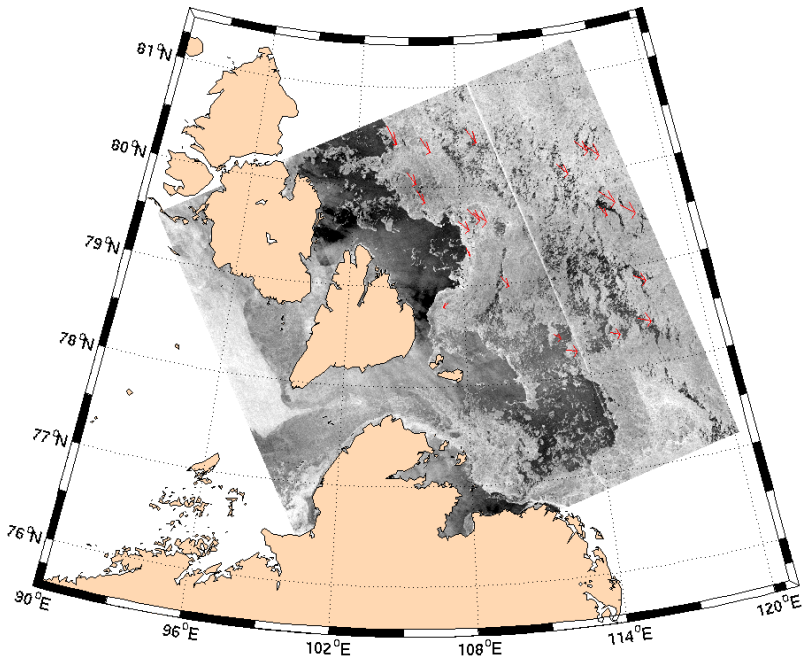

Figure 6.4: *RADARSAT ScanSAR image of August 14, 1997, with ice drift vectors and land mask superimposed. The mean ice drift speed, estimated between repeated ScanSAR images on August 14 and 15, is about 0.20 m/s.* ©*Canadian Space Agency, 1997.*

One day later, on August 15, another ScanSAR scene was obtained over almost the same area, allowing estimation of mean ice drift over a period of about 24 hours. In the Laptev Sea ice drifted in a southeasterly direction at a mean speed of 0.20 m/s, and in the eastern Vilkitsky Strait an ice displacement of 38 km was found corresponding to a mean speed of 0.44 m/s. West of the Vilkitsky Strait the winds in the period were west-southwesterly, 5-10 m/s, and air temperatures varied between 0° and -2° C, according to ECMWF data. East of Severnaya Zemlya, the westerly winds can be reduced by topographic effects, allowing open water to have the lower SAR signature in this area.

The western part of the Vilkitsky Strait including the area between Bolshevik Island and October Revolution Island, was covered with three consecutive ERS-2 images from August 14, 17 and 20 (Figure 6.5). Similar to the ScanSAR image the ERS images showed that the ice north and west of Cape Neupokoeva (78° N 100° E) drifted southwards into the Vilkitsky Strait and then merged with the eastward flowing ice coming from southwest. A cluster of 5-10 km large floes observed north of the cape on August 14, had moved about 60 km and was located south of the cape three days later, corresponding to a mean drift speed of 0.23 m/s. A 25 km large floe, which was located northwest of the cape on August 14, moved 20 km towards southeast in the same period, corresponding to a mean drift speed of 0.08 m/s. The ice along the Taymyr coast also drifted eastwards, as can be recognized by open water on the leeward side of the small islands. The floe displacement in this region between August 17 and 20 suggested a mean drift speed of 0.03 m/s.

6.3.3 August 26-31: Repeated ScanSAR survey of Vilkitsky Strait and western Laptev Sea

The ScanSAR image for August 26 (not shown) indicated a reduction of the ice in the Vilkitsky and Shokalsky Straits, as compared with the previous ScanSAR survey, and several well-developed ice edge eddies and vortex-pairs in the region west of the 100° E longitude. Ice edge eddies and vortex-pairs have previously been studied in the Greenland Sea (Johannessen et al., 1994b), where mixed barotropic/baroclinic instabilities of the currents was found to be probable generating mechanisms for these phenomena. In the western Laptev Sea the thick icepack drifted to the southwest at a speed of 0.05 m/s, while open water/new ice areas persisted east of Severnaya Zemlya.

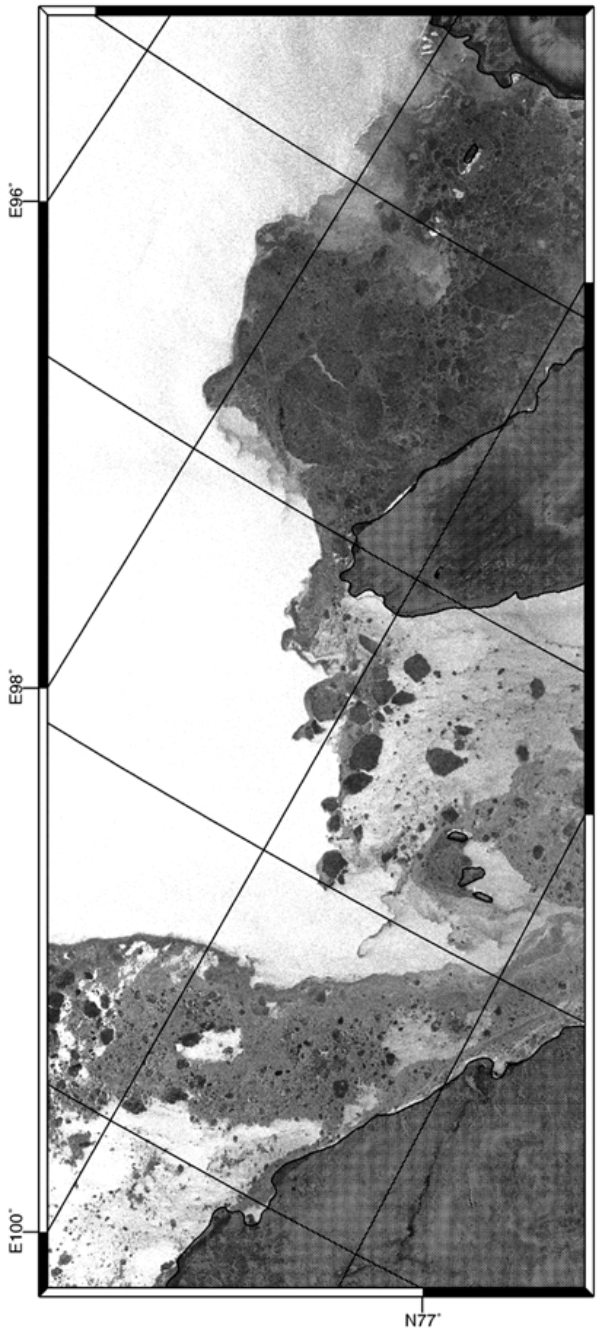

Figure 6.5: *ERS-2 SAR imagery of western Vilkitsky Strait and parts of Shokalsky Strait on August 17, 1997. ©ESA/TSS, 1997.*

URN:NBN:no-2344

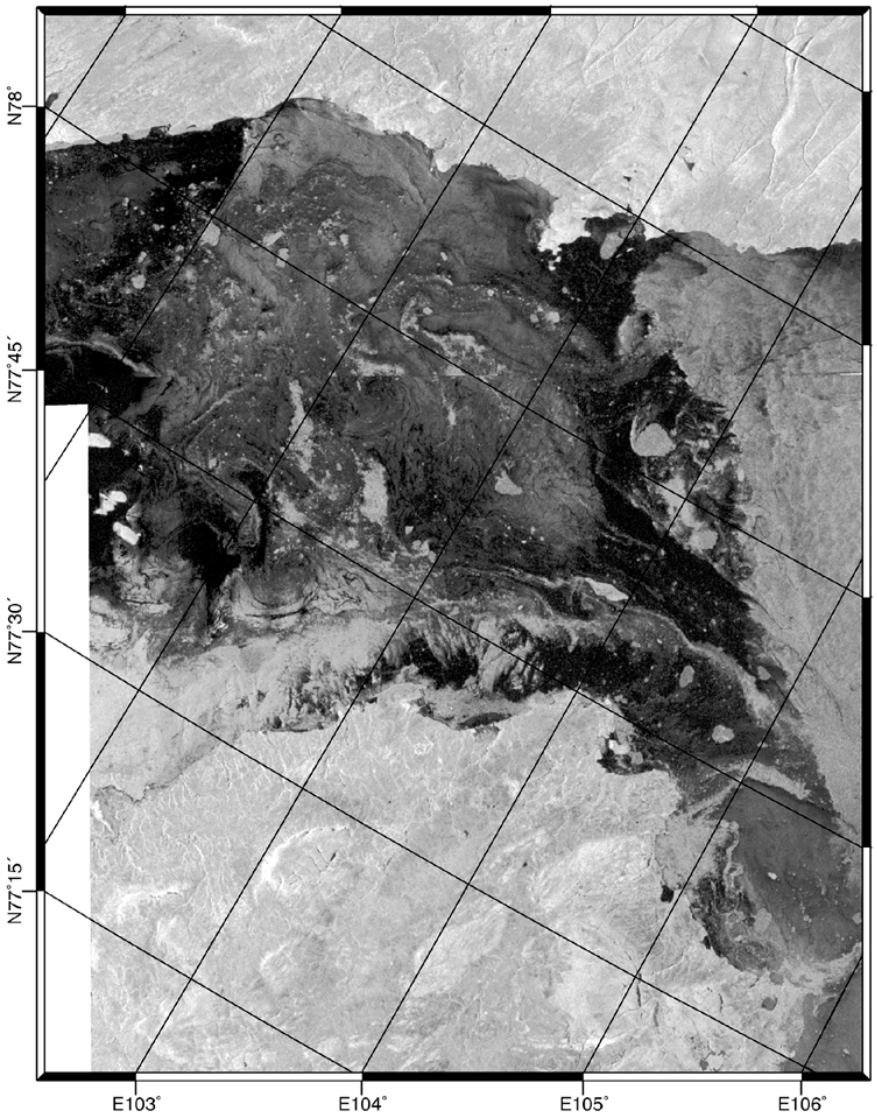

Figure 6.6: *ERS-2 SAR imagery of the central Vilkitsky Strait on August 27, 1997. The image is composed of two consecutive scenes. ©ESA/TSS, 1997.*

URN:NBN:no-2344

Ice drift in the Vilkitsky Strait was estimated from SAR images for August 24, 26 and 27 (Figure 6.6). The first image pair showed that two floes located near the northern coast of the strait moved towards south at 0.06-0.08 m/s in a period of easterly winds. In the central part of the strait floes moved eastwards at speeds up to 0.17 m/s even if the winds continued to be easterly 4-8 m/s. This suggests that the floes were captured by the eastbound currents which appear to dominate in the central and southern part of the strait.

6.3.4 September 3-6: ScanSAR coverage of more ice areas in western Laptev Sea and around New Siberian Islands

Two ScanSAR images for September 3 and 6 (not shown), which were obtained over a central part of the Laptev Sea, were used to estimate a southeasterly ice drift with a mean speed of 0.15 m/s. Several ScanSAR images, which were obtained in the area of the New Siberian Islands and parts of the East Siberian Sea, were used to make a mosaic and calculate ice drift for the period September 3 to 6 (Figure 6.7). The mosaic shows that the area to the north-east of the New Siberian Islands and a 100-200 km wide zone along the coast in the East Siberian Sea were ice free. Scattered ice was found in the New Siberian Straits and to the south of the islands. A diffuse ice edge extending from the east Siberian coast (at 162° E) to the north of the islands is clearly evident the mosaic. Ice concentration increased into the ice massif reaching 90-100 % in the northeastern corner of the images.

6.4 Validation of SAR ice observation using icebreakers

The most appropriate ScanSAR image for validation was obtained on September 7. I/B Sovetsky Soyuz operated in the area covered by this image during September 10-11, giving a time-delay of 3-4 days between image acquisition and ship observations. A subset of the September 7 image with superimposed ship track of I/B Sovetsky Soyuz is shown in Figure 6.8a. A series of photographs (Figure 6.9), ice log reports, ice charts from helicopter and meteorological observations taken from the icebreakers were used for this validation. Unfortunately, it was not possible to obtain RADARSAT images after this date because the satellite went into another mode of operation for monitoring of the

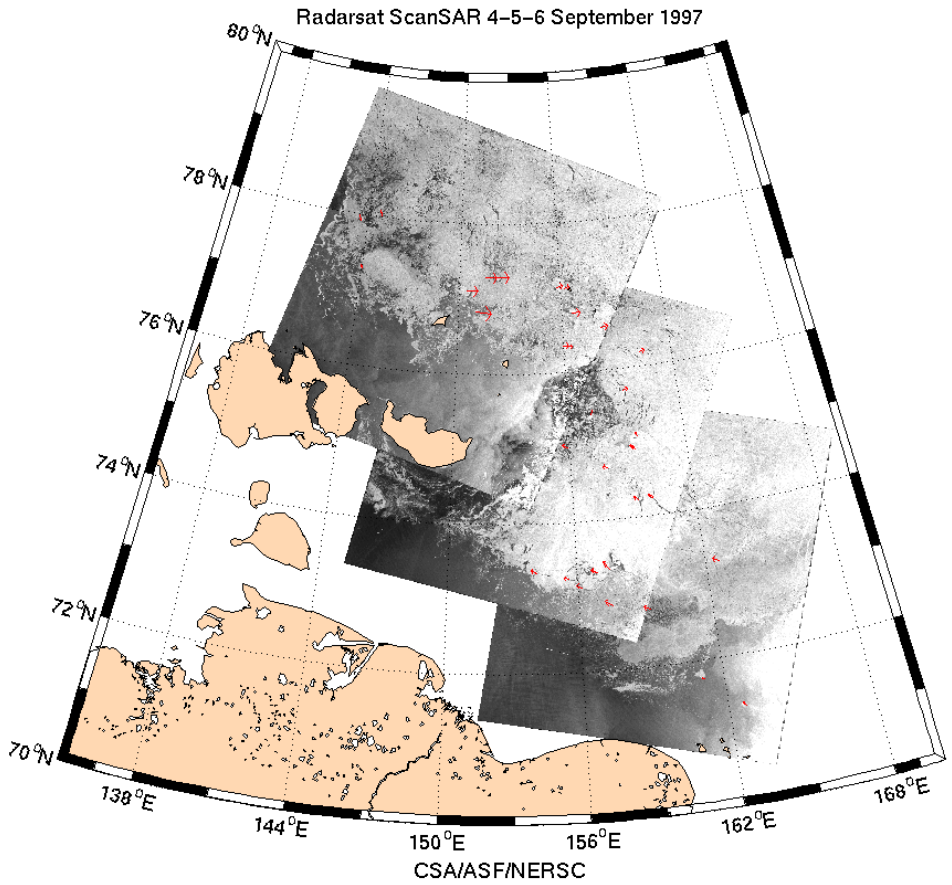

Figure 6.7: *Mosaic of three RADARSAT ScanSAR images taken in the area of New Siberian Islands from September 3 to 6, 1997, with ice drift vectors superimposed. The mean ice drift speed, estimated between repeated ScanSAR images, varies from 0.10 to 0.20 m/s. ©Canadian Space Agency, 1997.*

URN:NBN:no-2344

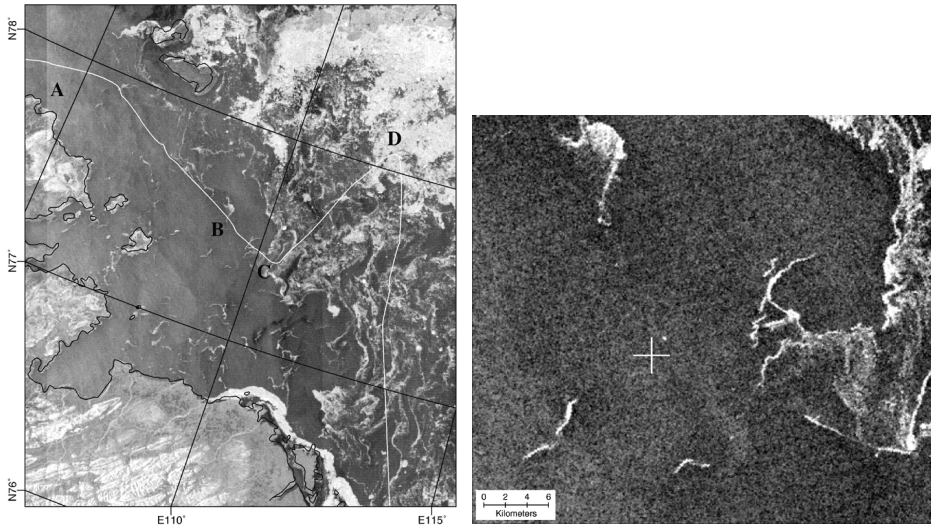

(a) (b)

Figure 6.8: *a. Subset of RADARSAT ScanSAR image on September 7, showing the area east of Vilkitsky Strait. The line marks the track of I/B Sovetsky Soyuz which sailed in the areas on September 10-11. The points A-D mark different characteristic ice conditions documented by observations onboard the icebreaker. b. Zoomed sub-image in full resolution (pixel spacing 100 m) of the area between B and C, showing the location of a small iceberg (white dot) near the cross which is the position of observation by icebreaker four days after SAR acquisition. The iceberg has a horizontal scale of about 100 m.* ©*Canadian Space Agency, 1997.*

Antarctic ice cap.

Due to quiet weather conditions, with temperatures below freezing and wind speed from 3-6 m/s, it is assumed that the properties which have impact on the SAR signatures, such as surface roughness and temperature, snow cover, and salinity of the Taymyr ice massif did not change much in this period. However, the currents observed within and eastwards of the Vilkitsky Strait (Figure 6.4) suggested that patches and stripes of first-year ice in the validation area drifted in a south-eastward direction. With persistent air temperature between -2° C and -6° C in the period September 2-16 and water temperature at the freezing point, formation of new ice was assumed to take place throughout this period.

URN:NBN:no-2344

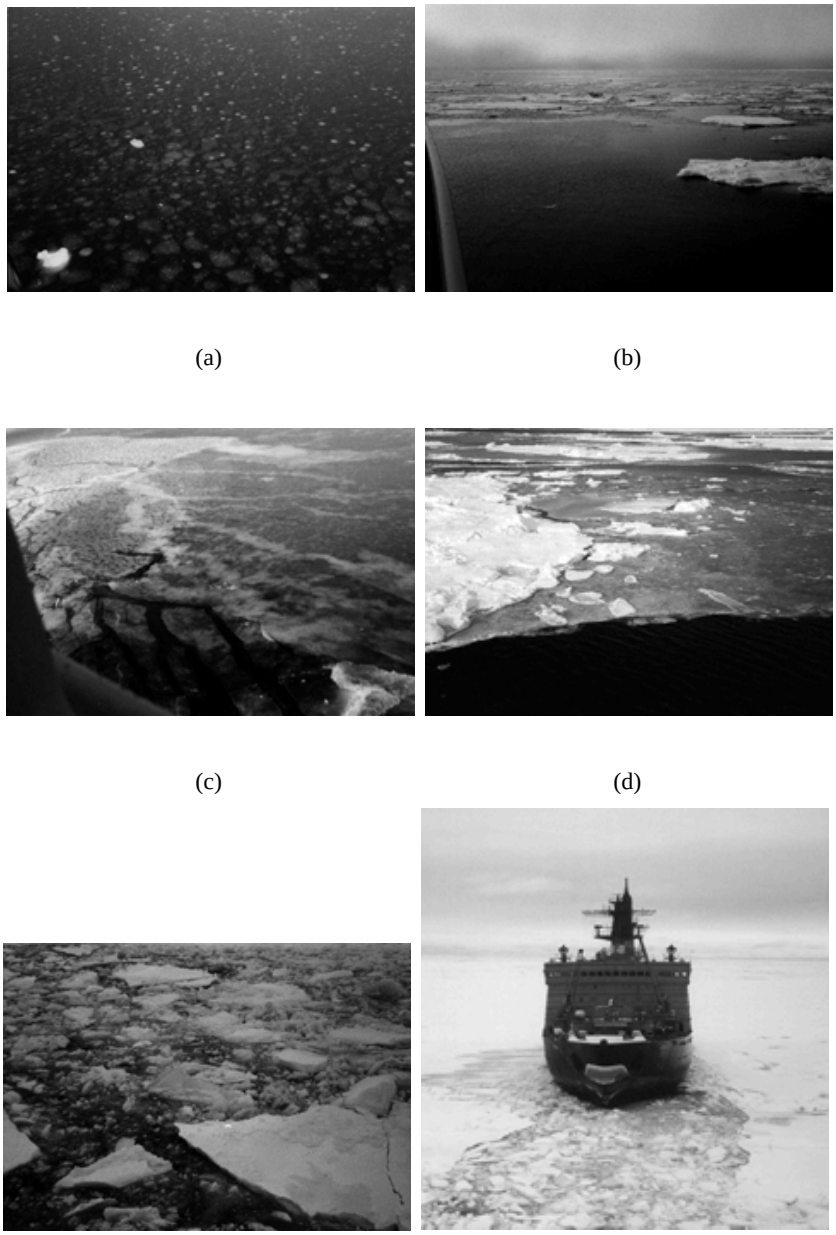

(a) (b)

(c) (d)

(e) (f)

Figure 6.9: *Photographs of different ice conditions observed by I/B Sovetsky Soyuz on September 10-11 within the SAR image of September 7. Pictures (a) and (b) were taken at point A in Figure 6.8, showing pancake ice and scattered floes of first year ice, respectively. Pictures (c) and (d) are from point C, where nilas covered up to 80-90 % of the ice area. Pictures (e) and (f) were taken at point D where up to 1.5 m thick first-year ice dominated. I/B Sovetsky Soyuz had a rendezvous with I/B Yamal (f) at this position.*

Our study attempted to provide an overall description of the ice signatures in the SAR image, being aware that validation of new ice areas is more difficult due to the freezing conditions in the period.

The area west of 110° E, between point A and C, was dominated by open water and new ice, which appear as homogeneous greyish signatures in the SAR image (Figure 6.8a) mixed with scattered patches and bands of brighter signature caused by clusters of ice floes. At site A, photographs were taken of pancake ice (Figure 6.9a) and scattered floes of first-year surrounded by open water and grease ice (Figure 6.9b). Ice observers on the icebreaker reported a total ice concentration of 20-30 %, of which 10-20 % were first-year ice and the same amount of pancake ice (Table 5.2). Between points A and B several bands of thick first-year ice were observed, and the largest of them can be seen as bright line features against darker background. Ice concentrations in this area were up to 50 %, and the ice mainly consisted of a mixture of grease ice and pancake ice (pancake size up to 1 m), with patches of smaller FY ice floes which were observed continuously. Due to low wind velocities (3-4 m/s), open water had similar low backscatter as grease ice and nilas. In the backscatter image, with pixel spacing of 500 m, it was also difficulty to identify first-year ice when floes were small (less than 100 m) and concentration less than 10-20 %.

An iceberg which was about 100 m in horizontal scale was observed from the icebreaker near B at position 77° 25′ N 109° 19′ E. This iceberg can be seen as a bright spot in the full-resolution blow-up of the ScanSAR image (Figure 6.8b). The position of the iceberg observed from the icebreaker four days later is marked by the cross in Figure 6.8b. The time difference of these observations, combined with the position accuracy of the image, suggests that the displacement of the iceberg is small, less than 2 km. Furthermore, this suggests that the iceberg is not located in the core of the southeastward coastal current in this area. Other icebergs were not observed in this expedition, but icebergs originating from the Severnaya Zemlya glaciers are not unusual in this region (Eicken et al., 1994).

Following the icebreaker track east of 110° E, starting at point C (Figure 6.8a), ice concentration generally increased to more than 60-70 %, most of it was nilas which can be partly rafted (Figure 6.9c) and mixed with floes of first-year ice (Figure 6.9d). At the northernmost position in the expedition (point D at 78° 05′ N, 112° 05′ E), patches of nilas and open water occurred between first-year ice with concentration of 80-90 %. The floe size increased to 50-200 m and the thickness to 100-150 cm. Typical ice concentra-

Time*/ site	Latitude (N)	Longitude (E)	Observed ice concentration [%]					Meteorological data		
			Total	FY ice	Nilas	Pancake	Grease ice	Wind direction	Wind speed	Temp-erature
10:35** a, b	77°55′	104°20′	30	10-20		10-20		300°	3 m/s	-3° C
00:00	77°56′	105°31′	30	10-20		10-20		240°	4 m/s	-4° C
00:40	77°54′	106°02′	90-100	0-10		40-50	30-40			
iceberg	77°25′	109°19′								
06.42 c, d	77°37′	111°01′	80-90		80-90					
08.00	77°58′	111°47′	70-80	10	60-70			180°	6 m/s	0° C
09:00 e, f	78°05′	112°05′	80-90	70-80	10			180°	7 m/s	1° C
13.30	77°43′	112°51′	60-70	10-20	50					
15.00	77°20′	113°00′	70-80	10-20	50	10				
16.20	76°57′	113°24′	60-70	30	30-40			200°	9 m/s	-1° C

Table 6.2: *Ice and weather observations on September 10-11.*
**Moscow time = GMT + 3 hours*
***September 10, all other entries are September 11.*

tion in Taymyr massif was 80-90 %. The SAR signature of the first-year ice was relatively bright. Individual floes larger than a few kilometers could be identified. Following the icebreaker track south of 78° N, the ice cover was again characterized by up to 50 % concentration of grease ice, nilas and pancakes, while the fraction of first-year was down to 10-20 %.

The ScanSAR image of September 4 extended further south between 115° and 120° E as compared with the September 7 image, covering an area of the Taymyr ice massif which was mapped in detail by helicopter surveys on September 10. A subset of the September 4 image is shown in Figure 6.10a, indicating the area mapped by helicopter as well as points of *in situ* ice observations from I/B Yamal. Note that I/B Yamal was sailing through the area on September 4 marked by the dashed line in the ice chart (Figure 6.10b) which was produced six days later from helicopter surveys. The ice map was produced using standard Russian ice symbols (see Appendix 5.A), indicating ice concentration (in tenths) of the two main ice types, including floe size, thickness/development stage and roughness index. The ice map covers a band of the Taymyr ice massif which extended towards the coast at 114° E and south of 76° 30′ N. This ice band, with concentration of 9-10 tenths, moved eastwards 20-30 km over the 6 day period by comparing its location in the SAR of September 4 and the ice map of September 10. The *in situ* observations from I/B Yamal from September 3, 4 and 5 were used to validate the ice concentration analysis described in Section 6.6.

6.5 Example of comparison of RADARSAT and ERS data

Near simultaneous coverage of the same ice area with both RADARSAT and ERS-2 SAR was only obtained on August 14, when the western Vilkitsky Strait and Shokalsky Strait was mapped by ERS-2 at 1354 GMT and by RADARSAT at 0933 GMT. A subset of the RADARSAT image was extracted covering the same area as the ERS-2 image (Figure 6.11). Both images covers incidence angles from 20° to 26° and have been prepared using the ‘ice’ Look-Up Table discussed in Section 6.2. The Look-Up Tables are range-normalizing functions designed to give homogeneous backscatter in range direction for an homogeneous ice surface. For RADARSAT the radiometric resolution is constant at about -0.37 dB per pixel. For ERS-2 it is varying from about -0.2 dB per pixel at pixel value of 40 to about -0.1 dB per pixel at pixel value of 80. The pixel spacing of the two

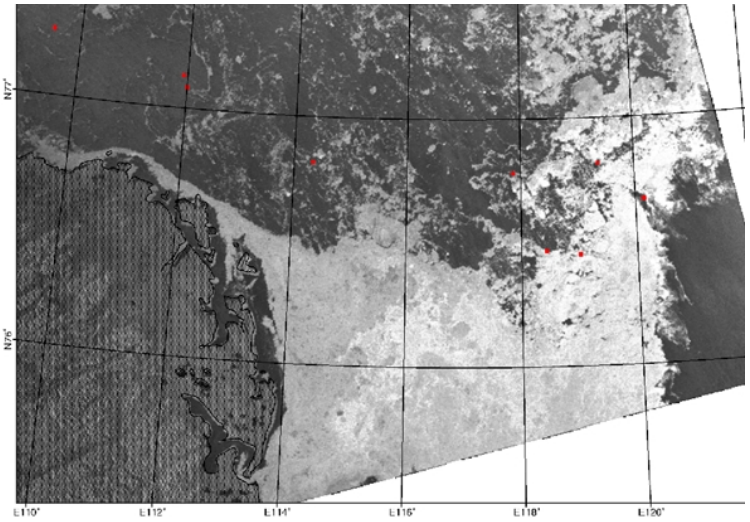

(a)

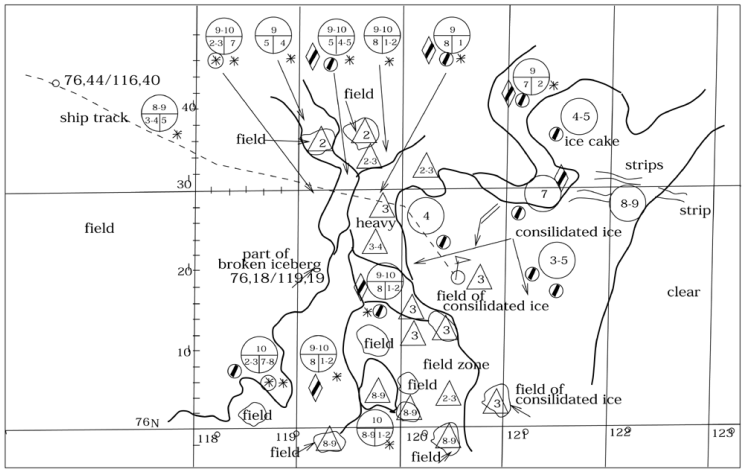

(b)

Figure 6.10: *a. Subset of RADARSAT ScanSAR image on September 4, showing the area east of Vilkitsky Strait where the Taymyr ice massif reaches the mainland coast. The dots mark positions where ice observations were obtained by I/B Yamal at the same time as the SAR image. The box shows the location of the ice chart in b., which was provided by I/B Yamal on September 4, based on helicopter surveillance. The ice chart uses Russian ice symbols, shown in Appendix 5.A. ©Canadian Space Agency, 1997.*

URN:NBN:no-2344

images shown in Figure 6.11 was 100 m for ERS-2 and 500 m for RADARSAT. In the subsequent analysis the ERS-2 pixels were averaged to 500 m to allow pixel-by-pixel comparison.

A general characterization of the ice conditions in this area was briefly described in Section 6.3, but due to lack of any *in situ* observations a clear definition of the ice types cannot be given. Since the RADARSAT image is not absolutely calibrated, two methods for comparison of the ERS-2 and RADARSAT images were chosen: 1) Six areas each with relatively homogeneous backscatter levels were selected by zigzag lines for pixel-by-pixel comparison (Figure 6.12), and 2) other smaller areas where the two data sets gives obvious different backscatter are described qualitatively.

The open water area (W1) is clearly identified as relatively bright area on the left side in both images. The wind was westerly 5-10 m/s which is sufficient to give open water higher backscatter than most ice types in ERS-2 images, as discussed by Sandven et al. (1999b). Also RADARSAT gives higher backscatter for this open water area compared to other parts of the image. In the northern part of the Vilkitsky Strait (W2) the ERS-2 image suggests open water with lower backscatter than in W1, possibly due to presence of new ice. Air temperature was constantly between 0° and -2°C in this period according to the ECMWF data and water temperature was assumed to be at freezing point. This is due to the observation that the surface water in this area was transported southwards along the western side of Severnaya Zemlya where ice cover will keep the surface temperature at the freezing point. The RADARSAT image shows a signature which is more similar to ice covered areas such as the southern part of the Vilkitsky Strait (I2) or the Shokalsky Strait (I4). The ice which drifts into the southern part of the Vilkitsky Strait (I2) and (I3) is assumed to consist mainly of ice which has survived the summer in the Nordenskjold Archipelago. As this ice breaks up in late summer it drifts eastwards with the currents. RADARSAT seems to be able to discriminate between I2 and I3, while ERS-2 shows similar backscatter for the two areas. RADARSAT also appears to discriminate between the ice in the southern Vilkitsky Strait (I2 and I3) and in the Shokalsky Strait (I4) while ERS-2 does not. The ice drifting southwards from the west coast of October Revolution Island (I1) has darker signatures than the other ice areas in the ERS-2 image, while RADARSAT shows similar backscatter between I1 and I2. All four ice areas (I1-I4) are assumed to be fast ice from the previous winter which is in the stage of breaking up and drift away mainly through the Vilkitsky Strait.

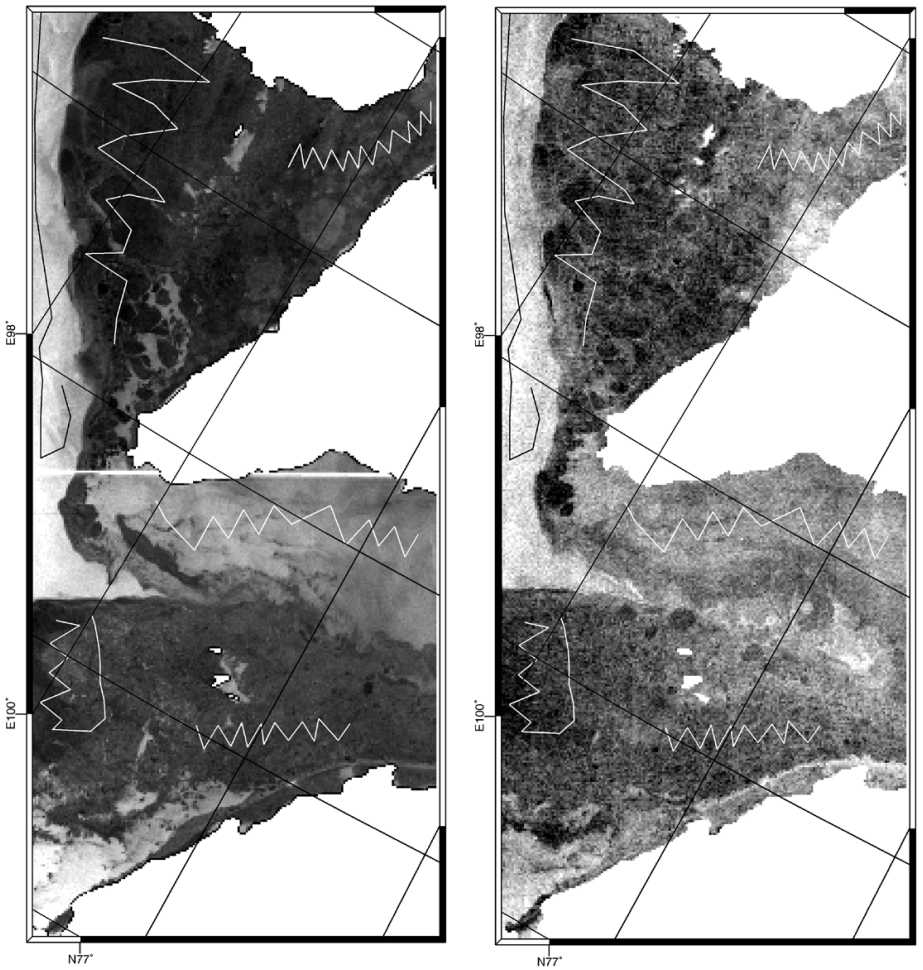

(a) (b)

Figure 6.11: *Near simultaneous SAR coverage by ERS-2 (a) and RADARSAT (b) of western Vilkitsky Strait and Shokalsky Strait on August 14 1997. The images were obtained at 0933 GMT and 1354 GMT for RADARSAT and ERS-2, respectively. The images are put into a common geographical coordinate system with a land mask superimposed. The zigzag lines represent profiles of pixels which were compared between the two images and presented in Figure 6.12.* ©*ESA/TSS and Canadian Space Agency, 1997.*

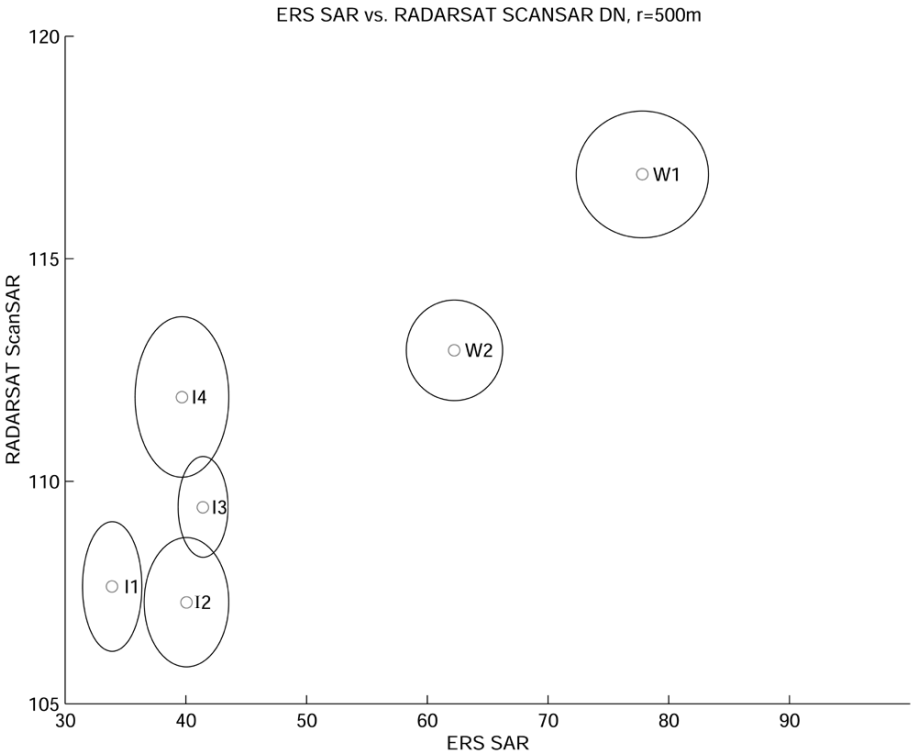

Figure 6.12: *Pixel-by-pixel comparison of ERS and RADARSAT images based on digital values of the profiles indicated in the images in Figure 6.11. W1 is the open water profile along the left side of the images; W2 is in the northern part of the Vilkitsky Strait; I1 and I4 is in the outer and inner part of Shokalsky Strait, respectively, while I2 and I3 are in the center and western part of the southern Vilkitsky Strait.*

URN:NBN:no-2344

Some specific small features, which are not included in the quantitative comparison in Figure 6.12, show pronounced difference between the two SAR systems: The lee side of the small islands in the Shokalsky Strait (78° 40′ N 98-99° E) show bright signature in the ERS-2 image due to open water in a wind-generated polynya while the signature in the RADARSAT image is dark. In the Vilkitsky Strait, a similar open polynya near the small islands at 77° 40′ N, 101-102° E is evident in the ERS-2 image but has no distinct signature in the RADARSAT image. The RADARSAT image shows brighter areas in Shokalsky Strait (78° 30′ N, 100° E) and in Vilkitsky Strait (77° 50′ N, 103° E) which are not evident in the ERS-2 images. There is no available *in situ* observations which can confirm these differences between RADARSAT and ERS-2 signatures.

The higher variability of RADARSAT backscatter compared to ERS-2 for I2, I3 and I4 can be caused by the different amount of water that is included in the ice pixels for the three areas. While homogeneous summer ice should have near-constant values around a given point in the diagram, water has a different response in the two sensors, both as function of wind speed at a given range, and of different distances in range-direction. As open water in case W1 has higher backscatter than ice, it can be concluded that I4 contains more open water and I2 has less open water within the pixels.

6.6 Ice concentration analysis

Ice concentration is one of the key quantitative parameters, important for ice navigation, which can be derived from RADARSAT ScanSAR images at a significant higher resolution than SSM/I ice concentration maps. Several investigators have suggested methods for retrieving ice concentration from SAR images (i.e. Dokken et al., 2000), but there is not yet established standard algorithms which are widely used. Especially during summer conditions when the ice surface is wet from melting and can be difficult to distinguish from open water, it is a challenge to develop reliable algorithms for retrieving ice concentration from SAR data.

A method to estimate total ice concentration in the ScanSAR image of September 7 have been tested using input from SSM/I observations of the same day. The first assumption of the method is that a threshold value separating ice from open water in leads in the ice-cover can be found in a SAR image without absolute calibration. However, range-correction must be in place to secure that the water-ice discrimination is possible across

the whole image using the same threshold value. It is well known that with increasing wind speed the SAR backscatter of open water rapidly attains higher values than for ice. The next assumption is that within the ice-cover water pixels will have a lower backscatter value than ice pixels, at least for the images analyzed in this study. However, sufficient high winds can occur in leads to generate higher backscatter than for the ice types. In such cases the method also need to use an upper threshold to discriminate high backscatter open leads from ice with lower backscatter. Close to the ice edge and within leads and polynyas the assumption that a lower and upper threshold can discriminate water from ice can also fail. Such areas can nevertheless easily be identified in the SAR image and then masked out.

The pixel spacing of the original ScanSAR image was first reduced from 50 m to 500 m in order to reduce the speckle noise. After all land areas had been removed from the image, open water regions were determined and masked out using ice concentrations estimated from SSM/I, obtained by the updated NORSEX algorithm (Svendsen et al., 1983). A threshold of 20 % ice cover was used for this operation. By analyzing the histogram of the remaining SAR pixels two distinct peaks were found, assuming to correspond to ice and water areas, respectively, within the ice-cover. The pixel value at the local minimum between the two peaks was chosen as the threshold value for separating the two surface types. In the next step all pixels with value above the threshold was set to 100 and all other pixels to 0, i.e. 100 % or 0 % ice concentration. Using SAR data ice concentration could be estimated over a certain unit area, defined by n by n pixels. The ice concentration was thus estimated at a resolution of 6.5 km, simply by computing the average mean over 13 by 13 pixels. The results of the analysis of the SAR image of September 7 is shown in Figure 6.13a, while the SSM/I concentration for the same day is shown in Figure 6.13b. These figures show that ice concentration can be mapped in detail with SAR data, while the SSM/I data will smear out all details less than 10-20 km.

One aspect of a simple thresholding procedure is the fact that newer ice types such as grease ice, nilas and grey ice also have relatively low backscatter signatures (Sandven et al., 1999b), similar to calm open water. This means that in several cases these ice types will be classified as open water, and as a result the ice concentration will be estimated only on the basis of first year ice and other ice types with backscatter signatures above the threshold value (including ridged young ice). For many practical purposes, including navigation and estimation of heat flux, this is not a severe drawback. Nevertheless, quan-

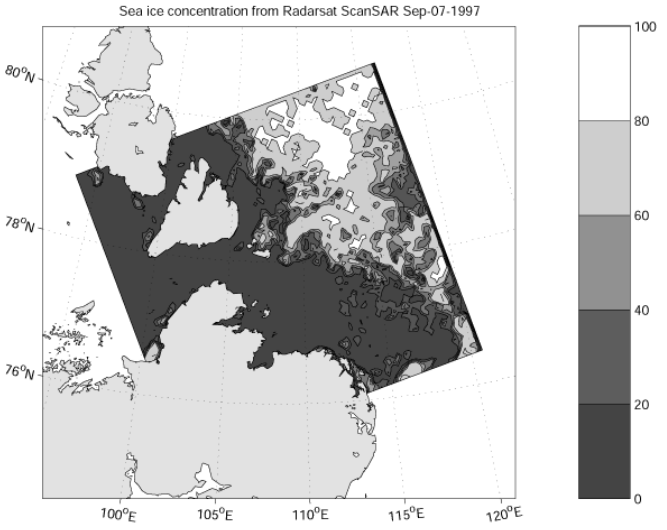

(a)

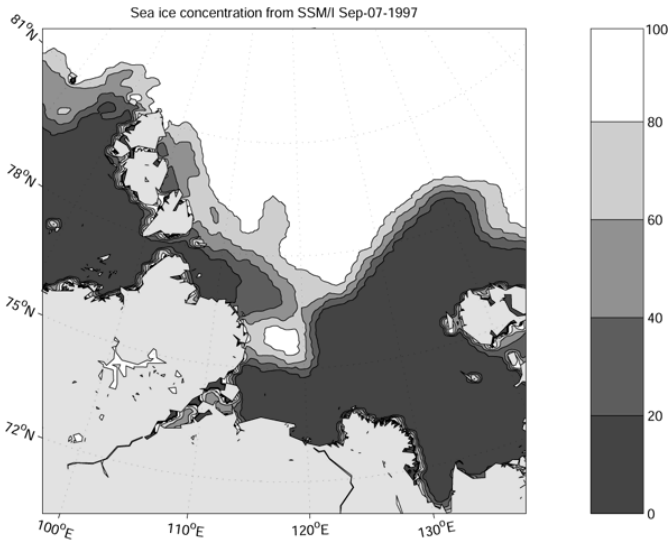

(b)

Figure 6.13: *a. Ice concentration analysis of the ScanSAR image of September 4, presented with a spatial resolution of about 6 km. b. Ice concentration estimated from SSM/I data on the same day using the NORSEX algorithm (Svendsen et al., 1983) with the 85 GHz channel.*

URN:NBN:no-2344

titative analysis should be carried out in order to assess the performance of various SAR ice concentration methods.

The performance of the SAR ice concentration algorithm was analyzed by comparing the resulting ice concentration map with a SSM/I derived ice concentration map. A linear regression analysis performed on a profile extracted from the two data sets, containing altogether 328 pixels, showed a correlation of 0.76 and a RMS of 12.4. The profiles are shown in Figure 6.14a. It can be seen that although the two data sets agree fairly well on an overall basis the RADARSAT algorithm tends to overestimate the ice concentration compared to SSM/I data. Taking into account the difference between SAR and SSM/I data, both radiometrically and in spatial resolution, it is not surprising that the two data sets give somewhat different results.

Another validation exercise was performed by comparing the SSM/I ice concentration with *in situ* observations from I/B Yamal shown in the Figure 6.10a. A profile of SSM/I and *in situ* observations of ice concentration is shown in Figure 6.14b, indicating that the SSM/I data agrees well with *in situ* observations for this particular case. Discrepancies between the two data types, as seen by the single *in situ* point which is far from the SSM/I estimate in Figure 6.14b, can be ascribed to the difference in resolution in the two observation methods. The coarse resolution in SSM/I data does not necessarily reflect smaller scale and local features which are captured by *in situ* observations. Another element is the standard of *in situ* observations taken on routinely basis onboard icebreakers, which is not necessarily of scientific quality.

6.7 Discussion and conclusions

The analysis of a sequence of ERS-2 and RADARSAT SAR images during late summer conditions shows that the ice motion in the Laptev Sea area is mainly directed in a south-southeasterly direction and that the ice drifts eastwards through the Vilkitsky Strait (Figure 6.15). A few images from the area around the New Siberian Island suggest easterly drift north of 76° N while it turns westerly between 76° N and the mainland. Westerly ice drift was also observed in Sannikov Strait, transporting ice from East Siberian Sea into the Laptev Sea. The prevailing winds were westerly, but wind speeds were low typical less than 10 m/s over the whole period. The SAR imagery showed unique capability to map ice drift in straits and near coasts where other methods provide very little

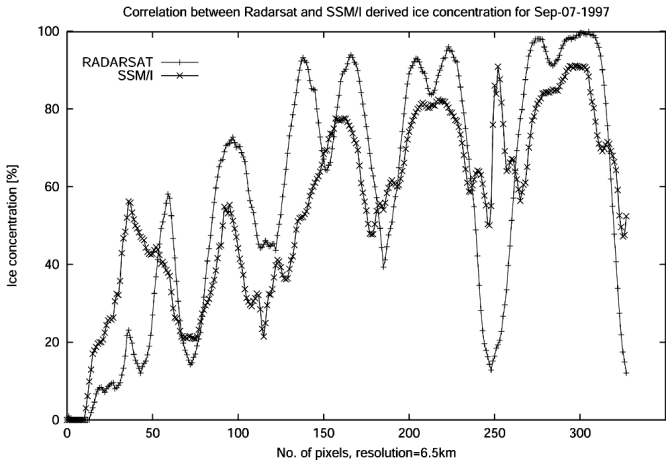

(a)

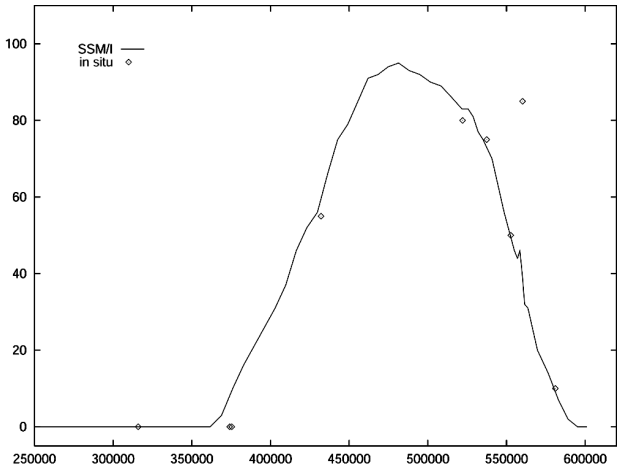

(b)

Figure 6.14: *a. Coinciding profiles of ice concentration obtained from ScanSAR data and SSM/I data shown in Figure 6.13. The profile, which is about 300 km long, is a combination of several shorter profiles cutting across the ice edge and penetrating into the compact ice massif several places in the image. b. Profile of SSM/I ice concentration from a profile taken along the points of in situ observations shown in Figure 6.10a. The ice concentration from the in situ observations are indicated by the dots. Units along x-axis is meter in west-east direction and y-axis is concentration in %.*

information.

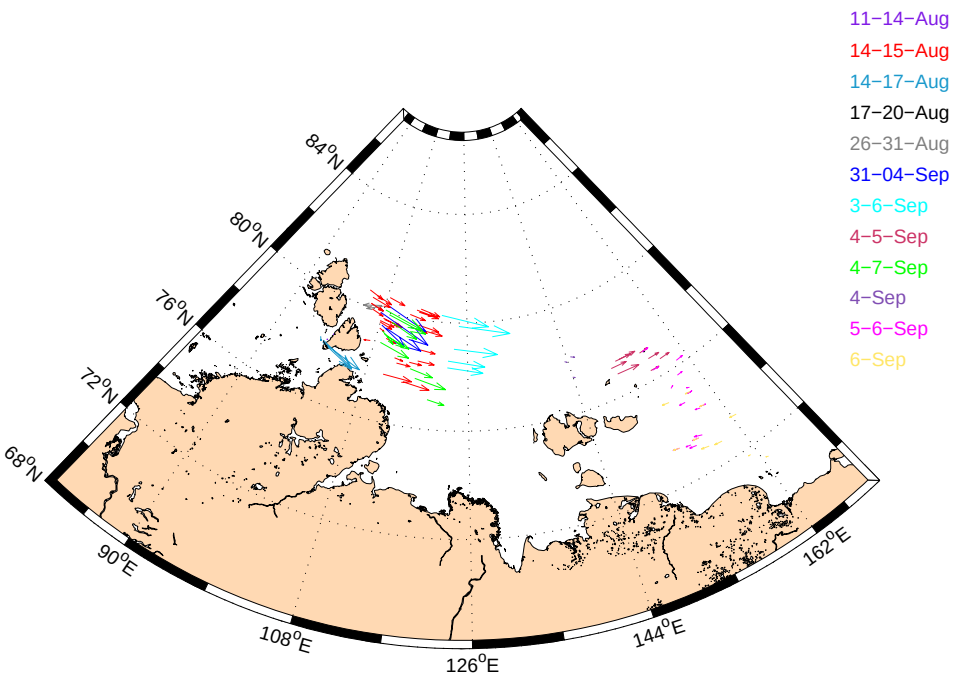

Figure 6.15: *Composite of all ice drift estimates from successive SAR images analyzed for the period from August 11 to September 7, 1997.*

In addition to describing dynamic features of the ice cover, it was attempted to compare RADARSAT and ERS signatures of the same areas, and analyze SAR backscatter to classify ice-water areas and derive ice concentration. The *in situ* observations obtained from the nuclear icebreakers I/B Sovetsky Soyuz and I/B Yamal have been used to validate ice types and ice phenomena observed in the SAR images. First-year ice which has survived the summer melt season, and therefore in the stage of transiting to second-year ice, has been well identified in the SAR images, except when concentration goes below 10 %. New ice types such as grease ice, nilas and young ice have been difficult to separate from open water in cases when the wind is low (< 5 m/s).

More systematic backscatter analysis of all SAR images have not been done due to lack of calibrated SAR images. By using SSM/I data to remove high backscatter areas in open water, it has been possible to determine a threshold value between ice and open water signatures within the ice pack which have been the basis for estimating ice con-

centration in a ScanSAR image. By use of SSM/I data within the ice pack, the SAR ice concentration estimates could be validated. *In situ* ice concentration observations from icebreakers were used to validate the SSM/I ice concentration due to lack of coincident *in situ* and SAR data. The most critical step in ice concentration estimation is to distinguish open water from various ice types in a robust manner. Further development of SAR ice concentration methods are needed taking into account that open water can attain a wide range of backscatter depending on the wind speed. Ice concentration from SAR images can improve the resolution significantly, which is useful in many applications, from ice navigation to calculation of heat flux through leads.

The study have showed that RADARSAT ScanSAR data can be successfully used to observe summer ice conditions in the Northern Sea Route where accurate ice data are essential for safe and cost-effective navigation. The expedition with I/B Sovetsky Soyuz to the Laptev Sea in September 1997 was the first opportunity to test use of RADARSAT ScanSAR images in this region and demonstrate applicability in summer ice navigation. SAR images for the Vilkitsky Strait area, including both RADARSAT and ERS-2, were ordered for delivery in near real-time from Tromsø Satellite Station, and were transmitted in digital form to I/B Sovetsky Soyuz during her voyage to the Laptev Sea. Since the INMARSAT system does not cover the Laptev Sea area, images were transmitted to the icebreaker while sailing in the Kara Sea. When the icebreaker arrived in the ice region the SAR images has already been analyzed onboard and the sailing route planned. The conclusion of this first exercise with RADARSAT images to support ice navigation in the Vilkitsky Strait and western Laptev Sea was that SAR data is a very useful supplement to traditional ice maps. In this region where ship traffic depends heavily on good quality ice data, the ice conditions are not very well known and SAR data can contribute significantly to better ice information.

Acknowledgments

RADARSAT ScanSAR data have been provided via ADRO-Project N259 and NASA/-ASF. The ERS-2 SAR data have been provided by ESA through the ICEWATCH Project. Support to data purchase and analysis has also been given by the IMSI project funded by EU (contract no. ENV4-CT96-0361). Murmansk Shipping Company's Icebreaker Fleet, and in particular the crews onboard I/B Sovetsky Soyuz and I/B Yamal are acknowledged

for excellent support during field observations and demonstration of SAR data transmission.

Appendix 5.A Russian ice charting symbols

Symbols	Ice parameters	
	Pack ice concentration, total (tenths) Ice concentration, partial (tenths)	
	Development (age)	**Thickness**
	Grey–white ice (GrW)	15 –30 cm
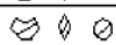	Thin first–year ice (WTh)	30 –70 cm
	Medium first–year ice (WMd)	70 –120 cm
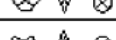	Thick first–year ice (WTk)	> 120 cm
	Combination (WMd/WTk)	
	Floe size	**Horizontal sizes**
	Vast floe	2 – 10 km
	Big floe	0.5 – 2 km
	Medium floe	100 –500 m
	Small floe	20 – 100 m
	Small ice cake/brash ice	< 2 m
	Ice age features	**Ice concentration**
	Combination (WMd/WTk, GrW)	9–10 [6 | 3–4]
	Combination (WMd/WTk, GrW)	8–9 [4–5 | 3–4]
	Combination (WTk, WMd, GrW)	7–8 [1–2 | 3 | 3]
	Combination (WMd/WTk, GrW)	7–8
	Combination (WMd/WTk)	4–5
	Combination (WMd/WTk)	1–3
	Ice free	0
	Forms of fast ice	**Thickness**
	Medium	70 – 120 cm
	Thick	> 120 cm
	Thick, brackish water ice	> 120 cm
	Grounded hummock	
	Miscellaneous features	
	Melting stage (0–5)	
	Ridge	

Chapter 7

Summary and conclusion

Sample areas from calibrated ERS-1/2 SAR PRI scenes from the Pechora and Kara Seas have been extracted. Mean and standard deviation values of the backscattering coefficients have been calculated. The samples were manually classified into seven categories, and day of the year, angle of incidence, latitude and longitude were assigned to the samples. Temperature and wind parameters have also been added to each SAR sample.

There was considerable overlap between the different sea ice categories and open water, when only mean and standard deviation values of the backscattering coefficient were considered. From mean values only, it may be possible to separate smooth first year ice and multi year ice. Under summer conditions this result would not be valid. Open water and multi year ice may be separated using standard deviation values only. As only a small part of the ice cover in the Pechora and Kara Seas is multi year ice, more parameters than mean and standard deviation have to be investigated to get a better separation of the different ice types and open water.

The separation of ice and water by constructing multivariate regression models produced rather promising results. Separation of open water from all ice types, open water from young ice and rough first year ice, and separation of young ice from rough first year ice were done in four calculations. First, in the separation of all ice types from water correlation coefficients up to 0.90 between predicted and actual data values were achieved. Second, young ice and rough first year ice were separated from the water samples. The correlation coefficients between predicted and actual values for open water and young ice and for open water and rough first year ice were as high as 0.93. When trying to

separate between the two ice types, correlation coefficients of about 0.60 were obtained. Mean and standard deviation values of the backscattering coefficient, temperature and possibly angle of incidence are the variables that are most useful for further studies using regression models.

Limitations of this study are that the SAR observations are only collected from a small region in the Arctic, and some of our manual sea ice interpretations may be doubtful. In addition, errors in the ECMWF data set were not assessed, and these data is not as optimal as *in situ* measurements of temperature and wind.

Coastal polynyas are found along the Siberian shelf during the ice season from November to May. The presence of open water and thin ice in these polynyas is important for heat transfer and for navigation in the winter season. Polynya areas from selected regions in the Pechora and Kara Seas are investigated with SAR and SSM/I data during the 1990s. A total of 94 ERS-1/2 SAR scenes from 1994 and 1996 and 71 RADARSAT ScanSAR Wide scenes from 1997 and 1998 have been acquired and analyzed. Daily ice concentration field from SSM/I data were extracted for January through March from 1990 to 1999. Daily averages of air temperature and wind information from the global NCEP reanalyzes dataset were also used. This study is limited to winter months in the 1990s, with the main focus on March when the maximum ice distribution in the Northern Hemisphere occurs. Polynya widths were quantified in detail using SAR data covering smaller areas. Ice concentration data from SSM/I, wind and air temperature were used in the description of polynya variability. Then the observed polynya widths from SAR were compared to polynya widths calculated by a one-dimensional polynya model for nine different areas.

The good spatial resolution of the SAR gave valuable information about the selected polynya areas. The largest polynyas were found along the Taymyr Peninsula with mean with of about 40 km. Along the western coast of Yamal Peninsula and the area around the outlets of the Yenisey and Ob Rivers typical polynya widths were in the range of 20 to 30 km, with variability of tens of kilometers. High values of the mean polynya widths were also accompanies by high standard deviation values. Large polynyas were measured in the Vaygach area (about 25 km) and around Franz Josef Land (about 23 km). The SAR backscattering signatures of freezing sea ice was investigated for four days in 1996. The backscattering of ice types in polynyas can have very large variability due to the variability in σ^o for young ice as well as open water, affecting the possibilities

URN:NBN:no-2344

for automatic classification of polynyas in SAR images. Among the limitations of this study was that the SAR observations were sparse in time. The day to day development during freezing or fast changes in wind direction are not possible to completely capture with sampling intervals of more than one or two days. The investigated areas are limited regions of the Arctic, and to draw conclusions for the whole Arctic may be doubtful. If the polynya was only partly covered by the SAR image, a too small or large width could be measured due to variable polynya width along the coast.

The polynya area north of Vaygach and along the southern part of Novaya Zemlya was selected for polynya index estimation, based on SSM/I data for March 1990 to 1999. The investigated polynya area was oriented towards north-east. The prevailing wind regime determined the number of polynya days. With prevailing south-westerly winds, polynyas occurred frequently such as in 1995 and 1996. Then a polynya occurred 55 and 56 out of 90 days. When the prevailing winds were in the opposite direction, polynyas occurred less frequently (i.e. 1991, 1994, 1998, 1999). Polynyas occurred only 7 and 8 days in 1999 and 1991, respectively. The polynya area was measured by the polynya index, which indicates both size and duration of each polynya event. Favourable ice navigation conditions in the area is directly related to the frequency of polynyas. The largest and longest lasting areas covered by polynyas occurred in 1995, and in 1991 only small polynyas with short duration occurred.

Polynya area appeared to be independent of wind speed, while it was closely correlated with wind direction. As expected polynyas were formed by a wind component in offshore direction, which means a wind direction between 150° and 300°. Polynya event were also closely correlated with increasing air temperature from about -15° C. This can be explained by the close correlation between south-westerly wind directions and higher temperatures. Temperature is not the driving force for the creation of the polynyas, but refreezing of the polynyas depend on low air temperatures. Errors in the NCEP dataset were not assessed, and these data may not be as optimal as *in situ* data of air temperature and wind for a single polynya event due to resampling of sparse observations over large areas. However, single point *in situ* measurements may not be representative for a large area, due to local influence on temperature and wind conditions.

It was concluded from mean angle plots and multivariate regression that the AMT method gave best results when the original SAR backscattering coefficients were used as input. The tested scaling approach gave less useful results from the separation of water and

URN:NBN:no-2344

ice using multivariate regression. Better results were obtained when using the mean and standard deviation of the backscattering coefficient together with temperature data in the multivariate regression. These variables were used together with mean angles from the AMT algorithm. In the separation of ice and water the correlation coefficients were 0.83 and 0.85. For water and young ice the correlation coefficients were 0.93, and for water and first year ice they were 0.80 and 0.86. For the separation of the ice types young ice and first year ice the correlation was still very low, the values 0.30 and 0.40 were achieved. The AMT algorithm may give some relevant information for separation of water and ice samples. Information from mean and standard deviation of the backscattering coefficient could be an alternative to the results from the more computer-demanding AMT algorithm. The speckle property of SAR images may be the reason why this approach is not as useful for this data type as for other types of data. Kerman et al. (1999) suggested to obtain estimated statistics of Arctic sea ice thickness from SAR imagery by using differences between neighboring pixel values. The speckle property of the SAR data was then given as a possible reason why pixel differences may not be optimal.

The analysis of a sequence of ERS-2 and RADARSAT SAR images from late summer shows that the ice motion in the Laptev Sea area is mainly directed in a south-southeasterly direction and that the ice drifts eastwards through the Vilkitsky Strait. A few images from the area around the New Siberian Island suggest easterly drift north of 76° N while it turns westerly between 76° N and the mainland. Westerly ice drift was also observed in Sannikov Strait, transporting ice from East Siberian Sea into the Laptev Sea. Westerly winds prevailed, and wind speeds were low typical less than 10 m/s over the whole period. The SAR imagery showed unique capability to map ice drift in straits and near coasts.

In addition to describing dynamic features of the ice cover, it was attempted to compare RADARSAT and ERS signatures of the same areas, analyze SAR backscatter to classify ice-water areas and derive ice concentration. The *in situ* observations obtained from the nuclear icebreakers I/B Sovetsky Soyuz and I/B Yamal have been used to validate ice types and ice phenomena observed in the SAR images. First year ice which has survived the summer melt season, and therefore in the stage of transiting to second year ice, has been well identified in the SAR images, except when ice concentrations are below 10 %. New ice types such as grease ice, nilas and young ice have been difficult to separate from open water in cases when the wind is low (< 5 m/s).

URN:NBN:no-2344

A more systematic backscattering analysis of all SAR images has not been done due to lack of calibrated SAR images. By using SSM/I data to remove areas of high backscattering in open water, it has been possible to determine a threshold value between ice and open water signatures within the ice pack. This has been the basis for estimating ice concentration in a ScanSAR image. By use of SSM/I data within the ice pack, the SAR ice concentration estimates could be validated. *In situ* ice concentration observations from icebreakers were used to validate the SSM/I ice concentration data due to lack of coincident *in situ* and SAR data. The most critical step in ice concentration estimation is to distinguish open water from various ice types in a robust manner. Further development of SAR ice concentration methods are needed, taking into account that open water can attain a wide range of backscatter values depending on the wind speed. Ice concentration data from SAR images can improve the resolution significantly, which is useful in many applications, from ice navigation to calculation of heat flux through leads.

The study have showed that RADARSAT ScanSAR data can be successfully used to observe summer ice conditions in the Northern Sea Route where accurate ice data are essential for safe and cost-effective navigation. The expedition with I/B Sovetsky Soyuz to the Laptev Sea in September 1997 was the first opportunity to test use of RADARSAT ScanSAR images in this region and demonstrate applicability in summer ice navigation. SAR images for the Vilkitsky Strait area, including both RADARSAT and ERS-2, were ordered for delivery in near real-time from Tromsø Satellite Station, and were transmitted in digital form to I/B Sovetsky Soyuz during her voyage to the Laptev Sea. Since the INMARSAT system does not cover the Laptev Sea area, images were transmitted to the icebreaker while sailing in the Kara Sea. When the icebreaker arrived in the ice region the SAR images has already been analyzed onboard and the sailing route planned. The conclusion of this first exercise with RADARSAT images to support ice navigation in the Vilkitsky Strait and western Laptev Sea was that SAR data is a very useful supplement to traditional ice maps. The ice conditions are not very well known in this region and ship traffic depends heavily on good quality ice data.

7.1 Future work

An objective for remote sensing research and development has been to increase the number of sensors and thereby increase the data coverage for sea ice research purposes and

near real-time navigation aid. New satellite missions will improve data coverage in time and space by several different sensors. The ENVISAT satellite was launched in February 2002, carrying Advanced Synthetic Aperture Radar (ASAR). It features enhanced capability in terms of coverage and modes of operation. ASAR will be operated at C band with multiple polarizations and incidence angles. Also, RADARSAT-2 with multi-polarization SAR is expected to be launched in late 2003. Advanced Land Observing Satellite (ALOS) is scheduled for 2003 and designed to have a 3 years lifetime. It will carry a sensor called Phased Array type L-band Synthetic Aperture Radar (PALSAR), and it will be the Japanese National Space Development Agency's second spaceborne SAR using L-band (1.27 GHz). PALSAR will have a ScanSAR mode with both HH and VV polarization. This mode will produce 250-350 km (depends on number of scans) wide SAR images with 100 m resolution, and it is useful for sea ice monitoring. The data from L-band is well suited for ridge and fracture detection, and less precise than C-band data for detection of floe boundaries (Onstott, 1992). Discrimination of open water from new ice types may also be limited.

The Radar Altimeter 2 (RA-2) is an instrument carried by ENVISAT for determining the two-way delay of the radar echo from the Earth's surface to a very high precision. It also measures the power and the shape of the reflected radar pulses. The RA-2 is able to map and monitor sea ice, but is mainly designed for sea surface monitoring. The separation of echoes from ice and water offers a clear potential to directly measure sea ice freeboard and hence estimate ice thickness. Initial investigations using the ERS-1/2 radar altimeter show promising results (Sandven et al., 2001). Key to the success of ice freeboard retrieval is the estimation of the (unobserved) sea surface height beneath the ice floe. The largest variation in sea surface height, due to the marine geoid, is eliminated using repeat track analysis. Mean profiles are generated for each of the 501 orbits which make up a 35 day repeat cycle. Superimposed on the time-invariant component of sea surface height are small temporal variations caused by dynamic topography. These are estimated by constructing a smoothed sea surface height anomaly field estimated from specular returns gathered during a particular repeat cycle. This field is then used as a reference against which estimates of the ice surface elevation are compared to retrieve sea ice freeboard.

Cryostat is a radar altimetry three-year mission scheduled for launch in 2004. It is dedicated to the observation of the polar regions and designed to determine variations in the

URN:NBN:no-2344

thickness of the Earth's continental ice sheets and marine ice cover with better resolution than previous radar altimeters (Sandven et al., 2001). Its primary objective is to test the prediction of thinning of Arctic ice due to global warming. CryoSat is the first satellite of the ESA Living Planet Programme. The methods that was tested with ERS-1/2 for measuring of sea ice freeboard and hence estimate ice thickness will produce higher resolution ice cover thickness. This can be used in combination with ice extent data from other sensors (i.e. ASAR, RADARSAT-2 SAR or SSM/I) or combined with results from a coupled ice-ocean model to produce sea ice volume estimates on regional hemispheric scale that are important for detection of Arctic climate change (Johannessen et al., 2002; Sandven et al., 2001).

The use of data collected from multispectral, dual-polarization, active and passive instruments increases the level of information that can be exploited in the data (Kerman, 1999). Nghiem and Bertoia (2001) have the evaluated the use of future ASAR data for Arctic sea ice mapping by studying multiple polarization C-band SAR signatures of various sea ice types. They found that for light wind conditions near an ice edge, horizontal backscatter is better to distinguish between first year ice and open ocean surface at large incidence angles. For high winds, vertical backscatter is more useful to separate most sea ice types (except multi year ice at large incidence angles) from open water over a large range of incidence angles. Through the use of multivariate statistical methods, not only is the data dimensionality minimized, but the effects of noise and imaging artifacts are reduced (Remund et al., 2000). The use of different sensors improve the ability to identify sea ice types by combining the benefits of each instrument. Combining data from sensors by data fusion techniques may give valuable information about various physical processes and sea ice types (Beaven et al., 1996; Pohl and van Genderen, 1998). The multivariate statistical methods tested for classification of sea ice types could also be extended by neural network methods (Alhumaidi et al., 1997; Bishop, 1995; Ripley, 1996).

The presence of open water and thin ice in these polynyas is important for heat transfer and for navigation in the winter season (Andreas and Cash, 1999; Eisen and Kottmeier, 2000; Johannessen et al., 2000). To extend the observation set of polynya areas with data from the ASAR sensor could be a possibility to get a more systematic data sampling over several months in a selected small study area like the south-western Kara Sea near Vaygach Island. The Wide Swath Mode will provide nearly daily coverage due to 400 km swath width. This is a key area for sea ice transport of radionuclides and sediments

(Dethleff et al., 2000; Sherwood, 1999). Data about the polynya ice edge relative to coastlines of different orientations and shapes may give valuable information for validation of a two-dimensional model where the affect of the coastline on polynya size and development are accounted for (Darby et al., 1995).

Appendix A

Multivariate statistical methods

A.1 Introduction

This chapter is mainly based on Johnson and Wichern (1992), Helland (1990), Mandel (1982), Höskuldsson (1998), Lang and Kalivas (1993), Golub and Van Loan (1996) and Martens and Næs (1989).

A.2 Descriptive statistics

A.2.1 Basic definitions

The measurement, x_{ij}, of the *i*th variable of the *j*th item for *n* measurements on *p* variables can be displayed as a rectangular array, $\mathbf{X}$ of *p* rows and *n* columns. Let $x_{11}, x_{12}, \ldots, x_{1n}$ be *n* measurements of the first variable. The average of these measurements, $\bar{x}_1$, is the sample mean for the first variable and is given by

$$\bar{x}_1 = \frac{1}{n}\sum_{j=1}^{n} x_{1j}$$

and in general for *p* sample means

$$\bar{x}_i = \frac{1}{n}\sum_{j=1}^{n} x_{ij} \qquad i = 1, 2, \ldots, p$$

The sample variance is a measure of spread, defined for *n* measurements on the first variable

$$s_1^2 = \frac{1}{n}\sum_{j=1}^{n}(x_{1j} - \bar{x}_1)^2$$

and in general for *p* variables

$$s_i^2 = \frac{1}{n}\sum_{j=1}^{n}(x_{ij} - \bar{x}_i)^2 \qquad i = 1, 2, \ldots, p$$

Although the s^2 is used for sample variance, it is convenient to use double subscripts, $s_{ii} = s^2$. The square root of the sample variance, $\sqrt{s_{ii}}$, is the sample standard deviation.

The sample covariance measures the association between the *i*th and *k*th variables. The covariance reduces to the sample variance when $k = i$. Also, $s_{ik} = s_{ki}$ for all *i* and *k*.

$$s_{ik} = \frac{1}{n}\sum_{j=1}^{n}(x_{ij} - \bar{x}_i)(x_{kj} - \bar{x}_k) \qquad i = 1, 2, \ldots, p, \quad k = 1, 2, \ldots, p$$

The sample correlation coefficient is also named the Pearson's product moment correlation coefficient. It is a measure of the linear association between two variables, and does not depend on the units of measurements. It is defined for the *i*th and *k*th variables as

$$r_{ik} = \frac{s_{ik}}{\sqrt{s_{ii}}\sqrt{s_{kk}}} = \frac{\sum_{j=1}^{n}(x_{ij} - \bar{x}_i)(x_{kj} - \bar{x}_k)}{\sqrt{\sum_{j=1}^{n}(x_{ij} - \bar{x}_i)}\sqrt{\sum_{j=1}^{n}(x_{kj} - \bar{x}_k)}}$$
$$i = 1, 2, \ldots, p, \quad k = 1, 2, \ldots, p$$

Also, $r_{ik} = r_{ki}$ for all *i* and *k*. The sample correlation coefficient is a standardized version of the sample covariance, and the product of the square roots of the sample variances provides the standardization. r_{ik} has the same value whether *n* or *n-1* is chosen as the common divisor for s_{ii}, s_{kk} and s_{ik}.

Covariance and correlation provide measures of linear association. Their values are less informative for other kind of association. These measures can be very sensitive to error observations or 'outliers', and may indicate association when little exists. The descriptive statistics can also be organized in arrays and matrices.

Sample mean $\qquad \overline{\mathbf{x}} = \begin{bmatrix} \overline{x}_1 \\ \overline{x}_2 \\ \vdots \\ \overline{x}_p \end{bmatrix}$

Sample variance and covariance $\mathbf{S}_n = \begin{bmatrix} s_{11} & s_{12} & \cdots & s_{1p} \\ s_{21} & s_{22} & \cdots & s_{2p} \\ \vdots & \vdots & \ddots & \vdots \\ s_{p1} & s_{p2} & \cdots & s_{pp} \end{bmatrix}$

Sample correlations $\mathbf{R} = \begin{bmatrix} 1 & r_{12} & \cdots & r_{1p} \\ r_{21} & 1 & \cdots & r_{2p} \\ \vdots & \vdots & \ddots & \vdots \\ r_{p1} & r_{p2} & \cdots & 1 \end{bmatrix}$

A.2.2 Vector and matrix algebra

Let $\mathbf{x}_1, \mathbf{x}_2, \ldots, \mathbf{x}_k$ be n vectors. If the crossproduct $\mathbf{x}_i\mathbf{x}_j = 0$ for all i,j, and $i \neq j$, then $\mathbf{x}_1, \mathbf{x}_2, \ldots, \mathbf{x}_k$ is orthogonal. If the length of the vectors are one, they are also orthonormal.

The transposed of a vector is denoted $\mathbf{x}'$ and the transposed of a matrix is denoted $\mathbf{X}'$. A square matrix is symmetric if $\mathbf{A} = \mathbf{A}'$ or $a_{ij} = a_{ji}$ for all *i* and *j*. If there exist a matrix $\mathbf{B}$ such that

$$\mathbf{B}_{(k\times k)} \quad \mathbf{A}_{(k\times k)} = \mathbf{A}_{(k\times k)} \quad \mathbf{B}_{(k\times k)} = \mathbf{I}_{(k\times k)}$$

then $\mathbf{B}$ is called the inverse of $\mathbf{A}$ and is denoted $\mathbf{A}^{-1}$. Another special class of square matrices are the orthogonal matrices, characterized by

$$\mathbf{Q}\mathbf{Q}' = \mathbf{Q}'\mathbf{Q} = \mathbf{I} \quad or \quad \mathbf{Q}' = \mathbf{Q}^{-1}$$

A square matrix $\mathbf{A}$ has an eigenvalue λ, with corresponding eigenvector $\mathbf{x} \neq 0$ if

$$\mathbf{A}\mathbf{x} = \lambda\mathbf{x}$$

Usually, $\mathbf{x}$ is normalized to length one so that $1 = \mathbf{x}'\mathbf{x}$.

Let $\mathbf{A}$ be a $k \times k$ square matrix and $\mathbf{I}$ be the $k \times k$ identity matrix. Then the scalars $\lambda_1, \lambda_2, \ldots, \lambda_k$ that satisfy the polynomial equation $|\mathbf{A} - \lambda\mathbf{I}| = 0$ are called the eigenvalues (or characteristic roots) of the matrix $\mathbf{A}$. The equation $|\mathbf{A} - \lambda\mathbf{I}| = 0$ (as a function of λ) is called the characteristic equation.

Let $\mathbf{A}$ be a $k \times k$ square matrix and let λ be an eigenvalue of $\mathbf{A}$. If $\mathbf{x}_{(k\times 1)}$ is a nonzero vector $(\mathbf{x}_{(k\times 1)} \neq \mathbf{0}_{(k\times 1)})$ such that $\mathbf{A}\mathbf{x} = \lambda\mathbf{x}$ then $\mathbf{x}$ is an eigenvector (characteristic vector) of the matrix $\mathbf{A}$ associated with the eigenvalue λ.

A.2.3 Symmetric matrices

When a $(k \times k)$ symmetric matrix $\mathbf{A}$ is such that

$$0 \leq \mathbf{x}'\mathbf{A}\mathbf{x}$$

for all $\mathbf{x}' = [x_1, x_2, \ldots, x_k]$, $\mathbf{A}$ is nonnegative definite. If the equality holds only for the vector $\mathbf{x}' = [0, 0, \ldots, 0]$ then $\mathbf{A}$ is positive definite. $\mathbf{A}$ is positive definite if

$$0 < \mathbf{x}'\mathbf{A}\mathbf{x}$$

for all vectors $\mathbf{x} \neq 0$. Because $\mathbf{x}'\mathbf{A}\mathbf{x}$ has only squared terms, x_i^2, and product terms, $x_i x_k$, it is called quadratic form.

To state the usefulness of symmetric matrices let $\mathbf{A}$ be a symmetric $n \times n$ matrix. Then the following properties are equivalent.

- $\mathbf{A}$ is positive definite.
- All the eigenvalues of $\mathbf{A}$ is positive.
- There exist a nonsingular $\mathbf{V}$ so that $\mathbf{V}\mathbf{A}\mathbf{V}' = \mathbf{I}$.
- There exist a nonsingular $\mathbf{M}$ so that $\mathbf{M}\mathbf{M}' = \mathbf{A}$.
- $\mathbf{A}^{-1}$ exist and is positive definite.

A.3 Multivariate linear regression

A.3.1 Classical linear regression model

Regression analysis is the statistical methodology for predicting values of one or more response (dependent) variables from predictor (independent) variable values. The classical linear regression model with a single response can be formulated as

$$\mathbf{Y}_{(n\times 1)} = \mathbf{Z}_{(n\times(r+1))} \quad \beta_{((r+1)\times 1)} + \varepsilon_{(n\times 1)}$$

$$E(\varepsilon) = \mathbf{0}_{(n\times 1)} \quad and \quad Cov(\varepsilon) = \sigma^2 \mathbf{I}_{(n\times n)}$$

where β and σ^2 are unknown and the design matrix $\mathbf{Z}$ has *j*th row $[z_{j0}, z_{j1}, \ldots, z_{jr}]$. $E(\varepsilon)$ is the expected value and $Cov(\varepsilon)$ is the covariance of the measurement errors.

One of the objectives of regression analysis is to develop an equation that can be used to predict the response for given values of the predictor variable. The values for the regression coefficient β and the error variance σ^2 are determined from the available data. The least squares estimate of β is given by

$$\hat{\beta} = (\mathbf{Z}'\mathbf{Z})^{-1}\mathbf{Z}'\mathbf{y}$$

When $\mathbf{Z}$ have full rank $r+1 \leq n$, it can be written $\mathbf{Z}'\mathbf{Z} = \lambda_1 e_1 e_1' + \lambda_2 e_2 e_2' + \ldots + \lambda_{r+1} e_{r+1} e_{r+1}'$ with use of spectral decomposition. If $\mathbf{Z}$ is not of full rank, $(\mathbf{Z}'\mathbf{Z})^{-1}$ is replaced by $(\mathbf{Z}'\mathbf{Z})^{-} = \sum_{i=1}^{r_1+1} \lambda_i^{-1} e_i e_i'$, a generalized inverse of $\mathbf{Z}'\mathbf{Z}$. The vector of residuals

$$\hat{\varepsilon} = \mathbf{y} - \hat{\mathbf{y}} = \mathbf{y} - \mathbf{Z}\hat{\beta} = [\mathbf{I} - \mathbf{Z}(\mathbf{Z}'\mathbf{Z})^{-1}\mathbf{Z}']\mathbf{y} = (\mathbf{I} - \mathbf{H})\mathbf{y}$$

contains information about the remaining unknown parameter σ^2, and the matrix $\mathbf{H} = \mathbf{Z}(\mathbf{Z}'\mathbf{Z})^{-1}\mathbf{Z}'$ is called the 'hat' matrix.

A.3.2 Multivariate multiple regression

Modeling the relationship between *m* responses, $Y_1, Y_2, \ldots, Y_m$, and a single set of predictor variables, $z_1, z_2, \ldots, z_r$ is considered. The multivariate linear regression model can be formulated as

$$\mathbf{Y}_{(n\times m)} = \mathbf{Z}_{(n\times(r+1))} \quad \beta_{((r+1)\times m)} + \varepsilon_{(n\times m)}$$

$$E(\varepsilon_{(i)}) = 0 \quad and \quad Cov(\varepsilon_{(i)}, \varepsilon_{(k)}) = \sigma_{ik}\mathbf{I} \qquad i,k = 1,2,\ldots,m$$

The *m* observations on the *j*th trial have covariance matrix $\mathbf{\Sigma} = \sigma_{ik}$, but observations from different trials are uncorrelated. Given the outcomes $\mathbf{Y}$ and the values of the predictor variables $\mathbf{Z}$ with full column rank, the least squares estimates $\hat{\beta}_i$ are determined exclusively from the observations Y_i on the *i*th response by

$$\hat{\beta}_{(i)} = (\mathbf{Z}'\mathbf{Z})^{-1}\mathbf{Z}'\mathbf{Y}_{(i)}$$

The residuals are

$$\hat{\varepsilon} = \mathbf{Y} - \hat{\mathbf{Y}} = [\mathbf{I} - \mathbf{Z}(\mathbf{Z}'\mathbf{Z})^{-1}\mathbf{Z}']\mathbf{Y}$$

A.3.3 Model fit

It is essential to examine the adequacy of the model before the estimated function becomes a permanent part of the decision-making process. Sample information on the lack of fit is contained in the residuals, $\hat{\varepsilon}$. Their covariance matrix $\sigma^2[\mathbf{I}-\mathbf{H}]$ is not a diagonal matrix. Residuals have unequal variances and nonzero correlations. The variances of $\hat{\varepsilon}_j$ can vary a lot if the diagonal elements of $\mathbf{H}$, the leverages h_{jj}, are substantially different. Graphical diagnostics based on studentized residuals are often useful. Using the residual mean square, $s^2 = \hat{\varepsilon}'\hat{\varepsilon}/(n-r-1)$, as an estimate of σ^2, and

$$\widehat{Var}(\hat{\varepsilon}_j) = s^2(1-h_{jj}) \qquad j = 1, 2, \ldots, n$$

and the studentized residual is

$$\hat{\varepsilon}_j^* = \frac{\hat{\varepsilon}_j}{\sqrt{s^2(1-h_{jj})}} \qquad j = 1, 2, \ldots, n$$

Although a residual analysis is useful in assessing model fit, departures from the regression model are often hidden by the fitting process. There may be 'outliers' that may have a considerable effect on the analysis. They are not easily detected from examination of residual plots and these outliers may determine the fit.

The leverage h_{jj} is associated with the jth data point and measures how far the jth observation is from the other $n-1$ observations. For simple linear regression with one variable z

$$h_{jj} = \frac{1}{n} + \frac{(z_j - \bar{z})^2}{\sum_{j=1}^{n}(z_j - \bar{z})^2}$$

For a data point with high leverage, h_{jj} approaches 1 and the prediction at z_j is almost solely determined by y_j, and the rest of the data have little influence. This follows because (change in $\hat{y}_j$)=h_{jj}(change in y_j), provided the other y values are fixed.

Various plotting procedures of the residuals can give information of possible anomalies, and assessment of different types of confidence intervals can also give valuable information.

Sum of squares decomposition

$\hat{\mathbf{y}}\hat{\varepsilon} = 0$ and the total response sum of squares $\mathbf{y}'\mathbf{y} = \sum_{j=1}^{n} y_j^2$ satisfy

$$\mathbf{y}'\mathbf{y} = (\hat{\mathbf{y}} + \mathbf{y} - \hat{\mathbf{y}})'(\hat{\mathbf{y}} + \mathbf{y} - \hat{\mathbf{y}}) = (\hat{\mathbf{y}} + \hat{\varepsilon})'(\hat{\mathbf{y}} + \hat{\varepsilon}) = \hat{\mathbf{y}}'\hat{\mathbf{y}} + \hat{\varepsilon}'\hat{\varepsilon}$$

The first column of the design matrix $\mathbf{Z}$ is one, representing the constant in the regression model. Due to this, $\bar{y} = \bar{\hat{y}}$ and subtracting $n\bar{y}^2 = n(\bar{\hat{y}})^2$ from both sides, the basic decomposition of the sum of squares about the mean are obtained from

$$\mathbf{y}'\mathbf{y} - n\bar{y}^2 = \hat{\mathbf{y}}'\hat{\mathbf{y}} - n(\bar{\hat{y}})^2 + \hat{\varepsilon}'\hat{\varepsilon}$$

or

$$\sum_{j=1}^{n}(y_j - \bar{y})^2 = \sum_{j=1}^{n}(\hat{y}_j - \bar{y})^2 + \sum_{j=1}^{n}\hat{\varepsilon}_j^2$$

where

(total sum of squares about mean) = (regression sum of squares)+(residual (error) sum of squares)

This suggest that the quality of the model fit can be measured by the coefficient of determination

$$R^2 = 1 - \frac{\sum_{j=1}^{n}\hat{\varepsilon}_j^2}{\sum_{j=1}^{n}(y_j - \bar{y})^2} = \frac{\sum_{j=1}^{n}(\hat{y}_j - \bar{y})^2}{\sum_{j=1}^{n}(y_j - \bar{y})^2}$$

The quantity R^2 gives the proportion of the total variation in the y_j's that is 'explained' by the predictor variables.

A.4 Principal component analysis

A.4.1 Principal components

Principal component analysis is used to explain the variance-covariance structure through a few linear combinations of the original variables. The two general objectives are data reduction and better interpretation. To reproduce the total system variability, *p* components are required. Much of this variability can be accounted for by a smaller number *k* principal components. Analysis of principal components are more of a means to an end rather than an end in themselves. They frequently serve as intermediate steps in larger investigations. For example, principal components may be used as inputs to multiple regression or cluster analysis.

Algebraically, principal components are linear combinations of the *p* random variables $X_1, X_2, \ldots, X_p$. Geometrically, these linear combinations represents selection of a new

coordinate system obtained by rotating the original system with $X_1, X_2, \ldots, X_p$ as the coordinate axes. The new axes represents the directions with maximum variability. Principal components depend solely on the covariance matrix $\mathbf{\Sigma}$ or the correlation matrix ρ of $X_1, X_2, ..., X_p$. A multivariate normal assumption is not required. Let the random vector $\mathbf{X}' = [X_1, X_2, \ldots, X_p]$ have the covariance matrix $\mathbf{\Sigma}$ with eigenvalues $\lambda_1 \geq \lambda_2 \geq \ldots \geq \lambda_p \geq 0$.

$$
\begin{aligned}
Y_1 &= \ell_1 \mathbf{X} = \ell_{11} X_1 + \ell_{21} X_2 + \cdots + \ell_{p1} X_p \\
Y_2 &= \ell_2 \mathbf{X} = \ell_{12} X_1 + \ell_{22} X_2 + \cdots + \ell_{p2} X_p \\
&\vdots \\
Y_p &= \ell_p \mathbf{X} = \ell_{1p} X_1 + \ell_{2p} X_2 + \cdots + \ell_{pp} X_p
\end{aligned}
$$

and

$$Var(Y_i) = \ell_i' \mathbf{\Sigma} \ell_i \qquad i = 1, 2, \ldots, p$$

and

$$Cov(Y_i, Y_k) = \ell_i' \mathbf{\Sigma} \ell_k \qquad i, k = 1, 2, \ldots, p$$

The principal components are uncorrelated linear combinations $Y_1, Y_2, \ldots, Y_p$ whose variances are as large as possible.

First principal component = linear combination $\ell_1 \mathbf{X}$ that maximizes
$Var(\ell_1 \mathbf{X})$ subject to $\ell_1 \ell_1 = 1$
Second principal component = linear combination $\ell_2 \mathbf{X}$ that maximizes
$Var(\ell_2 \mathbf{X})$ subject to $\ell_2 \ell_2 = 1$ and $Cov(\ell_1 \mathbf{X}, \ell_2 \mathbf{X}) = 0$
*i*th principal component = linear combination $\ell_i \mathbf{X}$ that maximizes
$Var(\ell_i \mathbf{X})$ subject to $\ell_i \ell_i = 1$ and $Cov(\ell_i \mathbf{X}, \ell_k \mathbf{X}) = 0$ for $k < i$.

Let $\mathbf{\Sigma}$ be the covariance matrix for the random vector $\mathbf{X}' = [X_1, X_2, \ldots, X_p]$. Let $\mathbf{\Sigma}$ have the eigenvalue-eigenvector pairs $(\lambda_1, \mathbf{e}_1), (\lambda_2, \mathbf{e}_2), \ldots, (\lambda_p, \mathbf{e}_p)$ where $\lambda_1 \geq \lambda_2 \geq \ldots \geq \lambda_p \geq 0$. The *i*th principal components is given by

$$Y_i = \mathbf{e}_i' \mathbf{X} = e_{1i} X_1 + e_{2i} X_2 + \cdots + e_{pi} X_p \qquad i = 1, 2, \ldots, p$$

with

$$Var(Y_i) = \mathbf{e}_i' \mathbf{\Sigma} \mathbf{e}_i = \lambda_i \qquad i = 1, 2, \ldots, p$$

$$Cov(Y_i, Y_k) = \mathbf{e}_i' \mathbf{\Sigma} \mathbf{e}_k = 0 \qquad i \neq k$$

also

$$\sigma_{11} + \sigma_{22} + \ldots + \sigma_{pp} = \sum_{i=1}^{p} Var(X_i) = \lambda_1 + \lambda_2 + \ldots + \lambda_p$$

$$= \sum_{i=1}^{p} Var(Y_i) = trace(\mathbf{\Sigma})$$

The proportion of the total population variance due to the *k*th principal component is $= \frac{\lambda_k}{\lambda_1+\lambda_2+\ldots+\lambda_p}$. The magnitude of e_{ki} measures the importance of the *k*th variable to the principal component, irrespective of the other variables. If $Y_1 = e_1'\mathbf{X}, Y_2 = e_2'\mathbf{X}, \ldots, Y_p = e_p'\mathbf{X}$ are the principal components obtained from the covariance matrix $\mathbf{\Sigma}$, then

$$\rho_{Y_i,X_k} = \frac{e_{ki}\sqrt{\lambda_i}}{\sqrt{\sigma_{kk}}} \qquad i,k = 1,2,\ldots,p$$

are the correlation coefficients between the components Y_i and the variables X_k. The eigenvalue-eigenvector pairs for $\mathbf{\Sigma}$ are $(\lambda_1, \mathbf{e}_1), (\lambda_2, \mathbf{e}_2), \ldots, (\lambda_p, \mathbf{e}_p)$.

A.4.2 Principal components from standardized variables

Principal components may also be obtained from standardized variables

$$Z_1 = \frac{(X_1 - \mu_1)}{\sqrt{\sigma_{11}}}$$

$$Z_2 = \frac{(X_2 - \mu_2)}{\sqrt{\sigma_{22}}}$$

$$\vdots$$

$$Z_p = \frac{(X_p - \mu_p)}{\sqrt{\sigma_{pp}}}$$

In matrix notation $\mathbf{Z} = (\mathbf{V}^{\frac{1}{2}})^{-1}(\mathbf{X} - \mu)$ where the diagonal standard deviation matrix $\mathbf{V}^{\frac{1}{2}}$ is contained in $\mathbf{V}^{\frac{1}{2}}\rho\mathbf{V}^{\frac{1}{2}} = \mathbf{\Sigma}$. $E(\mathbf{Z}) = \mathbf{0}$ and $Cov(\mathbf{Z}) = (\mathbf{V}^{\frac{1}{2}})^{-1}\mathbf{\Sigma}(\mathbf{V}^{\frac{1}{2}})^{-1} = \rho$. The principal components of $\mathbf{Z}$ may be obtained from the eigenvectors of the correlation matrix ρ of $\mathbf{X}$.

The *i*th principal components of the standardized variables $\mathbf{Z}' = [Z_1, Z_2, \ldots, Z_p]$ with $Cov(\mathbf{Z}) = \rho$ is given by

$$Y_i = \mathbf{e}_i'\mathbf{Z} = \mathbf{e}_i'(\mathbf{V}^{\frac{1}{2}})^{-1}(\mathbf{X} - \mu), \qquad i = 1,2,\ldots,p$$

and

$$\sum_{i=1}^{p} Var(Y_i) = \sum_{i=1}^{p} Var(Z_i) = p$$

and

$$\rho_{Y_i,Z_k} = e_{ki}\sqrt{\lambda_i} \qquad i,k = 1,2,\ldots,p$$

In this case $(\lambda_1, \mathbf{e}_1), (\lambda_2, \mathbf{e}_2), \ldots, (\lambda_p, \mathbf{e}_p)$ are the eigenvalue-eigenvector pairs for ρ with $\lambda_1 \geq \lambda_2 \geq \ldots \geq \lambda_p \geq 0$. The proportion of (standardized) population variance due to the *k*th principal component is $\frac{\lambda_k}{p}$ for $k = 1,2,\ldots,p$, and is the sum of the diagonal elements of the matrix ρ.

A.5 Principal component regression

This method combines the methodology from multivariate linear regression and principal component analysis. Least squares regression of $\mathbf{Y}$ on selected principal components of the original variables $\mathbf{X}$ is used, instead of on the original variables. This is especially useful in the case of collinearity. The principal components are by definition uncorrelated.

The principal components are extracted, named P_i in this section, and then which to use in the regression is decided. The components with measurement noise may not be used for further calculations.

$$P_i = \mathbf{e}_i'\mathbf{X} \qquad i = 1,2,\ldots,p$$

Then multivariate linear regression of $\mathbf{Y}$ on the $\mathbf{P}$ is applied

$$\mathbf{Y}_{(n\times m)} = \mathbf{P}_{(n\times(r+1))} \quad \beta_{((r+1)\times m)} + \varepsilon_{(n\times m)}$$

and

$$\hat{\beta}_{(i)} = (\mathbf{P}'\mathbf{P})^{-1}\mathbf{P}'\mathbf{Y}_{(i)}$$

The residuals are

$$\hat{\varepsilon} = \mathbf{Y} - \hat{\mathbf{Y}} = [\mathbf{I} - \mathbf{P}(\mathbf{P}'\mathbf{P})^{-1}\mathbf{P}']\mathbf{Y}$$

If all the components of the principal component analysis are used in the regression, then the same result as for ordinary multivariate linear regression is obtained.

$$\mathbf{Y} = \mathbf{X}\beta_{MLR} \Longleftrightarrow \mathbf{Y} = \mathbf{e}'\mathbf{X}\beta_{PCR}$$

and from that $\mathbf{X}\beta_{MLR} = \mathbf{e}'\mathbf{X}\beta_{PCR}$. This implies that for full rank of the problem

$$\beta_{MLR} = \mathbf{e}'\beta_{PCR}$$

A.6 Partial least squares regression

A.6.1 Partial least squares (PLS) algorithm

This is an empirical based method where the Y-variables are used during the decomposition of Z. The PLS regression method in its basic form applies for one single Y-variable, and it can be modified for two or more Y-variables simultaneously. The starting point is two data matrices, $\mathbf{Z}_{n\times m}$ and $\mathbf{Y}_{n\times k}$. No assumptions are needed concerning the dimensions of the matrices, and they may be scaled or centered.

1. start: set $\mathbf{u}$ to the first column of $\mathbf{Y}$
2. $\mathbf{w} = \frac{\mathbf{Z}'\mathbf{u}}{\mathbf{u}'\mathbf{u}}$
3. scale $\mathbf{w}$ to be the length of one
4. $\mathbf{t} = \mathbf{Z}\mathbf{w}$
5. $\mathbf{c} = \frac{\mathbf{Y}'\mathbf{t}}{\mathbf{t}'\mathbf{t}}$
6. scale $\mathbf{c}$ to be the length of one
7. $\mathbf{u} = \frac{\mathbf{Y}'\mathbf{c}}{\mathbf{c}'\mathbf{c}}$
8. if convergence then 9 else 2
9. Z-loadings: $\mathbf{p} = \frac{\mathbf{Z}'\mathbf{t}}{\mathbf{t}'\mathbf{t}}$
10. Y-loadings: $\mathbf{q} = \frac{\mathbf{Y}'\mathbf{u}}{\mathbf{u}'\mathbf{u}}$
11. regression ($\mathbf{u}$ upon $\mathbf{t}$): $b = \frac{\mathbf{u}'\mathbf{t}}{\mathbf{t}'\mathbf{t}}$
12. residual matrices: $\mathbf{Z} \Rightarrow \mathbf{Z} - \mathbf{t}\mathbf{p}'$ and $\mathbf{Y} \Rightarrow \mathbf{Y} - b\mathbf{t}\mathbf{c}'$

The next set of iterations starts with the new $\mathbf{Z}$ and $\mathbf{Y}$ matrices as the residual matrices from the previous iteration. The iterations is repeated until the end criteria is reached when $\mathbf{Z}$ becomes the zero matrix. At convergence it can be written

1. $\mathbf{YY'ZZ'u} = a\mathbf{u}$
2. $\mathbf{Y'ZZ'Yc} = a\mathbf{c}$
3. $\mathbf{ZZ'YY't} = a\mathbf{t}$
4. $\mathbf{Z'YY'Zw} = a\mathbf{w}$

a is the maximum eigenvalue of the eigenvalue problem. The vectors $\mathbf{u}$, $\mathbf{c}$, $\mathbf{t}$, and $\mathbf{w}$ are thus the eigenvectors of the appropriate matrices corresponding to the maximum eigenvalue. The PLS algorithm can thus be viewed as follows. For each set of residual matrices $\mathbf{Z}$ and $\mathbf{Y}$ the maximum eigenvalue and associated eigenvectors of the matrices are computed.

$$\mathbf{Z'YY'Z} \qquad \mathbf{Y'ZZ'Y} \qquad \mathbf{ZZ'YY'} \qquad \mathbf{YY'ZZ'}$$

and the eigenvectors are used to compute new residual matrices. In the computations only the eigenvector of $\mathbf{Z'YY'Z}$ is needed. The others may be computed as in the algorithm. It is an important aspect of the PLS algorithm that only one pair of eigenvectors at each step is selected. The PLS algorithm gives the usual multiple regression solution when all steps are carried out.

A.7 Preprocessing of data

Weighting of the variables is important in all the methods where least squares fitting is used. It can be done as an individual weighting of the Z-variables $z_{ik} = z_{ik,old} * weight_k$. The Y-variables may be weighted in the same way. Weighting may be important to balance the noise in the input variables to avoid informative variables to be masked by others that inhabit noise. Another reason is to weight the variables to similar variance, so that the modeling is not dominated by variables with large variance. This is often done by standardization, also for Y-variables. Different types of weighting must be applied with care, because of the danger of amplifying variables with little information and a lot of noise. Different filters can also be applied to remove noise and other unwanted effects in the data or to enhance important information.

A.8 Validation

The best method is to make a model on a known data set (test set/training set) and test it on another known data set (validation set). The predicted Y-values are compared with the known Y-values for each sample in the validation set and the average prediction error is calculated.

The concept 'model errors' concerns the fit of the model to the data. Since the modeling is a local approximation to some unknown, more or less non-linear function between $\mathbf{X}$ and $\mathbf{Y}$, all models must be expected to have some degree of error.

Lack of representativity is an error source which arises when the training data does not cover the total range of variability in the population of future objects. Also, random noise might be a problem both in $\mathbf{X}$ and $\mathbf{Y}$. The statistical methods must be robust, so that the influence of outliers can be reduced. These observations of extreme objects may span important variability in the data set, and must not be removed without considerations.

Under-fitting of a model happens when the model is not good enough to fit to the test set by using too few components. Over-fitting of a model exists when the fit to the test data is good by using to many components. When used in prediction, the model will fail to predict new data.

The average prediction error for the whole population of future objects to be predicted is defined as the mean squared error (MSE)

$$MSE = E(\mathbf{y} - \hat{\mathbf{y}})^2$$

and the root mean square error ($RMSE$) is defined

$$RMSE = \sqrt{E(\mathbf{y} - \hat{\mathbf{y}})^2}$$

With a sufficient and representative validation set with known levels of y, the average bias can be estimated

$$bias = \frac{1}{n}\sum_{i=1}^{n}(\mathbf{y}_i - \hat{\mathbf{y}}_i)$$

The root mean square error of prediction ($RMSEP$) is defined as

$$RMSEP = \sqrt{\frac{1}{n}\sum_{i=1}^{n}(\mathbf{y}_i - \hat{\mathbf{y}}_i)^2}$$

Internal validation concerns validation from the test set data itself, and an assessment based on internal validation is not as good as testing against an independent validation data set. The predictive ability can only be assessed by testing on new objects, but the two methods cross validation and leverage correction may give sensible results and valuable information.

In full cross validation one repeats the calculation of the model several times, each time leaving one part of the data set out. The models are tested on the left out validation samples. In the end all objects have been treated as a validation set, and the total estimated MSE can be computed.

Another internal estimate of prediction MSE is the C_p, developed by Mallows. C_p a is good statistic for variable selection and can be written

$$C_p = (\frac{\text{(residual sum of squares subset model with p parameters, including an intercept)}}{\text{(residual variance for full model)}}) - (n - 2p)$$

A.9 Singular value decomposition

Singular value decomposition (SVD) is used to rotate the coordinate axes to make them follow more closely the pattern made by the data points in the matrix to decompose. A better understanding of the structure of the matrix may be obtained.

The singular value decomposition of an *m* by *n* matrix $\mathbf{A}$ is given by

$$\mathbf{A} = \mathbf{U}\mathbf{\Sigma}\mathbf{V}' \qquad \mathbf{\Sigma} = diag(\sigma_1, \ldots, \sigma_p), \qquad p = min(m, n)$$

where $\mathbf{U}_{m\times m}$ and $\mathbf{V}_{n\times n}$ are orthogonal. $\mathbf{\Sigma}$ is an *m* by *n* diagonal matrix with the diagonal elements, σ_i such that $\sigma_1 \geq \sigma_2 \geq \ldots \geq \sigma_{min(m,n)} \geq 0$. The σ_i are singular values of $\mathbf{A}$ and the first min(*m*,*n*) columns of $\mathbf{U}$ and $\mathbf{V}$ are the left and right singular vectors of $\mathbf{A}$. The singular values and singular vectors satisfy $\mathbf{A}v_i = \sigma_i u_i$ and $\mathbf{A}'u_i = \sigma_i v_i$, where u_i and v_i are the *i*th columns of $\mathbf{U}$ and $\mathbf{V}$ respectively.

The SVD reveals information about the structure of a matrix. If the SVD of $\mathbf{A}$ is given, and r is defined by

$$\sigma_1 \geq \ldots \geq \sigma_r > \sigma_{r+1} = \ldots = \sigma_p = 0$$

Then

$$rank(\mathbf{A}) = r$$

$$null(\mathbf{A}) = span\{v_{r+1}, \ldots, v_n\} \qquad nullspace$$

$$ran(\mathbf{A}) = span\{u_1, \ldots, u_r\} \qquad range$$

and the SVD expansion

$$\mathbf{A} = \sum_{i=1}^{r} = \sigma_i u_i v_i'$$

A.10 Least squares estimation

Least squares estimates $\hat{\beta}$ and the residuals $\hat{\varepsilon}$ can be obtained from the matrix $\mathbf{Z}$ and response $\mathbf{y}$ by simple matrix operations.

$$\mathbf{Y}_{(n\times 1)} = \mathbf{Z}_{(n\times(r+1))} \quad \beta_{((r+1)\times 1)} + \varepsilon_{(n\times 1)}$$

$$E(\varepsilon) = \mathbf{0}_{(n\times 1)} \quad and \quad Cov(\varepsilon) = \sigma^2 \mathbf{I}_{(n\times n)}$$

where β and σ^2 are unknown and the design matrix $\mathbf{Z}$ has *j*th row $[z_{j0}, z_{j1}, ..., z_{jr}]$. Let $\mathbf{Z}$ have full rank $r + 1 \leq n$. The least squares estimate of β is given by

$$\hat{\beta} = (\mathbf{Z}'\mathbf{Z})^{-1}\mathbf{Z}'\mathbf{y}$$

Let $\hat{\mathbf{y}} = \mathbf{Z}\hat{\beta} = \mathbf{H}\mathbf{y}$ denote the fitted values of $\mathbf{y}$, where $\mathbf{H} = \mathbf{Z}(\mathbf{Z}'\mathbf{Z})^{-1}\mathbf{Z}'$. The residuals

$$\hat{\varepsilon} = \mathbf{y} - \hat{\mathbf{y}} = [\mathbf{I} - \mathbf{Z}(\mathbf{Z}'\mathbf{Z})^{-1}\mathbf{Z}']\mathbf{y} = (\mathbf{I} - \mathbf{H})\mathbf{y}$$

satisfy $\mathbf{Z}'\hat{\varepsilon} = \mathbf{0}$ and $\mathbf{y}'\hat{\varepsilon} = 0$. The residual sum of squares are

$$\sum_{j=1}^{n}(y_j - \hat{\beta}_0 - \hat{\beta}_1 z_{j1} - \ldots - \hat{\beta}_r z_{jr})^2 = \hat{\varepsilon}'\hat{\varepsilon} = \mathbf{y}'[\mathbf{I} - \mathbf{Z}(\mathbf{Z}'\mathbf{Z})^{-1}\mathbf{Z}']\mathbf{y} = \mathbf{y}'\mathbf{y} - \mathbf{y}'\mathbf{Z}\hat{\beta}$$

The matrix $[\mathbf{I} - \mathbf{Z}(\mathbf{Z}'\mathbf{Z})^{-1}\mathbf{Z}']$ satisfies

1. $[\mathbf{I} - \mathbf{Z}(\mathbf{Z}'\mathbf{Z})^{-1}\mathbf{Z}']' = [\mathbf{I} - \mathbf{Z}(\mathbf{Z}'\mathbf{Z})^{-1}\mathbf{Z}']$ symmetric
2. $[\mathbf{I} - \mathbf{Z}(\mathbf{Z}'\mathbf{Z})^{-1}\mathbf{Z}'][\mathbf{I} - \mathbf{Z}(\mathbf{Z}'\mathbf{Z})^{-1}\mathbf{Z}']$
   $= \mathbf{I} - 2\mathbf{Z}(\mathbf{Z}'\mathbf{Z})^{-1}\mathbf{Z}' + \mathbf{Z}(\mathbf{Z}'\mathbf{Z})^{-1}\mathbf{Z}'\mathbf{Z}(\mathbf{Z}'\mathbf{Z})^{-1}\mathbf{Z}' = [\mathbf{I} - \mathbf{Z}(\mathbf{Z}'\mathbf{Z})^{-1}\mathbf{Z}']$
3. $\mathbf{Z}'[\mathbf{I} - \mathbf{Z}(\mathbf{Z}'\mathbf{Z})^{-1}\mathbf{Z}'] = \mathbf{Z}' - \mathbf{Z}' = \mathbf{0}$

$\mathbf{Z}'\hat{\varepsilon} = \mathbf{Y}'(\mathbf{y} - \hat{\mathbf{y}}) = \mathbf{Z}'[\mathbf{I} - \mathbf{Z}(\mathbf{Z}'\mathbf{Z})^{-1}\mathbf{Z}']\mathbf{y} = \mathbf{0}$, so $\hat{\mathbf{y}}\hat{\varepsilon} = \hat{\beta}'\mathbf{Z}'\hat{\varepsilon} = 0$. In addition, $\hat{\varepsilon}'\hat{\varepsilon} = \mathbf{y}'[\mathbf{I} - \mathbf{Z}(\mathbf{Z}'\mathbf{Z})^{-1}\mathbf{Z}'][\mathbf{I} - \mathbf{Z}(\mathbf{Z}'\mathbf{Z})^{-1}\mathbf{Z}']\mathbf{y} = \mathbf{y}'[\mathbf{I} - \mathbf{Z}(\mathbf{Z}'\mathbf{Z})^{-1}\mathbf{Z}']\mathbf{y} = \mathbf{y}'\mathbf{y} - \mathbf{y}'\mathbf{Z}\hat{\beta}$. To verify the expression for $\hat{\beta}$, it is written

$$\mathbf{y} - \mathbf{Z}\mathbf{b} = \mathbf{y} - \mathbf{Z}\hat{\beta} + \mathbf{Z}\hat{\beta} - \mathbf{Z}\mathbf{b} = \mathbf{y} - \mathbf{Z}\hat{\beta} + \mathbf{Z}(\hat{\beta} - \mathbf{b})$$

and

$$S(\mathbf{b}) = \sum_{j=1}^{n}(y_j - b_0 - b_1 z_{j1} - ... - b_r z_{jr})^2 = (\mathbf{y} - \mathbf{Z}\mathbf{b})'(\mathbf{y} - \mathbf{Z}\mathbf{b})$$

$$= (\mathbf{y} - \mathbf{Z}\hat{\beta})'(\mathbf{y} - \mathbf{Z}\hat{\beta}) + (\hat{\beta} - \mathbf{b})'\mathbf{Z}'\mathbf{Z}(\hat{\beta} - \mathbf{b}) + 2(\mathbf{y} - \mathbf{Z}\hat{\beta})'\mathbf{z}(\hat{\beta} - \mathbf{b})$$

$$= (\mathbf{y} - \mathbf{Z}\hat{\beta})'(\mathbf{y} - \mathbf{Z}\hat{\beta}) + (\hat{\beta} - \mathbf{b})'\mathbf{Z}'\mathbf{Z}(\hat{\beta} - \mathbf{b})$$

since $(\mathbf{y} - \mathbf{Z}\hat{\beta})'\mathbf{Z} = \hat{\varepsilon}'\mathbf{Z} = \mathbf{0}'$, as above. The first term in $S(\mathbf{b})$ does not depend on $\mathbf{b}$ and the second is the squared length of $\mathbf{Z}(\hat{\beta} - \mathbf{b})$. Because $\mathbf{Z}$ has full rank, $\mathbf{Z}(\hat{\beta} - \mathbf{b}) \neq \mathbf{0}$ if $\hat{\beta} \neq \mathbf{b}$, so the minimum sum of squares is unique and occurs for $\mathbf{b} = \hat{\beta} = (\mathbf{Z}'\mathbf{Z})^{-1}\mathbf{Z}'\mathbf{y}$. Note that $(\mathbf{Z}'\mathbf{Z})^{-1}$ exists since $(\mathbf{Z}'\mathbf{Z})$ has rank $r + 1 \leq n$.

URN:NBN:no-2344

Appendix B

Sea ice glossary

This overview of sea ice terminology is based on the WMO Sea-Ice Nomenclature (World Meteorological Organization, 1970).

Brash ice Accumulation of floating ice made up of fragments not more than 2 m across (small ice cakes), the wreckage of other forms of ice.

Break up A general expression applied to the formation of a large number of fractures through a compact ice cover, followed by a rapid diverging motion of the separate fragments.

Concentration The ratio, in tenths, of the sea surface area covered by ice of any type to the total sea surface area. May be expressed in the following terms:
Compact ice: Concentration 10/10, no water visible.
Consolidated ice: Concentration 10/10, floes frozen together.
Very close ice: Concentration 9/10 to less than 10/10.
Close ice: Concentration 7/10 to 8/10, floes mostly in contact.
Open ice: Concentration 4/10 to 6/10, many leads and polynyas, floes generally not in contact.
Very open ice: Concentration 1/10 to 3/10.

Crack Any fracture which has not yet parted.

Deformed ice A general term for ice which has been squeezed together and in places forced upward (and downward). Forms of deformation include rafting, ridging and

hummocking.

Diverging ice Used to indicate a general diverging motion, reducing ice concentration or releasing stress. Divergence can be considered as the change in area per unit area at a given point.

Draft The distance, measured normal to the sea surface, between the lower surface of the ice and the water level.

Fast ice Sea ice of any origin which remains fast (attached with little horizontal motion) along a coast or to some other fixed object.

First year ice Sea ice of not more than one winter's growth, developed from young ice. The thickness is 0.3–3 m. May be subdivided into thin first year ice or white ice (0.3–0.7 m), medium first year ice (0.7–1.2 m) and thick first year ice (over 1.2 m).

Flaw A narrow separation zone between pack ice and fast ice, where the pieces of ice are in a chaotic state. It forms when pack ice shears under the effect of a strong wind or currents along the fast ice boundary.

Flaw lead A lead between pack ice and fast ice, navigable by a vessel.

Floe Any relatively flat piece of sea ice 20 m or more across. Floes are subdivided according to horizontal extent:
Giant floe: more than 10 km across.
Vast floe: 2–10 km across.
Big floe: 0.5–2 km across.
Medium floe: 100–500 m across.
Small floe: 20–100 m across.

Flooded ice Sea ice which has been flooded by melt-water or river water and is heavily loaded by water and wet snow.

Fracture Any break or rupture through very close, compact or consolidate pack ice, fast ice or a single floe resulting from deformation processes. Fractures may contain brash ice and be covered with nilas or young ice. The length may be from a few meters to many kilometers.

URN:NBN:no-2344

Frazil ice Fine needles or plates of ice, suspended in water. It sometimes forms at some depth, at an interface between water bodies of different physical characteristics, and floats to the surface. It may rapidly cover wide areas of water.

Grease ice A stage of the freezing, later than that of frazil ice, in which the crystals have coagulated to form a soupy layer on the surface. Grease ice reflects little light, giving the sea a matte appearance.

Grey ice Young ice, 0.10–0.15 m thick, less elastic than nilas, usually rafts under pressure and breaks on swell.

Grey-white ice Young ice, 0.15–0.30 m thick. Under pressure, it is more likely to ridge than to raft.

Hummock The raised area of multi year ice formed by ablation of the surrounding ice. Also, a pile of broken ice which has been forced upward by pressure. May be fresh or weathered. The submerged volume of broken ice under the hummock is called a bummock.

Iceberg A massive piece of ice of greatly varying shape with a freeboard of more than 5 m, which has broken away from a glacier and may be afloat or aground.

Ice cover The ratio of an area of ice of any concentration to the total area of sea surface within some large geographic area; this area may be global, hemispheric, or prescribed by a specific oceanographic entity, such as Baffin Bay or the Barents Sea.

Ice edge The demarcation at any given time between the open sea and sea ice of any kind. It may be compact or diffuse.

Ice field Area of pack ice greater than 10 km across, consisting of floes of any size. Subdivided as follows:
Large ice field: more than 20 km across.
Medium ice field: 15–20 km across.
Small ice field: 10–15 km across.

Ice free No sea ice present. There may, however, be some icebergs present (see also open water).

URN:NBN:no-2344

Ice limit Climatological term referring to the extreme minimum or extreme maximum extent of the ice edge in any given month or period, based on observations over a number of years.

Ice massif A concentration of sea ice covering hundreds of square kilometers, which is found in the same region every summer.

Ice patch An area of pack ice less than 10 km across.

Ice shelf A floating ice sheet of considerable thickness, showing 2–50 m or more above sea level, attached to the coast. Usually of great horizontal extent and with a level or gently undulating surface. The ice sheet is caused by glaciers extending into the ocean, so parts of it may be aground. The seaward edge is called an ice front.

Keel The underside of a ridge that projects downward below the lower surface of the surrounding sea ice.

Lead Any fracture or passage through sea ice that is generally navigable by a vessel. A lead may contain open water (open lead) or be covered by thin ice (frozen lead).

Level ice Sea ice which has been unaffected by deformation.

Melt pond An accumulation of melt water on the surface of sea ice.

Multi year ice Old ice 3 m or more thick, which has survived at least two summers' melt. The hummocks are even smoother than in second year ice, and the ice is almost salt-free. The color, where bare, is usually blue. The melt pattern consists of large inter-connecting irregular puddles and melt ponds, and a well-developed drainage system. In remote sensing, note that second year ice is often referred to as multi year ice.

New ice A general term for recently formed ice, which includes frazil ice, grease ice, slush and shuga. These types of ice are composed of ice crystals which are only weakly frozen together (if at all) and have a definite form only while they are afloat.

Nilas A thin elastic crust of ice up to 0.10 m thick. Bends easily under pressure, thrusting in a pattern of interlocking 'fingers' (finger rafting). Dark nilas, up to 0.05 m thick is very dark in color; light nilas, 0.05–0.10 m thick, is lighter in color.

URN:NBN:no-2344

Old ice Sea ice which has survived at least one summers melt. Most topographic features are smoother than first year ice. May be subdivided into second year ice and multi year ice.

Open water A large area of freely navigable water in which sea ice is present in less than 1/10 concentration (see also ice free).

Pack ice Any accumulation of of sea ice, other than fast ice, no matter what form it takes or how it is disposed.

Pancake ice Predominantly circular pieces of ice from 0.3–3 m in diameter, and up to about 0.10 m in thickness, with raised rims due to the pieces striking against one another. It may be formed on a slight swell from grease ice, shuga or slush, or as a result of the breaking up of ice rind, nilas, or under severe conditions of swell or waves, grey ice.

Polynya Any nonlinear shaped opening enclosed in ice. Polynyas may contain brash ice or be covered with new ice, nilas or young ice. If it is limited on one side by the coast, it is called shore polynya; if limited by fast ice, it is called a flaw polynya and if found in the same place every year, it is called a recurring polynya.

Pressure ridge A general expression for any elongated (in plan view) ridgelike accumulation of broken ice forced up by converging ice (ridging).

Rafting Process whereby one piece of ice overrides another. Most obvious in new and young (finger rafting) ice but common in ice of all thicknesses.

Second year ice Ice which has survived only one summers' melt. In contrast to multi year ice, second year ice during the summer melt shows a regular pattern of numerous small puddles.

Shear zone An area in which a large amount of shearing deformation has been concentrated.

Shore lead A lead between pack ice and the shore or between pack ice and an ice shelf or a glacier.

Shuga An accumulation of spongy white ice lumps a few centimeters across, formed from grease ice or slush and sometimes from ice formed at some depth rising to the surface.

URN:NBN:no-2344

Slush Snow which is saturated and mixed with water on land or ice surfaces, or forms as a viscous mass floating in water after a heavy snowfall.

Young ice Ice in the transition stage between nilas and first year ice, 0.10–0.30 m thick. May be subdivided into grey ice and grey-white ice. The expression young ice is also commonly used in a more general way to indicate the complete range of ice thickness between 0 and 0.30 m. Usually these difference in meaning are clear from the context of the discussion.

URN:NBN:no-2344

Appendix C

References

Aagaard, K., and Carmack, E. C., 1989, The role of sea ice and other fresh water in the Arctic circulation, Journal of Geophysical Research, Vol. 94, No. C10, pp. 14485-14498.

Abramov, V. (Ed.), 1996, Atlas of Arctic Icebergs, The Greenland, Barents, Kara, Laptev, East-Siberian and Chukchi Seas and the Arctic Basin. Backbone Publishing Company.

Adam, S., Wiebe, J., Collins, M., and Pietroniro, A., 1998, Radarsat flood mapping in the Peace-Athabasca Delta, Canada, Canadian Journal of Remote Sensing, Vol. 24, No. 1, pp. 69-79.

Agnew, T. A., Le, H., and Shokr M., 1999, Characteristics of large winter leads over the Arctic Basin from 85.5 GHz DMSP SSM/I and NOAA/AVHRR imagery, Canadian Journal of Remote Sensing, Vol. 25, No. 1, pp. 12-20.

Alexandrov, V. Y., Martin, T., Kolatschek, J., Eicken, H., Kreyscher, M., and Makshtas, A. P., 2000a, Sea ice circulation in the Laptev Sea and ice export to the Arctic Ocean: Results from satellite remote sensing and numerical modeling, Journal of Geophysical Research, Vol. 105, No. C7, pp. 17143-17159.

Alexandrov, V. Y., Sandven, S., Johannessen, O. M., Dalen, Ø., and Pettersson, L. H., 2000b, Winter navigation in the Northern Sea Route, Polar Record, Vol. 36, No. 199, pp. 333-342.

Alexandrov, V. Y., Sandven, S., Lundhaug, M., Dalen, Ø., Bogdanov, A., and Kloster, K., 1999, Analysis of winter sea ice in the Kara Sea region using SAR data and field observations, in 15th International Conference on Port and Ocean Engineering under

Arctic Conditions, Helsinki, Finland, August 23-27, pp. 181-190.

Alhumaidi, S. M., Linwood Jones, W., Park, J.-D., and Ferguson, S. M., 1997, A neural network algorithm for sea ice edge classification, IEEE Transactions on Geoscience and Remote Sensing, Vol. 35, No. 4, pp. 817-826.

AMAP, 1998, AMAP Assessment Report: Arctic Pollution Issues, Arctic Monitoring and Assessment Programme (AMAP), Oslo, Norway, ISBN 82-7655-061-4, Xii+859 pp.

Andreas, E. L., and Cash, B. A., 1999, Convective heat transfer over wintertime leads and polynyas, Journal of Geophysical Research, Vol. 104, No. C11, pp. 25721-25734.

Andreeva, E. N., 1998, The Russian Arctic coastal zone management problems: past lessons and new realities, Ocean & Coastal Management, Vol. 41, No. 2-3, pp. 237-256.

Andrle, R., 1994, The angle measure technique: A new method for characterizing the complexity of geomorphic lines, Mathematical Geology, Vol. 26, No. 1, pp. 83-97.

Andrle, R., 1996a, Complexity and scale in geomorphology: statistical self-similarity vs. characteristic scales, Mathematical Geology, Vol. 28, No. 3, pp. 275-293.

Andrle, R., 1996b, The west coast of Britain: statistical self-similarity vs. characteristic scales in the landscape, Earth Surface Processes and Landforms, Vol. 21, pp. 955-962.

Arctic Climatology Project, 2000, Environmental Working Group Arctic Meteorology and Climate Atlas, F. Fetterer and V. Radionov, Eds., Boulder, CO, National Snow and Ice Data Center, CD-ROM.

Backlund, A., 1995, III.01.3 Development of oil and gas exports from northern Russia, INSROP Working Paper No. 22, ISBN 82-7613-119-0, 76 pp., Available from The INSROP Secretariat, The Fridtjof Nansen Institute, P.O. Box 326, N-1326 Lysaker, Norway.

Barber, D. G., and LeDrew, E. F., 1991, SAR sea ice discrimination using texture statistics: a multivariate approach, Photogrammetric Engineering & Remote Sensing, Vol. 57, No. 4, pp. 385-395.

Barber, D. G., Shokr, M. E., Fernandes, R. A., Soulis, E. D., Flett, D. G., and LeDrew, E. F., 1993, A comparison of second-order classifiers for SAR sea ice discrimination, Photogrammetric Engineering & Remote Sensing, Vol. 59, No. 9, pp. 1397-1408.

Barber, D. G., Thomas, A., and Papakyriakou, T. N., 1998, Role of SAR in surface energy flux measurements over sea ice, in Analysis of SAR Data of the Polar Oceans, C.

Tsatsoulis and R. Kwok, Eds., New York, Springer-Verlag, pp. 35-67.

Barber, D. G., Yackel, J. J., and Hanesiak, J. M., 2001, Sea ice, RADARSAT-1 and Arctic climate processes: a review and update, Canadian Journal of Remote Sensing, Vol. 27, No. 1, pp. 51-61.

Barnett, D., 1991, Sea ice distribution in the Soviet Arctic, in the Soviet Maritime Arctic, L. W. Brigham, Ed., Belhaven Press, 25 Floral Street, London WC2E 9DS, pp. 47-62.

Beaven, S. G., Gogineni, S., and Carsey, F. D., 1996, Fusion of satellite active and passive microwave data for sea ice type concentration estimates, IEEE Transactions on Geoscience and Remote Sensing, Vol. 34, No. 5, pp. 1172-1183.

Bertoia, C., Falkingham, J., and Fetterer, F., 1998, Polar SAR data for operational sea ice mapping, in Analysis of SAR Data of the Polar Oceans, C. Tsatsoulis and R. Kwok, Eds., New York: Springer-Verlag, pp. 202-231.

Biggs, N. R. T., Morales Maqueda, M. A., and Willmott, A. J., 2000, Polynya flux model solutions incorporating a parameterization for the collection thickness of consolidated new ice, Journal of Fluid Mechanics, Vol. 408, pp. 179-204.

Bishop, C. M., 1995, Neural networks for pattern recognition, Oxford University Press Inc., New York, ISBN 0 19 853864 2, 482 pp.

Bjørgo, E., Johannessen, O. M., and Miles, M. W., 1997, Analysis of merged SMMR-SSMI time series of Arctic and Antarctic sea ice parameters 1978-1995, Geophysical Research Letters, Vol. 24, No. 4, pp. 413-416.

Brigham, L. W., 2000, Natural conditions, ice navigation and ship design - pushing the limits, in The 21st Century - Turning Point for the Northern Sea Route?, Proceedings from the Northern Sea Route User Conference, Oslo, 18-20 November 1999, C. L. Ragner, Ed., Dordrecht/Boston/London: Kluwer Academic Publishers, ISBN 0-7923-6365-5, pp. 57-62.

Budéus, G., and Schneider, W., 1995, On the hydrography of the Northeast Water polynya, Journal of Geophysical Research, Vol. 100, No. C3, pp. 4287-4299.

Bushuev, A.,V., Grishchenko, V.D., and Masanov, A.D., 1985, Sea ice interpretation on radar satellite images, Issledovanie Zemli iz Kosmosa, No. 3, pp. 9-15. (in Russian).

Bushuev, A., Loshilov, V., Bychenkov, Yu., Devyataev, O., Shcherbakov, Yu., Grishch-

enko, V., Yakshevich, E., Shigabutdinov, A., and Sandven, S., 1998, I.2.3 An overview of Russian satellite data for the Northern Sea Route, INSROP Working Paper No. 109, ISBN 82-7613-263-4, 32 pp., Available from The INSROP Secretariat, The Fridtjof Nansen Institute, P.O. Box 326, N-1326 Lysaker, Norway.

Carnec, C., and Delacourt, C., 2000, Three years of mining subsidence monitored by SAR interferometry, near Gardanne, France, Journal of Applied Geophysics, Vol. 43, No. 1, pp. 43-54.

Carsey, F. D., Barry, R. G., and Weeks, W. F., 1992, Introduction to Microwave Remote Sensing of Sea Ice, F. D. Carsey, Ed., Geophysical Monograph 68, American Geophysical Union, Washington, pp. 1-7.

Cavalieri, D. J., Crawford, J., Drinkwater, M. R., Eppler, D., Farmer, L. D., Jentz, R. R., and Wackerman, C. C., 1991, Aircraft active and passive microwave validation of sea ice concentration from the DMSP SSM/I, Journal of Geophysical Research, Vol. 96, No. C12, pp. 21989-22009.

Cavalieri, D. J., Gloersen, P., and Campbell, W. J., 1984, Determination of sea ice parameters with the Nimbus 7 SMMR, Journal of Geophysical Research, Vol. 89, No. D4, pp. 5355-5369.

Cavalieri, D. J., Gloerson, P., and Zwally, J., 1990-2000, DMSP SSM/I daily polar gridded sea ice concentrations, J. Maslanik and J. Stroeve, Eds., Boulder, CO, National Snow and Ice Data Center. HTML version at
http://nsidc.org/data/docs/daac/nsidc0002_ssmi_seaice.gd.html.

Cavalieri, D. J., and Martin, S., 1994, The contribution of Alaskan, Siberian, and Canadian Coastal polynyas to the cold halocline layer of the Arctic Ocean, Journal of Geophysical Research, Vol. 99, No. C9, pp. 18343-18362.

Cavalieri, D. J., Parkinson, C. L., Gloerson, P., Comiso, J. C., and Zwally, J., 1999, Deriving long-term time series of sea ice cover from satellite passive-microwave multisensor data sets, Journal of Geophysical Research, Vol. 104, No. C7, pp. 15803-15814.

Cole, D. M., 2001, The microstructure of ice and its influence on mechanical properties, Engineering Fracture Mechanics, Vol. 68, No. 17-18, pp. 1797-1822.

Comiso, J. C., 1986, Characteristics of Arctic winter sea ice from satellite multispectral microwave observations, Journal of Geophysical Research, Vol. 91, No. C1, pp. 975-

994.

Comiso, J. C., 1990-2000, DMSP SSM/I daily polar gridded sea ice concentrations, J. Maslanik and J. Stroeve, Eds., Boulder, CO, National Snow and Ice Data Center. HTML version at http://nsidc.org/data/docs/daac/nsidc0002_ssmi_seaice.gd.html.

Comiso, J. C., Cavalieri, D., Parkinson, C., and Gloersen, P., 1997, Passive microwave algorithms for sea ice concentrations: A comparison of two techniques, Remote Sensing of the Environment Vol. 60, No. 3, pp. 357-384.

Comiso, J. C., and Gordon, A. L., 1996, Cosmonaut polynya in the Southern Ocean: Structure and variability, Journal of Geophysical Research, Vol. 101, No. C8, pp. 18297-18313.

Comiso, J. C, Grenfell, T.C., Lange, M., Lohanick, A., Moore, R., and Wadhams, P., 1992, Microwave remote sensing of the Southern Ocean ice cover, in Microwave Remote Sensing of Sea Ice, F. D. Carsey, Ed., Geophysical Monograph 68, American Geophysical Union, Washington, pp. 243-259.

Comiso, J. C., and Kwok, R., 1996, Surface and radiative characteristics of summer Arctic sea ice cover from multisensor satellite observations, Journal of Geophysical Research, Vol. 101, No. C12, pp. 28397-28416.

Comiso, J. C., and Sullivan, C. W., 1986, Satellite microwave and in-situ observations of the Weddell Sea ice cover and its marginal ice zone, Journal of Geophysical Research, Vol. 91, No. C8, pp. 9663-9681.

Cracknell, A. P., 1998, Synergy in remote sensing - what's in a pixel?, International Journal of Remote Sensing, Vol. 19, No. 11, pp. 2025-2047.

Darby, M. S., Willmott, A. J., and Mysak, L. A., 1994, A nonlinear steady-state model of the North Water Polynya, Baffin Bay, Journal of Physical Oceanography, Vol. 24, No. 5, pp. 1011-1020.

Darby, M. S., Willmott, A. J., and Somerville, T. A., 1995, On the influence of coastline orientation on the steady state width of a latent heat polynya, Journal of Geophysical Research, Vol. 100, No. C7, pp. 13625-13633.

Davis, N. R., and Wadhams, P., 1995, A statistical analysis of Arctic pressure ridge morphology, Journal of Geophysical Research, Vol. 100, No. C6, pp. 10915-10925.

Dethleff, D., Loewe, P., and Kleine, E., 1998, The Laptev Sea flaw lead detailed investigation on ice formation and export during 1991/1992 winter season, Cold Regions Science and Technology, Vol. 27, No. 3, pp. 225-243.

Dethleff, D., Nies, H., Harms, I. H., and Karcher, M. J., 2000, Transport of radionuclides by sea-ice and dense-water formed in western Kara Sea flaw leads, Journal of Marine Systems, Vol. 24, No. 3-4, pp. 233-248.

Dmitrenko I.A., Gribanov, V.A., Volkov, D.L., Kassens, H., Eicken, H., 1999, Impact of river discharge on the sea land fast ice extension in the Russian shelf area, J. Tuhkuri and K. Riska Eds., in the 15th International Conference on Port and Ocean Engineering under Arctic Conditions, Espoo, Finland, Vol. 1, pp. 311-321.

Dokken, S. T., Haakansson B., and Askne, J., 2000, Inter-comparison of Arctic sea ice concentration using RADARSAT, ERS, SSM/I and in-situ data, Canadian Journal of Remote Sensing, Vol. 26, No. 6, pp. 521-536.

Dokken, S. T., Winsor, P., Markus, T., Askne, J., and Bj”ørk, G., 2002, ERS SAR characterization of coastal polynyas in the Arctic and comparison with SSM/I and numerical model investigations, Remote Sensing of Environment, Vol. 80, No. 2, pp. 321-335.

Drinkwater, M. R., 1998, Satellite microwave radar observations of Antarctic sea ice, in Analysis of SAR Data of the Polar Oceans, C. Tsatsoulis and R. Kwok, Eds., New York, Springer-Verlag, pp. 145-187.

Drinkwater, M. R., and Lytle, V. I., 1997, ERS 1 radar and field-observed characteristics of autumn freeze-up in the Weddell Sea, Journal of Geophysical Research, Vol. 102, No. C6, pp. 12593-12608.

Eicken, H., Alexandrov, V., Bogdanov, A., Martin, T., Reimnitz, E., and Syrtsov, S., 1994, Iceberg observations, Berichte zur Polarforschung, Vol. 149, pp. 76-78.

Eicken, H., Kolatschek, J., Freitag, J., Lindemann, F., Kassens, H., and Dmitrenko, I., 2000, A key source area and constraints on entrainment for basin-scale sediment transport by Arctic sea ice, Geophysical Research Letters, Vol. 27, No. 13, p. 1919-1922.

Eicken, H., Reimnitz, E., Alexandrov, V., Martin, T., Kassens, H., and Viehoff, T., 1997, Sea-ice processes in the Laptev Sea and their importance for sediment export, Continental Shelf Research, Vol. 17, No. 2, pp. 205-233.

Eisen, O., and Kottmeier, C., 2000, On the importance of leads in sea ice to the energy

URN:NBN:no-2344

balance and ice formation in the Weddel Sea, Journal of Geophysical Research, Vol. 105, No. C6, pp. 14045-14060.

Eppler, D. T., Farmer, L. D., Lohanick, A. W., Anderson, M. R., Cavalieri, D. J., Comiso, J., Gloersen, P., Garrity, C., Grenfell, T. C., Hallikainen, M., Maslanik, J. A., Mätzler, C., Melloh, R. A., Rubinstein, I., Swift, C. T., 1992, Passive microwave signatures of sea ice, in Microwave remote sensing of sea ice, F. D. Carsey Ed., Geophysical Monograph 68, American Geophysical Union, Washington, pp. 47-72.

Esbensen, K. H., Guyot, D., Westad, F., Houmøller, L. P., 2001, Multivariate data analysis - in practice, 5th Ed., CAMO Publ., ISBN 82-993330-2-4, 598 pp.

Esbensen, K. H., Hjelmen, K. H., and Kvaal, K., 1996, The AMT approach in chemometrics - first forays, Journal of Chemometrics, Vol. 10, No. 5-6, pp. 569-590.

Falk-Petersen, S., Hop, H., Budgell, W. P., Hegseth, E. N., Korsnes, R., Løyning, T. B., Ørbæk, J. B., Kawamura, T., and Shirasawa, K., 2000, Physical and ecological processes in the marginal ice zone of the northern Barents Sea during the summer melt period, Journal of Marine Systems, Vol. 27, No. 1-3, pp. 131-159.

Farrelly, B. A., Johannessen, J. A., Johannessen, O. M., Svendsen, E., Kloster, K., Horjen, I., Matzler, C., Campbell, W. J., Crawford, J., Harrington, R., Jones, L., Swift, C., Delnore, V. E., Cavalieri, D., Gloersen, P., Hsiao, S. V., Shemdin, O. H., Thomson, T. W., and Ramseier, R. O., 1983, Norwegian Remote Sensing Experiment in a marginal ice zone, Science, Vol. 220, No. 4599, pp. 781-787.

Fetterer, F. M., Gineris, D., and Kwok, R., 1994, Sea ice type maps from Alaska Synthetic Aperture Radar Facility imagery: An assessment, Journal of Geophysical Research, Vol. 99, No. C11, pp. 22443-22458.

Fichefet, T., and Goosse, H., 1999, A numerical investigation of the spring Ross Sea polynya, Geophysical Research Letters, Vol. 26, No. 8, pp. 1015-1018.

Fisher, P., 1997, The pixel: a snare and a delusion, International Journal of Remote Sensing, Vol. 18, No. 3, pp. 679-685.

Flato, G. M., and Brown, R. D., 1996, Variability and climate sensitivity of landfast Arctic sea ice, Journal of Geophysical Research, Vol. 101, No. C10, pp. 25767-25777.

Frank, S. O., 2000, International shipping on the Northern Sea Route - Russia's perspective, in The 21st Century - Turning Point for the Northern Sea Route?, Proceedings from

URN:NBN:no-2344

the Northern Sea Route User Conference, Oslo, 18-20 November 1999, C. L. Ragner, Ed., Dordrecht/Boston/London: Kluwer Academic Publishers, ISBN 0-7923-6365-5, pp. 7-14.

Furevik, B. R., Johannessen, O. M., and Sandvik, A. D., 2001, SAR-retrieved wind in polar regions-comparison with *in situ* data and atmospheric model output, IEEE Transactions on Geoscience and Remote Sensing, accepted.

Gade, M., and Alpers, W., 1999, Using ERS-2 SAR images for routine observation of marine pollution in European coastal waters, The Science of the Total Environment, Vol. 237-238, pp. 441-448.

Gavrilo, M., Bakken, V., Firsova, L., Kalyakin, V., Morozov, V., Pokrovskaya, I., and Isaksen, K., 1998, II.4.2 Oil vulnerability assessment for marine birds occuring along the Northern Sea Route area, INSROP Working Paper No. 97, ISBN 82-7613-238-3. 62 pp., Available from The INSROP Secretariat, The Fridtjof Nansen Institute, P.O. Box 326, N-1326 Lysaker, Norway.

Gill, R. S., 2001, Operational detection of sea ice edges and icebergs using SAR, Canadian Journal of Remote Sensing, Vol. 27, No. 5, pp. 411-432.

Gill, R. S., Rosengreen, M. K., and Valeur, H. H., 2000, Operational ice mapping with Radarsat for ship navigation in the Greenlandic Waters, Canadian Journal of Remote Sensing, Vol. 26, No. 2, pp. 121-132.

Gineris, D. J., and Fetterer, F. M., 1994, An examination of the radar backscatter of sea ice in the East Siberian and Chukchi Seas, in 1994 IEEE International Geoscience and Remote Sensing Symposium, 'Surface and Atmospheric Remote Sensing: Technologies, Data Analysis and Interpretation', California Institute of Technology, Pasadena, California USA, August 8-12, Vol. 1, pp. 499-502.

Gloersen, P., and Cavalieri, D. J., 1986, Reduction of weather effects in the calculation of sea ice concentration from microwave radiances, Journal of Geophysical Research, Vol. 91, No. C3, pp. 3913-3919.

Gogineni, S. P., Moore, R. K., Grenfell, T. C., Barber, D. G., Digby, S., and Drinkwater, M., 1992, The effect of freeze-up and melt processes on microwave signatures, in Microwave Remote Sensing of Sea Ice, F. D. Carsey Ed., Geophysical Monograph 68, American Geophysical Union, Washington, pp. 329-341.

URN:NBN:no-2344

Golub, G. H., and Van Loan, C. F., 1996, Matrix Computations, The Johns Hopkins University Press, 694 pp.

Goosse, H., and Fichefet, T., 2001, Open-ocean convection and polynya formation in a large-scale ice-ocean model, Tellus, Vol. 53A, No. 1, pp. 94-111.

Govorukha, L. S., 1988, Modern glaciation of the Soviet Arctic, Leningrad: Gidrometeoizdat (in Russian).

Granberg, A. G., 1998, The Northern Sea Route: trends and prospects of commercial use, Ocean & Coastal Management, Vol. 41, No. 2-3, pp. 175-207.

Gray, A. L., Short, N., Mattar, K. E., and Jezek, K. C., 2001, Velocities and flux of the Filchner ice shelf and its tributaries determined from speckles tracking interferometry, Canadian Journal of Remote Sensing, Vol. 27, No. 3, pp. 193-206.

Grenfell, T. C., Cavalieri, D. J., Comiso, J. C., Drinkwater, M. R., Onstott, R. G., Rubinstein, I., Steffen, K., and Winebrenner, D. P., 1992, Considerations for microwave remote sensing of thin sea ice, in Microwave remote sensing of sea ice, F. D. Carsey Ed., Geophysical Monograph 68, American Geophysical Union, Washington, pp. 291-301.

Grishchenko, V. D., Smirnov, V. G., Deviatayev, O. S., Shcherbakov, Yu. A., and Kovachev, S. V., 1999, I.3.5 Hydrometeorological and navigational support for NSR navigation, INSROP Working Paper No. 127, ISBN 82-7613-299-5, 54 pp., Available from The INSROP Secretariat, The Fridtjof Nansen Institute, P.O. Box 326, N-1326 Lysaker, Norway.

Gudkovich, Z. M., Kirillov, A. A., Kovalev, E. G., Smetannikov, A. V., and Spichkin, V. A., 1972, The basis of techniques for long-term ice forecasts in the Arctic Seas, Leningrad: Gidrometeoizdat (in Russian).

Gudmandsen, P., Thomsen, B. B., Pedersen, L. T., Skriver, H., and Minnett, P. J., 1995, North-East Water polynya: satellite observations summer 1992 and 1993, International Journal of Remote Sensing, Vol. 16, No. 17, pp. 3307-3324.

Guneriussen, T., Johnsen, H., and Lauknes, I., 2001, Snow cover mapping capabilities using RADARSAT Standard Mode Data, Canadian Journal of Remote Sensing, Vol. 27, No. 2, pp. 109-117.

Haarpaintner, J., Gascard, J.-C., and Haugan, P. M., 2001, Ice production and brine formation in Storfjorden, Svalbard, Journal of Geophysical Research, Vol. 106, No. C7, pp.

URN:NBN:no-2344

14001-14013.

Haas, C., and Eicken, H., 2001, Interannual variability of summer sea ice thickness in the Siberian and central Arctic under different atmospheric circulation regimes, Journal of Geophysical Research, Vol. 106, No. C3, pp. 4449-4462.

Hallikainen, M., and Winebrenner, D. P., 1992, The physical basis for sea ice remote sensing, in Microwave Remote Sensing of Sea Ice, F. D. Carsey, Ed., Geophysical Monograph 68, American Geophysical Union, Washington, pp. 29-46.

Hanesiak, J. M., Barber, D. G., De Abreu, R. A., and Yackel, J. J., 2001, Local and regional albedo observations of arctic first-year sea ice during melt ponding, Journal of Geophysical Research, Vol. 106, No. C1, pp. 1005-1016.

Hanesiak, J. M., Barber, D. G., and Flato, G. M., 1999, Role of diurnal processes in the seasonal evolution of sea ice and its snow cover, Journal of Geophysical Research, Vol. 104, No. C6, pp. 13593-13603.

Harms, I. H., and Karcher, M. J., 1999, Modeling the seasonal variability of hydrography and circulation in the Kara Sea, Journal of Geophysical Research, Vol. 104, No. C6, pp. 13431-13448.

Harms, I. H., Karcher, M. J., and Dethleff, D., 2000, Modelling Siberian river runoff, implications for contaminant transport in the Arctic Ocean, Journal of Marine Systems, Vol. 27, No. 1-3, pp. 95-115.

Haverkamp, D., Soh, L. K., and Tsatsoulis, C., 1995, A comprehensive, automated approach to determining sea ice thickness from SAR data, IEEE Transactions on Geoscience and Remote Sensing, Vol. 33, No. 1, pp. 46-57.

Haverkamp, D., and Tsatsoulis, C., 1999, Information fusion for estimation of summer MIZ ice concentration from SAR imagery, IEEE Transactions on Geoscience and Remote Sensing, Vol. 37, No. 3, pp. 1278-1291.

Helland, I. S., 1990, Partial least squares regression and statistical models, Scandinavian Journal of Statistics, Vol. 17, pp. 97-114.

Henderson, F. M., and Lewis, A. J., Eds., 1998, Principles and applications of imaging radar, Manual of remote sensing, Third edition, Vol. 2, American Society for Photogrammetry and Remote Sensing, John Wiley and Sons, Inc.

URN:NBN:no-2344

Hill, M. J., Smith, A. M., and Foster, T. C., 2000, Remote sensing of grassland with RADARSAT; Case studies from Australia and Canada, Canadian Journal of Remote Sensing, Vol. 26, No. 4, pp. 285-296.

Hilmer, M., and Lemke, P., 2000, On the decrease of Arctic sea ice volume, Geophysical Research Letters, Vol. 27, No. 22., pp. 3751-3754.

Holloway, G., and Sou, T., 2001, Has Arctic sea ice rapidly thinned?, Journal of Climate, accepted.

Huang, J., and Esbensen, K. H., 2000, Applications of angle measure technique (AMT) in image analysis, Part I. A new methodology for *in situ* powder characterization, Chemometrics and Intelligent Laboratory Systems, Vol. 54, No. 1, pp. 1-19.

Huang, J., and Esbensen, K. H., 2001, Applications of AMT (angle measure technique) in image analysis, Part II. Prediction of powder functional properties and mixing components using multivariate AMT regression (MAR), Chemometrics and Intelligent Laboratory Systems, Vol. 57, No. 1, pp. 37-56.

Höskuldsson, A., 1988, PLS Regression Methods, Journal of Chemometrics, Vol. 2, pp. 211-228.

Höskuldsson, A., 1996, Prediction methods in science and technology, Vol. 1, Basic Theory, Thor Publishing, Denmark, 405 pp.

Johannessen, J. A., Digranes, G., Espedal, H., Johannessen, O. M., Samuel, P., Browne, D., and Vachon, P., 1994a, SAR ocean feature catalogue, ESA Publications Division, Noordwijk, The Netherlands, ESA SP-1174, 106 pp.

Johannessen, O. M., Bengtsson, L., Kuzmina, S. I., Miles, M. W., Hasselmann, K., Semenov, V. A., Alekseev, G. V., Nagurny, A. P., Bobylev, L. P., Pettersson, L. H., and Zakharov, V. F., 2002, Arctic climate change - will the ice disappear in this century?, submitted to Science.

Johannessen, O. M., Campbell, W. J., Shuchman, R., Sandven, S., Gloersen, P., Johannessen, J. A., Josberger, E. G., and Haugan, P. M., 1992a, Microwave study programs of air-ice-ocean interactive processes in the seasonal ice zone of the Greenland and Barents Sea, in Microwave Remote Sensing of Sea Ice, F. D. Carsey, Ed., Geophysical Monograph 68, American Geophysical Union, Washington, pp. 261-289.

Johannessen, O. M., and Miles, M. W., 2000, Arctic sea ice and climate change - will the

ice disappear in this century?, Science Progress, Vol. 83, No. 3., pp. 209-222.

Johannessen, O. M., Miles, M. W., and Bjørgo, E., 1995, The Arctic's shrinking sea ice, Nature, Vol. 376, pp. 126-127.

Johannessen, O. M., Sandven, S., Budgell, W. P., Johannessen, J. A., and Shuchman, R., 1994b, Observation and simulation of ice tongues and vortex-pairs in the marginal ice zone, in The Polar Oceans and Their Role in Shaping the Global Environment, The Nansen Centennial Volume, O. M. Johannessen, R. D. Muench, and J. E. Overland Eds., Geophysical Monograph 85, Washington DC, USA, American Geophysical Union, pp. 109-136.

Johannessen, O. M., Sandven, S., Drottning, Å., Kloster, K., Hamre, T., and Miles, M., 1997a, ERS-1 SAR sea ice catalogue, ESA Publications Division, Noordwijk, The Netherlands, ESA SP-1193, 89 pp.

Johannessen, O. M., Sandven, S., Kloster, K., Pettersson, L. H., Melentyev, V. V. Bobylev, L. P., and Kondratyev, K. Ya., 1997b, ERS-1/2 SAR monitoring of dangerous ice phenomena along the western part of Northern Sea Route, Journal of Remote Sensing, Vol. 18, No. 12, pp. 2477-2481.

Johannessen, O. M., Sandven, S., and Melentyev, V., 1996b, ICEWATCH: Ice SAR monitoring of the Northern Sea Route, in Second ERS Applications Workshop, London, 6-8 December 1995, Noordwijk, The Netherlands, No. ESA SP-383, ESA Publications Division, pp. 291-296.

Johannessen, O. M., Sandven, S., Pettersson, L. H., Miles, M., Kloster, K., Melentyev, V. V., Bobylev, L. P., and Kondratyev, K. Ya., 1996a, Near-real-time sea ice monitoring in the Northern Sea Route using ERS-1 SAR and DMSP SSM/I microwave data, Acta Astronautica, Vol. 38, No. 4-8, pp. 457-465.

Johannessen, O. M., Sandven, S., Skagseth, Ø., Kloster, K., Kovacs, Z., Sauvadet, P., Geli, L., Weeks, W., and Louet, J., 1992b, ERS-1 SAR ice routing of 'L′Astrolabe' through the Northeast Passage, in Central Symposium of the 'International Space Year' Conference, Munich, 30 March-4 April 1992, Noordwijk, The Netherlands, No. ESA SP-341, ESA Publications Division, pp. 997-1002.

Johannessen, O. M., Shalina, E. V., and Miles, M. W., 1999, Satellite evidence for an Arctic Sea ice cover in transformation, Science, Vol. 286, No. 5446, pp. 1937-1939.

URN:NBN:no-2344

Johannessen, O. M., Volkov, A. M., Bobylev, L. P., Grishenko, V. D., Sandven, S., Pettersson, L. H., Melentyev, V. V., Asmus, V., Milekhin, O. E., Krovotyntsev, V. A., Smirnov, V. G., Alexandrov, V., Duchossois, G., Kozlov, V., Kohlhammer, G., and Solaas, G., 2000, ICEWATCH: Real-time sea-ice monitoring in the Northern Sea Route (a cooperative Earth observation project between the Russian and the European Space Agencies), Earth Observation and Remote Sensing, Vol. 16, No. 2, pp. 269-281.

Johnson, R. A., and Wichern, D. W., 1992, Applied multivariate statistical analysis, Prentice-Hall, Inc., 642 pp.

Kalnay, E., Kanamitsu, M., Kistler, R., Collins, W., Deaven, D., Gandin, L., Iredell, M., Saha, S., White, G., Woollen, J., Zhu, Y., Leetmaa, A., Reynolds, B., Chelliah, M., Ebisuzaki, W., Higgins, W., Janowiak, J., Mo, K. C., Ropelewski, C., Wang, J., Jenne, R., and Joseph, D., 1996, The NCEP/NCAR 40-Year Reanalysis Project, Bulletin of the Meteorological Society, Vol. 77, No. 3, pp. 437-472.

Kerman, B., 1999, Fusion of dual-frequency SAR imagery of sea ice, Atmosphere-Ocean, Vol. 37, No. 4, pp. 417-438.

Kerman, B., Wadhams, P., Davis, N., and Comiso, J., 1999, Informational equivalence between Synthetic Aperture Radar imagery and the thickness of Arctic pack ice, Journal of Geophysical Research, Vol. 104, No. C12, pp. 29721-29731.

Khvochtchinski, N. I., and Batskikh, Y. M., 1998, The Northern Sea Route as an element of the ICZM system in the Arctic: problems and perspectives, Ocean & Coastal Management, Vol. 41, No. 2-3, pp. 161-173.

Kolatschek, J., Viehoff, T., Eicken, H., Nagelsbach, E., and Alexandrov, V., 1995, Ice dynamics in the southwestern Laptev Sea as derived from ERS-1 SAR images, Berichte zur Polarforschung, Vol. 176, pp. 20-24.

Korsbakken, E., Johannessen, J. A., and Johannessen, O. M., 1998, Coastal wind field retrievals from ERS Synthetic Aperture Radar images, Journal of Geophysical Research, Vol. 103, No. C4, pp. 7857-7874.

Kourti, N., Shepherd, I., Schwartz, G., and Pavlakis, P., 2001, Integrating spaceborne SAR imagery in to operational systems for fisheries monitoring, Canadian Journal of Remote Sensing, Vol. 27, No. 4, pp. 291-305.

Krasnopolsky, V. M., Gemmill, W. H., and Breaker, L. C., 2000, A neural network mul-

tiparameter algorithm for SSM/I ocean retrievals; Comparisons and validations, Remote Sensing of Environment, Vol. 73, No. 2, pp. 133-142.

Kvaal, K., Wold, J. P., Indahl, U. G., Baardseth, P., and Næs, T., 1998, Multivariate feature extraction from textural images of bread, Chemometrics and Intelligent Laboratory Systems, Vol. 42, No. 1-2, pp. 141-158.

Kwok, R., 1998, The RADARSAT Geophysical Processor System, in Analysis of SAR Data of the Polar Oceans, C. Tsatsoulis and R. Kwok, Eds., New York, Springer-Verlag, pp. 235-257.

Kwok, R., 2000, Recent changes in Arctic Ocean sea ice motion associated with the North Atlantic Oscillation, Geophysical Research Letters, Vol. 27, No. 6, pp. 775-778.

Kwok, R., Comiso, J. C., and Cunningham G. F., 1996, Seasonal characteristics of the perennial ice cover of the Beaufort Sea, Journal of Geophysical Research, Vol. 101, No. C12, pp. 28417-28439.

Kwok, R., and Cunningham, G. F., 1994, Backscatter characteristics of the winter ice cover in the Beaufort Sea, Journal of Geophysical Research, Vol. 99, No. C4, pp. 7787-7802.

Kwok, R., Schweiger, A., Rothrock, D. A., Pang, S., and Kottmeier, C., 1998, Sea ice motion from satellite passive microwave imagery assessed with ERS SAR and buoy motions, Journal of Geophysical Research, Vol. 103, No. C4, pp. 8191-8214.

Lang, P. M., and Kalivas, J. H., 1993, A global perspective on multivariate calibration methods, Journal of Chemometrics, Vol. 7, No. 3, pp. 153-164.

Laur, H., Bally, P., Meadows, P., Sanchez, J., Schaettler, B., Lopinto, E., and Esteban, D., 1998, ERS SAR calibration. Derivation of the backscattering coefficient σ^o in ESA ERS SAR PRI products, Tech. Rep. ESTNRSPMHL09, Issue 2.5b, ESA/ESRIN, Frascati, Italy, September 7.

Lebedev, V. L., 1968, Maximum size of a wind-generated lead during sea freezing, Oceanology, Engl. Transl., Vol. 8, pp. 313-318.

Li, S., Cheng, Z., and Weeks, W. F., 1998, Extraction of intermediate scale sea ice deformation parameters from SAR ice motion products, in Analysis of SAR Data of the Polar Oceans, C. Tsatsoulis and R. Kwok, Eds., New York, Springer-Verlag, pp. 69-90.

URN:NBN:no-2344

Liu, Q., 2000, An improved look-up table technique for geophysical parameters from SSM/I, International Journal of Remote Ssensing, Vol. 21, No. 8, pp. 1571-1582.

Liu, A. K., and Peng, C. Y., 1998, Wavelet analysis of SAR images in the marginal ice zone, in Analysis of SAR Data of the Polar Oceans, C. Tsatsoulis and R. Kwok, Eds., New York, Springer-Verlag, pp. 111-128.

Liu, A. K., Peng, C. Y., and Weingartner, T. J., 1994, Ocean-ice interaction in the marginal ice zone using Synthetic Aperture Radar imagery, Journal of Geophysical Research, Vol. 99, No. C11, pp. 22391-22400.

Liu, A. K., Wu, S. Y., Tseng, W. Y., and Pichel, W. G., 2000, Wavelet analysis of SAR images for coastal monitoring, Canadian Journal of Remote Sensing, Vol. 26, No. 6, pp. 494-500.

Luis, A. J., and Kawamura, H., 2001, Characteristics of atmospheric forcing and SST cooling events in the Gulf of Mannar during winter monsoon, Remote Sensing of Environment, Vol. 77, No. 2, pp. 139-148.

Lundhaug, M., 2001, ERS SAR studies of sea ice signatures in the Pechora and Kara Sea region, Canadian Journal of Remote Sensing, in press.

Løset, S., Shkhinek, K., Gudmestad, O. T., Strass, P., Michalenko, E., Frederking, R., and Kärnä, T., 1999, Comparison of the physical environment of some Arctic seas, Cold Regions Science and Technology, Vol. 29, No. 3, pp. 201-214.

Mandel, J., 1982, Use of singular value decomposition in regression analysis, The American Statistician, Vol. 36, No. 1, pp. 15-24.

Markus, T., and Burns, B. A., 1995, A method to estimate subpixel-scale coastal polynyas with satellite passive microwave data, Journal of Geophysical Research, Vol. 100, No. C3, pp. 4473-4487.

Martens, H., and Næs, T., 1989, Multivariate calibration, John Wiley & Sons Ltd., 417 pp.

Martin, S., and Cavalieri, D. J., 1989, Contributions of the Siberian shelf polynyas to the Arctic Ocean intermediate and deep water, Journal of Geophysical Research, Vol. 94, No. C9, pp. 12725-12738.

Martin, S., Drucker, R., and Yamashita, K., 1998, The production of ice and dense shelf

water in the Okhotsk Sea polynyas, Journal of Geophysical Research, Vol. 103, No. C12, pp. 27771-27782.

Martin, S., Wakatsuchi, M., and Ono, N., 1995, Ice and ocean processes in the Tatarskiy Strait, Japan Sea, as revealed by ERS-1 SAR, International Journal of Remote Sensing, Vol. 16, No. 17, pp. 3227-3243.

Maykut, G. A., 1978, Energy exchange over young sea ice in the central Arctic, Journal of Geophysical Research, Vol. 83, No. C7, pp. 3646-3658.

Melentyev, V. V., Johannessen, O. M., Sandven, S., and Pettersson, L. H., 1999, Ice regime study for the Ob-Yenisey Estuaries using ERS SAR Data, in 1999 IEEE International Geoscience and Remote Sensing Symposium 'Remote Sensing of the System Earth - A Challenge for the 21st Century', Jun 28-Jul 2, Hamburg, Germany, Vol. 2, pp. 1037-1039.

Melling, H., 1998, Detection of features in first-year pack ice by Synthetic Aperture Radar (SAR), International Journal of Remote Sensing, Vol. 19, No. 6, pp. 1223-1249.

Miles, M. W., and Barry, R. G., 1998, A 5-year satellite climatology of winter sea ice leads in the western Arctic, Journal of Geophysical Research, Vol. 103, No. C10, pp. 21723-21734.

Milne, A. K., Horn, G., and Finlayson, M., 2000, Monitoring wetlands inundation patterns using RADARSAT multitemporal data, Canadian Journal of Remote Sensing, Vol. 26, No. 2, pp. 133-141.

Morales Maqueda, M. A., and Willmott, A. J., 2000, A two-dimensional time-dependent model of a wind-driven coastal polynya: application to the St. Lawrence Island polynya, Journal of Physical Oceanography, Vol. 30, No. 6, pp. 1281-1304.

Morland, J. C., Grimes, D. I. F., and Hewison, T. J., 2001, Satellite observations of the microwave emissivity of a semi-arid land surface, Remote Sensing of Environment, Vol. 77, No. 2, pp. 149-164.

Mulherin, N. D., 1996, The Northern Sea Route-its development and evolving state of operations in the 1990s, CRREL Report 96-3, US Army Corps of Engineers, Cold Regions Research & Engineering Laboratory, 72 Lyme Road Hanover, New Hampshire 037551290, 76 pp.

Mulherin, N. D., Sodhi, D. S., and Smallidge, E., 1994, Northern Sea Route and ice-

breaking technology an overview of current conditions, CRREL Report MP 3520, US Army Corps of Engineers, Cold Regions Research & Engineering Laboratory, 72 Lyme Road Hanover, New Hampshire 03755-1290, 162 pp.

Murtha, P. A., 2000, Surficial geology and climatic effects on forest clearcut tone in RADARSAT images of Northern Vancouver Island, Canadian Journal of Remote Sensing, Vol. 26, No. 3, pp. 253-262.

Mysak, L. A., 2001, Patterns of Arctic circulation, Science, Vol. 293, No. 5533, 1269-1270.

Mysak, L. A., and Huang, F., 1992, A latent- and sensible-heat polynya model for the North Water, Northern Baffin Bay, Journal of Physical Oceanography, Vol. 22, No. 6, pp. 596-608.

National Snow and Ice Data Center, 1999, Bootstrap sea ice concentrations from Nimbus-7 SMMR and DMSP SSM/I. Digital data available from nsidc@kryos.colorado.edu. Boulder, Colorado. NSIDC Distributed Active Archive Center, University of Colorado at Boulder.

Nghiem, S.V., and Bertoia, C., 2001, Study of multi-polarization C-Band backscatter signatures for Arctic Sea ice mapping with future satellite SAR, Canadian Journal of Remote Sensing, Focus Issue on Ice and Icebergs, Vol. 27, No. 5, pp. 387-402.

Nghiem, S. V., Martin, S., Perovich, D. K., Kwok, R., Drucker, R., and Gow, A. J., 1997, A laboratory study of the effect of frost flowers on C band radar backscatter from sea ice, Journal of Geophysical Research, Vol. 102, No. C2, pp. 3357-3370.

Nystuen, J. A., and Garcia, Jr. F. W., 1992, Sea ice classification using SAR backscatter statistics, IEEE Transactions on Geoscience and Remote Sensing, Vol. 30, No. 3, pp. 502-509.

Olmsted, C., 1993, Alaska SAR Facility Scientific SAR User's Guide, HTML version at http://www.asf.alaska.edu.

Onstott, R. G., 1992, SAR and Scatterometer signatures of sea ice, in Microwave Remote Sensing of Sea Ice, F. D. Carsey, Ed., Geophysical Monograph 68, American Geophysical Union, Washington, pp. 73-104.

Ou, H. W., 1988, A time-dependent model of a coastal polynya, Journal of Physical Oceanography, Vol. 18, No. 4, pp. 584-590.

URN:NBN:no-2344

Parkinson, C. L., Rind, D., Healy, R. J., Martinson, D. G., 2001, The impact of sea ice concentration accuracies on climate model simulations with the GISS GCM, Journal of Climate, Vol. 14, No. 12, pp. 2606-2623.

Pavlov, V. K., and Pfirman, S. L., 1995, Hydrographic structure and variability of the Kara Sea: Implications for pollutant distribution, Deep Sea Research Part II: Topical Studies in Oceanography, Vol. 42, No. 6, pp. 1369-1390.

Pavlov, V. K., and Stanovoy, V. V., 2001, The problem of transfer of radionuclide pollution by sea ice, Marine Pollution Bulletin, Vol. 42, No. 4, pp. 319-323.

Pease, C. H., 1987, The size of wind-driven coastal polynyas, Journal of Geophysical Research, Vol. 92, No. C7, pp. 7049-7059.

Peresypkin, V. I., 2000, Introduction to the Northern Sea Route history and INSROP's background, in The 21st Century - Turning Point for the Northern Sea Route?, Proceedings from the Northern Sea Route User Conference, Oslo, 18-20 November 1999, C. L. Ragner, Ed., Dordrecht/Boston/London: Kluwer Academic Publishers, ISBN 0-7923-6365-5, pp. 23-32.

Perovich, D. K., and Richter-Menge, J. A., 1994, Surface characteristics of lead ice, Journal of Geophysical Research, Vol. 99, No. C8, pp. 16341-16350.

Perovich, D. K., and Richter-Menge, J. A., 2000, Ice growth and solar heating in springtime leads, Journal of Geophysical Research, Vol. 105, No. C3, pp. 6541-6548.

Pettersson, L. H., Sandven, S., Dalen, Ø., Melentyev, V. V., and Babich, N. I., 2000, Satellite radar ice monitoring for ice navigation of a tanker convoy in the Kara Sea, in Journal of the 10th International Offshore and Polar Engineering Conference (ISOPE-2000), ISBN 1-880653-47-8, Seattle, USA, May 28-June 2, Vol. 1, pp. 691-696.

Pfirman, S. L., Eicken, H., Bauch, D., and Weeks, W. F., 1995, The potential transport of pollutants by Arctic sea ice, The Science of The Total Environment, Vol. 159, No. 2-3, pp. 129-146.

Pfirman, S. L., Kögeler, J. W., and Rigor, I., 1997, Potential for rapid transport of contaminants from the Kara Sea, The Science of the Total Environment, Vol. 202, pp. 111-122.

Pohl, C., and van Genderen, J. L., 1998, Multisensor image fusion in remote sensing: concepts, methods and applications, International Journal of Remote Sensing, Vol. 19, No. 5, pp. 823-854.

URN:NBN:no-2344

Pond, S., and Pickard, G. L., 1983, Introductory dynamical oceanography, 2nd Edition, Pergamon Press plc, Headington Hill Hall, Oxford OX3 0BW, England, ISBN 0-08-028728-X, 329 pp.

Power, D., Youden, J., Lane, K., Randell, C., and Flett, D., 2001, Iceberg detection capabilities of RADARSAT Synthetic Aperture Radar, Canadian Journal of Remote Sensing, Vol. 27, No. 5, pp. 476-486.

Preller, R. H., Walsh, J. E., and Maslanik, J. A., 1992, The use of satellite observations in ice cover simulations, in Microwave Remote Sensing of Sea Ice, F. D. Carsey, Ed., Geophysical Monograph 68, American Geophysical Union, Washington, pp. 385-404.

Proshutinsky, A. Yu., Proshutinsky, T., and Weingartner, T., 1999, I.5.8 Environmental conditions affecting commercial shipping on the Northern Sea Route, INSROP Working Paper No. 126, ISBN 82-7613-296-0, 52 pp., Available from The INSROP Secretariat, The Fridtjof Nansen Institute, P.O. Box 326, N-1326 Lysaker, Norway.

Pulliainen, J., and Hallikainen, M., 2001, Retrieval of regional snow water equivalent from space-borne passive microwave observations, Remote Sensing of Environment, Vol. 75, No. 1, pp. 76-85.

Qin S. J., and McAvoy, T. J., 1992, Nonlinear PLS modeling using neural networks, Computers & Chemical Engineering, Vol. 16, No. 4, pp. 379-391.

RADARSAT, 1997, Data Products Specifications, RSI-GS-026, by RADARSAT International, Richmond, Canada.

Ramsay B., Manore M. J., Weir L., Wilson K., and Bradley, D., 1998, Use of RADARSAT data in the Canadian Ice Service, Canadian Journal of Remote Sensing, Vol. 24, No. 1, pp. 36-42.

Rees, W. G., and Satchell, M. J. F., 1997, The effect of median filtering on Synthetic Aperture Radar images, International Journal of Remote Sensing, Vol. 18, No. 13, pp. 2887-2893.

Reimnitz E., Eicken, H., Martin, T., 1995, Multiyear fast ice along the Taymyr Peninsula, Siberia, Arctic, Vol. 48, No. 4, pp. 359-367.

Remund, Q. P., Long, D. G., and Drinkwater, M. R., 2000, An iterative approach to multisensor sea-ice classification, IEEE Transactions on Geoscience and Remote Sensing, Vol. 38, No. 4, pp. 1843-1856.

URN:NBN:no-2344

Rigor, I., and Colony, R., 1997, Sea-ice production and transport of pollutants in the Laptev Sea, 1979-1993, The Science of The Total Environment, Vol. 202, No. 1-3, pp. 89-110.

Ripley, B. D., 1996, Pattern recognition and neural networks, Cambridge University Press, Cambridge, ISBN 0 521 46086 7, 403 pp.

Robinson, I. S., 1994, Satellite oceanography, An introduction for oceanographers and remote sensing scientists, Wiley-PRAXIS series in remote sensing, John Wiley and Sons, Inc.

Romanov, I. P., 1995, Atlas of ice and snow of the Arctic Basin and Siberian Shelf Seas, A. Tunik, Ed., Backbone Press, New York, Second edition, ISBN 0-9644311-3-0, 277 pp.

Rothrock, D. A., Yu, Y., and Maykut, G. A., 1999, Thinning of the Arctic sea-ice cover, Geophysical Research Letters, Vol. 26, No. 23, pp. 3469-3472.

Ruffieux, D., Persson, P. O. G., Fairall, C. W., and Wolfe, D. E., 1995, Ice pack and lead surface energy budgets during LEADEX 1992, Journal of Geophysical Research, Vol. 100, No. C3, pp. 4593-4612.

Sakshaug, E. (Ed.), 1992, Økosystem Barentshavet (Pro Mare), Norges forskningsråd, Universitetsforlaget, ISBN 82-90565-17-8, (in Norwegian), 304 pp.

Sandven, S., Alexandrov, V., Dalen, Ø., Lundhaug, M., Melentyev, V., Smirnov, V., Babich, N., and Kloster, K., 1999a, I.2.4 Practical demonstration of real-time RADARSAT SAR data for ice navigation on the Northern Sea Route, INSROP Working Paper No. 134, ISBN 82-7613-316-9, 40 pp., Available from The INSROP Secretariat, The Fridtjof Nansen Institute, P.O. Box 326, N-1326 Lysaker, Norway.

Sandven, S., Johannessen, O. M., Kloster, K., and Miles, M., 1994, SIZEX'92 ERS-1 SAR ice validation experiment, in Microwave Remote Sensing of Sea Ice (Ed. J. Askne), EARSeL Proceedings, pp. 50-56.

Sandven, S., Johannessen, O. M., Miles, M. W., Pettersson, L. H., and Kloster, K., 1999b, Barents Sea seasonal ice zone features and processes from ERS 1 Synthetic Aperture Radar: seasonal ice zone experiment 1992, Journal of Geophysical Research, Vol. 104, No. C7, pp. 15843-15857.

Sandven, S., Laxon, S., Drange, H., Lisæther, K. A., Sagen, H., and Evensen, G., 2001,

Study on the quantification of the importance of the sea ice budget in the climate system, Final report under ESA ESTEC Contract No. 13971/00/NL/DC, Nansen Environmental and Remote Sensing Center, Bergen, Norway, and Centre for Polar Observations and Modelling, Department of Space and Climate Physics, University College London, UK, 163 pp.

Schneider, W., and Budéus, G., 1995, On the generation of the Northeast Water Polynya, Journal of Geophysical Research, Vol. 100, No. C3, pp. 4269-4286.

Sephton, A. J., and Partington, K. C., 1998, Towards operational monitoring of Arctic sea ice by SAR, in Analysis of SAR Data of the Polar Oceans, C. Tsatsoulis and R. Kwok, Eds., New York, Springer-Verlag, pp. 259-279.

Sherwood, C. R., 1999, Numerical model of frazil ice and suspended sediment concentrations and formation of sediment laden ice in the Kara Sea, Journal of Geophysical Research, Vol. 105, No. C6, pp. 14061-14080.

Shokr, M. E., 1991, Evaluation of second-order texture parameters for sea ice classification from radar images, Journal of Geophysical Research, Vol. 96, No. C6, pp. 10625-10640.

Shokr, M. E., Jessup, R., and Ramsay, B., 1999, An interactive algorithm for derivation of sea ice classifications and concentrations from SAR images, Canadian Journal of Remote Sensing, Vol. 25, No. 1, pp. 70-79.

Shokr, M. E., Ramsay B., and Falkingham J. C., 1996, Operational use of ERS-1 SAR images in the Canadian ice monitoring programme, International Journal of Remote Sensing, Vol. 17, No. 4, pp. 667-682.

Siegert, F., and Hoffmann, A. A., 2000, The 1998 forest fires in East Kalimantan (Indonesia); A quantitative evaluation using high resolution, multitemporal ERS-2 SAR images and NOAA-AVHRR hotspot data, Remote Sensing of Environment, Vol. 72, No. 1, pp. 64-77.

Smith, D. M., Barrett, E. C., and Scott, J. C., 1995, Sea-ice type classification from ERS-1 SAR data based on grey level and texture information, Polar Record, Vol. 31, No. 177, pp. 135-146.

Smith, S. D., Muench, R. D., and Pease, C. H., 1990, Polynyas and leads: An overview of physical processes and environment, Journal of Geophysical Research, Vol. 95, No.

URN:NBN:no-2344

C6, pp. 9461-9479.

Steffen, K., and Heinrichs, J., 1994, Feasibility of sea ice typing with Synthetic Aperture Radar (SAR): merging of Landsat Thematic Mapper and ERS 1 SAR satellite imagery, Journal of Geophysical Research, Vol. 99, No. C11, pp. 22413-22424.

Steffen, K., Key, J., Cavalieri, D. J., Comiso, J., Gloersen, P., St. Germain, K., and Rubinstein, I., 1992, The estimation of geophysical parameters using passive microwave algorithms, in Microwave Remote Sensing of Sea Ice, F. D. Carsey, Ed., Geophysical Monograph 68, American Geophysical Union, Washington, pp. 201-231.

Steffen, K., and Schwieger, A., 1991, NASA Team algorithm for sea ice concentration retrieval from Defense Meteorological Satellite Program Special Sensor Microwave/-Imager: Comparison with Landsat satellite imagery, Journal of Geophysical Research, Vol. 96, No. C12, pp. 21971-21988.

Stirling, I., 1997, The importance of polynyas, ice edges, and leads to marine mammals and birds, Journal of Marine Systems, Vol. 10, No. 1-4, pp. 9-21.

Svendsen, E., Kloster, K., Farrelly, B., Johannessen, O. M., Johannessen, J. A., Campbell, W. J., Gloersen, P., Cavalieri, D., and Matzler, C., 1983, Norwegian Remote Sensing Experiment: evaluation of the Nimbus 7 Scanning Multichannel Microwave Radiometer for sea ice research, Journal of Geophysical Research, Vol. 88, No. C5, pp. 2781-2791.

Thomas, D., Martin, S., Rothrock, D., and Steele, M., 1996, Assimilating satellite concentration data into an Arctic sea ice mass balance model, 1979-1985, Journal of Geophysical Research, Vol. 101, No. C9, pp. 20849-20868.

Toudal, L., 1999, Ice extent in the Greenland Sea 1978-1995, Deep Sea Research Part II: Topical Studies in Oceanography, Vol. 46, No. 6-7, pp. 1237-1254.

Toudal, L., Hansen, K. Q., Valeur, H., Wadhams, P., Aldworth, E., and Comiso, J. C., 1999, Mapping of ice in the Odden by satellite and airborne remote sensing, Deep Sea Research Part II: Topical Studies in Oceanography, Vol. 46, No. 6-7, pp. 1255-1274.

Tucker III, W. B., Perovich, D. K., Gow, A. J., Weeks, W. F., and Drinkwater, M. R., 1992, Physical properties of sea ice relevant to remote sensing, in Microwave Remote Sensing of Sea Ice, F. D. Carsey, Ed., Geophysical Monograph 68, American Geophysical Union, Washington, pp. 9-28.

Tucker III, W. B., Weatherly, J. W., Eppler, D. T., Farmer, L. D., Bentley, D. L., 2001,

Evidence for rapid thinning of sea ice in the western Arctic Ocean at the end of the 1980s, Geophyscal Research Letters, Vol. 28, No. 14, pp. 2851-2854.

Ulander, L. M. H., Carlström, A., and Askne, J., 1995, Effect of frost flowers, rough saline snow and slush on the ERS-1 SAR backscatter of thin Arctic sea-ice, International Journal of Remote Sensing, Vol. 16, No. 17, pp. 3287-3305.

Vachon, P. W., and Dobson, F. W., 2000, Wind retrieval from RADARSAT SAR images: Selection of a suitable C-band HH polarization wind retrieval model, Canadian Journal of Remote Sensing, Vol. 26, No. 4, pp. 306-313.

Vainio, J., Similä, M., and Grönvall, H., 2000, Operational use of RADARSAT SAR data as aid to winter navigation in the Baltic Sea, Canadian Journal of Remote Sensing, Vol. 26, No. 4, pp. 314-317.

Van Woert, M. L., 1999, Wintertime dynamics of the Terra Nova Bay polynya, Journal of Geophysical Research, Vol. 104, No. C4, pp. 7753-7769.

Vefsnmo, S., 1999, I.5.7 Statistical oil spill simulations for the Northern Sea Route, IN-SROP Working Paper No. 136, ISBN 82-7613-319-3, 58 pp., Available from The IN-SROP Secretariat, The Fridtjof Nansen Institute, P.O. Box 326, N-1326 Lysaker, Norway.

Vinje, T., 2001, Anomalies and trends of sea-ice extent and atmospheric circulation in the Nordic Seas during the period 1864-1998, Journal of Climate, Vol. 14, No. 3, pp. 255-267.

Vinnikov, K. Y., Robock, A., Stouffer, R. J., Walsh, J. E., Parkinson, C. L., Cavalieri, D. J., Mitchell, J. F. B., Garrett, D., and Zakharov, V. F., 1999, Global warming and Northern Hemisphere sea ice extent, Science, Vol. 286, No. 5446, pp. 1934-1937.

Volkov, V. A., Johannessen, O. M., Borodachev, V. E., Voinov, G. N., Pettersson, L. H., Bobylev, L. P., and Kouraev, A. V., 2002, Polar seas oceanography: An integrated case study of the Kara Sea, Springer-Praxis books in environmental sciences, Praxis Publishing Ltd., in press.

Wadhams, P., 2000, Ice in the ocean, Gordon and Breach, ISBN 9056992961, 351 pp.

Wadhams, P., and Comiso, J. C., 1992, The ice thickness distribution inferred using remote sensing techniques, in Microwave remote sensing of sea ice, F. D. Carsey Ed., Geophysical Monograph 68, American Geophysical Union, Washington, pp. 375-383.

URN:NBN:no-2344

Wadhams, P., and Davis, N. R., 2000, Further evidence of ice thinning in the Arctic Ocean, Geophysical Research Letters, Vol. 27, No. 24, pp. 3973-3976.

Wendler, G. Gilmore, D., and Curtis, J., 1997, On the formation of coastal polynyas in the area of Commonwealth Bay, Eastern Antarctica, Atmospheric Research, Vol. 45, pp. 55-75.

Wettlaufer, J. S., Grae Worster, M., and Huppert, H. E., 2000, Solidification of leads: Theory, experiment, and field observations, Journal of Geophysical Research, Vol. 105, No. C1, pp. 1123-1134.

Willmott, A. J., Morales Maqueda, M. A., and Darby, M. S., 1997, A model for the influence of wind and oceanic currents on the size of a steady-state latent heat coastal polynya, Journal of Physical Oceanography, Vol. 27, No. 10, pp. 2256-2275.

Winebrenner, D. P., Long, D. G., and Holt, B., 1998, Mapping the progression of melt onset and freeze-up on Arctic sea ice using SAR and Scatterometry, in Analysis of SAR Data of the Polar Oceans, C. Tsatsoulis and R. Kwok, Eds., New York, Springer-Verlag, pp. 129-144.

Winebrenner, D. P., Holt, B., and Nelson, E. D., 1996, Observation of autumn freeze-up in the Beaufort and Chukchi Seas using the ERS 1 Synthetic Aperture Radar, Journal of Geophysical Research, Vol. 101, No. C7, pp. 16401-16419.

Winebrenner, D. P., Nelson, E. D., Colony, R., and West, R. D., 1994, Observation of melt onset on multiyear Arctic sea ice using the ERS 1 Synthetic Aperture Radar, Journal of Geophysical Research, Vol. 99, No. C11, pp. 22425-22441.

Winsor, P., 2001, Arctic sea ice thickness remained constant during the 1990s, Geophysical Research Letters, Vol. 28, No. 6, pp. 1039-1041.

Winsor, P., and Björk, G., 2000, Polynya activity in the Arctic Ocean from 1958 to 1997, Journal of Geophysical Research, Vol. 105, No. C4, pp. 8789-8803.

Wise, B. M., and Gallagher, N. B., 1998, PLS_Toolbox version 2.0 for use with Matlab, Eigenvector Research, Inc., 830 Wapato Lake Road, Manson, WA 98831, 320 pp.

Wohl, G. M., 1995, Operational sea ice classification from Synthetic Aperture Radar imagery, Photogrammetric Engineering & Remote Sensing, Vol. 61, No. 12, pp. 1455-1462.

URN:NBN:no-2344

World Meteorological Organization, 1970, WMO Sea-Ice Nomenclature, Secretariat of the World Meteorological Organization, Publication No. 259, Tp. 145, Geneva, Switzerland.

Xuwu, X., and Smith, E. A., 1997, Feasibility of simultaneous surface temperature-emissivity retrieval using SSM/I measurements from HAPEX-Sahel, Journal of Hydrology, Vol. 188-189, No. 1-4, pp. 330-360.

Yackel, J. J., and Barber, D. G., 2000, Melt ponds on sea ice in the Canadian Archipelago, 2., On the use of RADARSAT-1 Synthetic Aperture Radar for geophysical inversion, Journal of Geophysical Research, Vol. 105, No. C9, pp. 22061-22070.

Yackel, J. J., Barber, D. G., and Hanesiak, J. M., 2000, Melt ponds on sea ice in the Canadian Archipelago, 1., Variability in morphological and radiative properties, Journal of Geophysical Research, Vol. 105, No. C9, pp. 22049-22060.

Zabel, I. H. H., Jezek, K. C., Gogineni, S. P., and Kanagaratnam, P., 1996, Search for proxy indicators of young sea ice thickness, Journal of Geophysical Research, Vol. 101, No. C3, pp. 6697-6709.

Zakharov, V.F., 1966, The role of flaw leads off the edge of fast ice in the hydrological and ice regime of the Laptev Sea, Oceanology, Vol. 6, pp. 815-821, (in Russian).

Zhang, J., Rothrock, D., and Steele, M., 2000, Recent changes in Arctic Sea ice: the interplay between ice dynamics and thermodynamics, Journal of Climate, Vol. 13, No. 17, pp. 3099-3114.

Zhang, Y., and Hunke, E. C., 2001, Recent Arctic change simulated with a coupled ice-ocean model, Journal of Geophysical Research, Vol. 106, No. C3, pp. 4369-4390.

Østreng, W., (ed.), 1999, The Natural and Societal Challenges of the Northern Sea Route. A reference Work. Dordrecht/Boston/London: Kluwer Academic Publishers, ISBN 0-7923-6112-1, 466 pp.

URN:NBN:no-2344